

NO-A105 004

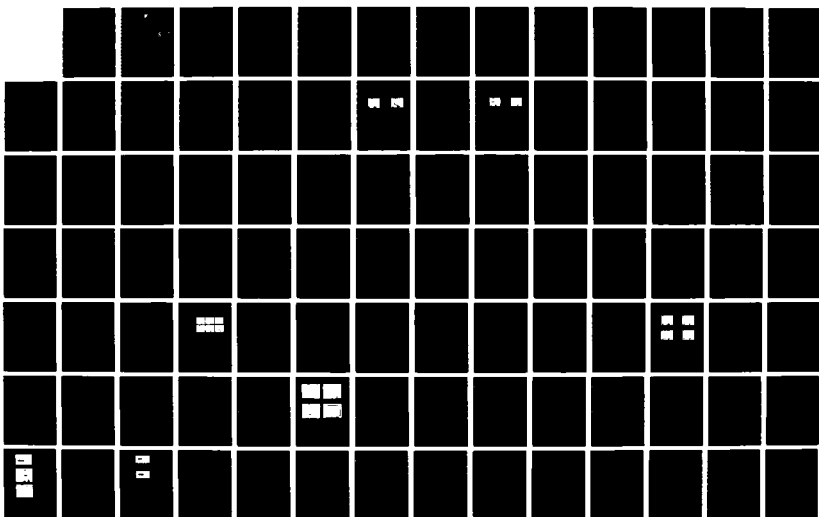
SPACE-BASED BLUE-GREEN LASER(U) AVCO EVERETT RESEARCH
 LAB INC EVERETT WA J C HSIA ET AL. OCT 81
 N00123-80-C-1135

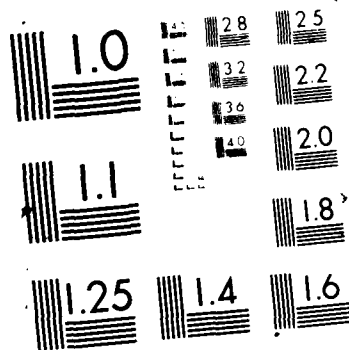
1/3

UNCLASSIFIED

F/G 9/3

ML





DTIC FILE COPY

1

AD-A185 884



SPACE-BASED BLUE-GREEN LASER

J. C. Hsia, M. W. McGeoch and D. E. Klimek
AVCO EVERETT RESEARCH LABORATORY, INC.
a Subsidiary of Avco Corporation
Everett, MA. 02149

October 1981

Final Technical Report for Period June 9, 1980 - June 8, 1981

DTIC
ELECTE
OCT 15 1987
S D

DISTRIBUTION UNLIMITED

Prepared for

NAVAL OCEAN SYSTEMS CENTER
271 Catalina Boulevard
San Diego, California 92152

Naval Regional Contracting Office
Long Beach, California 90822

APPROVED FOR PUBLIC RELEASE;
DISTRIBUTION UNLIMITED

87 10 8 111

UNCLASSIFIED

SECURITY CLASSIFICATION OF THIS

REPORT DOC

AD-A185 884

READ INSTRUCTIONS
BEFORE COMPLETING FORM
REPORT'S CATALOG NUMBER

1. REPORT NUMBER

4. TITLE (and Subtitle)

Space-Based Blue-Green Laser

5. TYPE OF REPORT & PERIOD COVERED
Final Technical Report
6/9/80 - 6/8/81

6. PERFORMING ORG. REPORT NUMBER

7. AUTHOR(s)

J.C. Hsia, M.W. McGeoch, D.E. Klimek,
J. Moran, C.T. Pike, P.N. Everett,
J. Eninger

8. CONTRACT OR GRANT NUMBER(s)

N00123-80-C-1135

9. PERFORMING ORGANIZATION NAME AND ADDRESS

Avco Everett Research Laboratory (AERL)
2385 Revere Beach Parkway
Everett, Massachusetts 0214910. PROGRAM ELEMENT, PROJECT, TASK
AREA & WORK UNIT NUMBERS

11. CONTROLLING OFFICE NAME AND ADDRESS

Naval Ocean Systems Center
271 Catalina Boulevard
San Diego, California 92152

12. REPORT DATE

October 1981

13. NUMBER OF PAGES

247

14. MONITORING AGENCY NAME & ADDRESS (if different from Controlling Office)

Naval Regional Contracting Office
Long Beach, California 90822

15. SECURITY CLASS. (of this report)

Unclassified

15a. DECLASSIFICATION/DOWNGRADING
SCHEDULE

16. DISTRIBUTION STATEMENT (of this Report)

APPROVED FOR PUBLIC RELEASE;
DISTRIBUTION UNLIMITED

17. DISTRIBUTION STATEMENT (of the abstract entered in Block 20, if different from Report)

18. SUPPLEMENTARY NOTES

19. KEY WORDS (Continue on reverse side if necessary and identify by block number)

Electron Beam Sustained Discharge HgBr Laser,
Electron Collisional Processes, on HgBr₂
Laser Gain, and Absorption,
Laser Efficiency,
Design of 200 W Laser

20. ABSTRACT (Continue on reverse side if necessary and identify by block number)

An experimental and theoretical program has been completed which thoroughly characterizes the e-beam sustained discharge HgBr laser. The preliminary design of a 100 Hz, 2 J HgBr laser has been performed. From measurements of HgBr fluorescence efficiency as a function of E/N the primary laser excitation process has been identified as the collisional excitation of HgBr₂ by electrons. A self-consistent set of excitation cross sections is

UNCLASSIFIED

SECURITY CLASSIFICATION OF THIS PAGE(When Data Entered)

(20)

derived from the experiment. The formation efficiency of HgBr(B) in a discharge is 6%. The stimulated emission cross section at 502 nm is measured to be $1.6 \times 10^{-16} \text{ cm}^2$. Absorbing species are identified as HgBr(X) (absorption cross section $5 \times 10^{-20} \text{ cm}^2$ at 520 nm) and HgBr_2^+ ($2 \times 10^{-18} \text{ cm}^2$ at 520 nm). The maximum laser intrinsic efficiency is measured to be 3.3%. The maximum electrical efficiency is 2.4%. Lasing energy density is 2 J/l in a HgBr_2/Ar mix. Maximum lasing energy is 9.8 J. Detailed design conditions are given for a 100 Hz, 2 J HgBr e-beam sustained discharge laser, of overall efficiency 1.2%.



Accession for	
NTIS CRA&I	<input checked="" type="checkbox"/>
DTIC TAB	<input type="checkbox"/>
Unannounced	<input type="checkbox"/>
Justification	
By	
Distribution /	
Availability Codes	
1-1	
A-1	

UNCLASSIFIED

SECURITY CLASSIFICATION OF THIS PAGE(When Data Entered)

TABLE OF CONTENTS

<u>Section</u>	<u>Page</u>
List of Illustrations	5
List of Tables	11
I. INTRODUCTION	13
II. TECHNICAL PROGRESS	15
A. Kinetic Model and Experiments	15
1. Introduction	15
2. Small-Scale Experiments	16
a. Experimental Methods	16
b. Modeling of $\text{HgBr}^*(\text{B})$ Formation Process	16
c. Comparison with Experiment in Different Gases	28
d. Specific Fluorescence with Different Buffer Gases	38
e. Laser Performance with Different Buffers: Choice of Argon	38
f. Framework of Laser Kinetic Model for Argon/ HgBr_2	42
g. Formation Efficiency: Absolute Measurement	45
h. Gain Measurement: Stimulated Emission Cross Section	49
i. Absorption Measurements	51
j. Electron Quenching	56
k. Lower Level Deactivation	56
l. Recombination	59
m. Attachment	61
n. Discharge Impedance and Arcing	63
o. Injection and Single Line Lasing	65
p. Voltage Standoff Recovery	67

3.	1 M Device Experiments	68
a.	Summary	68
b.	Experimental Equipment and Methods	69
c.	Laser Intrinsic Efficiency	75
d.	Laser Electrical Efficiency	75
e.	Laser Reproducibility	75
f.	Discharge Energy Loading Limits	80
g.	Streak Photography of Laser Output	81
h.	Measurement of Deposition Uniformity	86
i.	Modeling of E-Beam Deposition	89
j.	Laser Output Spatial Profile	89
k.	Modeling of Anode-Cathode Variation in Lasing	91
III.	PRELIMINARY DESIGN OF 2 J, 100 Hz HgBr LASER	98
A.	Design Requirements	98
B.	Overview of Design	98
C.	Laser Active Medium Design	101
1.	Geometrical Trade-off	101
2.	Laser Efficiency	102
3.	E-Beam Deposition Profiles	106
4.	Anode-to-Cathode Uniformity	106
D.	Laser Cavity Design	110
1.	Discharge Electrodes	110
2.	Current Returns	115
3.	High Voltage Feedthroughs	118
E.	Flow-Loop Design	119
1.	Phase Distortion	119
2.	Flow System Design Criteria	120
a.	Muffler Performance Predictions	123
3.	Flow-Loop Design Approach, Arrangements and Sizing	128
4.	Cavity Thermal Conditioning Requirements	128
5.	Boundary Layer Thermal Control Require- ments	131

6.	Treatment of Foil and Discharge Electrodes	134
7.	Heat Exchanger Performance Requirements	138
8.	Flow Conditioning	141
	a. Cavity Diffuser Design Criteria	143
	b. Heat Exchanger Design Criteria	146
	c. Transition Sections, Turns and Return Leg	147
	d. Fan and Fan Diffuser	148
	e. Velocity Stabilizer	149
	f. Nozzle, Upstream Muffler and Boundary Layer Suction	150
	g. Summary	151
9.	Fan and Drive Train Requirements	153
10.	Liquid Coolant Loop Design	154
11.	Floo-Loop Design Summary	158
F.	Optics and Injection Laser	160
	1. Approach	160
	2. Resonator for the Injection Locked Oscillator (ILO)	161
	3. Injection Interface	165
	4. Master Oscillator for Injection	168
	5. Spectral Control	168
	6. Choice of Shared Mirror between Resonators	170
	7. Injection Laser	172
G.	E-Beam	175
	1. Design Approach and Rationale	175
	2. E-Gun Design Description	177
	a. Vacuum Chamber	177
	b. High-Voltage Terminal	177
	c. High-Voltage Busing	179
	d. Pumping Bakeout and System	179
	e. Foil and Foil Support	181
	3. E-Beam Pulsed Power	181
	a. Internal Grid Switching Option	182
	b. External High-Voltage Pulsing	182
	c. E-Beam Power Requirement	183

H.	Magnetic Field Design	184
1.	Field Requirements	184
2.	Field Uniformity	185
3.	Coil Design	185
4.	Dewar Construction	190
5.	Refrigerator Power	191
6.	Use of Niobium Tin	192
I.	Pulse Discharge Modulator Design	193
1.	Circuit Topology	193
a.	Blumlein Circuit	193
b.	Line Pulser Circuit	195
2.	Networks	195
3.	Thyratrons	197
4.	Modulator Efficiency	208
J.	Gas Cleanup/Makeup	210
1.	Chemical Processes	210
2.	Gas Cleanup System	216
K.	Overall System Description and Performance	220
1.	Efficiency	220
2.	Beam Quality	222
3.	Lifetime	229

Appendicies

A.	Buildup of Lasing and Savings from Injection	233
B.	Design of Master Oscillator for Injection	241
C.	Narrow Band HgBr Laser Operation	243

LIST OF ILLUSTRATIONS

<u>Figure</u>		<u>Page</u>
1	Detail of the Small-Scale Laser Chamber	17
2	Schematic of Small-Scale E-Beam and Discharge Circuit	18
3	Small-Scale E-Beam and Capacitor Discharge Characteristics	19
4	Schematic of Small-Scale Cable PFL	20
5	Typical Laser Discharge, Sidelight and Output Characteristics with Cable PFL	21
6	Apparatus for Gain and Absorption Experiments	22
7	HgBr*(B) Formation Efficiency as a Function of E/N	27
8	HgBr ₂ Electronic Cross Sections from Fitting Procedure	29
9	Computed Discharge Fractional Power vs E/N	30
10	Computed Formation Efficiency vs HgBr ₂ Concentration	31
11	Computed Drift Velocity vs HgBr ₂ Concentration	33
12	Computed Fluorescence Efficiency for Various Buffer Gases	34
13	Theoretical and Experimental Fluorescence for Argon and Neon Buffers	35
14	Computed Single-Step Arcing Fields of Argon and Neon	36
15	Theoretical and Experimental Fluorescence for Neon, 10% Xenon, and Argon, 5% Xenon Buffers	37

<u>Figure</u>		<u>Page</u>
16	Integrated Fluorescence with Different Buffers at Constant E-Beam	39
17	Experimental Relative Fluorescence Efficiencies for Different Buffers	40
18	Kinetic Scheme for HgBr_2 /Argon Laser	46
19	Geometry for Absolute Fluorescence Measurement	47
20 (a)	Experimental and Modeled Voltage and Current Waveforms	48
(b)	Observed and Calculated Sidelight Fluorescence (Without Lasing)	48
21	Measured Small-Signal Gain Near Band Center	50
22	Small-Signal Gain vs Sidelight as a Function of Time	52
23 (a)	Experimental and Modeled Voltage and Current Waveform	53
(b)	Experimental and Computed Absorption for Capacitor Circuit	53
24	Experimental and Computed Absorption for PFL Circuit	55
25	Fluorescence vs Electron Density: an Upper Bound on Electron Quenching	57
26	Experimental Sidelight Depression as a Function of Discharge Power	58
27	Computed Sidelight Depression as a Function of Discharge Power	60
28	Computed Attachment vs E/N, and Experimental Point	62
29	Experimental and Computed Discharge Current	64
30	Sidelight and Laser Output vs Injected Power	66
31	Schematic of 1 m Experiment	70
32	Schematic of 1 m Cable Pulser	72

<u>Figure</u>		<u>Page</u>
33	Voltage, Current and Laser Pulses for 1 m Experiment	74
34	Experimental Laser Intrinsic Efficiency vs E/N	76
35	Computed Intrinsic Efficiency vs E/N	77
36	Experimental Laser Energy vs PFN Stored Energy	78
37	Shot-to-Shot Reproducibility of Laser Output	79
38	Observed Discharge Energy Loading vs Deposition Uniformity, E-Beam Current Density and Discharge Enhancement Ratio	82
39	Streak Photograph of Volumetric Arc Conditions	83
40	Streak Photograph of Spatial Arc Caused by Nonuniform Deposition	85
41	Measured E-Beam Deposition with Uniform Magnetic Field	87
42	Measured E-Beam Deposition with Diverging Magnetic Field	88
43	Computed E-Beam Deposition for Uniform 1 kG Magnetic Field	90
44	Measured Spatial Distribution of Laser Output with 800 G Magnetic Guide Field	92
45	Measured Spatial Distribution of Laser Output with No Magnetic Guide Field	93
46	Computed Evolution of Local Field Between Anode and Cathode	95
47	Computed Anode to Cathode Variation of Laser Energy, and Overall Electrical Efficiency	96
48	Design Point Energy and Electrical Efficiency vs Output Coupling	104
49	Computed Impedance Evolution for Design Point Discharge	105
50	Isodeposition Contours for Design Point	107

<u>Figure</u>		<u>Page</u>
51	Deposition Profiles Transverse to the Anode-Cathode Axis, at Various Depths	108
52	Equipotential Plot of Discharge Region	111
53	Equipotential Plot in the Region Near the Cathode	113
54	Discharge Electrode Geometry	117
55	Flow Channel Mufflers with Finite Backing Volume	125
56	Transmitted Peak Wave Strength Through Perforated Side Wall Muffler	126
57	Sectional View of the Laser Flow Loop, Side View	129
58	Sectional View of the Laser Flow Loop, Upstream View	130
59	Boundary Layer Portion of Unacceptable Beam Quality vs Wall to Cavity Temperature Difference	133
60	Section to Show Details in the Region of the Laser Cavity	135
61	Gas and Liquid Average Temperature vs Distance Through the Heat Exchanger	142
62	Flow Regimes in Straight-Wall, Two-Dimensional Diffusers	145
63	Liquid Coolant Loop Operation Schematic	157
64	Proposed Resonator for Unstable ILO (Schematic)	162
65	Increased Output of ILO vs Injected Power	163
66	Divergence of Injected Gaussian TME ₀₀ Mode as it Propagates in ILO	167
67	Proposed Master Oscillator for Injection ILO (Schematic)	169
68	Power for Master Oscillator vs Reflectance	171

Figure

66	Diagram of a Typical Feedback Mirror	187
67	B-Scan of a Typical Mirror	188
71	Dispenser Cathode Assembly	189
72	Magnetic Field Configuration	190
73	Typical Superconducting Cathode Assembly	191
74	Blumlein Circuit	194
75	Line Pulser	196
76	Equivalent Forms for Five-Section Gillemin Voltage-Fed Network	198
77	Transmission Line Pulse Forming Network	199
78	Performance of Unmodified Type B Network	200
79	Performance of Modified Type B Network	201
80	Performance of Modified Type B Network with Change in Output Inductor	202
81	Conceptual Drawing of Pulse Forming Network Configuration	203
82	Anode Heating in a Transmission Line Circuit (Adapted from Ref. 37)	206
83	Amount of HgBr_2 Processed vs Fraction of the Flow Removed	211
84	Schematic of Flow Purification Cycle	218
85	Computed Intensity Profile for 4 cm Dimension of Design Point Unstable Resonator	224
86	Aberration Multiplier for Unstable Resonators	226
87	Far Field Encircled Energy as a Function of Spot Size, for Centered Feedback Mirror Resonator	228

Appendix

A-1	Saving at Least Energy by Direction	230
-----	-------------------------------------	-----

LIST OF TABLES

<u>Table</u>	<u>Page</u>
1. Relative Laser Intrinsic Efficiency of Different Mixes	41
2. List of Species Followed in Kinetic Model	43
3. Design Specifications	99
4. Laser Cavity Operating Conditions	124
5. Heating Loads on Foil and Discharge Electrodes	136
6. Elements of Flow-Loop Stagnation Pressure Loss	152
7. Heat Load Sources and Distribution	155
8. E-Beam Design Parameters	176
9. Calculated Field Intensities	187
10. Energy Budget for Modulator	209
11. Total Power Consumption 2 J/Pulse	221
A-1 Buildup Time With Injection	236
B-1 Parameters for Oscillator	242

I. INTRODUCTION

This report covers the Phase I contract performance period from June 9, 1980 to June 8, 1981. All the program objectives were achieved, and indeed the demonstrated HgBr laser electrical efficiency of 2% was rather higher than had been predicted before the work began. The HgBr single pulse laser energy was scaled to 10 J.

In the course of this work we have substantially advanced the kinetic understanding of the HgBr laser, and in this report we present the first detailed description of the excitation mechanism by direct electron impact on HgBr_2 .

From our extensive parametric studies we have identified the dominant kinetic processes (quenching, absorption, and attachment) which govern the HgBr laser behavior in an e-beam sustained discharge. A model has been developed which predicts laser performance to an accuracy of $\pm 10\%$.

In the second half of this report we apply the discharge model to the design of a 2 J, 100 Hz long life HgBr laser system. Our conclusion is that such a design is entirely feasible. The precise control that is possible in e-beam sustained discharges allows a conservative design of the laser cavity and flow loop within a compact overall system.

In conclusion, the e-beam sustained HgBr laser has been demonstrated to be efficient and powerful. An approach to design has been developed which is relevant to a wide range of potential applications.

II. TECHNICAL PROGRESS

A. KINETIC MODEL AND EXPERIMENTS

1. Introduction

An extensive range of experiments has been performed in order to understand the HgBr laser kinetics and discharge characteristics. This has been successful to the extent that there are no remaining uncertainties in the laser modeling which might otherwise affect the design.

The main achievements have been to demonstrate laser electrical efficiency over a wide range of operating conditions and to generate a model of the laser performance which is capable of predicting laser efficiency to within $\pm 10\%$ accuracy.

Because of its importance in the model, a detailed study has been made of the HgBr*(B) formation process and the first complete set of electronic excitation cross sections has been derived from the experiments. Use of this set in a Boltzmann code has given a complete description of the formation efficiency as a function of applied electric field and HgBr₂ number density.

The experiments were performed on two different machines. The small-scale device had an e-beam entry aperture of 1 x 23 cm and discharge spacing of 1 cm. The 1 m device had an e-beam aperture of up to 10 x 100 cm and a discharge spacing of 4.5 to 8 cm. The discussion is divided into Section II-A-2 which deals exclusively with experiments on the small-scale device and the associated kinetic modeling, and Section II-A-3 which covers the 1 m device experiments and modeling.

2. Small-Scale Experiments

a. Experimental Methods

The discharge chamber is shown in Figure 1. The e-beam voltage was 125 to 150 kV and its current density was controlled by attenuator screens in the range 0.5 A/cm^2 to 2.5 A/cm^2 . The discharge anode had a Chang profile to give a field uniform to $\pm 10\%$ over a 1.1 cm width. The chamber was kept at 220°C and HgBr_2 density was varied by controlling the temperature of a 'sidearm' reservoir.

The discharge was driven either by a capacitor or a "PFL," a pulse forming line consisting of paralleled cables with a nominal impedance of 3.36Ω . The capacitor circuit is shown in Figure 2 and typical waveforms are shown in Figure 3. The PFL circuit is shown in Figure 4 and typical waveforms in Figure 5. The "square topped" nature of the PFL pulse was important in determining steady-state fluorescence and laser behavior, and contributed much to the precision of the kinetic modeling.

For the purpose of gain and absorption measurements a tunable dye laser was employed as shown schematically in Figure 6. The measurement of small absorptions required a double-pass configuration. This was actually collinear, although separated in Figure 6 for clarity.

Voltage and current measurements were estimated to be better than $\pm 10\%$ accurate. Sidelight fluorescence was viewed through a bandpass filter by vacuum photodiode. Laser output was monitored by photodiode and calorimeter.

The foil material was 'Kapton', 2 mil thick, aluminized on the side facing the e-beam cathode. Windows were fused silica. The magnetic guide field was 1 kG. Throughout the experiment the e-beam, driven by a dc charged cable, functioned very reliably. This reliability was a major factor in the completion of extensive parameter variations in both discharge conditions and gas mix.

b. Modeling of $\text{HgBr}^*(\text{B})$ Formation Process

In the first report of a discharge HgBr laser,⁽¹⁾ Schimitschek and Celto suggested that the excitation mechanism

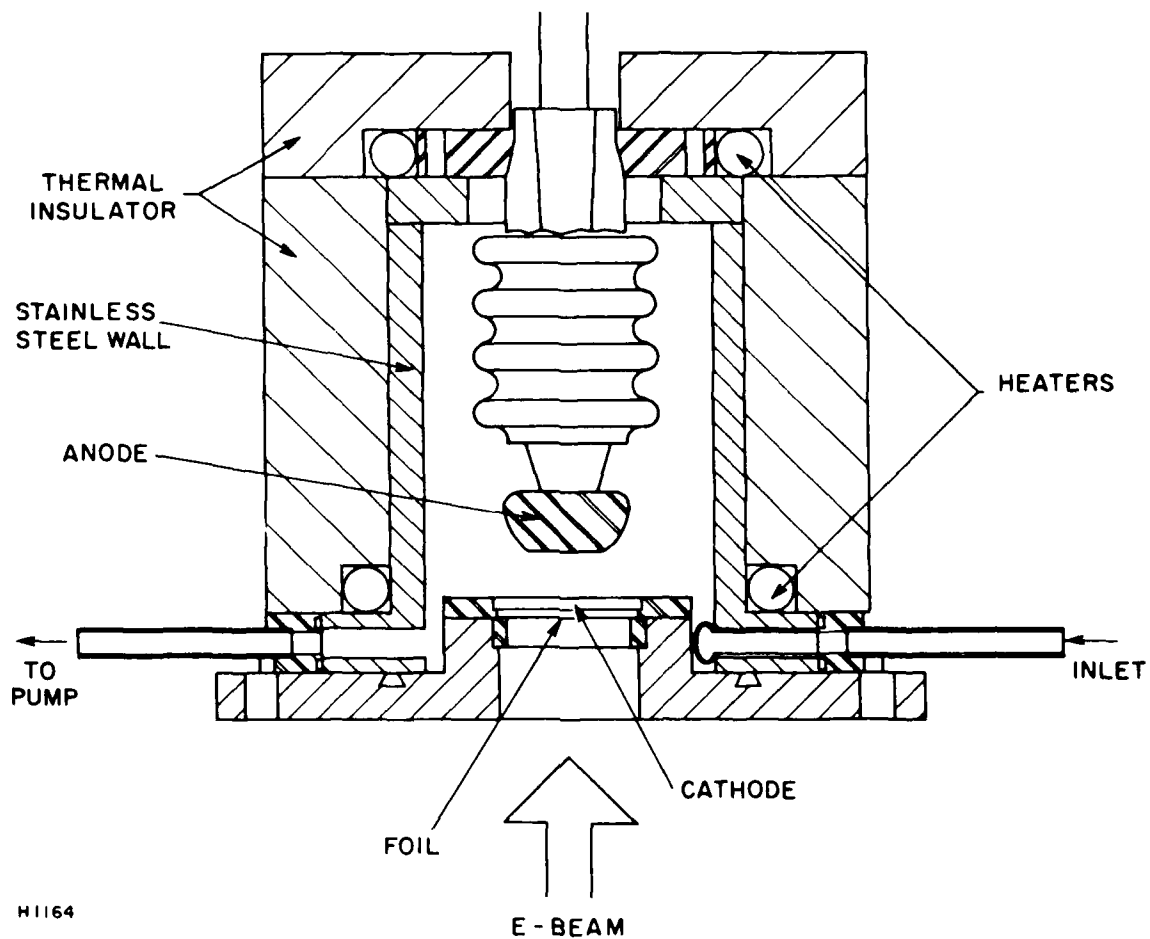


Figure 1. Detail of the Small-Scale Laser Chamber

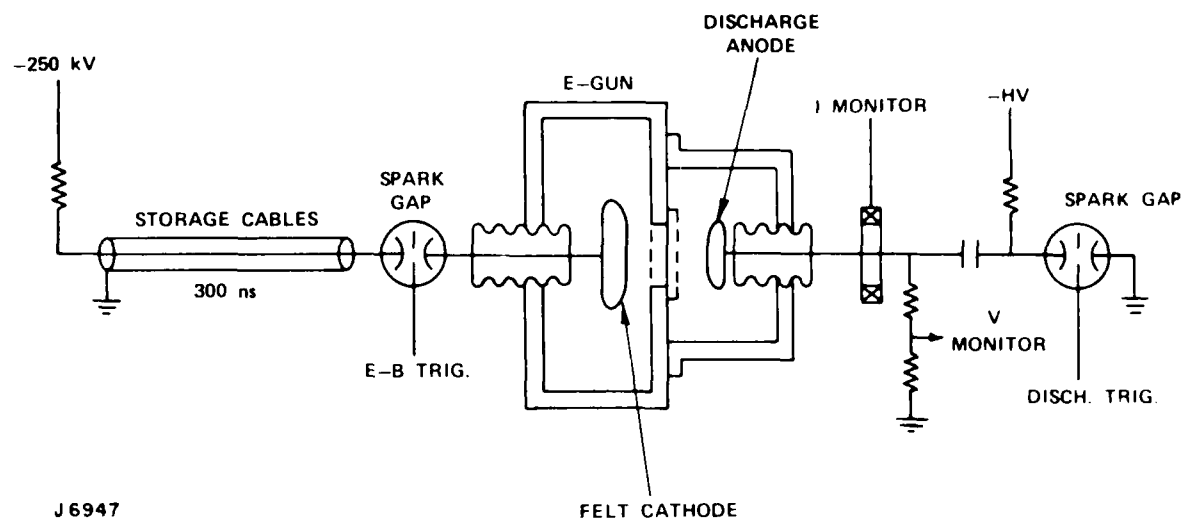
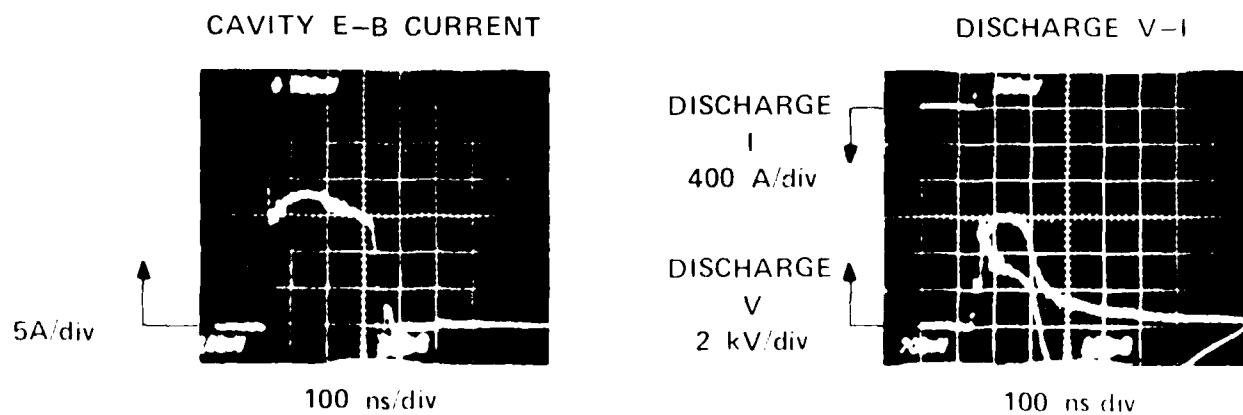
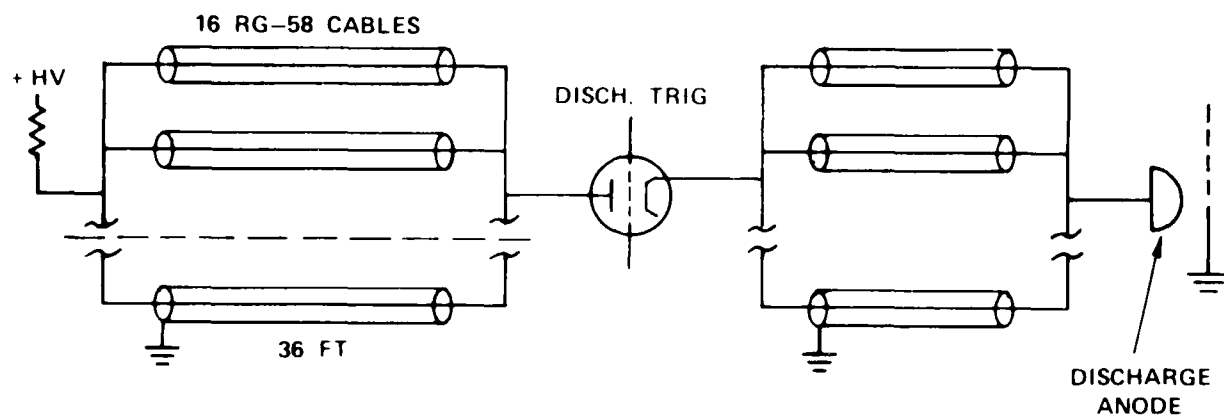


Figure 2. Schematic of Small-Scale E-Beam and Discharge Circuit



J6944

Figure 3. Small-Scale E-Beam and Capacitor Discharge Characteristics

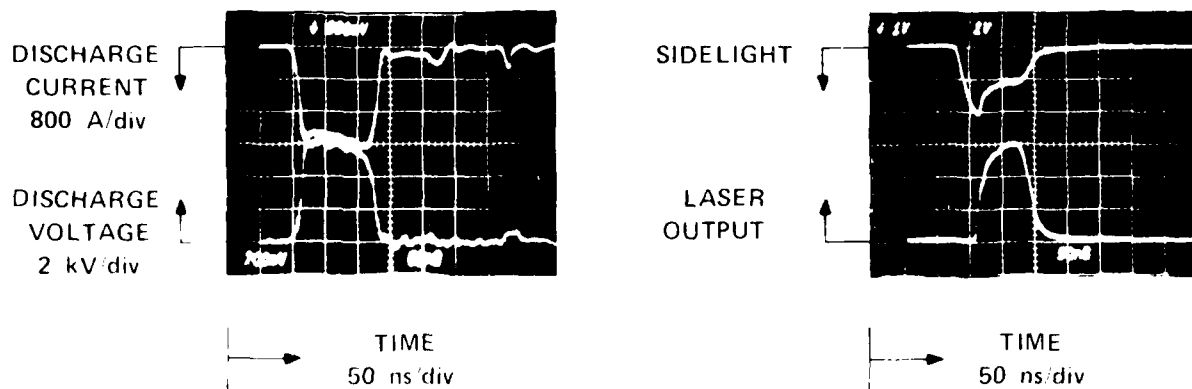


J6953

NOM IMPEDANCE = 3.356Ω

Figure 4. Schematic of Small-Scale Cable PFL

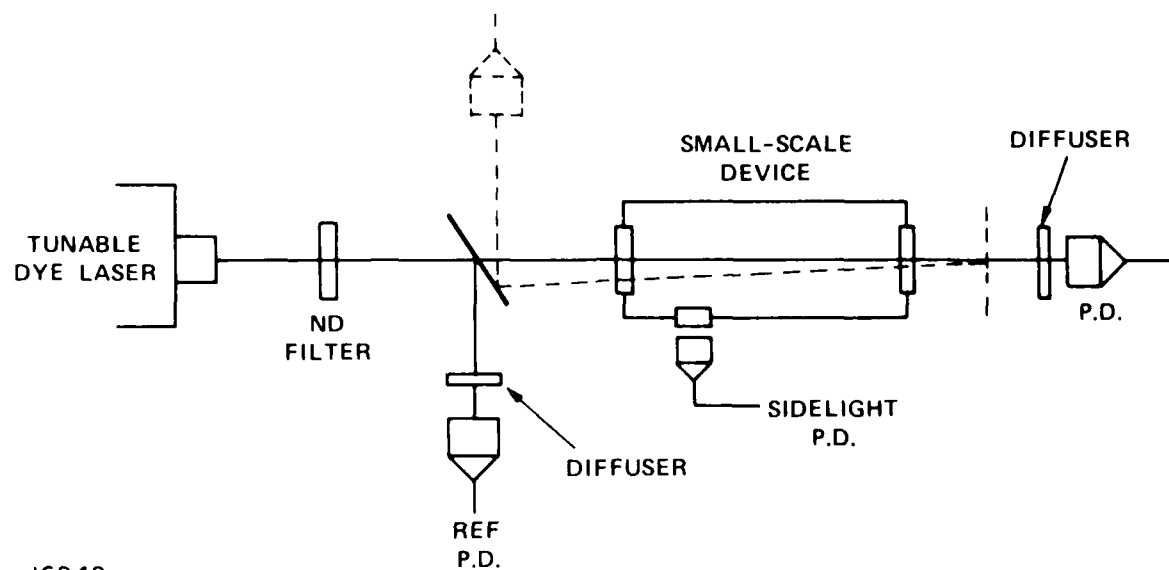
(20 TORR HgBr_2 / 2 AMA Ar)



ELECTRICAL COUPLING EFFICIENCY ≈ 0.75

J6547

Figure 5. Typical Laser Discharge, Sidelight and Output Characteristics with Cable PFL



J6949

Figure 6. Apparatus for Gain and Absorption Experiments

might be a collisional dissociation of HgBr_2 by electrons analogous to the well known photodissociation process. They did not, however, estimate a rate constant for electronic excitation. In 1978 Allison and Zare ⁽²⁾ reported absolute measurements for the electronic excitation of HgBr_2 to give $\text{HgBr}(\text{B}+\text{X})$ fluorescence, which gave a cross section $\sigma < 1 \times 10^{-20} \text{ cm}^2$ for electrons between 5 and 25 eV and a peak cross section at $\sim 200 \text{ eV}$ of only $1 \times 10^{-19} \text{ cm}^2$. Because of these small cross sections several later authors sought to explain HgBr laser action in N_2/Ne mixes and Xe/Ne mixes in terms of (a) electronic energy transfer from excited N_2 or rare gas species to HgBr_2 , ^(3,4) or (b) recombination ⁽⁵⁾ of HgBr_2^+ . It was also suggested ⁽⁶⁾ that $\text{HgBr}^*(\text{B})$ could be formed in an attachment process producing Br^- .

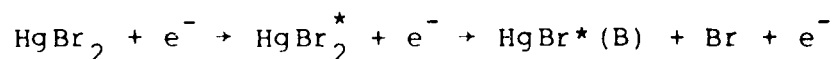
Our preliminary experiments showed an approximately equal formation efficiency in any of the rare gas buffers Ne , $\text{Ne}(10\% \text{ Xe})$, Ar , $\text{Ar}(5\% \text{ Xe})$, and moreover strong $\text{HgBr}(\text{B}+\text{X})$ fluorescence was observed in Ar buffer at E/N values where the excitation of the Argon resonance levels ($\text{Ar}^* \text{ } ^3\text{P}_1, \text{ } ^3\text{P}_2$) at 11.5 eV was extremely small. The inference was that here Ar^* could not be involved in the production of $\text{HgBr}^*(\text{B})$, whether by a Penning

1. Schimitschek, E.J. and Celto, J.E., Optics Lett. 2 p. 65 (1978).
2. Allison, J. and Zare, R.N., Chem. Phys. 35, p. 263 (1978).
3. Chang, R.S.F. and Burnham, R., Appl. Phys. Lett. 36, p. 397 (1980).
4. Nighan, W.L., Appl. Phys. Lett. 36, p. 173 (1980).
5. Schimitschek, E.J. and Celto, J.E., Appl. Phys. Lett 36, p. 176 (1980).
6. Degani, J., Rokni, M. and Yatsiv, S., J. Chem. Phys. 75, p. 164 (1981)

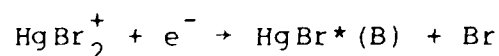
process to HgBr_2^+ followed by recombination, or by a direct energy transfer such as $\text{Ar}^* + \text{HgBr}_2 \rightarrow \text{HgBr}^*(\text{B})$. (In any case, Chang and Burnham⁽³⁾ had not observed any $\text{HgBr}(\text{B} \rightarrow \text{X})$ fluorescence from HgBr_2 in the presence of $\text{Ar}(^3\text{P}_2)$ metastable atoms). It was concluded that the primary $\text{HgBr}^*(\text{B})$ formation process, at least in Argon buffers, had to be a direct electronic excitation of HgBr_2 .

Three candidate process were considered for this role:

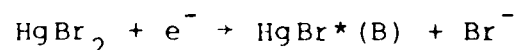
(1) Inelastic Collision



(2) Ion Channel



(3) Attachment



Process (2) and (3) were not compatible with our experimental observations. In particular, our measurements of absolute fluorescence efficiency and attachment rate coefficient led us to conclude that the Attachment Channel (3) was 10 to 20 times too slow to explain the observed fluorescence power. The Ion Channel (2) implied discharge ionization rates that were incompatible with the stable attachment-dominated discharge that we observed over a wide E/N range. Also, no delay in fluorescence was observed ($\tau_{\text{delay}} < 10$ ns) which would have necessitated an Ion Channel recombination rate of ~ 100 times greater than rates typical of dissociative recombination.

We concluded that Inelastic Collision was the dominant $\text{HgBr}^*(\text{B})$ formation process in Argon buffers, and attempted to synthesize a realistic set of HgBr_2 electronic cross sections to describe the process and allow extension of the modeling to other gases.

As a starting point we had available cross-section measurements⁽⁷⁾ of the attachment process $\text{HgBr}_2 + e^- \rightarrow \text{HgBr}(X) + \text{Br}^-$ and also of the ionization process $\text{HgBr}_2 + e^- \rightarrow \text{HgBr}_2^+ + 2e^-$. As trial Inelastic Collision processes we chose HgBr_2 dipole allowed processes which appeared in optical absorption at ~ 5 eV, ~ 6.4 eV and ~ 7.9 eV. These will be discussed in turn.

5 eV Process: In optical absorption this extends⁽⁸⁾ from 250 nm down to 210 nm and has been associated^(9,10) with the photodissociation of HgBr_2 into only non-fluorescing products, probably⁽¹¹⁾ $\text{HgBr}(X) + \text{Br}$. Although the 230 nm optical absorption is assigned⁽¹¹⁾ to the $1^1\Sigma_g^+ \rightarrow 1^1\pi_u$ transition, nearby $3^1\pi_u$ and $3^1\Sigma_u^+$ states are also accessible by electronic collision and could provide the dominant contribution to the excitation cross section near 5 eV because of the relatively peaked behavior of singlet-triplet processes near threshold. We, therefore, assumed that the 5 eV process peaked at 6.5 eV and had unit branching to $\text{HgBr}(X) + \text{Br}$.

6.4 eV Process: This corresponds to a band between 190 and 210 nm in optical absorption, which leads to $\text{HgBr}^*(B)$ fluorescence with unit quantum efficiency.⁽⁸⁾ Its assignment⁽¹¹⁾ of $1^1\Sigma_g^+ \rightarrow 1^1\Sigma_u^+$ has been confirmed by a measurement⁽¹²⁾ of the polarization dependence of $\text{HgBr}^*(B)$ fluorescence following photodissociation at 193 nm. We assume that the electronic excitation cross-section peaks at ~ 4 times the threshold energy by analogy with other singlet-singlet transitions. Also, we suppose

7. Wiegand, W.J., ONR Report R80-924789-1 (1980).

8. Wilcomb, B.E., Burnham, R. and Djed, N., Chem. Phys. Lett. 75, p. 239 (1980).

9. Wieland, K., Z. Phys. 76, p. 801 (1932); 77 p. 157 (1932).

10. Maya, J. IEEE JQE QE-15, p. 579 (1979).

11. Watt, W.P., J. Chem. Phys. 72, p. 2469 (1980).

12. Burnham, J., Wiesenfeld, J.R. and Zare, R.N., J. Chem. Phys. 72, p. 2479 (1980).

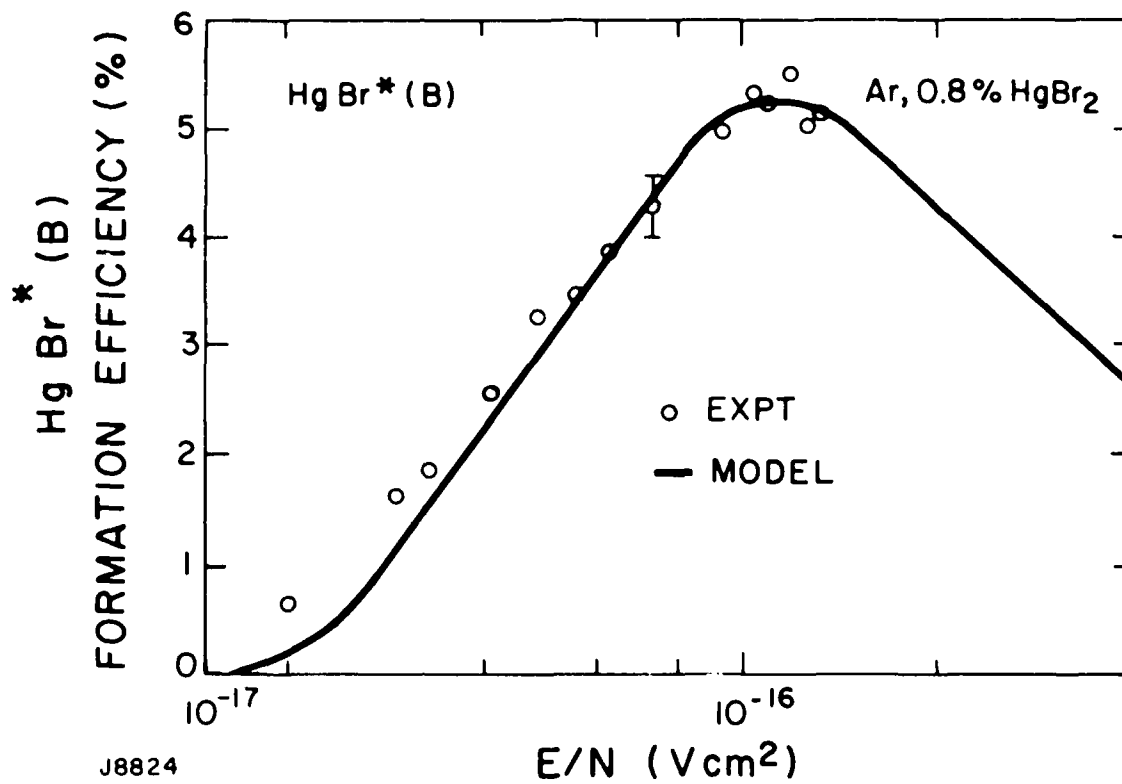
that in the 6.4 eV process HgBr_2 dissociates rapidly ($\gg 10^9/\text{s}$) into $\text{HgBr}^*(\text{B})$ with unit branching, by analogy with photodissociation.

7.9 eV Process: There is a very large process at 7.9 eV in the electron energy loss spectrum for HgBr_2 .⁽¹³⁾ Also at 159 nm (7.8 eV) there is a strong optical absorption⁽⁹⁾ which leads to fluorescence in the 270-250 nm region. Accordingly we give this process a singlet-singlet shape of cross section, peaking four times above threshold, but with zero branching to $\text{HgBr}^*(\text{B})$. We shall refer to this HgBr_2^* (7.9 eV) state as the HgBr_2 'complex' level and use it both as the terminal level of dissociative recombination and as a reservoir for a two-step ionization process. As a first estimate we give the levels in the 'complex' an average 10^8 sec^{-1} decay rate, with 0.5 branching to $\text{HgBr}_2(\text{X})$ and 0.5 to $\text{HgBr}(\text{X}) + \text{Br}$. The exact value of this decay rate has no influence on the laser modeling predictions.

Given this trial set of three inelastic processes, and using the UTRC attachment and ionization cross sections a fit could be made to our experimental fluorescence versus E/N data. For this purpose an established Boltzmann code was used, which handled elastic, inelastic, ionization and attachment processes. A tested set of Argon cross sections was employed, the only really operative one of which, that for momentum transfer being very accurately known. It was verified that the code predicted experimental pure Ar drift velocities to better than 10% accuracy. The following routine was used to achieve the fit to data shown in Figure 7:

1. The magnitude of the 7.9 eV complex cross section was varied until ionization equaled attachment at the experimental argon E/N of $1.4 \times 10^{-16} \text{ Vcm}^2$ (for 0.8% HgBr_2 in Ar). Because the complex cross section was large ($\sim 10^{-15} \text{ cm}^2$), subsequent variation of the smaller 5 and 6.4 eV processes had a negligible effect on the E/N for ionization runaway.

13. Dillon, M. (Argonne Natl. Lab.), private communication.



J8824

Figure 7. $\text{HgBr}^*(\text{B})$ Formation Efficiency as a Function of E/N

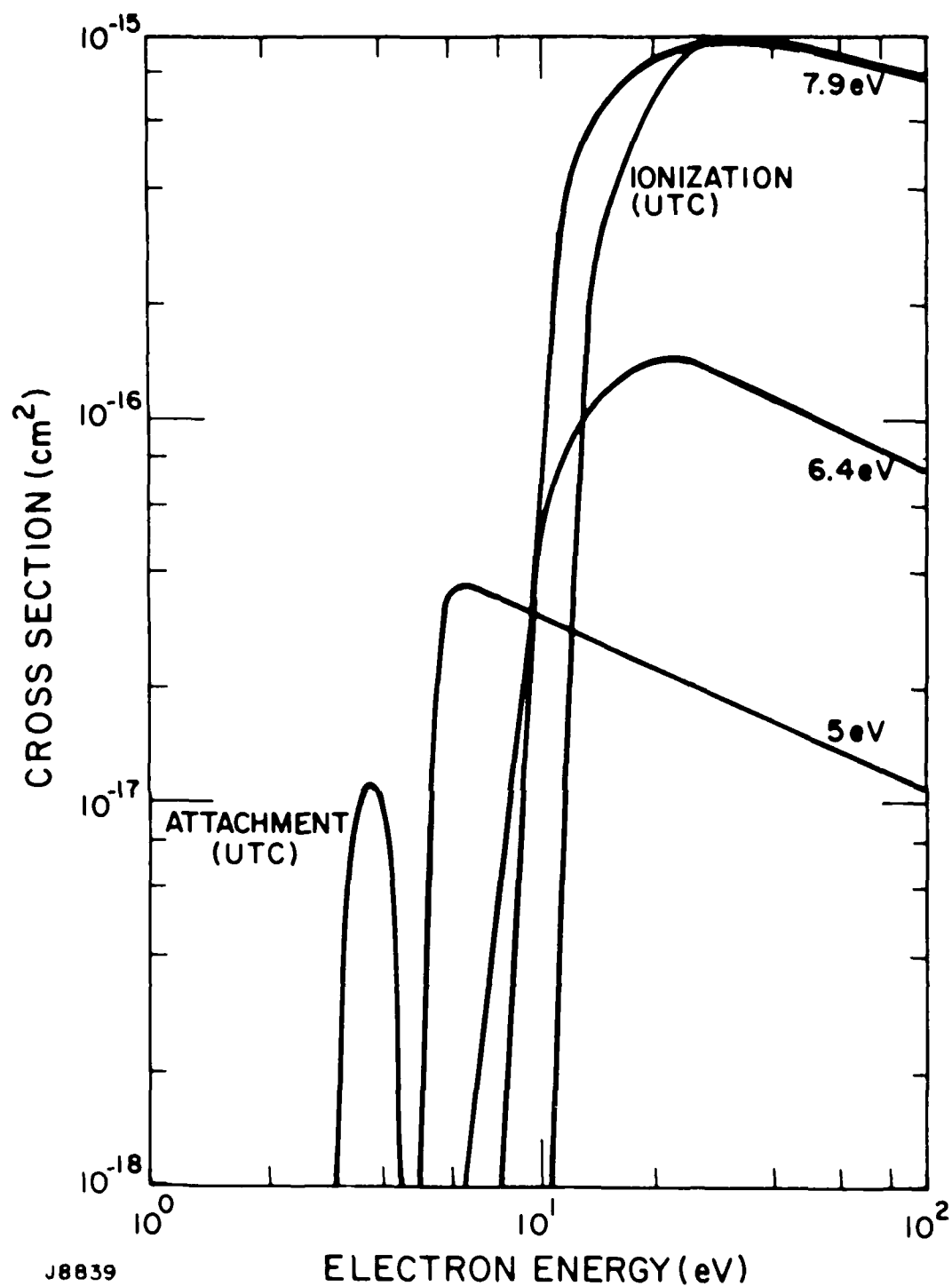
2. The magnitudes of the 5 and 6.4 eV processes were adjusted in tandem until the observed fluorescence efficiency and voltage dependence were fitted by the 6.4 eV process.

Figure 7 shows that a good fit was obtained, which tends to confirm the three-process assumption. It was not possible to fit the data accurately with a two-process model (i.e., leaving out the 5 eV process) because the 6.4 eV excitation would then peak at $E/N \approx 6 \times 10^{-17} \text{ Vcm}^2$ and not at the higher experimental value.

Vibration, rotation and elastic processes for HgBr_2 were tried, but had negligible effect on the excitation rates or drift velocity for $E/N > 1 \times 10^{-17} \text{ Vcm}^2$. They were therefore omitted from the cross-section set, which is shown in Figure 8. In order to give better agreement of the computed attachment rate (Figure 28) with the Avco experiment, the UTRC attachment cross section was scaled up by 1.1. The best fit cross-section set is shown in Figure 8. It is difficult to put accurate estimates on the magnitude of the 5, 6.4 and 7.9 eV cross sections, because assumptions have been made about shape and branching ratio. If these assumptions are correct, then the magnitudes are determined to a tolerance of $\pm 50\%$. However, the predictive power of the cross-section set in HgBr_2/Ar mixes is considerably more accurate than this, being determined by the experimental error bounds of $\pm 10\%$ on formation efficiency.

c. Comparison with Experiment in Different Gases

Argon: The discharge fractional power to each process is shown in Figure 9. The 6.4 eV process takes only 13% of the power at its maximum, and the largest process is the dissociation of HgBr_2 via the 5 eV channel. There is still almost a 10% argon elastic loss in the $5 \times 10^{-17} - 1 \times 10^{-16} \text{ Vcm}^2$ E/N range of most interest to lasing. The effect of this elastic loss becomes apparent in Figure 10 where the HgBr_2 percentage is varied. The formation efficiency declines at low HgBr_2 concentration because of increasing Ar elastic loss. At the E/N for most efficient



J8839

Figure 8. HgBr₂ Electronic Cross Sections from Fitting Procedure

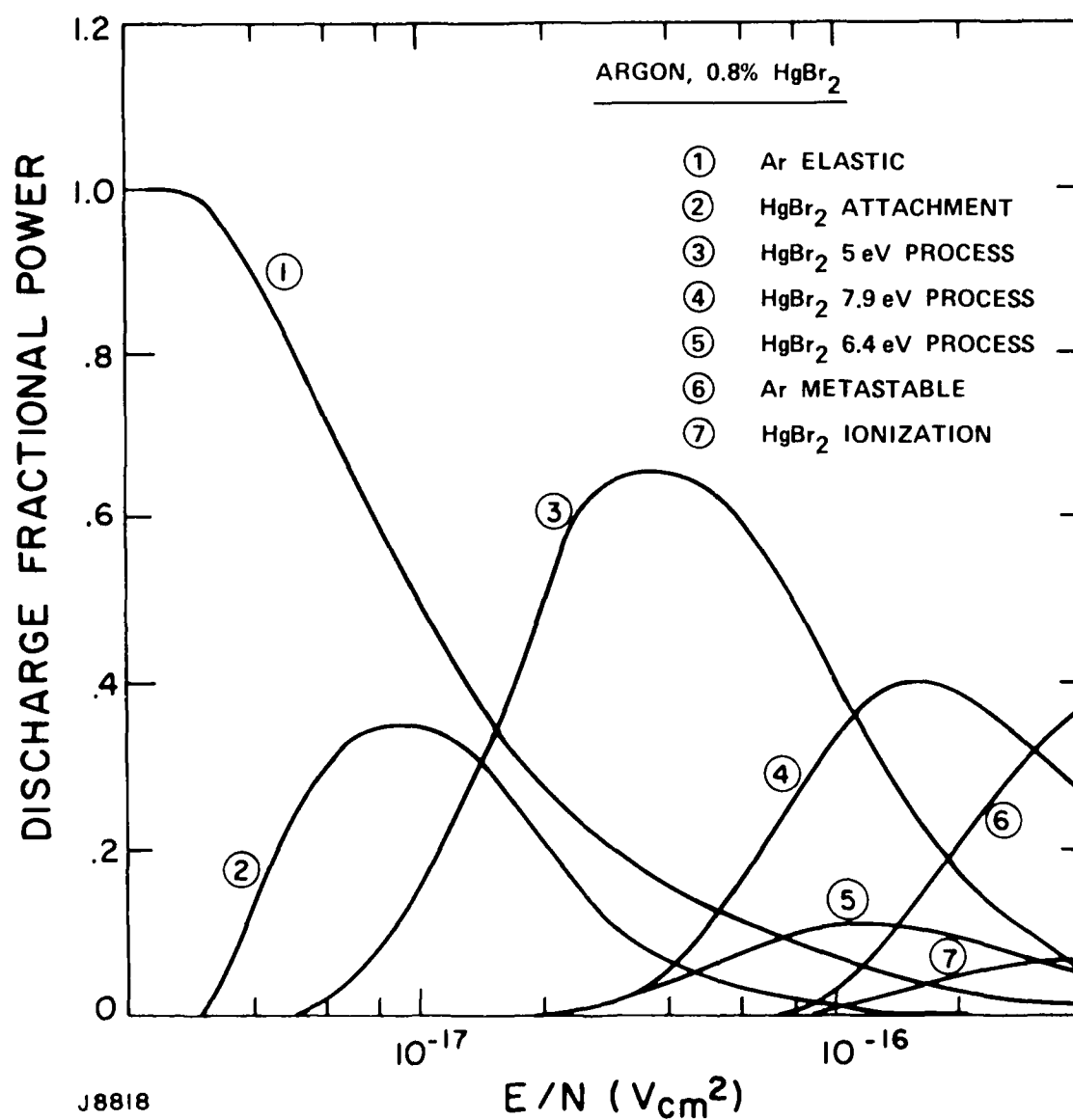


Figure 9. Computed Discharge Fractional Power vs E/N

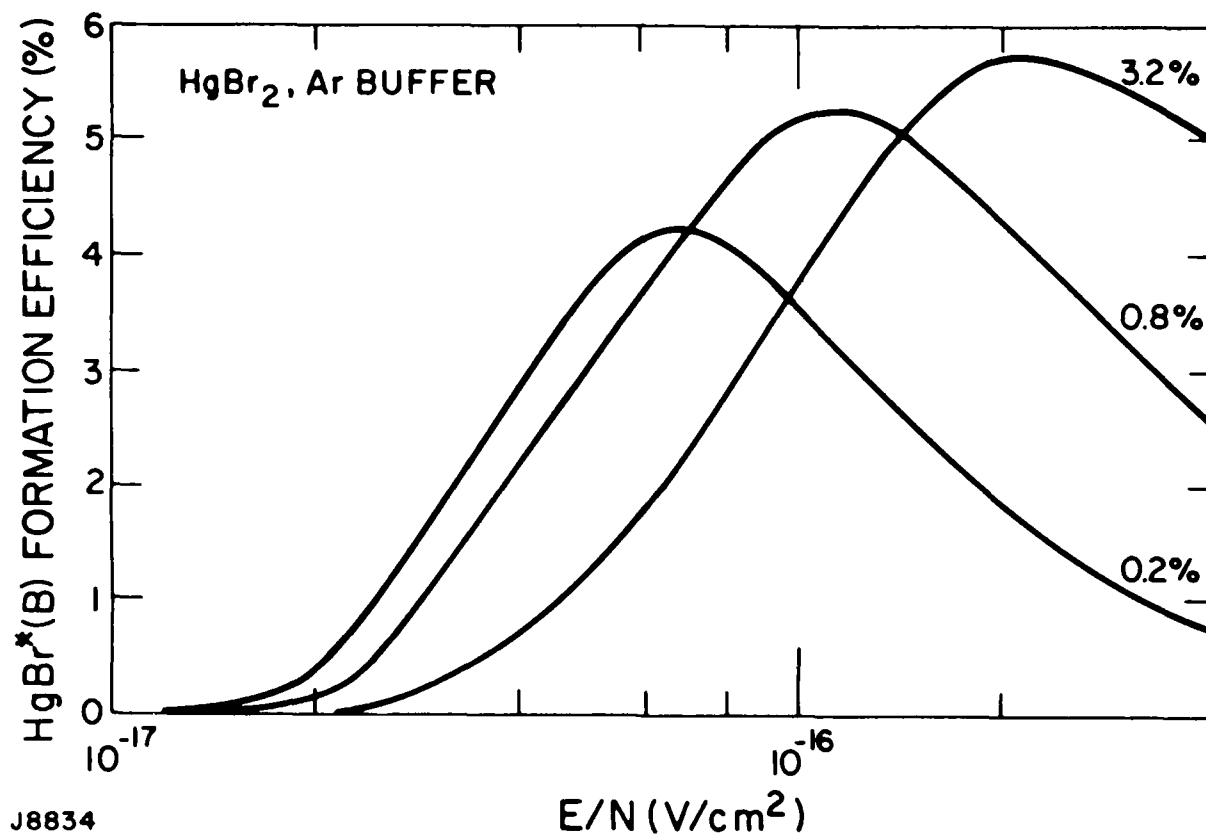


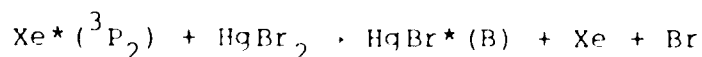
Figure 10. Computed Formation Efficiency vs HgBr_2 Concentration

lasing ($\sim 1 \times 10^{-16} \text{ Vcm}^2$) Figure 10 shows that the efficiency of formation is predicted to optimize at $\sim 0.8\%$ HgBr_2 , which is also the experimental optimum lasing concentration.

The drift velocity predictions are shown in Figure 11. The drift velocity is increased dramatically by the presence of HgBr_2 , an effect which is traceable to the 5 and 6.4 eV cross sections principally, because electrons return to an energy region of low elastic loss following collisions. The comparison of discharge impedance with experiment (Section II-A-2-n) indicates that there is definitely an enhancement of drift velocity over that in pure Ar.

Neon: The computed fluorescence efficiency in neon is shown in Figures 12 and 13. It peaks at lower E/N than in argon but is of approximately the same magnitude. Experimental points lie slightly below the theoretical curve, but the qualitative behavior is well predicted. Remembering that the ionization/attachment balance was used to fit the 7.9 eV process in Ar, the predicted point of arcing in neon (Figure 14) is in excellent agreement with the highest E/N that can be achieved in a stable discharge in neon (Figure 13).

Neon, 10% Xe: The computed fluorescence efficiency for this mixture is compared with experiment in Figure 15. Both theory and experiment lie between the pure Ne and pure Ar cases, in good qualitative agreement. However, in order to obtain this fit an assumption had to be made concerning the effective branching ratio from Xe^* to HgBr_2 . Experiments have shown ⁽³⁾ a unit branching ratio for the process



However, the branching ratio for $\text{Xe}^*(^3\text{P}_1)$ is not known, nor is the relative discharge production ratio of $^3\text{P}_1$ to $^3\text{P}_2$ well known. The present theoretical curves assume that only 30% of all

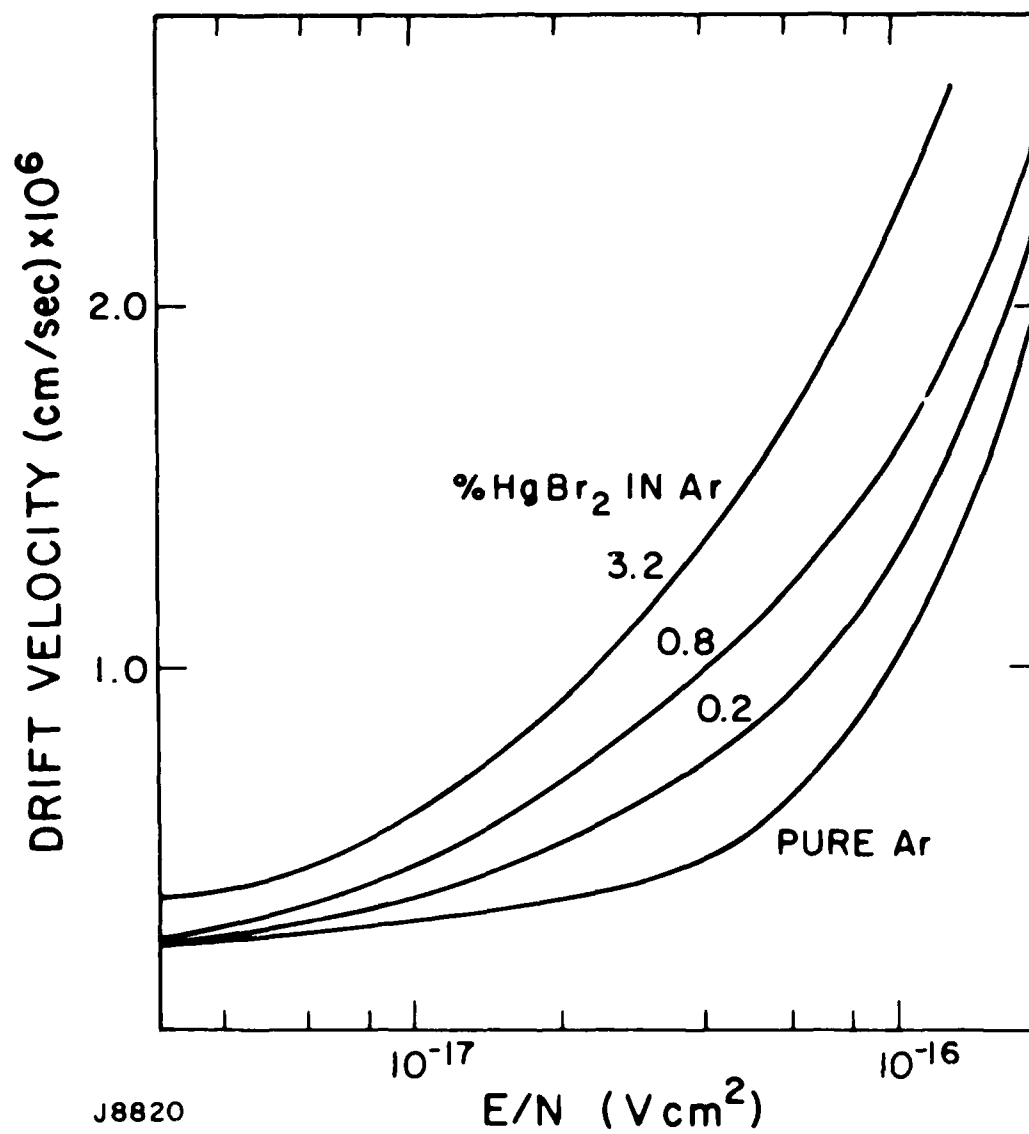


Figure 11. Computed Drift Velocity vs HgBr_2 Concentration

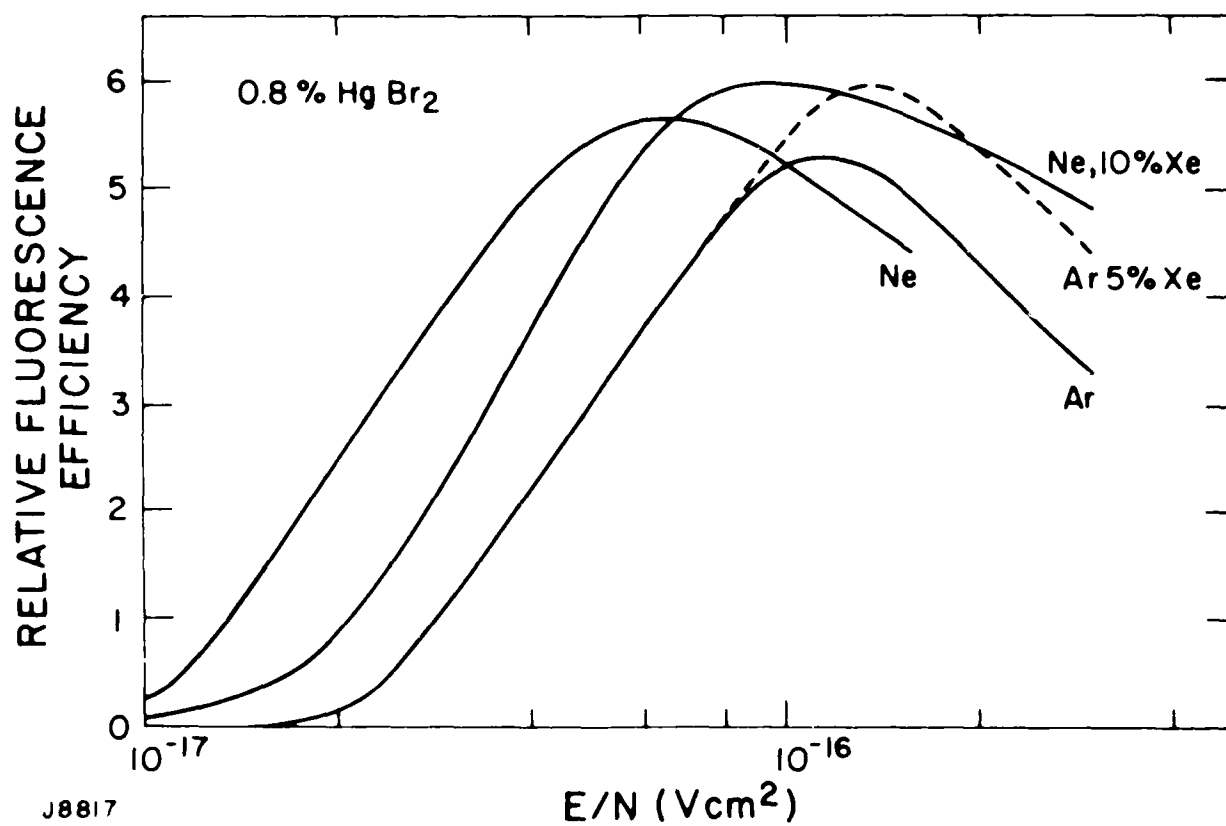


Figure 12. Computed Fluorescence Efficiency for Various Buffer Gases

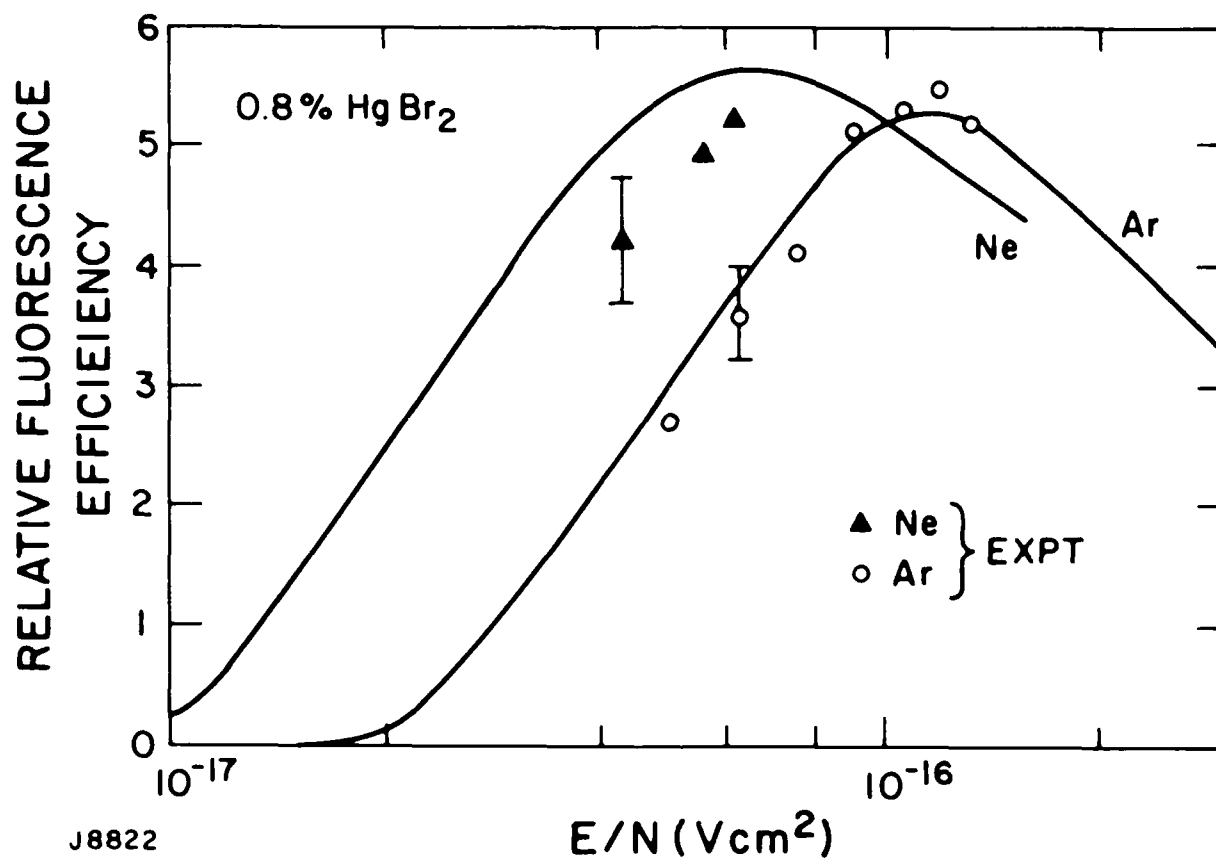
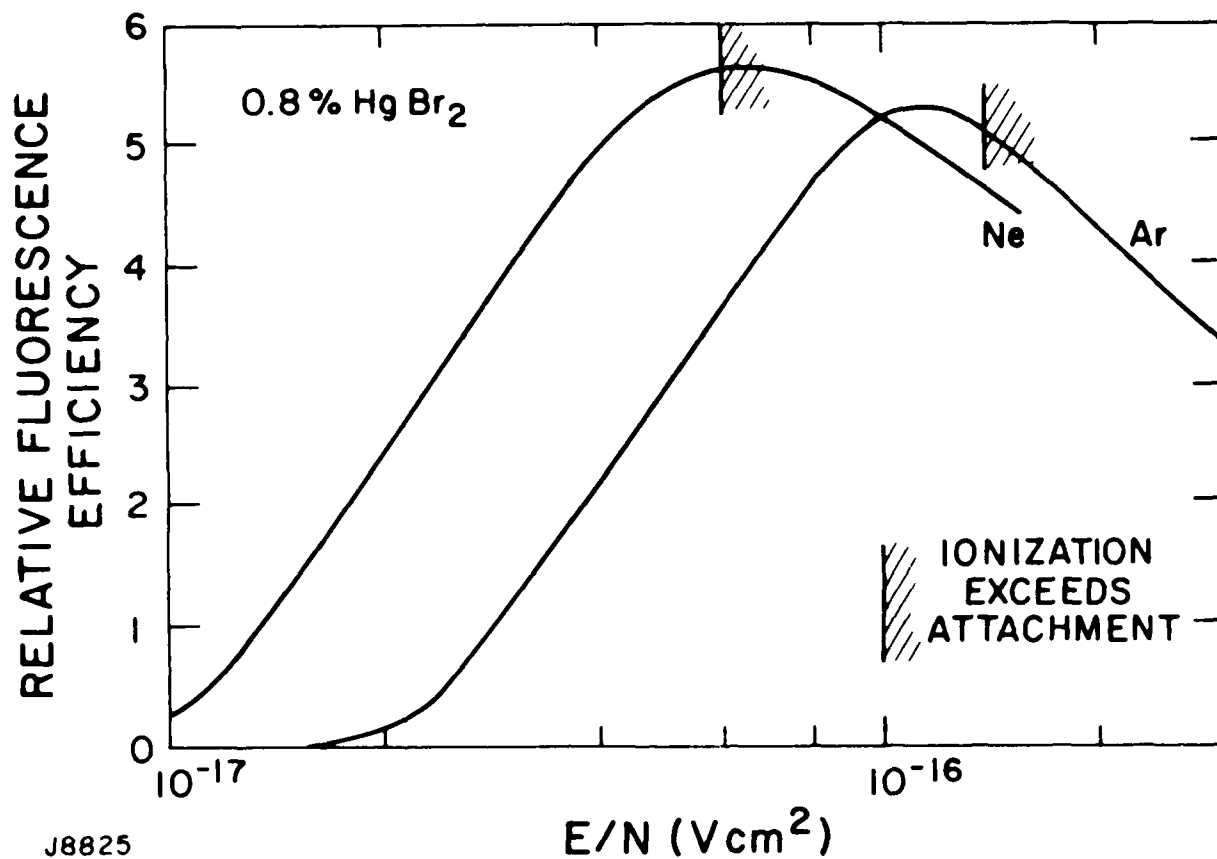


Figure 13. Theoretical and Experimental Fluorescence for Argon and Neon Buffers



J8825

Figure 14. Computed Single-Step Arcing Fields for Argon and Neon

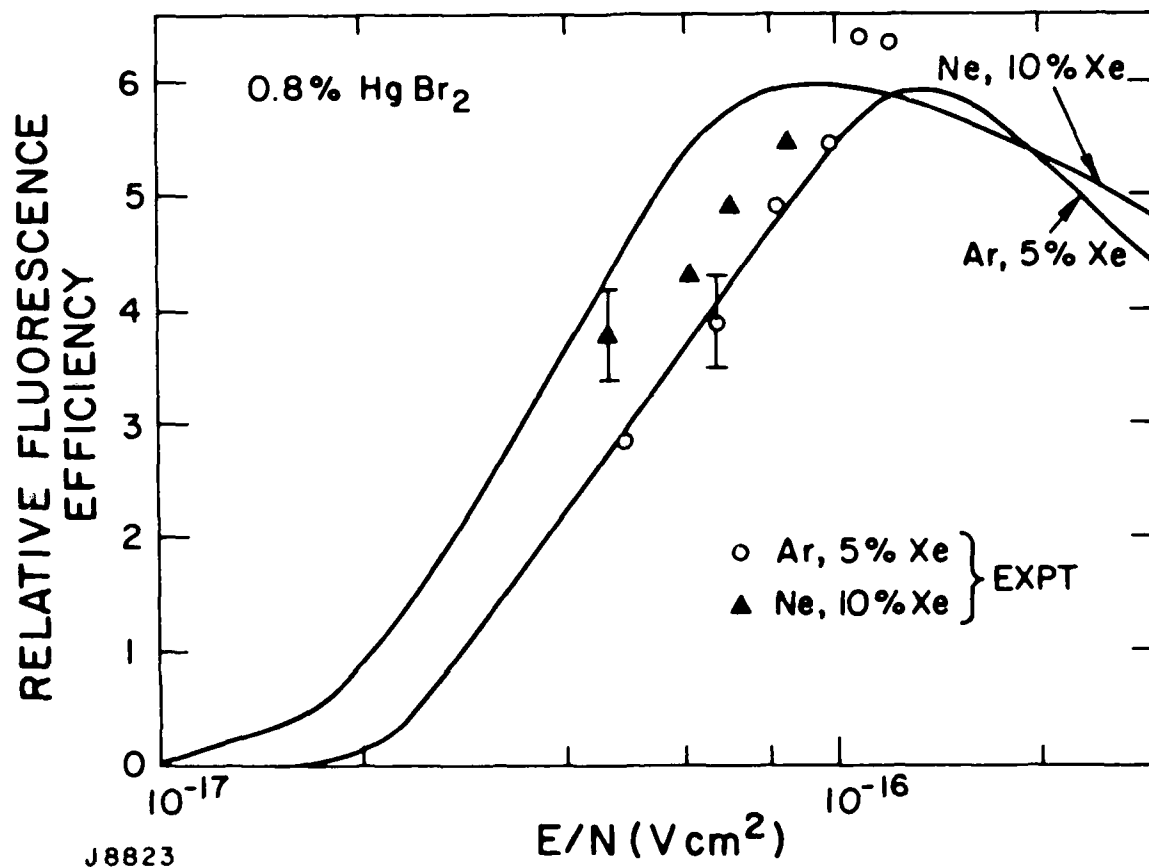


Figure 15. Theoretical and Experimental Fluorescence for Neon, 10% Xenon and Argon, 5% Xenon Buffers

discharge excitation of $\text{Xe}^*(^3\text{P}_1, ^3\text{P}_2)$ contributes to $\text{HgBr}^*(\text{B})$ by a process with unit branching. At $E/N = 8 \times 10^{-17} \text{ Vcm}^2$, Xe^* accounts for 40% of the $\text{HgBr}^*(\text{B})$ fluorescence in the Ne, 10% Xe mix.

Argon, 5% Xe: This mix showed a higher fluorescence efficiency than pure Ar in our experiments. The theoretical curve, again with 30% Xe^* branching, is shown in Figure 15. At $E/N = 1.4 \times 10^{-16} \text{ Vcm}^2$ the Xe^* contributes $\sim 35\%$ of the $\text{HgBr}^*(\text{B})$ fluorescence.

Because in both Ar*, 5% Xe and in Ne, 10% Xe the $\text{HgBr}(\text{B})$ fluorescence is well modeled, even for substantial Xe^* contributions, further confidence is gained in the HgBr_2 cross-section set. However, the prospects for using higher Xe concentrations to obtain higher laser efficiency are not good, in view of the low (30%) utilization of Xe^* excitation.

d. Specific Fluorescence with Different Buffer Gases

At constant e-beam current density of 0.5 A/cm^2 , different buffer gas mixtures were used in the capacitor driven discharge. The fluorescence of each mix was integrated over the stable discharge duration before arcing and plotted against discharge electric field (Figure 16). These curves are a measure of the relative lasing specific energy to be expected in the different buffer gases. Although the Ne, 10% N_2 buffer gives the highest potential specific energy, the relative fluorescence efficiency (Figure 17) is five times less than for any of the rare gas buffers. The poor fluorescence efficiency in Ne, 10% N_2 led us to discontinue work on this mix.

e. Laser Performance with Different Buffers: Choice of Argon

Although the fluorescence efficiency is very constant for different rare gas buffer mixtures, the lasing performance and discharge stability are substantially different. Relative laser intrinsic efficiency is shown in Table 1 for 0.8% HgBr_2 in 2 Amagat of various buffer mixes. Also included is a 1.6% HgBr_2 in 1 Amagat Ar data point.

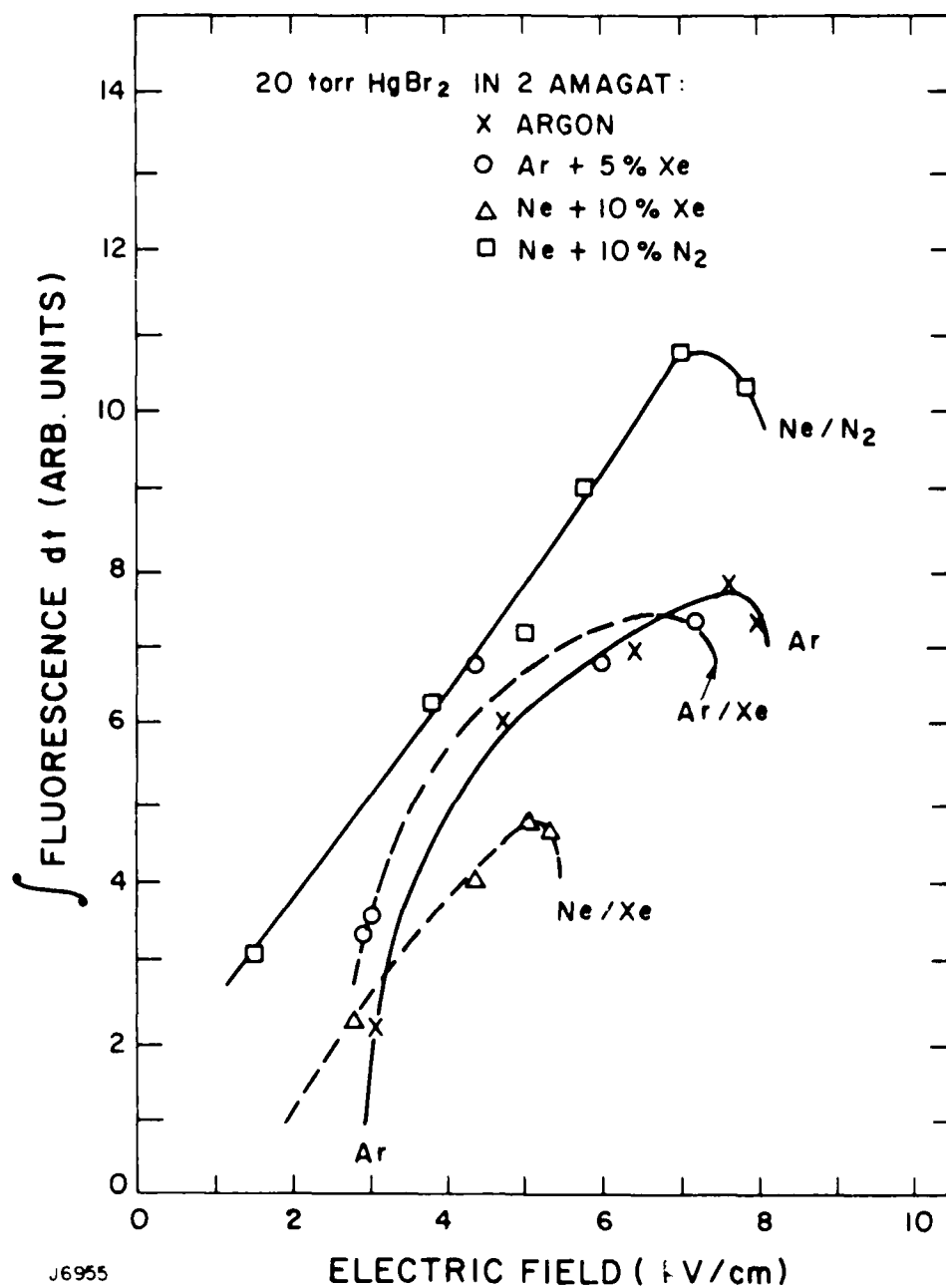
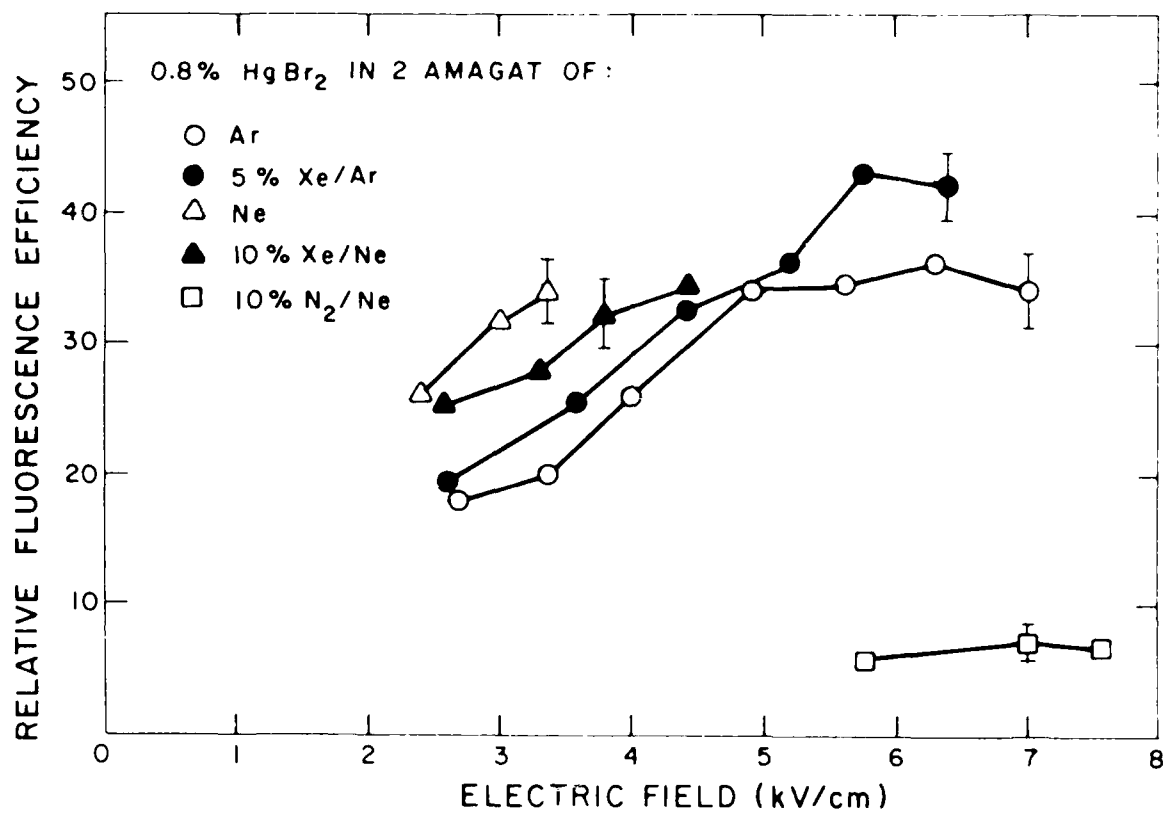


Figure 16. Integrated Fluorescence with Different Buffers at Constant E-Beam



J8853

Figure 17. Experimental Relative Fluorescence Efficiencies for Different Buffers

TABLE 1. RELATIVE LASER INTRINSIC EFFICIENCY OF DIFFERENT MIXES

BUFFER GAS	PERCENT HgBr ₂	E/N (Vcm ²)	RELATIVE INTRINSIC EFFICIENCY
2 Amag Ar	0.8%	1.1×10^{-16}	1.0
2 Amag Ar, 3% Xe	0.8%	1.0×10^{-16}	0.74
2 Amag Ne	0.8%	6.4×10^{-17}	0.69
2 Amag Ne, 5% Xe	0.8%	6.7×10^{-17}	0.61
1 Amag Ar	1.6%	9.2×10^{-17}	0.74

The highest laser output energy and highest efficiency were both achieved with the pure Ar buffer. The addition of Xe to either Ar or Ne had the effect of reducing laser efficiency rather sharply. This appears to be the consequence of a Xe_2 molecular absorption at the laser wavelength, although this point was not pursued in the present study.

The data for 1 Amagat Ar is almost identical to that for 2 Amagat Ar + 3% Xe, both showing lower efficiency and energy loading than for 2 Amagat Ar. In our kinetic model the efficiency difference at 1 Amagat Ar is explained by a lower deactivation rate for the lower laser level.

The sidelight depression for the Ne buffer indicated a slower deactivation rate of the lower laser level than for Ar. This fact, coupled with the relatively lower energy loading obtainable in Ne (~ 0.5 of that in Ar) implied that in order to achieve specific energies of up to 2 J/l in Ne, a Ne density of 4 Amagat would be required. By contrast, Argon gives 2 J/l at 2 Amagat.

f. Framework of Laser Kinetic Model for Argon/ HgBr_2

Coupled rate equations were written for the populations of atomic and molecular species, ions, electrons, and the spatially averaged cavity photon flux (averaged in the propagation direction). The photon equation is derived in Ref. 14. A list of the species followed is given in Table 2. The populations of HgBr_2 (6.4 eV) and HgBr_2 (5 eV) states were assumed negligible because of their fast relaxation into products. The coupled equations were solved using the Gear routine "DIFSUB" for stiff systems. Solution time was typically 2 s on an IBM 3700.

Excitation rates for the HgBr_2 processes were computed by a Boltzmann routine which had been tested carefully for a wide variety of gases against experiment and other codes. In order to avoid repetitious calculations of Boltzmann solutions, a rates table was compiled for ranges of HgBr_2 concentration and E/N.

TABLE 2. LIST OF SPECIES FOLLOWED IN KINETIC MODEL

Ar , Ar^* , Ar_2^* , Ar^+ , Ar_2^+
 HgBr_2 , HgBr_2^{**} (7.9 eV), HgBr_2^+
 $\text{HgBr}(X) \ v \approx 0$, $\text{HgBr}(X) \ v \approx 22$, $\text{HgBr}(B)$
 Br , Br_2 , Br^- , electron density, photon flux

Stepwise voltage changes were applied to the discharge to approximate the smooth experimental waveform. At each voltage change the table was consulted by log-log interpolation to derive new excitation rates, drift velocity, characteristic energy, and ionization and attachment rates. The errors introduced by the interpolation were $\lesssim 5\%$.

In order to model the effects of nonuniform e-beam deposition in the anode to cathode direction, the space was divided into 8 segments and a separate laser kinetic code was run in each segment. The segment E/N values were calculated by an iteration procedure which used the running electron density in a segment and consulted the Boltzmann table for the drift velocity. This segmentation with ordinary differential equation solutions is appropriate when

$$v_d \tau_p \lesssim d \quad (1)$$

where v_d is the electron drift velocity, τ_p is the duration of the discharge pulse and d is the thickness of a segment. If Eq. (1) were not satisfied, the proper accounting of particle flux between segments would require the use of a partial differential equation approach. Further, the segmented model does not account for optical flux between segments, and is therefore only strictly applicable to plane-plane optical cavities where the individual segment has a large Fresnel number. The comparison with the 1 m x 8 cm cavity experiments is valid by these criteria.

The existence of simultaneous lasing on the 502 and 504 nm lines has been considered. Because the saturation flux is almost identical for these lines (see Section II-A-2-h) for the experimental gain cross section) they obey the same photon equation. Also, because of our experimental evidence (from single

14. Jacob, J.H., Hsia, J.C., Mangano, J.A., Rokni, M., J. Appl. Phys. 50, p. 5130 (1979).

line extraction, Section II-A-2-o) and other work on narrow band operation,⁽¹⁵⁾ the terminal vibrational levels are considered to be homogeneously broadened. As a consequence we may add the photon equations for 502 and 504 nm to obtain a single equation which represents the flux integrated over lasing wavelength. This will be compared to experiments which are "broadband," but it also accurately represents the single wavelength behavior of the system.

The dominant kinetic processes are shown in Figure 18. The experimental evidence for this scheme will be described, process by process, with modeling of the experiment where appropriate.

g. Formation Efficiency: Absolute Measurement

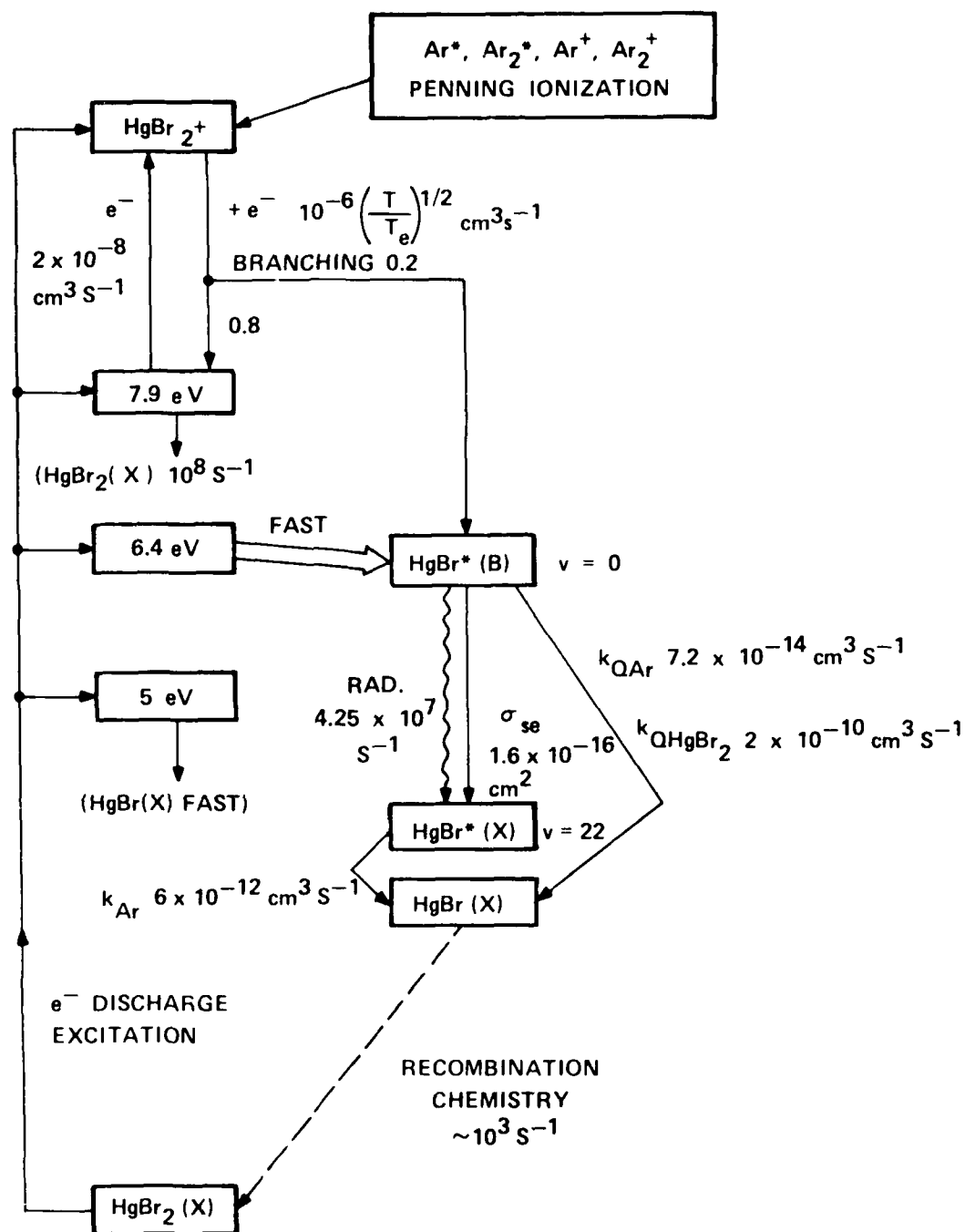
The arguments for direct excitation have been given in Section II-A-2-b. However, the absolute value of formation efficiency has not been discussed in detail. An absolute measurement of formation efficiency was made in order to "close the circle" of the separate measurements of quenching, absorption and laser efficiency.

Using the "cable gun" pulser with a 1 x 1.2 cm discharge cross section, sidelight was measured in a geometry defined by two circular apertures (Figure 19). The photodiode was calibrated ($\pm 15\%$) using repetitively-pulsed dye laser (at 502 nm) of measured pulse shape and average power. Uncertainty in the collection volume was $\pm 10\%$ after corrections had been made for the transverse variation of the discharge as determined by photography. The discharge current and voltage monitors each had an uncertainty of $< 10\%$. The time dependence of fluorescence was accurately modeled by the kinetic code (Figure 20) in order to derive the formation efficiency. In this calculation electron quenching of $\text{HgBr}^*(\text{B})$ was zero (Experiment, Section II-A-2-j) and quenching by HgBr_2 was given the rate $2.0 \times 10^{-10} \text{ cm}^3 \text{ sec}^{-1}$.^(16,17)

15. Schimitschek, E.J., private communication.

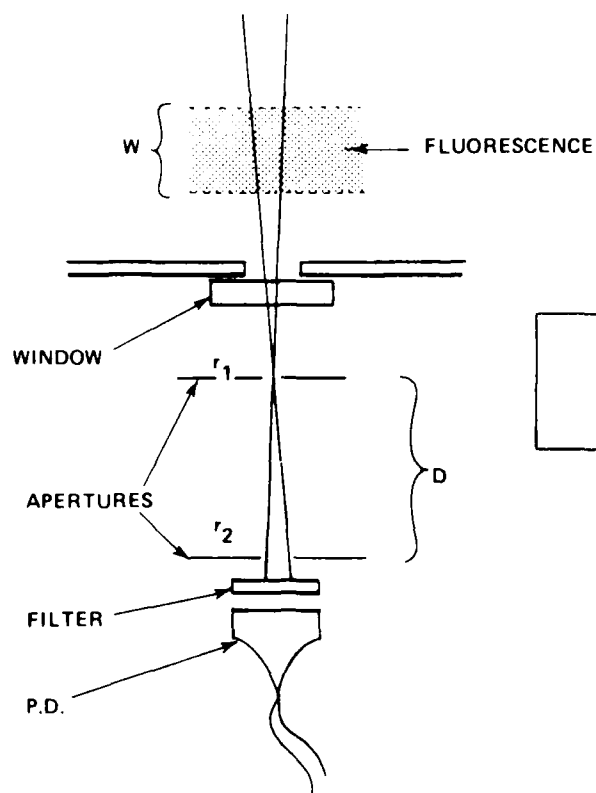
16. Waynant, R.W. and Eden, J.G., Appl. Phys. Lett. 33, p. 708 (1978).

17. Helvajian, H. and Wittig, C., Opt. Comm. 30, p. 189 (1979).



J8843

Figure 18. Kinetic Scheme for HgBr₂/Argon Laser



$$V_{\text{eff}} = \frac{\pi}{4} \frac{(r_1 r_2)^2}{D^2} W$$

$$\text{HgBr}^* \text{ DENSITY} = \frac{S}{F} \cdot \frac{1}{V_{\text{eff}}} \cdot \frac{\tau_r}{h \nu}$$

S = PHOTODIODE SIGNAL

F = PHOTODIODE RESPONSE & FILTER TRANS.

τ_r = RADIATIVE LIFETIME

J8842

Figure 19. Geometry for Absolute Fluorescence Measurement

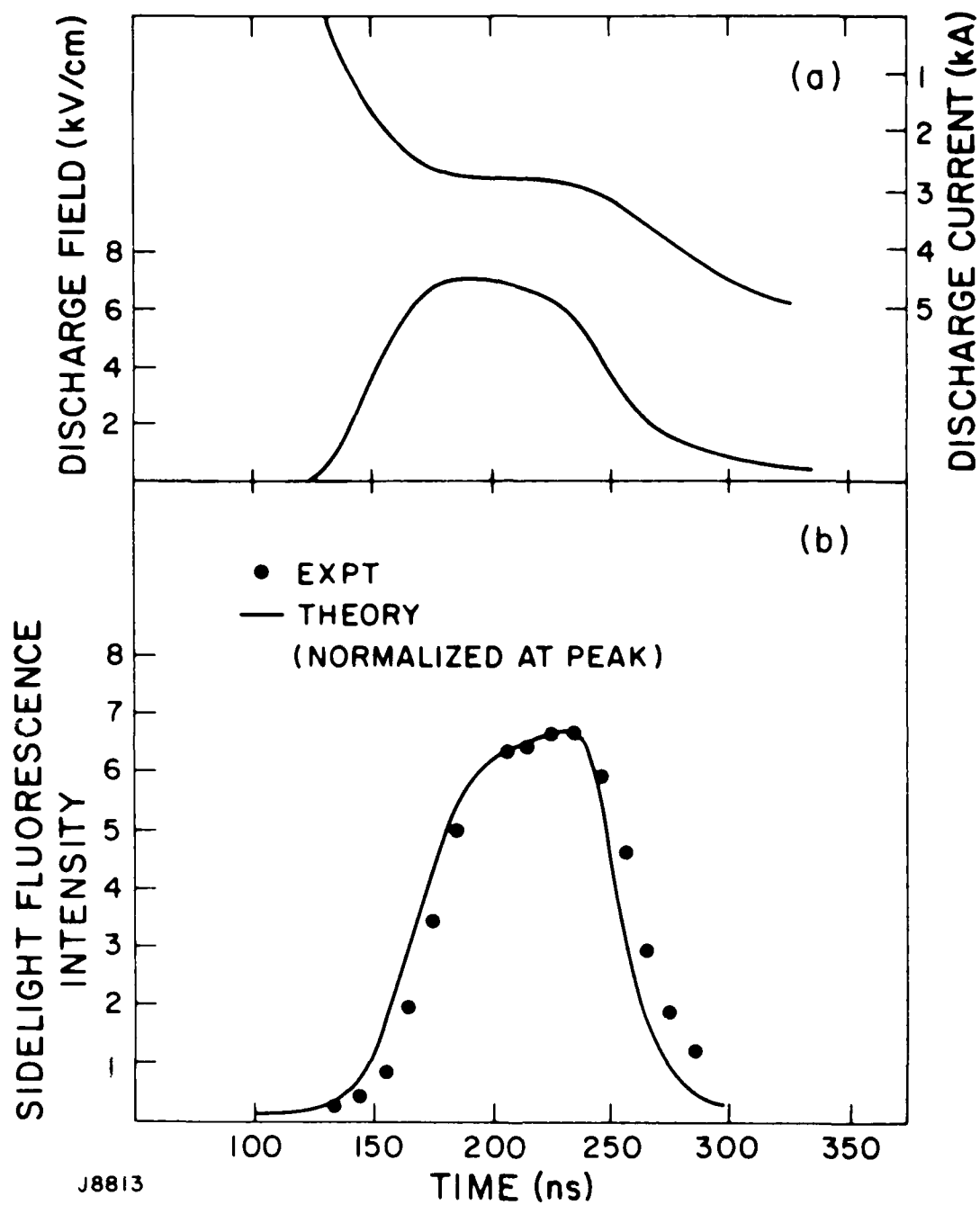


Figure 20. (a) Experimental and Modeled Voltage and Current Waveforms
 (b) Observed and Calculated Sidelight Fluorescence (without Lasing)

The formation efficiency (= fluorescence power without quenching/discharge power) was determined to be 4.5% (error \pm 30%) for 0.8% HgBr₂ in Ar at $E/N = 1.2 \times 10^{-16}$ Vcm₂. This value is too low (by 30%) to explain the observed lasing efficiency when it is used in the complete kinetic model with absorptions. The prediction of laser efficiency will be discussed in Sections II-A-3-c and II-A-3-d where a higher formation efficiency (6.1%) is chosen as a more accurate fit to experiment.

h. Gain Measurement: Stimulated Emission Cross Section

Gain measurements were made on the small-scale device at wavelengths throughout the HgBr band. A tunable dye laser of bandwidth 1 cm^{-1} was aligned down the discharge axis and its 5 ns pulse was delayed to probe the gain at various times before, during and after the discharge pulse.

1) Measured Small Signal Gain versus Wavelength

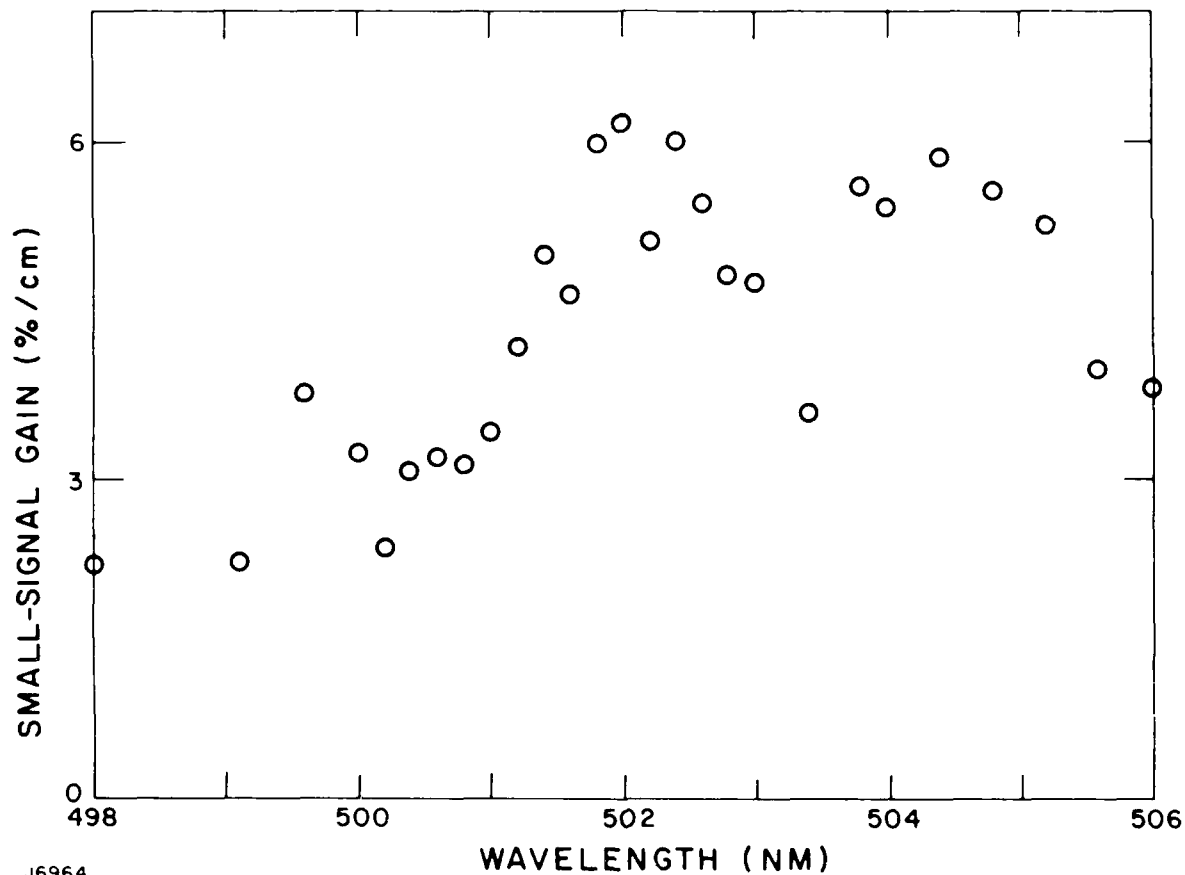
Data was taken through the peak of fluorescence in the capacitor driven discharge (Figure 21). The principal gain peaks were at 502 and 504 nm, and gain was observed to vary smoothly near the peaks, indicating a merging of rotational-vibrational transitions at least over the 1 cm^{-1} bandwidth sampled by the probe laser. At 2 Amagats the pressure broadening of individual lines is also $\sim 1 \text{ cm}^{-1}$ so that this gain measurement did not miss any very narrow high-gain line structure.

Taking the measured HgBr*(B) population in identical experimental conditions (Section II-A-2-g) and allowing for lower level HgBr*(X) $v = 22$ population the stimulated emission cross section was found to be $\sigma_{SE} = 2.1 \times 10^{-16} \text{ cm}^2 \pm 35\%$. However, the measured HgBr*(B) population appears to be an underestimate. Using the more accurate formation efficiency of 6.1% (Section II-A-2-g) we obtain $\sigma_{SE} = 1.6 \times 10^{-16} \text{ cm}^2 \pm 20\%$ at 502 nm.

2) Stimulated Emission Cross Section by Other Methods

- (a) The HgBr fluorescence profile was recorded on a multi-channel analyzer. The details of the band center profile were taken from the data in Figure 21. Using

HgBr LASER IS TUNABLE OVER 100 Å RANGE
MEASURED SMALL-SIGNAL GAIN vs WAVELENGTH



J6964

Figure 21. Measured Small-Signal Gain Near Band Center

$$\int \sigma d\lambda = \frac{\lambda^4 A}{8\pi C}$$

where A equals spontaneous emission rate, λ equals wavelength, we calculate the peak $\sigma_{SE} = 2.0 \times 10^{-16} \text{ cm}^2 \pm 30\%$.

- (b) The lasing buildup time is obtained from sidelight fluorescence (Figure 27) and the simulation of this buildup time from spontaneous noise levels required $\sigma_{SE} = 1.6 \times 10^{-16} \text{ cm}^2 \pm 30\%$.

3) Measured Small-Signal Gain versus Time

With the dye laser tuned to 502 nm the temporal behavior of the gain was studied. As expected, the gain precisely followed the sidelight (Figure 22). This behavior indicated that there was a steady state rapid depopulation of the lower laser level, as was confirmed in the measurement of sidelight depression (Section II-A-2-k).

i. Absorption Measurements

The dye laser was employed in a double pass collinear arrangement and tuned between 530 nm and the line center at 502 nm. Because of residual gain between 502 and 515 nm, absorption measurements were only made between 515 and 530 nm. Residual gain precluded any measurement on the blue side of the line down to 470 nm.

Figure 23 shows the time dependence of the absorption at 520 nm. During the discharge there was a linearly rising absorption, which averaged 0.3%/cm. (In the same experiment the gain reached 10%/cm).

Before the start of the discharge a low absorption of $\sim 0.1\%/cm$ was seen, and this was present with just the e-beam on. At the end of the discharge there was a rapidly growing absorption which was correlated with the discharge arc and persisted for several tens of nsec. In a similar experiment with the PFN driven

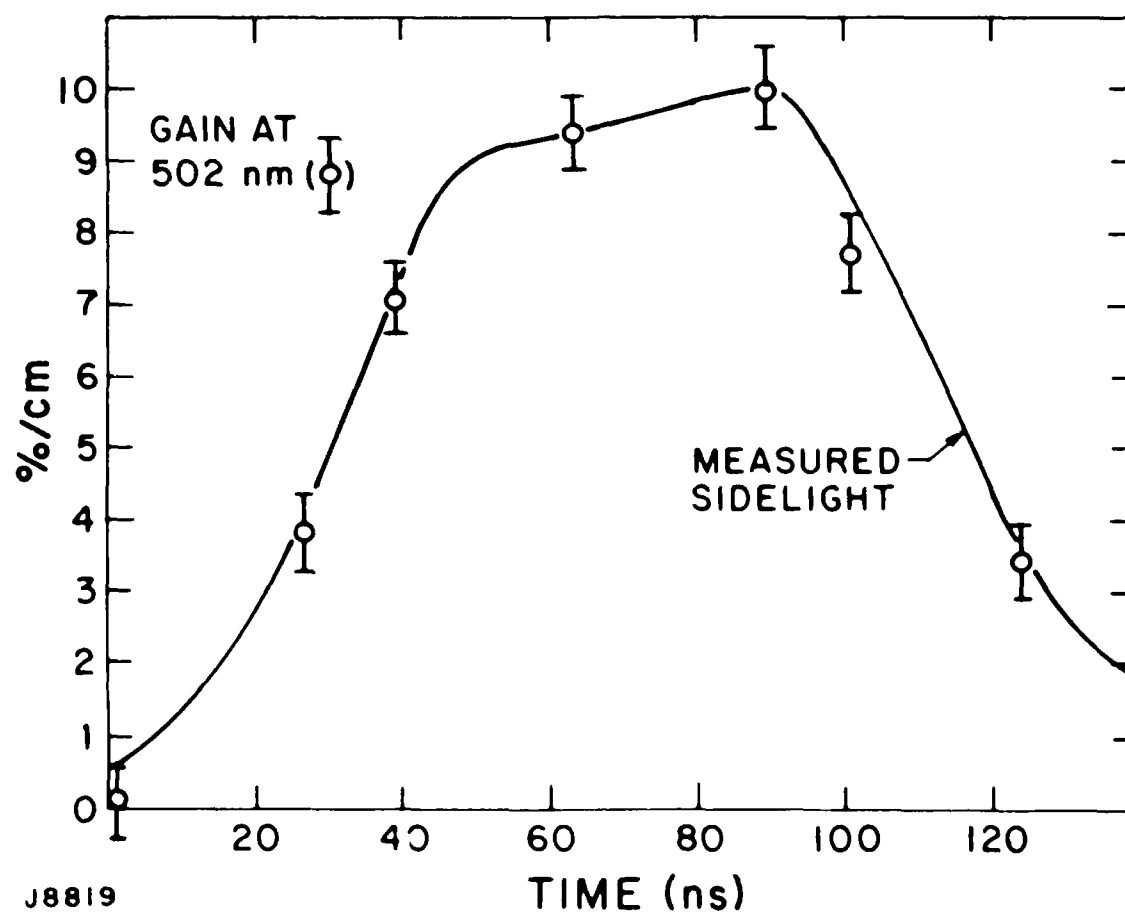


Figure 22. Small-Signal Gain vs Sidelight as a Function of Time

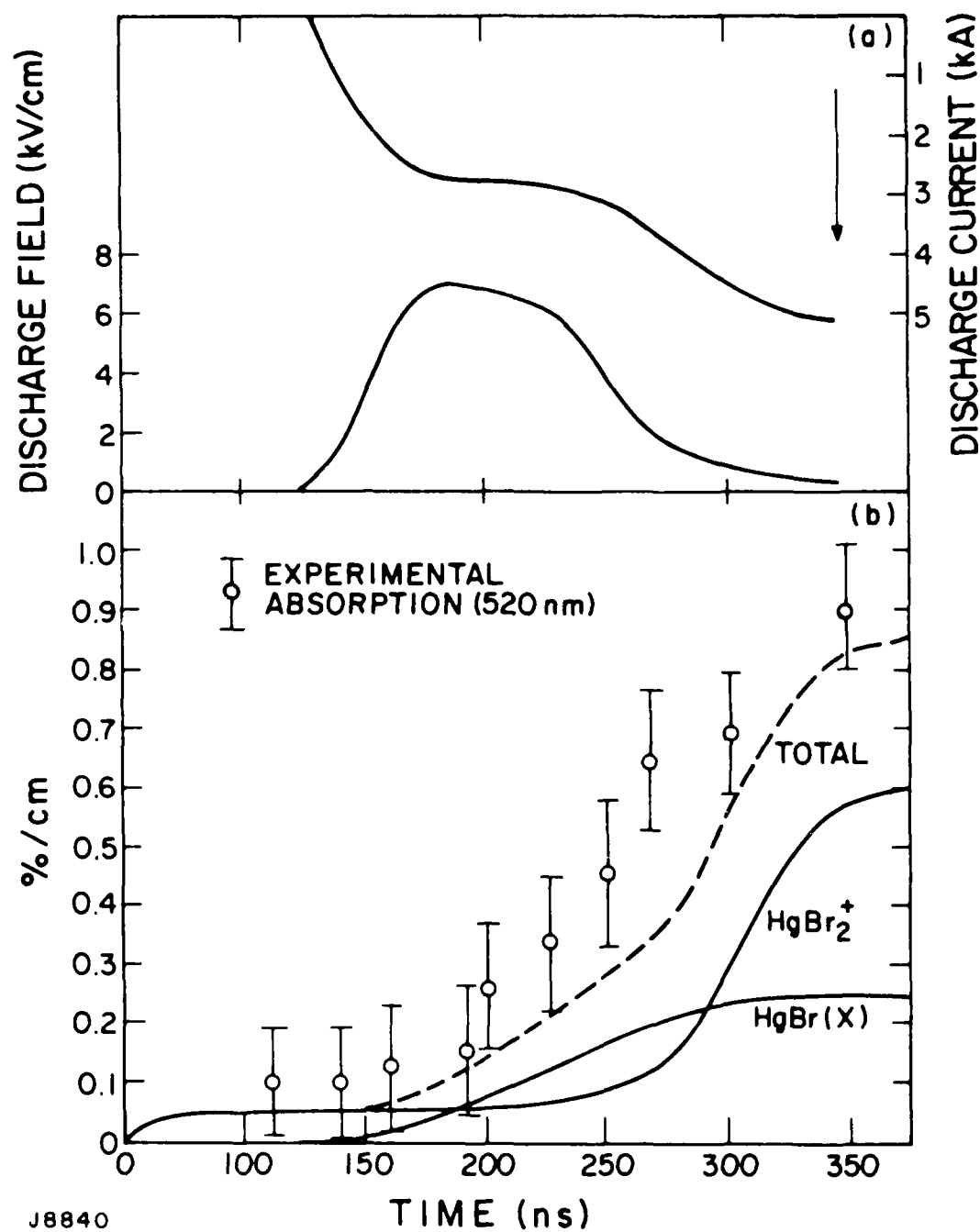


Figure 23. (a) Experimental and Modeled Voltage and Current Waveform
(b) Experimental and Computed Absorption for Capacitor Circuit

discharge (Figure 24), arcing was suppressed by the early voltage fall and the absorption did not increase after the discharge pulse, but decreased to a steady value, which held for at least 700 ns.

From the above data we identified the most probable absorbing species as HgBr_2^+ (the dominant ion), and HgBr(X) . Further evidence on the intrinsic laser efficiency as a function of e-beam current density also confirmed the assignment of an absorption to HgBr_2^+ . It had been expected from the structure of HgBr that a visible HgBr(X+A) absorption would exist. A similar process has been predicted for HgCl ⁽¹⁸⁾ and degrades the HgCl laser efficiency.

The kinetic code was run with varying absorption cross sections for the two processes, to give the theoretical curves in Figures 23 and 24. From this procedure, the measured absorptions at 520 nm are

$$\sigma(\text{HgBr}_2^+) = 2 \times 10^{-18} \text{ cm}^2$$

$$\sigma(\text{HgBr(X)}) = 5 \times 10^{-20} \text{ cm}^2$$

In our initial modeling of the lasing behavior at 502 nm, it was assumed that the 520 nm absorptions applied. This was suggested by the less than 30% variation of the measured absorptions from 530 to 515 nm, and, in case of the HgBr(X+A) absorption, the expectation that the absorption is a broad continuum. ⁽¹⁸⁾ All aspects of the lasing behavior are modeled reasonably well using these absorptions. However, detailed modeling of the intrinsic laser efficiency as a function of e-beam current density (Section II-A-3-c) and also of the electrical efficiency, Section II-A-3-k) has led us to use $\sigma(\text{HgBr(X)}) = 3 \times 10^{-20} \text{ cm}^2$, $\sigma(\text{HgBr}_2^+) = 2 \times 10^{-18} \text{ cm}^2$ at 502 nm.

18. Julianne, P.S., Konowalow, D.D., Krauss, M., Rosenkrantz, M.E., and Stevens, W.J., Appl. Phys. Lett. 36, p. 132 (1980).

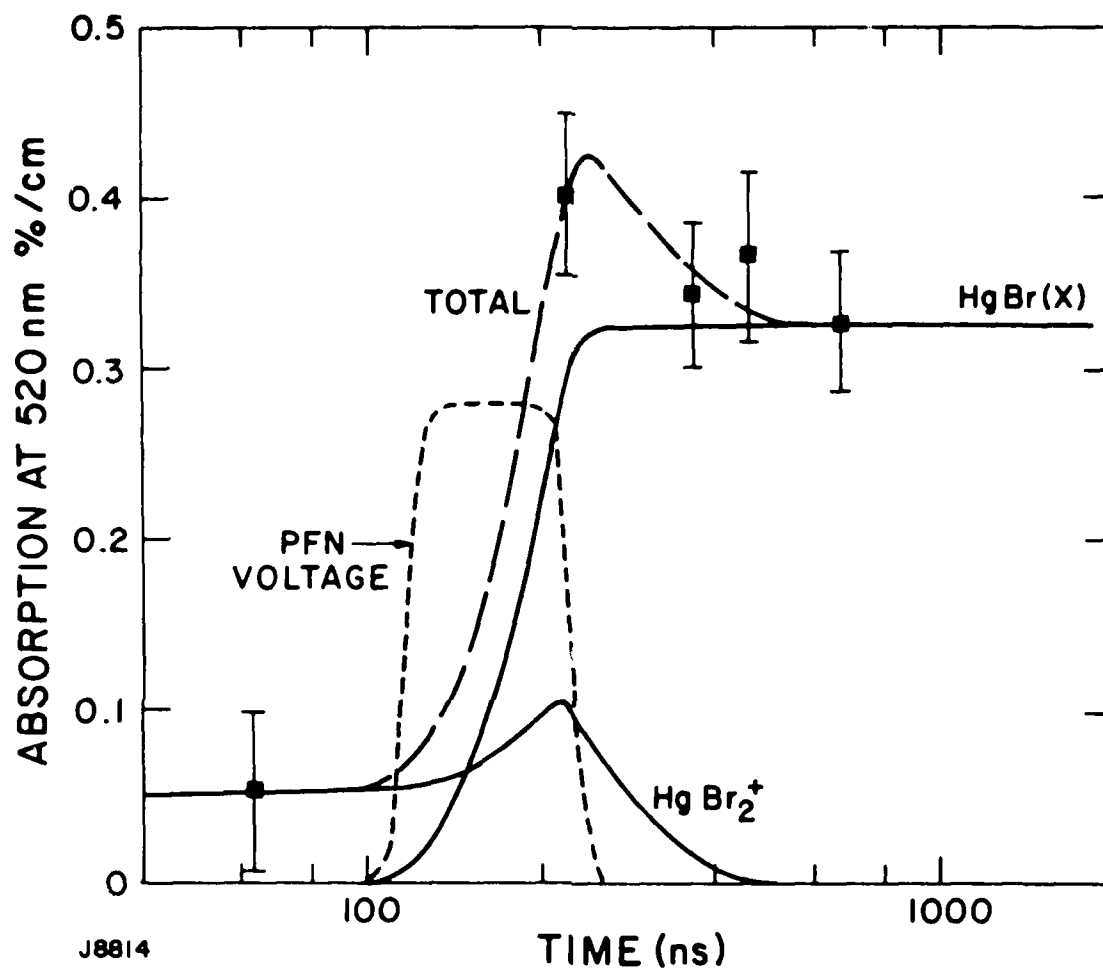


Figure 24. Experimental and Computed Absorption for PFL Circuit

The relative excitation curves of Figure 9 show that over 80% of the discharge power goes into the production of $\text{HgBr}(X)$, which absorbs.

j. Electron Quenching

An upper bound was placed on the rate constant for $\text{HgBr}^*(B) + e^- \rightarrow \text{HgBr}(X) + e^-$ of $K_Q = 5 \times 10^{-9} \text{ cm}^3 \text{ sec}^{-1}$. Using the PFN driven discharge (Section II-A-2-a), the e-beam current density was varied between 0.6 A/cm^2 and 2.4 A/cm^2 , and the fluorescence efficiency monitored. In order to have an accurate comparison between the different e-beam cases, an externally controlled e-beam attenuator was used, which allowed different current densities to be used with the same gas fill of HgBr_2 (0.8%) and Ar.

The data is shown in Figure 25, where the e-beam current density has been translated into electron density using the kinetic code. When $K_Q = 0$, the fluorescence rises slightly with increasing e-beam, due to the recombination channel into $\text{HgBr}^*(B)$. Kinetic code runs for $K_Q = 1 \times 10^{-8} \text{ cm}^3/\text{sec}$ are shown (dashed curve), giving an upper bound on K_Q of $5 \times 10^{-9} \text{ cm}^3 \text{ sec}^{-1}$.

This result is for a typical operating E/N, where the characteristic electron energy from the Boltzmann calculation is 6.3 eV.

k. Lower Level Deactivation

The existence of a relatively high sidelight level during lasing is evidence for a 'bottleneck' in the deactivation of $\text{HgBr}^*(X)$ v = 22, the lower laser level.

In experiments with a PFN driven discharge, sidelight was monitored as a function of e-beam current density, with and without lasing. The lasing was with 100% - 90% reflectors in order to have rapid pulse buildup and high intracavity flux. Traces of sidelight fluorescence with and without lasing are shown in Figure 26. Data which shows a more constant sidelight appears in Figure 27. The sidelight appears to be independent of the laser power, was 0.40 independent of intracavity power.

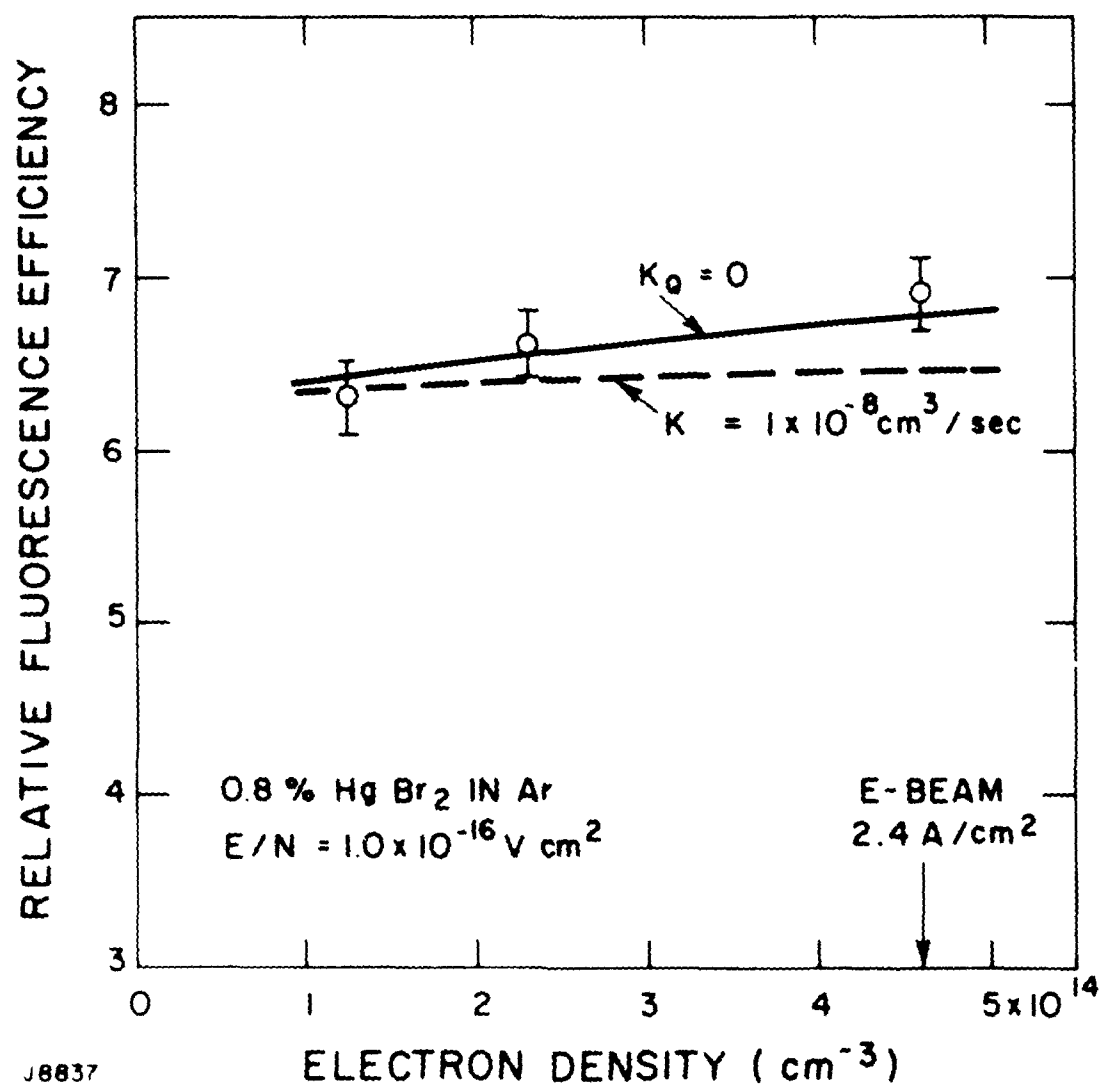
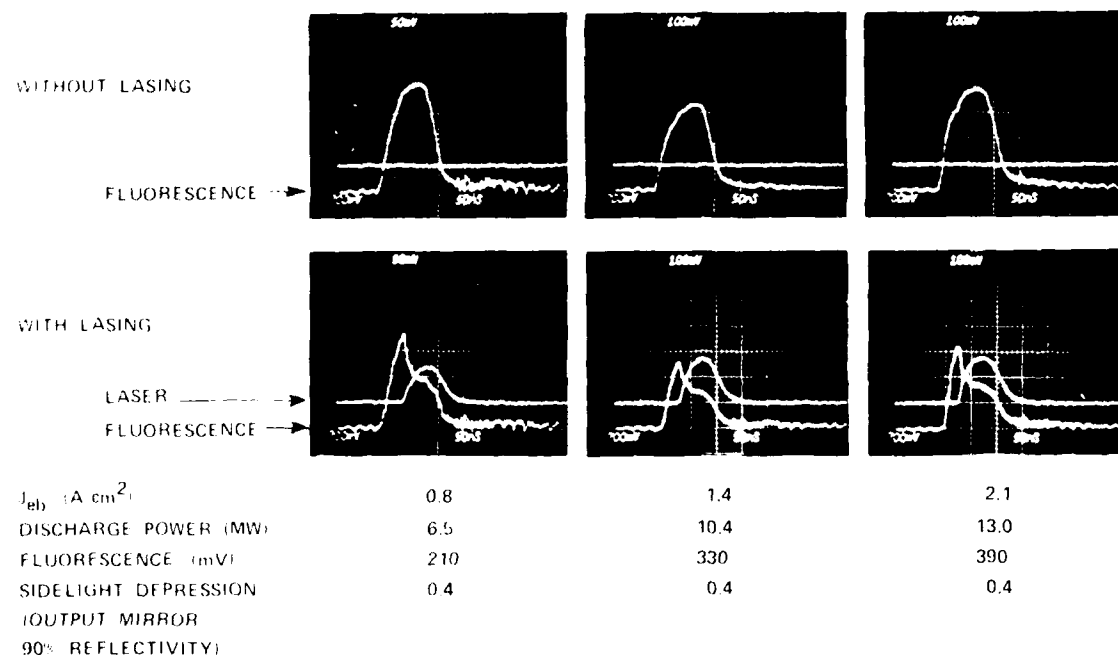


Figure 25. Fluorescence vs Electron Density: an Upper Bound on Electron Quenching



J8852

Figure 26. Experimental Sidelight Depression as a Function of Discharge Power

A computer simulation of the same experiment is shown in Figure 27. The lower laser level was given the deactivation process $\text{HgBr}(X) v' + \text{Ar} \rightarrow \text{HgBr}(X) v'' + \text{Ar}$ with a rate constant of $6.0 \times 10^{-12} \text{ cm}^3/\text{sec}$.

The simulated sidelight depression varied between 0.35 and 0.37, at different discharge powers. A correction was applied to the experimental sidelight depression to allow for the transverse variation in discharge power, which accounted for less intense lasing in the discharge fringe regions. After this correction the true experimental sidelight depression in the most intense region of lasing was estimated to be 0.35, which was used to fit the deactivation constant.

1. Recombination

It was estimated that the dominant discharge ion species was HgBr_2^+ , and that recombination occurred principally via $\text{HgBr}_2^+ + e^- \rightarrow \text{HgBr}_2^{**}$ followed by dissociation on a rapid timescale into

(1) $\text{HgBr}^*(B)$ with branching 0.2

(2) $\text{HgBr}(X) + \text{Br}$ with branching 0.8

By analogy with similar processes the recombination was estimated to be

$$10^{-6} \left(\frac{T_{\text{GAS}}}{\epsilon} \right)^{1/2} \text{ cm}^3 \text{ sec}^{-1}$$

where T_{GAS} is the gas temperature and ϵ is the electron characteristic energy ($^{\circ}\text{K}$). Because the characteristic energy was in the range of 5 eV, the effective recombination rate coefficient was $\sim 1 \times 10^{-7} \text{ cm}^3 \text{ sec}^{-1}$. This gave the observed attachment-dominated discharge conditions (Section II-A-2-n), except possibly at the higher e-beam current densities ($\geq 2 \text{ A/cm}^2$), where there were indications that a slightly lower recombination coefficient might apply.

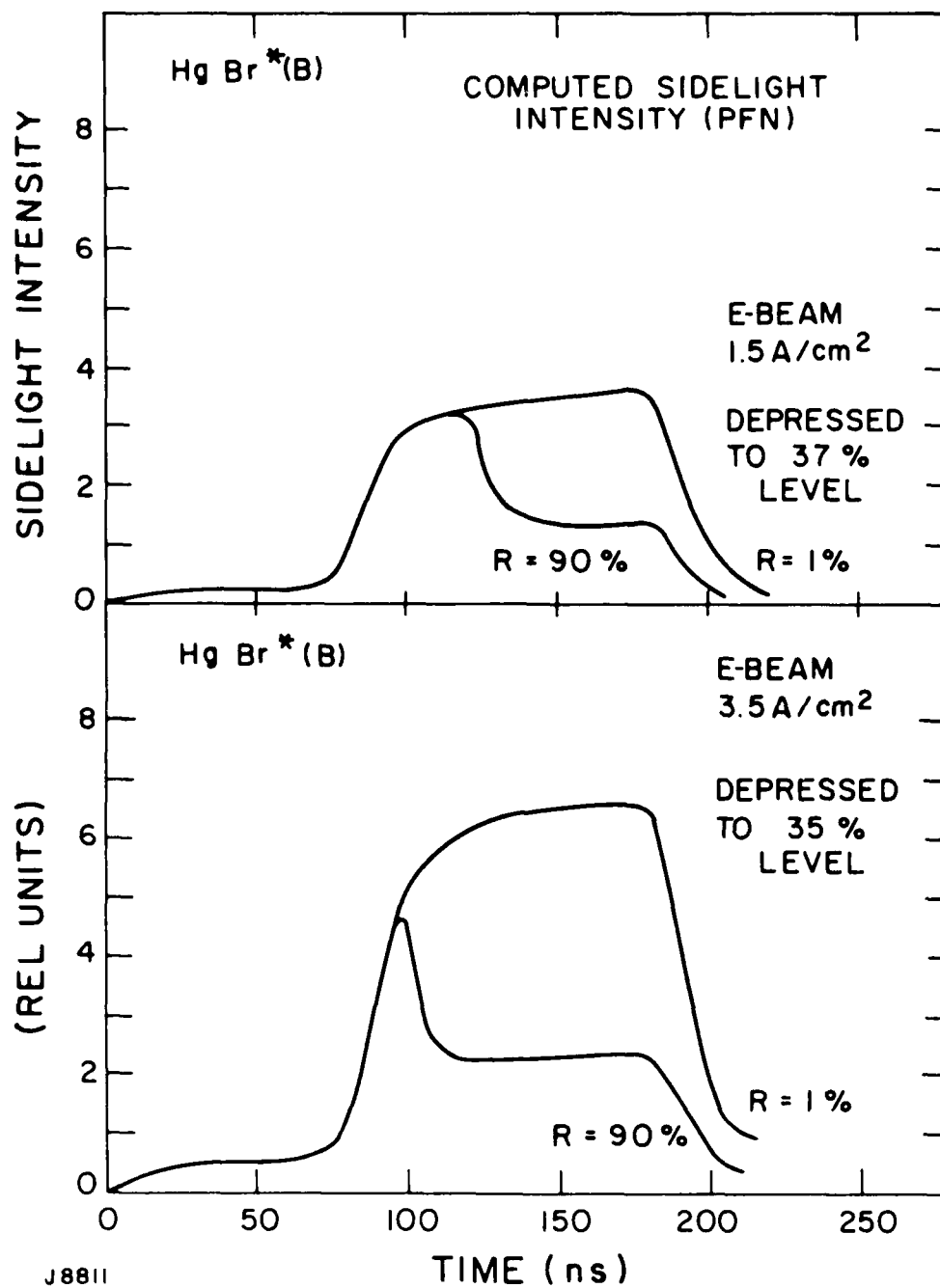
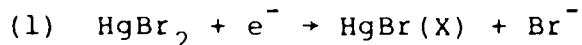


Figure 27. Computed Sidelight Depression as a Function of Discharge Power

m. Attachment

In principle, dissociative attachment could occur by two processes



However, theoretical analysis⁽¹⁹⁾ has shown that there is no curve crossing to allow process (2) to occur, and that it should have a very low rate. The attachment rate for process (1) had been the subject of a number of measurements,^(6,7,20) not all in agreement, so a new measurement was undertaken in discharge conditions relevant to the HgBr laser. The capacitor driven discharge was run at relatively low E/N ($4.5 \times 10^{-17} \text{ Vcm}^2$) and the current was monitored following the e-beam termination. The current decayed exponentially and an attachment rate of $1.1 \times 10^{-10} \text{ cm}^3/\text{sec}$ was deduced at the operating E/N. This value was close to that predicted by the Boltzmann code, using 1.1 times the UTRC cross section (Section II-A-2-b).

Experimental constraints prevented accurate attachment measurements at either higher, or lower E/N values. The predicted attachment rate (Figure 28) was relatively constant through the operating E/N range. However, in later experiments on the 1 m device clear evidence emerged for a slope on the attachment rate in the sense that it increased with applied field, with a slope of ~ 1 in the E/N range $5 \times 10^{-17} \rightarrow 7 \times 10^{-17} \text{ Vcm}^2$. This is seen in Figure 33(B) where the applied voltage increases after 150 ns and the current dips. Possible explanations for this discrepancy are:

1. The attachment cross section may be modified by vibrational excitation of HgBr_2 .
2. A second attachment channel exists via an excited HgBr_2 state, which has been missed in the UTRC cross-section measurement.

19. Krauss, M., private communication.

20. Brooks, H.L., Sierra, R.A., Nygaard, K.J. and Fletcher, J., private communication.

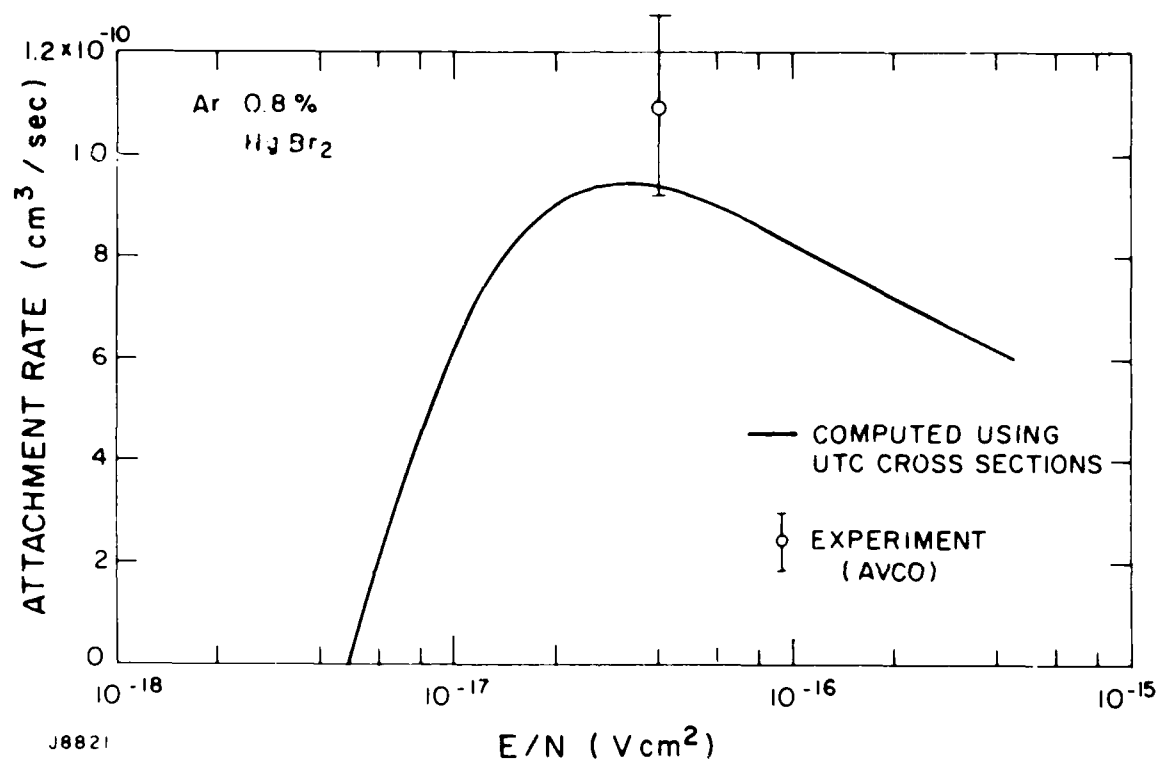


Figure 28. Computed Attachment vs E/N, and Experimental Point

Further refinement in the discharge modeling will require a re-examination of attachment as a function E/N .

n. Discharge Impedance and Arcing

(1) Discharge Impedance

The kinetic model was able to give a good prediction of the discharge impedance, as determined by experiments with the PFN driven discharge. Without a two-step ionization process we obtained the solid lines in Figure 29. In order to remove discharge geometrical factors and e-beam deposition from this comparison of the model with experiment a separate experiment was performed in pure Ar, which has a precisely known drift velocity and zero attachment. In pure Ar the measured discharge impedance agreed with theory to within 15%, at an e-beam current density of 0.55 A/cm^2 . If we believe that the attachment rate is known to within 20% then it follows that the drift velocity in HgBr_2 mixtures has been predicted correctly to within $\pm 30\%$, confirming its calculated two times enhancement over that in pure Ar.

(2) Two-Step Ionization

In Figure 29 the experimental points stop at the E/N at which the discharge arced before the termination of the 120 ns PFN pulse. At the highest e-beam current density the arcing occurred at a substantially lower E/N . This is not explicable by a single-step ionization process, but is characteristic of a two-step ionization process. From photography on the small-scale discharge and streak photography on the 1 m experiment the arcing was shown to be volumetric, rather than in spatial channels.

A two-step process was added to the model by giving a direct ionization process to the $7.9 \text{ eV HgBr}_2^{**}$ state. Because the threshold for this process was only 2.7 eV and the characteristic electron energy was 5 eV the process was given a constant rate, independent of E/N . The dashed curves in Figure 29 show the effect of a two-step process rate of $2 \times 10^{-8} \text{ cm}^3/\text{sec}$. (This value is of course dependent on our assumption of a blanket 10^8 sec^{-1} decay rate for the 7.9 eV state.) With the two-step process it is possible to cause discharge arcing at decreasing E/N as

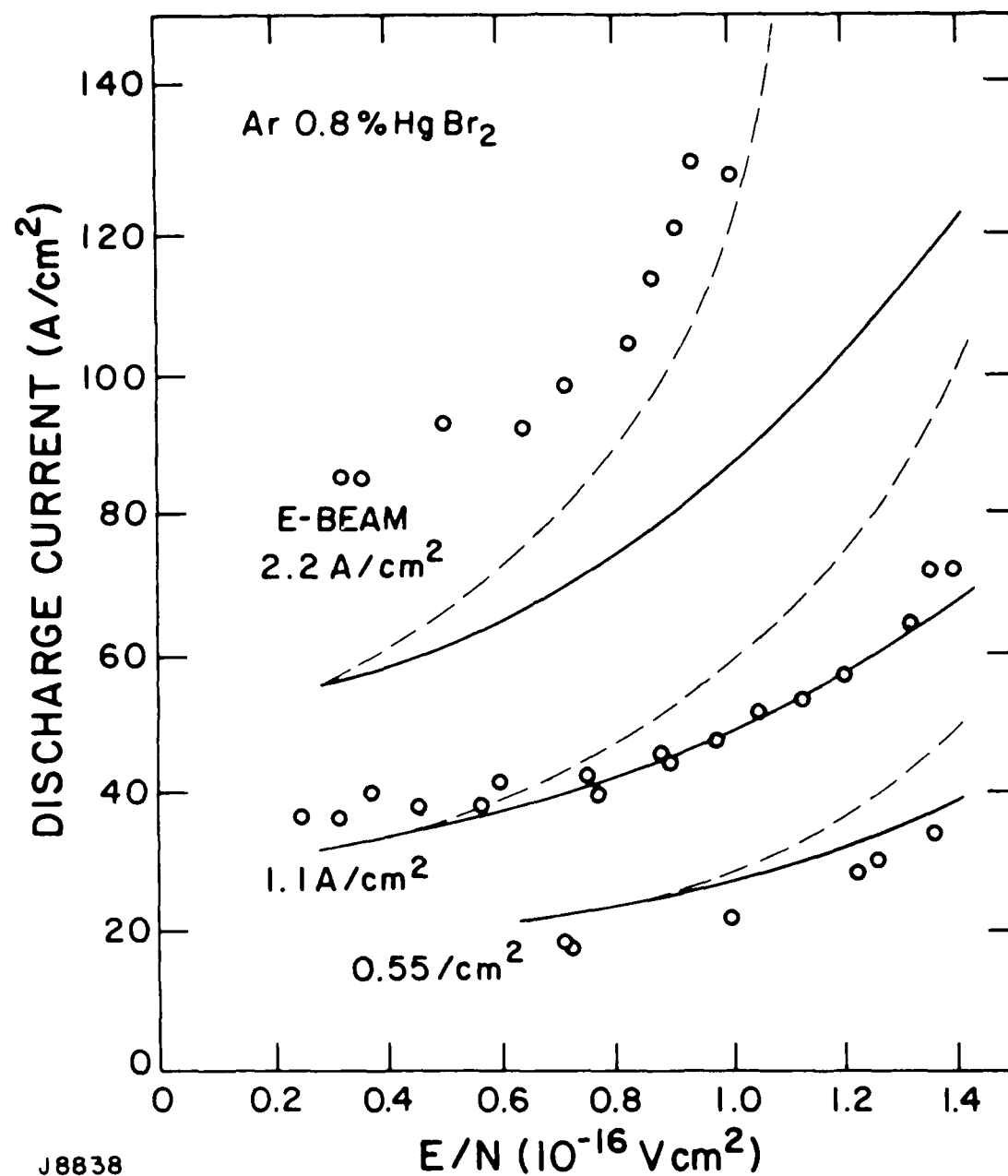


Figure 29. Experimental and Computed Discharge Current. Broken curve includes two-step ionization process.

the e-beam current density increases, in qualitative agreement with experiment. The slope of the computed two-step curves (Figure 29) is too high, but would be modified in the right direction by the use of an attachment rate which increased with increasing E/N , as suggested in Section II-A-2-m.

In conclusion, there is good evidence for a two-step volumetric arcing process as the primary limitation on discharge energy loading. The kinetic model predicts discharge impedance to $\pm 20\%$ in the 1 A/cm^2 e-beam range, which is adequate for design purposes, since either HgBr_2 concentration, total pressure, or e-beam current density may be used for "fine tuning" of the discharge impedance, if necessary.

o. Injection and Single Line Lasing

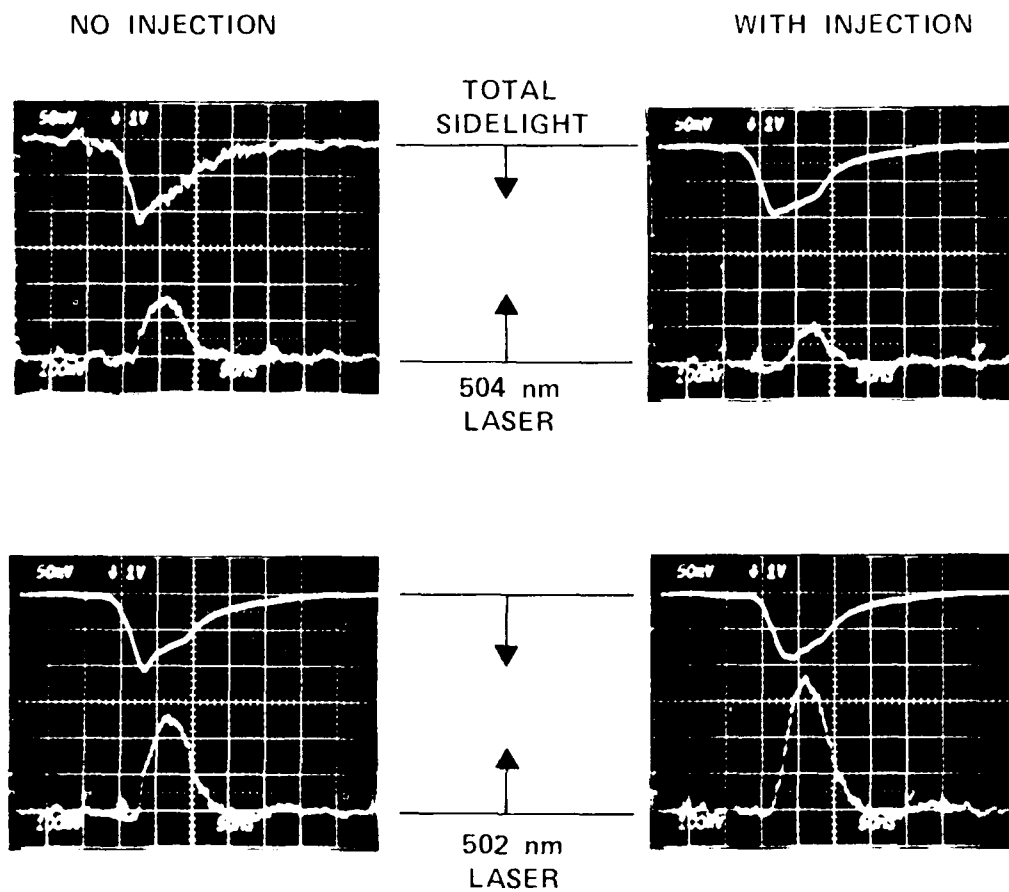
Injection serves the twofold purpose of decreasing the laser flux buildup time and locking the oscillator frequency to the injected frequency. In the small-scale experiments the buildup time without injection was $\sim 25 \text{ ns}$, as seen for example in Figure 26. An experiment was performed with a pulsed dye laser tuned to 502 nm to explore the possibilities for increased energy extraction and single line operation.

Without frequency selection the small-scale laser oscillated with an energy ratio $502 \text{ nm} (62\%):504 \text{ nm} (38\%)$. With a 10 ns 10^4 W pulse of bandwidth $\Delta\lambda < 0.1 \text{ \AA}$ at 502 nm injected at the beginning of the discharge the energy ratio changed to $502 \text{ nm} (80\%):504 \text{ nm} (20\%)$ with a frequency narrowing to $\Delta\lambda < 1 \text{ \AA}$ at 502 nm . Without injection the bandwidth of both lines was $\Delta\lambda \approx 6 \text{ \AA}$.

Additionally an increase of 10% (40 to 44 mJ) occurred in the total output energy. A higher injection power would have been needed to extract the further 10% of energy still being lost through buildup time.

Figure 30 shows the sidelight and laser pulses at 504 and 502 nm , with and without injection. A measure of the effect is the decrease in the initial sidelight level, which is due to a higher intracavity flux at early times.

LASER OUTPUT WITH AND WITHOUT INJECTION AT 502 nm



J6963

Figure 30. Sidelight and Laser Output vs Injected Power

Evidence from this experiment and also from other work⁽¹⁵⁾ shows that complete energy extraction will be possible on a single line (502 nm) at very nearly the same efficiency as is observed with two wavelength extraction. This is good evidence for the rapid vibrational mixing of the terminal laser levels, which already is thought to be faster than the $3 \times 10^8 \text{ sec}^{-1}$ overall decay of the lower laser level (Section II-A-2-k).

In conclusion, energy loss due to cavity buildup time can be recovered; energy can be extracted in one line with little loss in efficiency; and narrow banding down to 0.2 Å should not present any problem.

p. Voltage Standoff Recovery

The flow velocity required for the gas moving through the discharge region is established by two criteria. One is the amount of time required for the recovery of medium homogeneity. The other is the distance that discharge heated gas must be moved after each pulse so that there is no possibility of arcing through this hot gas region during the next pulse. Since the flow power goes up as the cube of the flow velocity, it is important to determine the lower bound on the flow velocity (flush factor) set by each of these criteria. The potential difficulty of downstream arcing through the discharge heated gas was investigated by a series of experiments conducted on the small-scale device.

In these experiments, two voltage pulses were applied to the discharge electrodes. The first with the normal e-beam current, and the second, 2.5 to 5 ms later, without the e-beam. The voltage applied during the first pulse was the normal 6 kV/cm. In excess of 10 kV/cm could be applied during the second pulse without seeing any signs of breakdown. Since the 2.5 ms pulse separation correspond to a 400 Hz rep-rate, it is clear from these experiments that when e-beam controlled discharge is used arcing through discharge heated gas is not a consideration in establishing the gas flow velocity in the HgBr laser system.

3. 1 M Device Experiments

a. Summary

An extensive range of experiments has provided a solid data base for HgBr laser modeling and scaling predictions:

1. Discharge power has been supplied by
 - a) Capacitor
 - b) 150 ns 0.6 Ω Cable PFN
 - c) 300 ns 0.6 Ω Cable PFN
 - d) 300 ns modified PFN
2. E-beam current density has been varied from 0.5 A/cm² to 4 A/cm².
3. Discharge polarity, magnetic field, HgBr₂ density and e-beam voltage have been varied as parameters.
4. The laser pulse shape, energy and output spatial distribution have been measured.
5. Streak photographs have been taken to explore the onset of arcing and its dependence on the above parameters.
6. The e-beam spatial deposition pattern has been measured.

The lasing performance will be discussed in more detail in subsequent sections. Here we give the efficiency definitions and summarize the best lasing performance. All data is with Argon buffer at 2 Amagat.

Definitions:

$$\text{Electrical efficiency} = \frac{\text{laser output energy}}{\text{energy stored in PFN}}$$

$$\text{Intrinsic efficiency} = \frac{\text{laser output energy}}{\text{discharge energy during lasing}}$$

The latter definition is useful because there is a < 10 ns delay between discharge power and fluorescence power, and the fluorescence decay rate (including quenching) is $\geq 1 \times 10^8 \text{ sec}^{-1}$.

The electrical efficiency is lower than the intrinsic efficiency for four principal reasons:

1. Energy is lost in the switch between PFN and discharge. In the present experiment this loss is estimated to be 10% of the stored energy.

2. Energy is reflected from the discharge back into the PFN by impedance mismatch. This loss tended to be higher for the highest e-beam cases.
3. Energy is lost during the buildup time for lasing. This is typically 30 to 60 ns in the present experiments.
4. Energy is lost if an arc prematurely terminates the discharge before the PFN has unloaded.

Highlights:

1. Maximum Energy: 9.8 J at 1.9% electrical efficiency (300 ns modified PFN, 2.0 J/l)
2. Maximum Intrinsic Efficiency: 3.2% at 7.0 J (300 ns modified PFN, 1.4 J/l)
3. Maximum Electrical Efficiency: 2.4% at 3.5 J (150 ns PFN, 0.7 J/l)

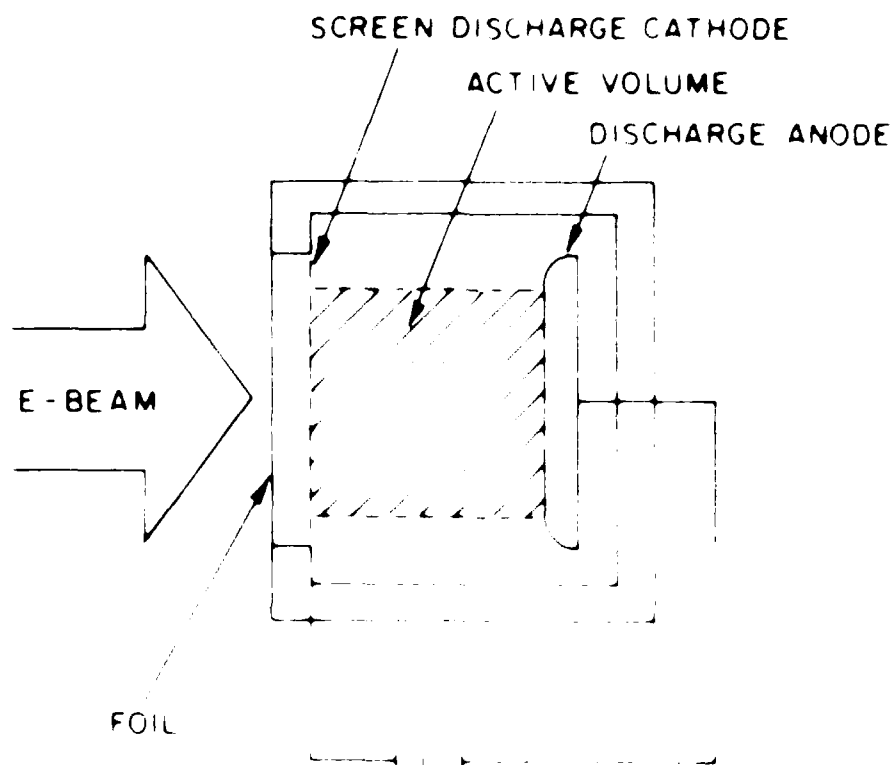
b. Experimental Equipment and Methods

The experimental scheme is shown in Figure 31. Details will be noted under separate headings.

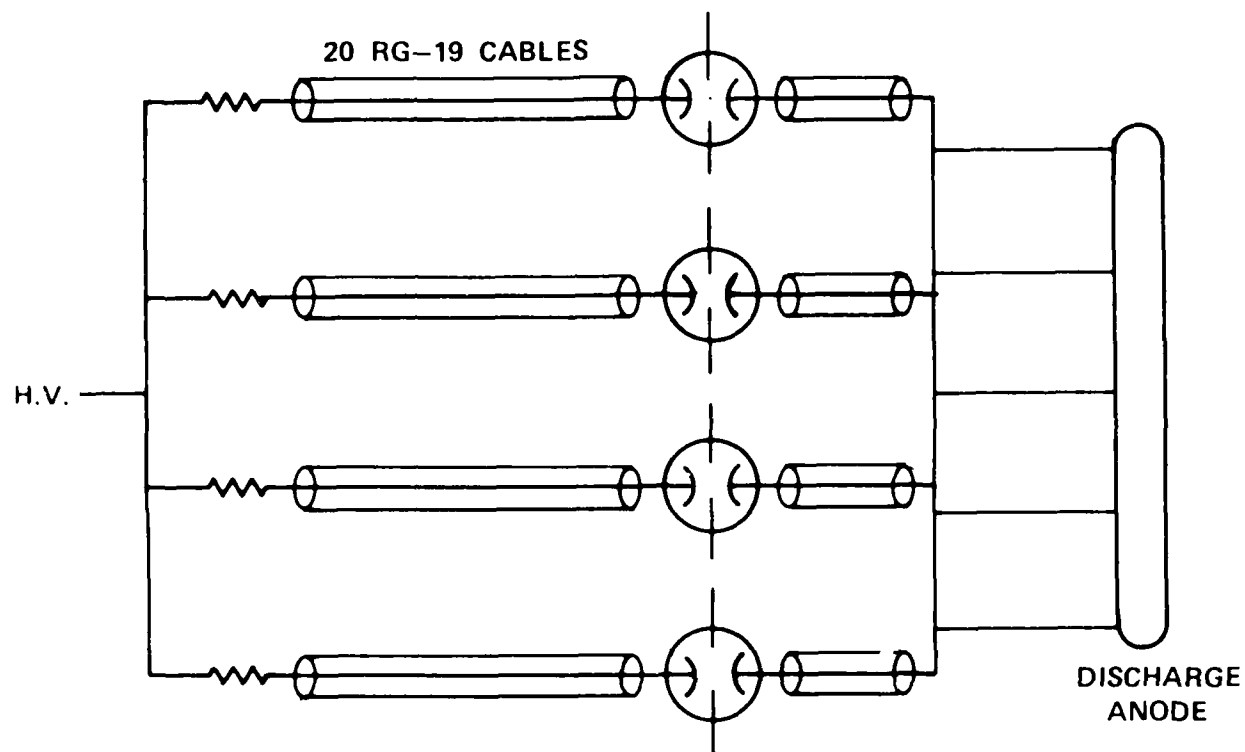
Laser Cavity: The total cavity volume was 40 l. Its body was of stainless steel, with viton and PTFE "O" rings and window gaskets. Two 7" fused silica windows were aligned accurately parallel to the laser mirrors, which were plane, and mounted externally. All the results to be discussed were taken with a 99% reflector and a 35% reflector at a separation of 200 cm. The body of the cavity was heated to 450⁰F and the HgBr₂ density was set by the temperature of a "sidearm" reservoir.

Electrodes: The electrode next to the e-beam foil was a stainless plane mesh of 50% transmission, and hole size 1 mm. The other electrode had a Chang profile designed for $\pm 10\%$ uniformity in electric field over a width of 7 cm. Its material was stainless steel. Beyond a machine shop polish with abrasive, no special care was taken to ensure a smooth surface, and in fact electrode roughness had no effect on discharge energy output, even when the polarity was reversed. The grid-cathode and an

E-BEAM CONTROLLED DISCHARGE PUMPING



J6728



ENERGY STORED = 3.25 J/ns AT 90 kV

TOTAL SERIES INDUCTANCE ≈ 40 nH

$T_R \approx 35$ ns

$Z_0 \approx 0.6 \Omega$

J6948

Figure 32. Schematic of 1 m Cable Pulser

voltage and current were compatible with the 0.6 PFN impedance and accurately calibrated charge voltage.

Laser Energy Measurement: The calorimeter was a Scientech Model 36-0401, 4" thermopile used with a Model 36-4002 indicator. The following methods of calibration were used:

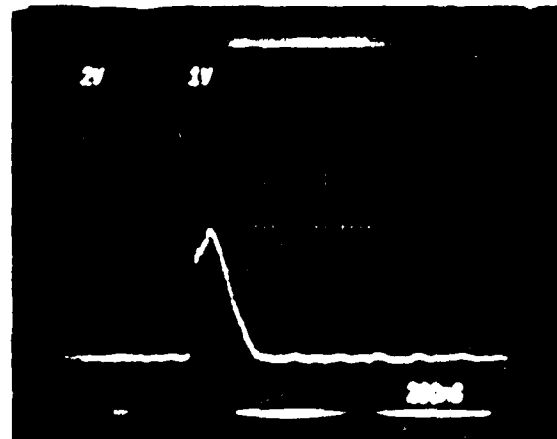
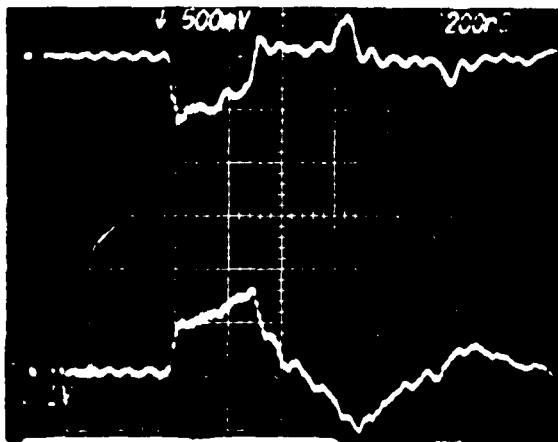
1. Use of dc substitution power to heat the 91.281 Ω Manganin wires embedded in the calorimeter head. The dc supply voltage was calibrated with an HP Model 6920B calibrator ($\pm 1\%$ traceable to NBS). A correction for 98% absorption in the visible was applied. The overall calibration accuracy was $\pm 2\%$.
2. Pulsed substitution energy from a capacitor (known to $\pm 5\%$) charged to a known voltage ($\pm 1\%$) and discharged into the manganin heater wires. Overall accuracy $\pm 5.4\%$.
3. Comparison with another Model 36-0401 calorimeter.

In the measurement of laser output energy the entire laser beam impinged on the calorimeter surface and no assumptions were made on its spatial homogeneity.

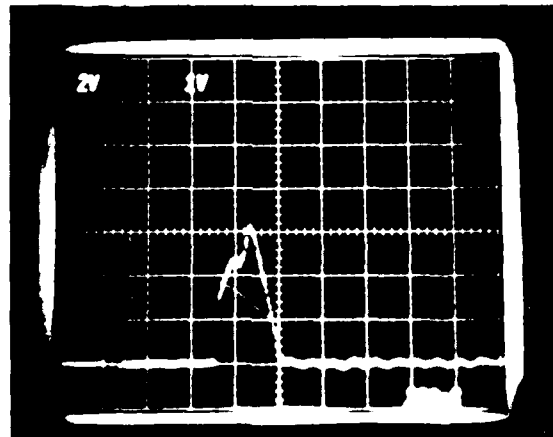
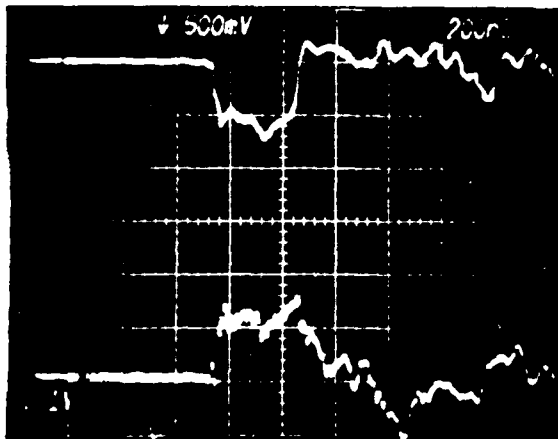
The laser temporal pulse shape was measured with a Hamamatsu Model R617-02 vacuum photodiode terminated into 50 Ω and displayed on a Tektronix Model 7844 oscilloscope.

Efficiency of Energy Transfer: Typical voltage, current and laser intensity traces are shown in Figure 33. In that figure, part A resulted from the use of a simple PFN which consisted of the paralleled cables described in this section. The discharge impedance dropped by approximately a factor of 2 during the pulse. Part B refers to the use of a matched impedance line pulser, referred to here as a modified PFN, where the net result is an extremely good average impedance match to the discharge. The present experiment has demonstrated that $\sim 95\%$ energy transfer can be achieved from a cable energy storage device to a typical laser discharge load where impedance is falling off. In the case of the HBr laser an added advantage of keeping E/N high is the relatively greater laser efficiency at high E/N .

(A) SIMPLE PFN



(B) MODIFIED PFN



DISCHARGE VOLTAGE (UPPER) 20 kV/div
DISCHARGE CURRENT (LOWER) 10 kA/div

08259

Figure 1. Discharge voltage and current waveforms for a simple PFN and a modified PFN.

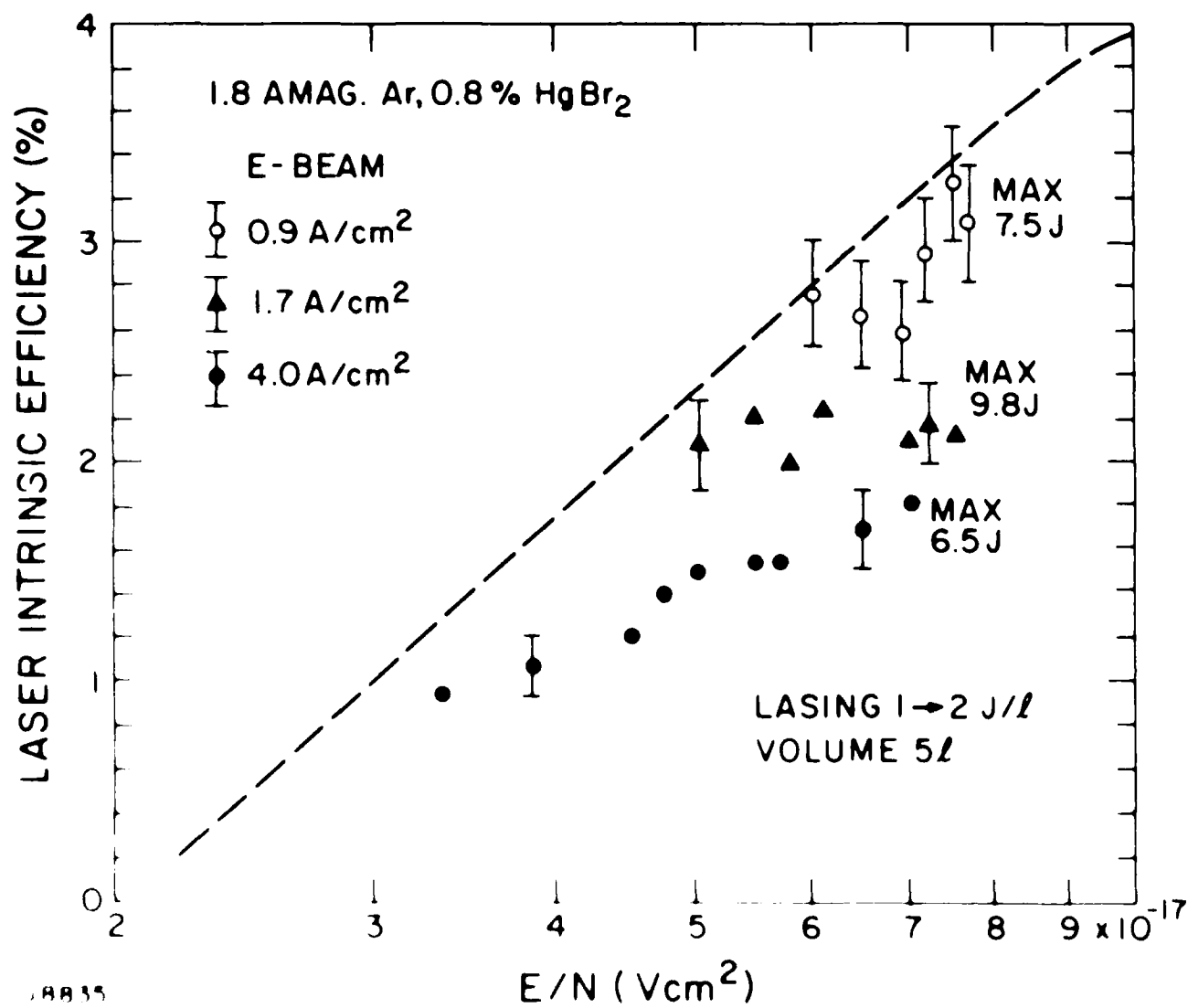
Without the modified PFN, laser intrinsic efficiency was substantially lower in the second half of the pulse.

c. Laser Intrinsic Efficiency

The intrinsic efficiency is defined in Section II-A-3-a. Figure 34 shows the observed intrinsic efficiency as a function of E/N and e-beam current density. We note that the experimental efficiencies lie below the curve (dashed line) derived from the formation efficiency as a function of E/N (Section II-A-2-b) multiplied by 0.65, the energy extraction in the absence of absorption (Section II-A-2-k). At increasing current density the ion absorption (Section II-A-2-l) reduced the intrinsic efficiency. The kinetic code predictions are shown in Figure 35 for 0.6% $HgBr_2$, 1.8 Amagat Ar and a 35% reflectivity output mirror. Further computer simulation verified that 0.35 was the optimum output reflectivity for the e-beam current density of 1.7 A/cm² and close to optimum for the other cases. From the comparison with experiment (Figure 34) we conclude that the ion absorption has been accurately modeled, but that possibly the $HgBr_2$ absorption coefficient might be lower than 1.5×10^{-21} cm² at 302 nm. The best fit is obtained for 1.2×10^{-21} cm².

1. *Journal of the American Medical Association*, 1997; 277: 1039-1043.

There is a growing body of research on the effects of WBI on the health of people with mental health problems. The research has been carried out in a number of countries, including the UK, and has found that WBI can have a positive impact on the health of people with mental health problems. This research has been carried out in a number of ways, including through the use of randomised controlled trials, cohort studies, and qualitative research. The research has found that WBI can help to improve the health of people with mental health problems in a number of ways, including by helping to reduce the risk of relapse, by helping to improve the quality of life, and by helping to improve the ability to cope with stress. The research has also found that WBI can help to improve the health of people with mental health problems in a number of other ways, including by helping to improve the ability to manage symptoms, by helping to improve the ability to access services, and by helping to improve the ability to participate in the community. The research has found that WBI can have a positive impact on the health of people with mental health problems in a number of other ways, including by helping to improve the ability to manage symptoms, by helping to improve the ability to access services, and by helping to improve the ability to participate in the community. The research has found that WBI can have a positive impact on the health of people with mental health problems in a number of other ways, including by helping to improve the ability to manage symptoms, by helping to improve the ability to access services, and by helping to improve the ability to participate in the community.



JB835

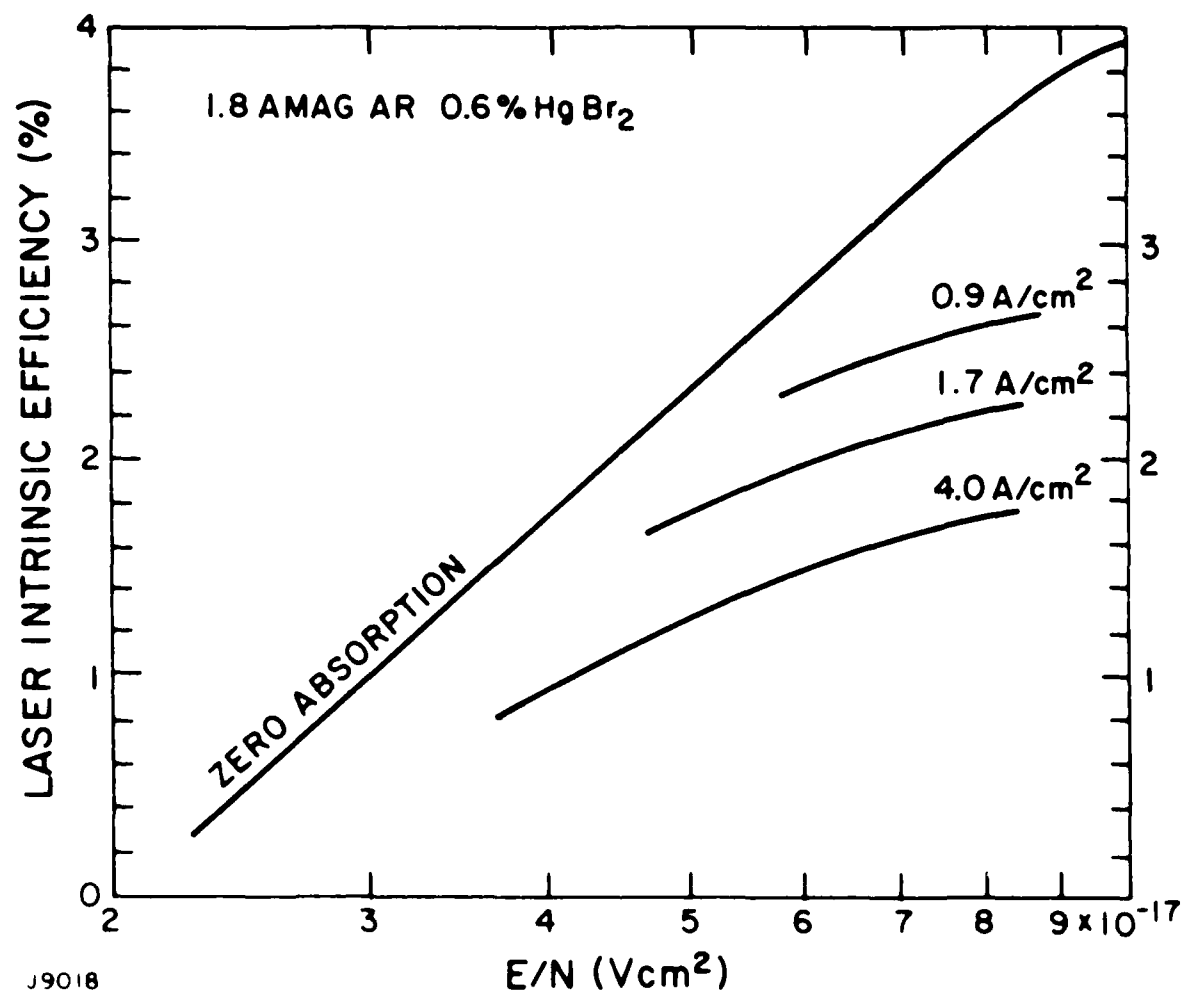


Figure 35. Computed Intrinsic Efficiency vs E/N

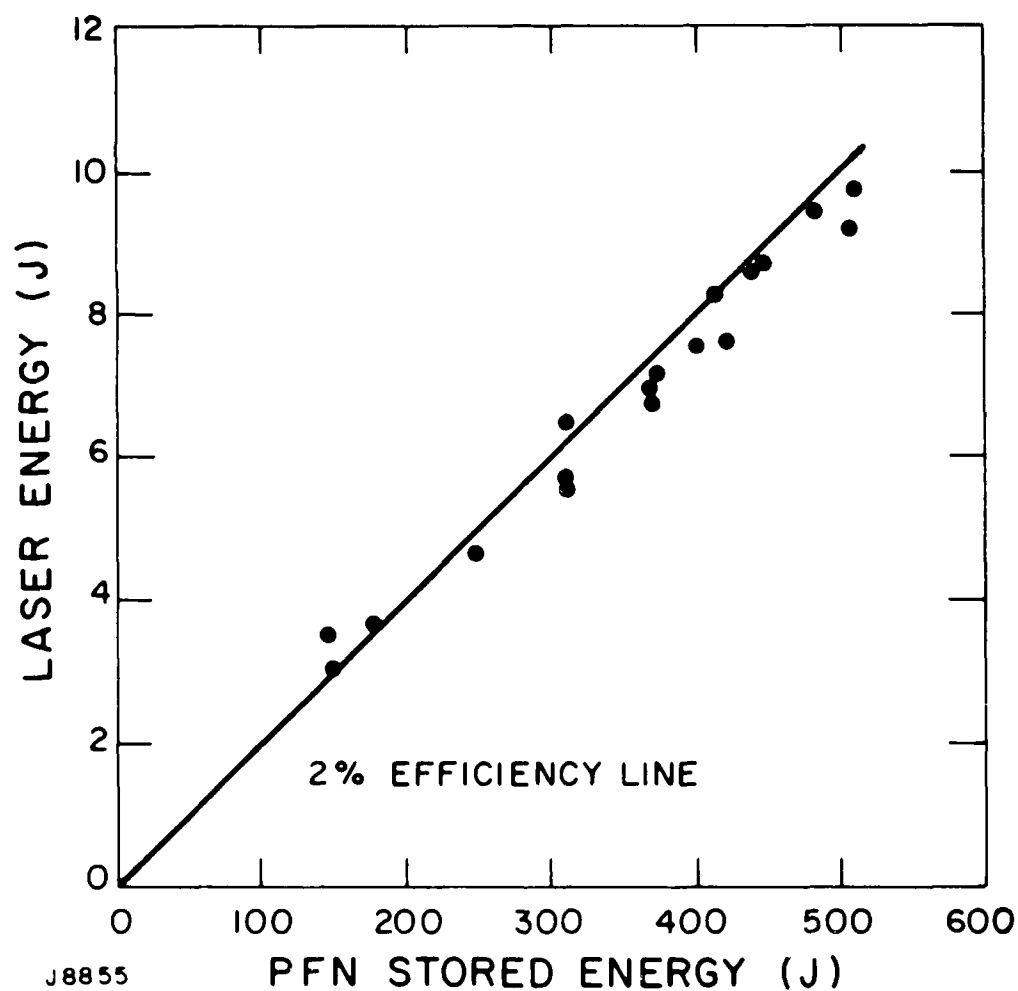


Figure 36. Experimental Laser Energy vs PFN Stored Energy

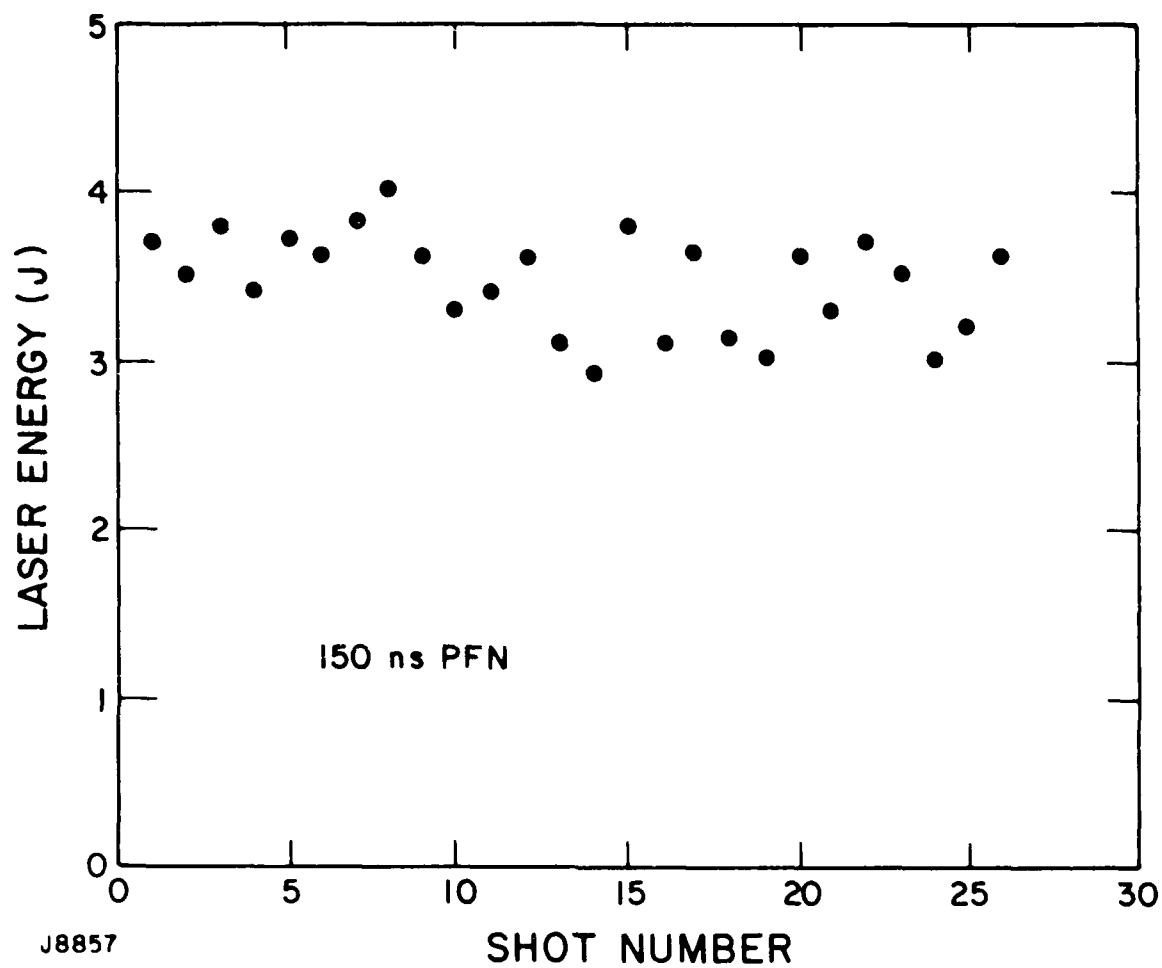


Figure 37. Shot-to-Shot Reproducibility of Laser Output

The fractional variation was less in the 8 J + 10 J energy range because of the relatively smaller contribution of the calorimeter zero fluctuation at these energies.

There was a slight decline in output during this sequence, which we believe was due to the use of a stainless steel chamber and viton "O" rings which upset the HgBr equilibrium chemistry by binding Br atoms. There are several possible ways in which Br depletion can reduce the laser efficiency:

1. By leaving free Hg or Hg_2Br_2 in the vapor phase, which alters the electron energy distribution and hence the excitation efficiency of the 6.4 eV HgBr₂ process.
2. By causing the production of volatile bromides which absorb at the laser wavelength.
3. By reducing the HgBr₂ density (at an E/N value where the formation efficiency reduces with reduced HgBr₂).

A further, less likely, possibility is that chamber outgassing produced enough N₂ to affect the formation efficiency. As little as 0.5% N₂ in Ar reduced the formation efficiency by 20% in an experiment on the small-scale device.

Contamination issues are addressed in Section III-J of the proposed 2 J design.

f. Discharge Energy Loading Limits

During the course of the 1 m experiments insight was gained into the factors affecting energy loading in HgBr₂/Ar sustained discharges. Streak photography confirmed that the arcing which limited energy loading was truly volumetric and indicated its dependence on the uniformity of e-beam deposition.

The deposition uniformity will be defined as the ratio of deposition at the electrode furthest from the e-beam entry foil to the deposition adjacent to that foil. A measurement of deposition, described below, gave a uniformity of 0.6 for the 8 cm anode-cathode spacing and a uniformity of 0.5 for the 4.5 cm spacing. The uniformity was estimated to be 0.6 for the 1 m discharge gap of the small-scale experiment.

The energy loading for a given e-beam current and deposition uniformity was a weak function of either E/N in the range $5 \times 10^{-17} \rightarrow 8 \times 10^{-17} \text{ Vcm}^2$, or HgBr_2 concentration in the range 0.4% to 1%. This suggested the graphical presentation in Figure 38 for the experimental energy loading limits. Maximum energy loading occurs at $\sim 2 \text{ A/cm}^2$. The physical reason for such a maximum is the rise of a two-step (n_e dependent) arcing process as the e-beam increases, which offsets the stability gained by having a source-dominated ionization rate.

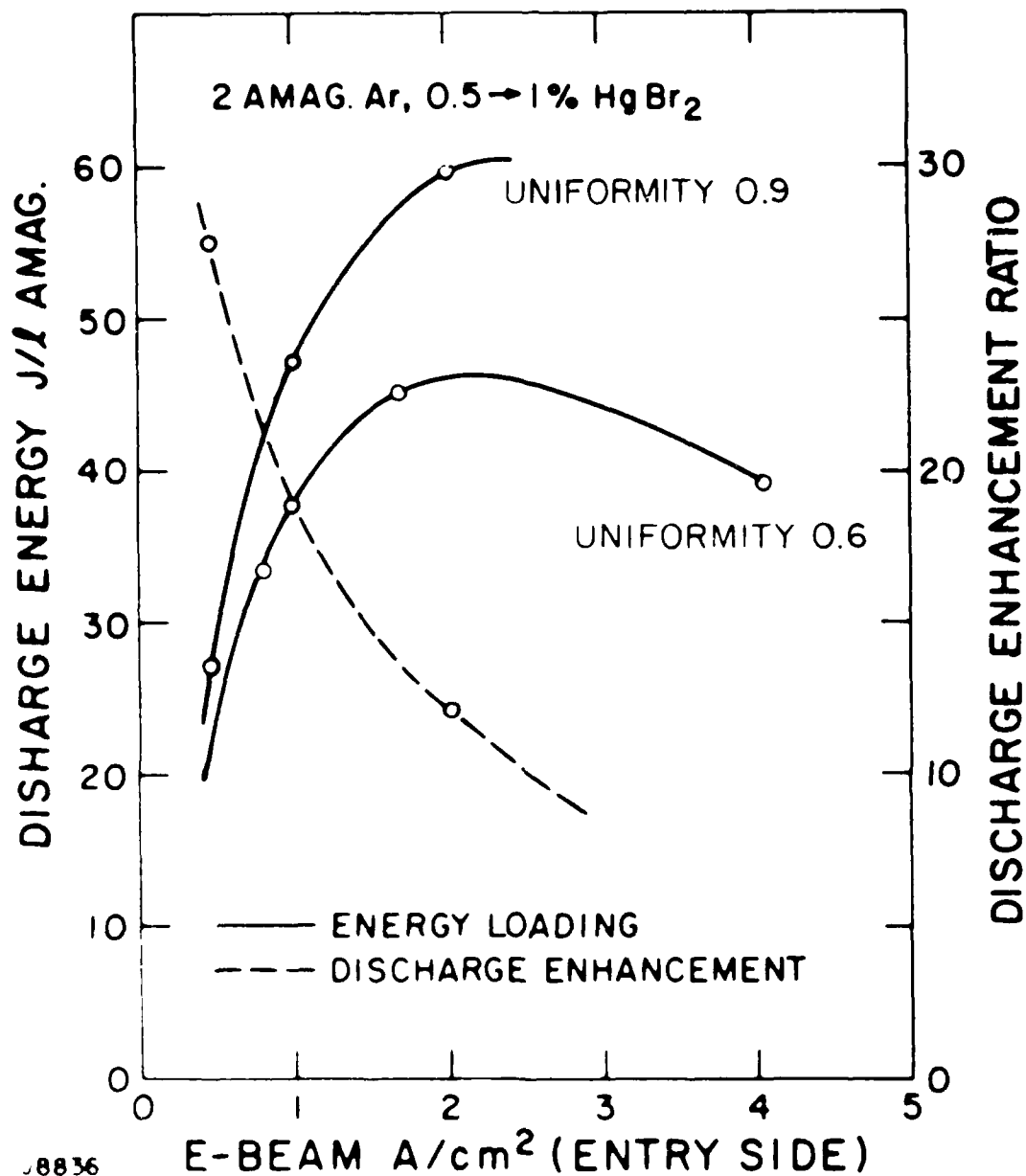
The discharge energy loading degrades with decreasing deposition uniformity, but is still tolerably good at 0.6, where most of the 1 m device experiments were performed. The major effect of nonuniformity is to cause high electric fields in regions of low deposition, which then have a higher ionization rate. As the electron density becomes more uniform, the power input to the high deposition regions is relatively increased, leading to a two-step ionization runaway. The streak photography supports this picture, as does the spatially-dependent modeling described below.

Figure 38 represents the upper bound in discharge energy loading that applies for any given pair of e-beam and deposition uniformity. It is necessary to accurately predict the uniformity for the purpose of design, and this capability is included in Section II-A-4-1.

4. Streak Photography and Modeling

The first streak photo of the plane-plane cavity was taken with a white light source at 1.5 m from the output mirror, and a 100 ns exposure time. The image was 1 cm high and 1 cm wide. The image of the cathode was visible as a dark horizontal band at the bottom of the image. The image of the anode was visible as a dark horizontal band at the top of the image. The image of the plasma was visible as a bright horizontal band in the middle of the image.

The streak photo was taken with a 100 ns exposure time. The image was 1 cm high and 1 cm wide. The image of the cathode was visible as a dark horizontal band at the bottom of the image. The image of the anode was visible as a dark horizontal band at the top of the image. The image of the plasma was visible as a bright horizontal band in the middle of the image.



J8836

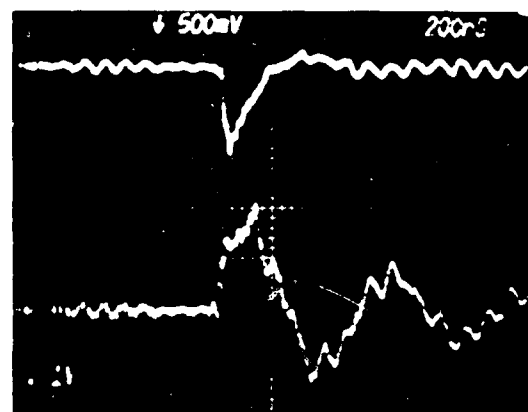
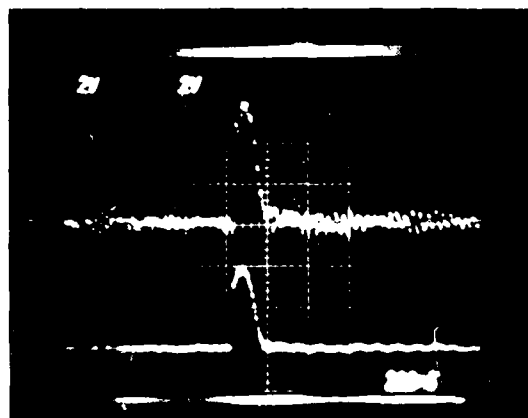
E-BEAM A/cm² (ENTRY SIDE)

Discharge Energy Loading vs. Deposition
Rate for Beam Current Density

ANODE
CATHODE -



FIGURE 1. Schematic Diagram of Vacuum Tube



19258

Figure 1. Schematic Diagram of Vacuum Tube and Connections

FIGURE 2. Current vs. Voltage Characteristics of Vacuum Tube

FIGURE 3. Current vs. Voltage Characteristics of Vacuum Tube

FIGURE 4. Current vs. Voltage Characteristics of Vacuum Tube

FIGURE 5. Current vs. Voltage Characteristics of Vacuum Tube

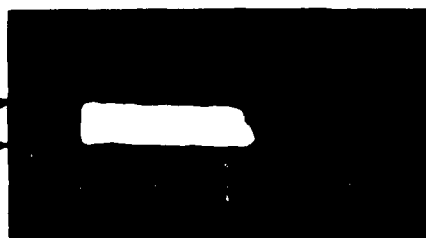
FIGURE 6. Current vs. Voltage Characteristics of Vacuum Tube

CATHODE
ANODE



(A) E BEAM 280 kV

CATHODE
ANODE



(B) E BEAM 320 kV

STREAK OF LASER O.P., 50 ns/div

CONDITIONS

2 AMAGAT Ar

15 torr HgBr₂

E BEAM 15 A cm², ENTERING THROUGH ANODE

ANODE CATHODE SPACING 8 cm

CABLE VOLTAGE 70 kV, PFN 150 ns

J8256

Figure 40. Streak Photograph of Spatial Arc Caused by Nonuniform Deposition

Measurement of Deposition Uniformity

The laser fluorescence proved to be a good monitor of e-beam deposition, at the anode of a discharge voltage. Low HgBr concentrations were used ($\sim 2 \times 10^{-6}$ Torr) in 1.6 Atmos Ar. It was verified that the fluorescence was linear in e-beam current density. Also, the time scales for Penning ionization from excited Ar atoms were sufficiently fast to give time-resolved deposition, within the 1 μ s e-beam pulse.

Fluorescence was viewed by photomultiplier through a narrow band filter at 502 nm and two aligned pinholes which gave a spatial resolution of 0.5 cm in the deposition volume. Vertical and horizontal scans were made through the discharge aperture and isodeposition contours interpolated between data points. Care was taken to shield the photomultiplier from x-rays, and a small correction was made for the measured effect of the steady applied magnetic field on PMT gain.

Data were taken for a uniform a kG magnetic field case (Figure 41) and also for a diverging field case (800 G at the e-beam entry side and 500 G at the opposite electrode (Figure 42)).

The highest discharge energy loading was actually achieved using the diverging field, for a reason connected with the self-field of the discharge current (up to 300 G) which was in a direction to slightly pinch the e-beam in the discharge cell. This effect does not show up in the deposition experiment, where there is no discharge current. However, it is evident in the spatial dependence of the laser output on applied magnetic field (Section II-A-3-j). Evidently, the diverging field counteracts the pinching effect, to create optimum discharge uniformity.

In general, the magnetic field is necessary to obtain the best overall efficiency from the sustained discharge HgBr laser, for the following reasons:

1. By guiding the e-beam into the cell through the foil aperture, the e-beam power requirement is minimized.

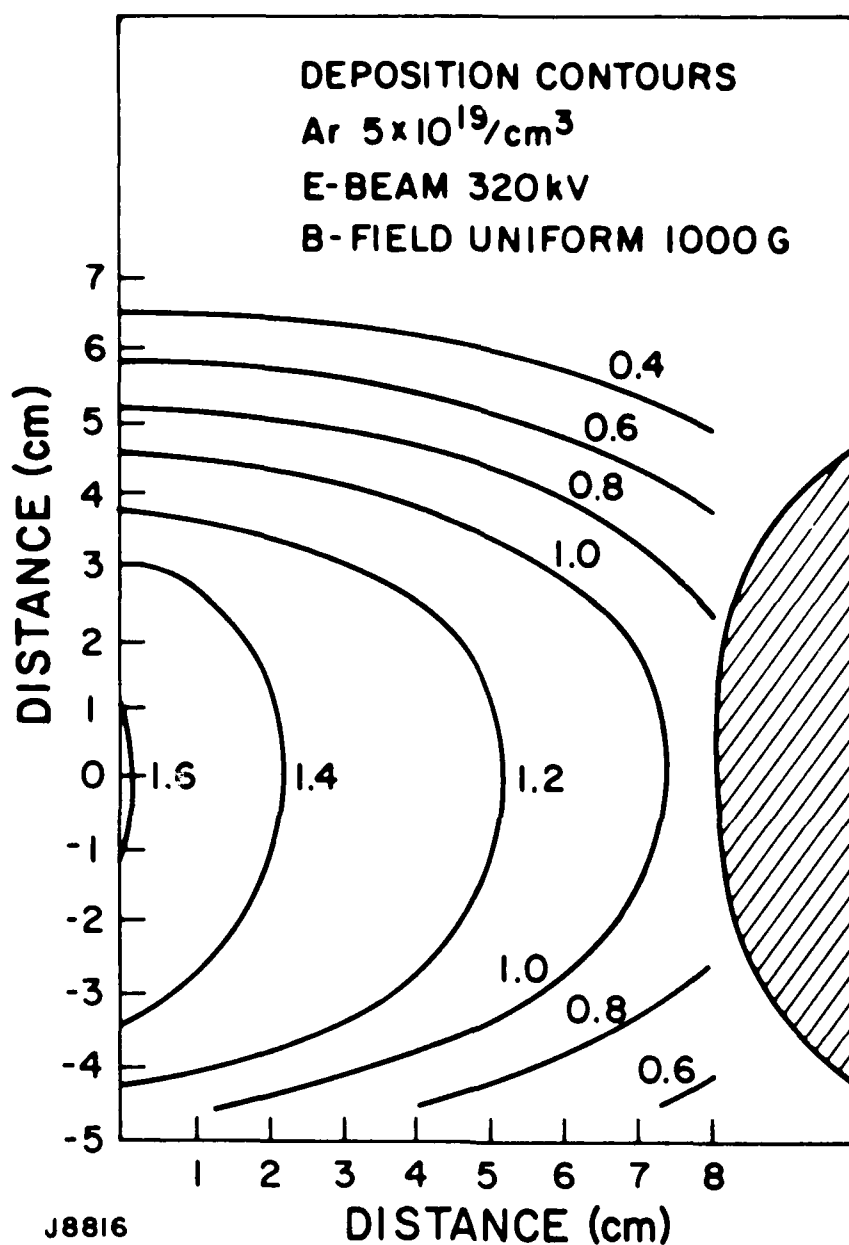


Figure 41. Measured E-Beam Deposition with Uniform Magnetic Field

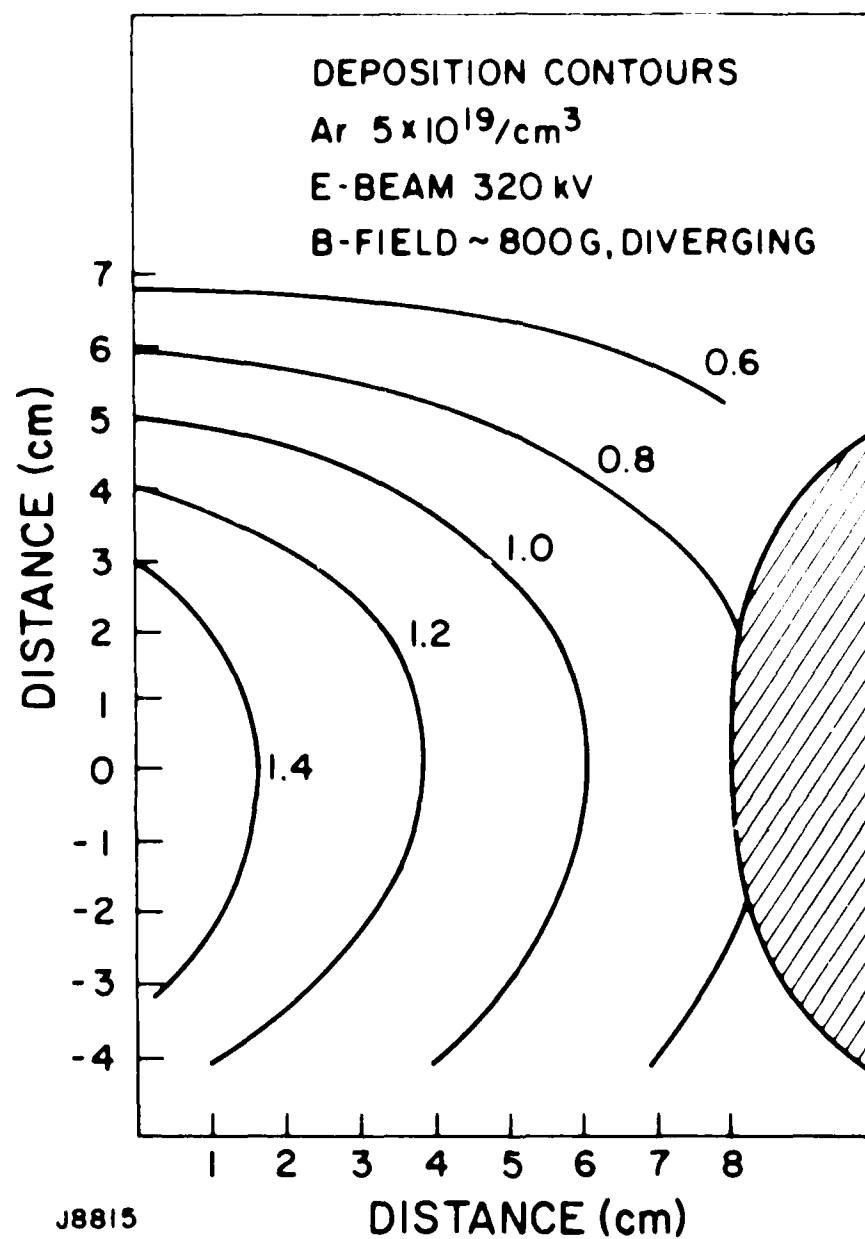


Figure 42. Measured E-Beam Deposition with Diverging Magnetic Field

- h. By using the data from the previous stage, the profile of the electron beam at the cathode can be determined. The electron beam profile at the cathode is determined by the electron beam profile at the anode and the electron beam profile at the cathode.
- i. By using the data from the previous stage, the profile of the electron beam at the cathode can be determined. The electron beam profile at the cathode is determined by the electron beam profile at the anode and the electron beam profile at the cathode.
- j. A similar procedure can be used to determine the electron beam profile at the anode. The electron beam profile at the anode is determined by the electron beam profile at the cathode and the electron beam profile at the anode.
- k. The electron beam profile at the cathode can be determined by the electron beam profile at the anode and the electron beam profile at the cathode. The electron beam profile at the anode is determined by the electron beam profile at the cathode and the electron beam profile at the anode.

The accurate prediction of the electron beam profile is clearly important in the design process, and is discussed below.

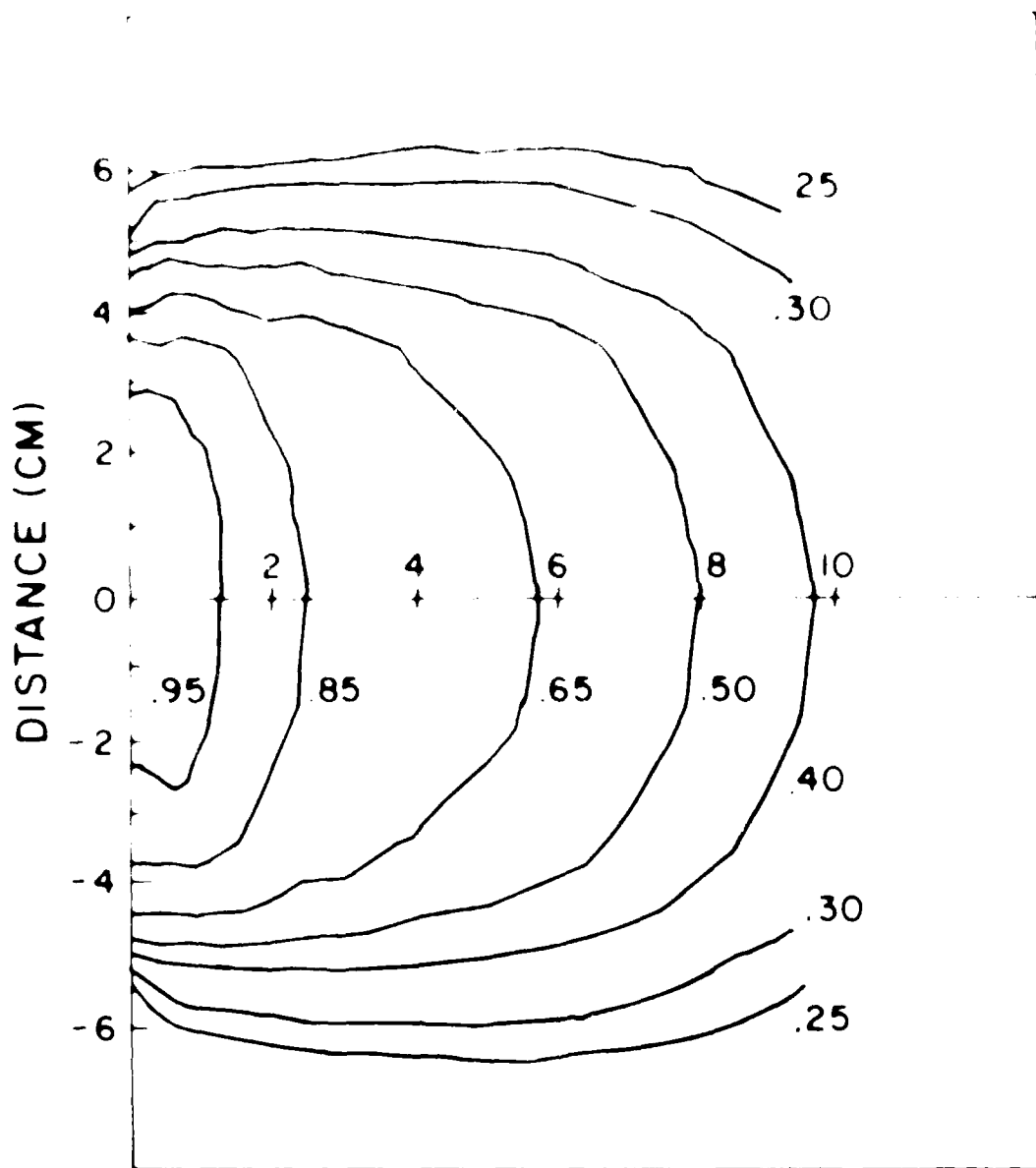
1. Modeling of E-beam Deposition

Using an e-beam deposition code which has been developed under internal funding we are able to predict deposition in very good agreement with the present experiment. The results of such a computation are shown in Figure 43, which applies to precisely the experimental conditions of Figure 41. The same code has also given excellent agreement with another well-documented deposition experiment at 600 kV without a magnetic field.

Without going into details of the code at this point we shall use its results to design the magnetic guide fields which control the discharge volume, confident of a deposition accurate of better than $\pm 10\%$.

j. Laser Output Spatial Profile

Photographic measurements were made of the laser output on a white screen at 2.5 m beyond the output mirror. The laser cavity was plane-plane and produced a well-collimated beam whose intensity profile reflected the spatial distribution of discharge power across the laser aperture. The film was calibrated for quantitative intensity measurements by the use of known neutral density filters.



J9062

DISTANCE (CM)

Figure 43. Computed E-Beam Deposition for Uniform 1 kG Magnetic Field

The electron beam is directed into the cathode field. The cathode field is designed to give a beam diameter of about 1 mm. It is seen that the electron beam is directed into the cathode spatially within a distance of 1 mm. We conclude that the spatial distribution of the power is almost completely controlled by the cathode field. (The pulse duration is too short for a significant discharge to develop. The electrons move only a small fraction of the distance of the discharge).

k. Modeling of Anode-Cathode Variation in Lasing

AVCO EVERETT

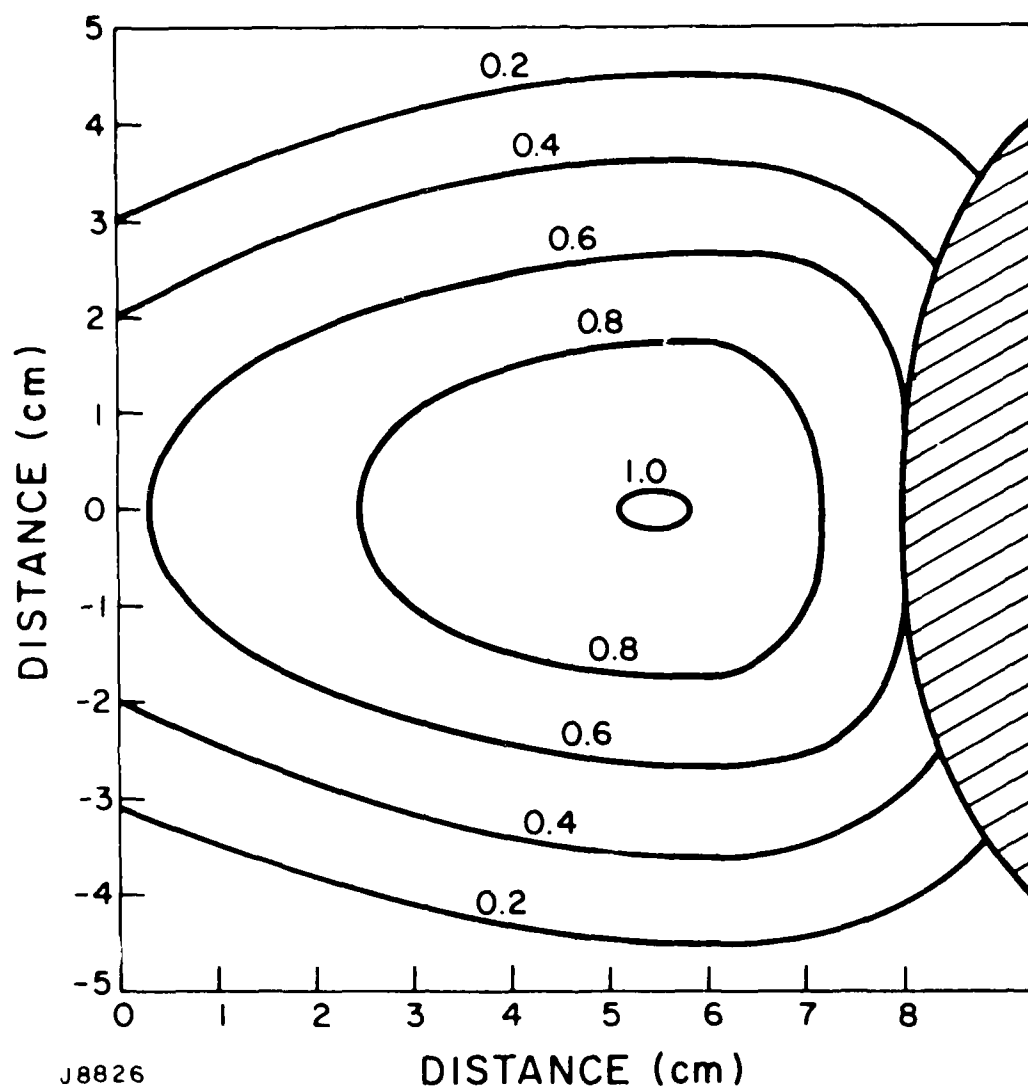


Figure 44. Measured Spatial Distribution of Laser Output with 800 G Magnetic Guide Field

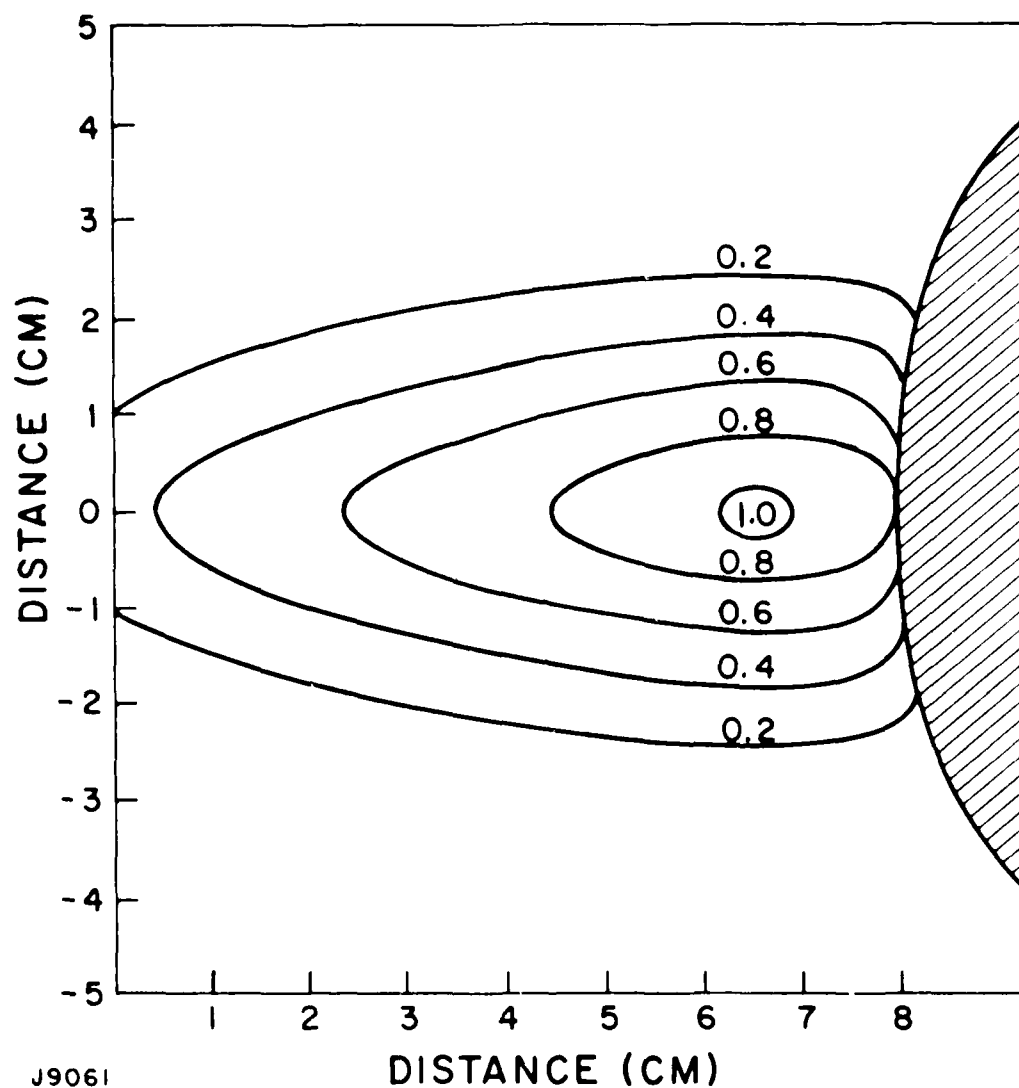


Figure 45. Measured Spatial Distribution of Laser Output with No Magnetic Guide Field

leads to an initially higher E/N near the curved electrode, and hence to more efficient lasing. This increased efficiency is due to: (1) higher E/N causing increased excitation efficiency, and (2) higher initial gain causing a more rapid laser buildup. In addition, the discharge power is higher in the region of higher E/N because the current density is constant in the θ direction. The combined effect of greater laser efficiency and higher discharge power cause the observed spatial nonuniformity, which is a very strong function of the external magnetic field.

The laser kinetic model was used to compute the observed anode-cathode intensity profile. The tube was divided into eight segments, in each of which a low-order laser model was run, with the appropriate E/N which was obtained by interpolation. The applicability of this model is shown in Section II-A-3-f.

The application of this model to the 100 ns laser pulse will be discussed. The measured deposition rate from Section II-A-3-hi was 6.6. The computed evolution of the laser electric field is shown in Figure 46, where it is noted that the initial field distribution rapidly relaxed into a more uniform distribution which persists stably for the duration of the 300 ns applied pulse (at constant 32 kV total anode-cathode voltage). This is accounted for by the relatively higher ionization rate in the high E/N region. The energy distribution from the same run is shown in Figure 47, for $t = 150$ ns and $t = 300$ ns. We note that good overall agreement is obtained in the anode-cathode energy variation, apart from the edge regions near the electrode which suffer optical losses in the experiment, but not in the simulation. At 150 ns it is striking to note that the variation is much greater, and this is traceable to the substantially faster laser buildup in the region of low deposition.

We conclude that the reasons for the observed anode-cathode laser variation are well understood and that the code will predict

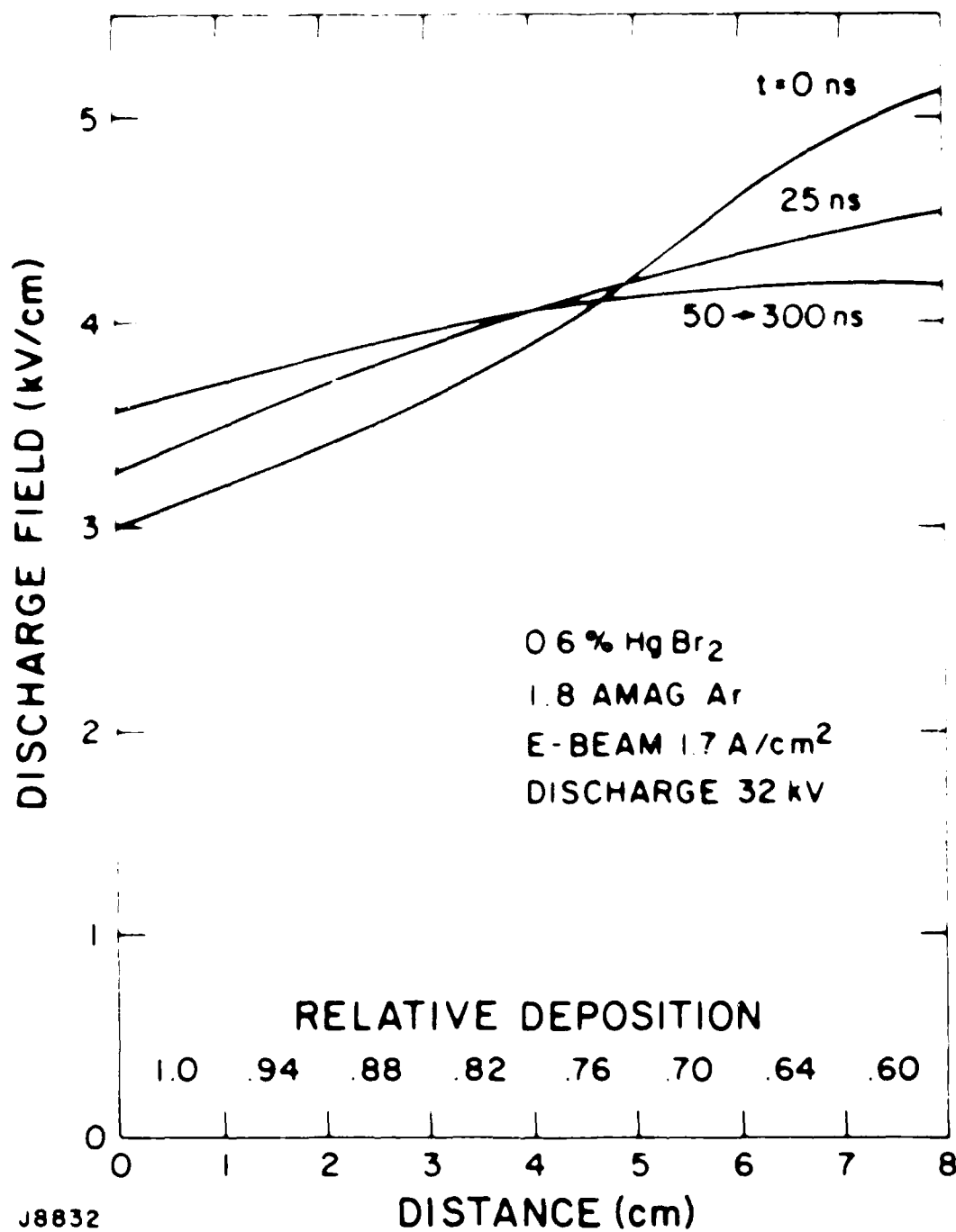


Figure 46. Computed Evolution of Local Field Between Anode and Cathode

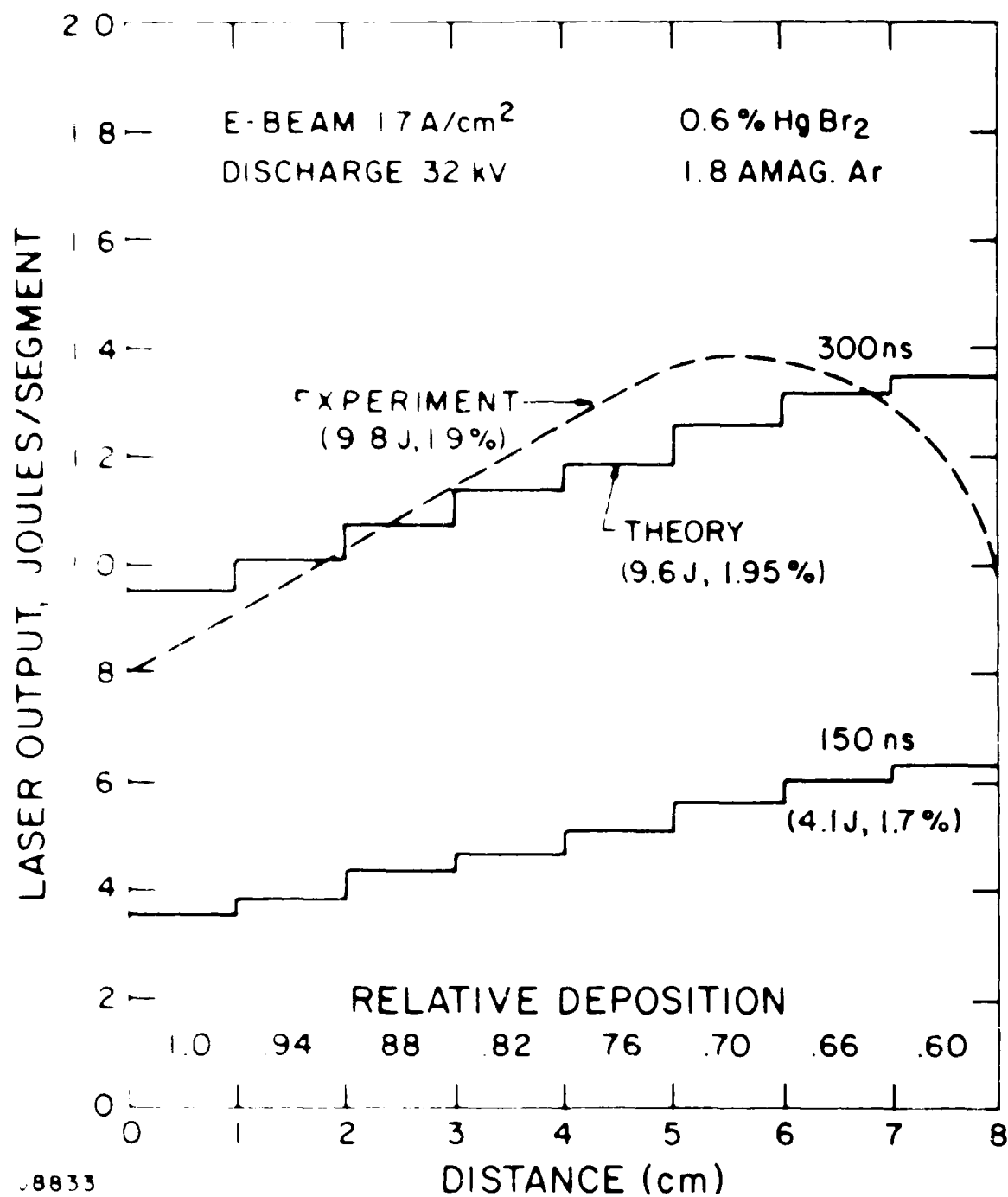


Figure 4.1. Computer Analysis of the Variation of Laser Energy, and Overall Efficiency.

NO-A185 884

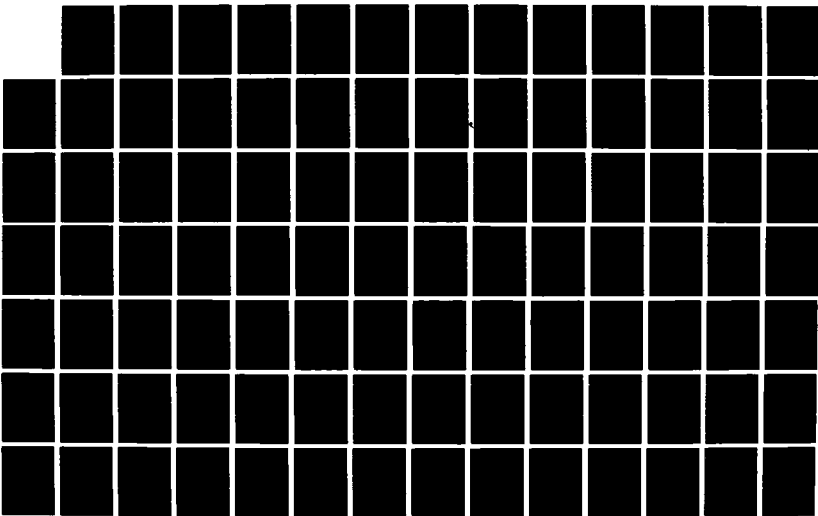
SPACE-BASED BLUE-GREEN LASER(U) AVCO EVERETT RESEARCH
LAB INC EVERETT WA J C HSIA ET AL. OCT 81
NO0123-88-C-1135

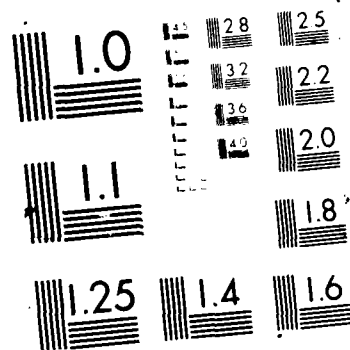
2/3

UNCLASSIFIED

F/G 9/3

NL





this variation accurately for different e-beam deposition uniformities. In the proposed 2 J design the deposition uniformity is 0.8 and the presence of injected light eliminates the buildup differences, so that an energy uniformity of better than 0.95 is predicted in the anode-cathode direction.

The laser electrical efficiency was discussed in Section II-A-3-d, but modeling of the efficiency has been delayed to the present section to include correctly the anode-cathode variation. As seen in Figure 47 the electrical efficiency is predicted to be 1.95%, after allowance has been made for an energy transfer factor of 0.95 from the PFN to the discharge. In order to obtain this agreement with experiment, the formation efficiency (Section II-A-2-g) had to be modified to 6.1%, slightly higher than the 5.3% used in the cross section derivation, and higher again than the 4.3% derived from the absolute fluorescence measurement. However, the errors in the absolute fluorescence measurement are considered to be $\pm 30\%$, whereas the measurement of laser electrical efficiency is accurate to better than $\pm 10\%$. For design purposes we employ the 6.1% formation efficiency, which gives best agreement with the observed laser efficiency (both intrinsic and electrical).

III. PRELIMINARY DESIGN OF 2 J, 100 Hz HgBr LASER

A. DESIGN REQUIREMENTS

The preliminary design presented in the following sections meets all the specifications outlined in Table 3. While the lifetime specification is 10^8 shots, design solutions have always been chosen which are compatible with an ultimate 10^{10} shot lifetime.

A number of the subsystems have already been tested to a 10^7 - 10^8 shot lifetime under other AERL programs or in other laboratories.

The discharge parameters chosen for 2 J operation have already been explored on the 1 m device experiments (Section II-A-3) in which energy scaling to 9.8 J at 1.9% electrical efficiency was demonstrated. The laser kinetic model (Section II-A) has been verified to a precision of $\pm 10\%$ over a wide range of discharge conditions, and therefore the overall efficiency prediction of 1.19% (Section III-K-1) can be stated with confidence.

It is to be noted that the present 200 W system is only one choice out of a wide spectrum of point designs which can be generated from the generic sustainer discharge concept demonstrated here. For instance, a 10 J, 100 Hz system could have been designed at similar operating efficiency using identical technology.

B. OVERVIEW OF DESIGN

The design considerations were dominated by the available intrinsic efficiency and specific energy loading in the laser active medium. The intrinsic efficiency can experimentally be as high as 3.3% (Section II-A-3-c) with argon as the buffer gas. From the comparison of energy loading in different buffer gases (Section II-A-2-e) it emerged that argon was decisively superior as a buffer when compared to Ne, Ar + 5% Xe, Ne + 10% Xe, giving

TABLE 3. DESIGN SPECIFICATIONS

Output Pulse Energy	2 J
Average PRF	100 Hz
Interpulse Recovery Time	< 5 ms
System Efficiency	> 1%
Beam Divergence (at 80% point)	10 x DL
Beam Uniformity \pm (%)	20
Bandwidth	0.1 nm
Lifetime (> 90% power)	10^8 shots
Wavelength	450 - 510 nm
Wavelength Stability	\pm 0.01 nm
Pulse-to-Pulse Intensity Jitter	< (\pm 10%)

an energy loading of up to 60 J/l Amag. Because it was desirable to work at high discharge enhancement ratio (= discharge power/e-beam power), the discharge design point chosen in Section III-C was not at the highest energy loading point, but was set at 33 J/l Amag where an e-beam current density as low as 0.6 A/cm² could be used (Section II-A-3-f).

The geometry of the laser active medium was chosen after several design iterations in which the overall system efficiency and the optical beam uniformity were calculated. The penetration depth allowed for the e-beam was a compromise between the need for a good deposition uniformity (Section II-A-3-f) and the competing requirement for a high aspect ratio to minimize the flow power. Essential to the deposition uniformity was uniform, reasonably high magnetic field.

The flow loop design (Section III-E) was driven by the optical homogeneity requirements. It was found that 10 x DL could be achieved easily with a very compact flow loop. A detailed plan of this is presented in Figure 57. The principal features of the flow design are sidewall acoustic wave suppression, an upstream velocity stabilizer, and a downstream heat exchanger. Additional medium uniformity was achieved by boundary layer suction upstream of the anode plate.

An unstable optical resonator was chosen (Section II-F) because it offered the required overall beam quality (further discussed in Section III-K). Spectral control was obtained by injection at the required frequency. Injection also raised the optical extraction efficiency by 11%. The injection oscillator itself had only a modest drive power of 240 W (electrical) and was specified as an avalanche discharge laser of simple and rugged design. Detailed consideration was given to the mode matching between the injection oscillator and the unstable resonator.

The e-beam design (Section III-G) was based on a thermionic emitter, which could either be grid-controlled at high voltage (300 kV) or pulsed for the laser duration of 250 ns by a high-voltage pulse transformer. The most important aspect of the design was its resemblance to long-life high-vacuum modulator tubes, which have been adequately proven in other space applications.

A dc magnetic field coil was included in the design in order to increase the laser efficiency and beam uniformity. It acted principally by controlling the discharge shape (as discussed in Section II-A-3-h) and through this it increased the optical beam interception of the discharge power to 92% (Section III-c) and decreased the flush factor to 1.75 (minimum) or 3.5 (average) (Section III-E). For highest efficiency a superconducting magnet was specified, and in Section III-H its design is discussed in some detail. Advantage was taken of the recent development of efficient refrigerators for space usage.

Discharge modulator design is discussed in Section III-I, where the Blumlein and Simple Changed Line circuits are contrasted. It is concluded that the line circuit will better favor long thyratron lifetime. A lumped element PFN was designed which gave the rapid risetime and falltime required for high laser electrical efficiency.

The question of gas chemistry and cleanup is covered in Section III-J. The major problems are identified and the design allows for continuous gas cleanup and monitoring, with a limited makeup of fresh HgBr_2 .

Overall system performance is discussed in Section III-K, where an overall laser efficiency of 1.19% is demonstrated.

C. LASER ACTIVE MEDIUM DESIGN

1. Geometrical Trade-off

In this subsection we present qualitatively the trade-offs which lead to the chosen design point for active medium geometry.

The flow power decreases with increasing laser specific energy (J/l) but higher specific energy requires increased e-beam

(Section II-A-3-f). Taking into account the aspect ratio trade-off (below) an optimum specific energy of 1.5 J/l was chosen.

The aspect ratio is H/W where H is the discharge anode to cathode dimension and W is the discharge width in the flow direction. The flow power is minimized for high aspect ratio, since the flow power scales as $(Wf)^3$, where f is the "flush factor". However, the e-beam deposition uniformity must equal 0.8 for the design energy loading, and good uniformity is more easy to achieve with a low aspect ratio.

The physical value of H is determined by the e-beam maximum voltage constraint and the computed deposition uniformity (Section III-C-3). The e-beam voltage should be high relative to the foil voltage loss. It should also be high in order to minimize the e-beam current and thereby the cathode heater requirements within the total ionization power requirement. We have adopted a 300 kV practical e-beam voltage maximum, and thereby set H at 6 cm, in order to have good deposition uniformity.

In order to reduce the flow power we have set $W = 4$ cm. At 1.5 J/l and 2.25 J potential laser output (actual output discussed below), the active volume must be 1.5 l, implying a length L_A of 62.5 cm.

The dimensions of the design point laser active medium are: $H = 6$ cm, $W = 4$ cm, $L_A = 62.5$ cm.

2. Laser Efficiency

The code prediction of laser efficiency has been accurately verified in Section II-A-3-k, where it compares well with experiment. The same code has been run for the design point discharge in order to predict electrical efficiency and optimum output coupling. A constant 30 kV has been applied to the discharge representing an operating $E/N = 0.9 \times 10^{-16}$ Vcm². The deposition uniformity is designed to be 0.8, as discussed in more detail below. For our 1.5 l discharge volume, lasing with a specific energy of 1.5 J, we require a discharge total energy of 100 J.

Through the dependence of discharge energy on e-beam current density (Section II-A-3-f), we are required to have $J_{EB} \geq 0.6 \text{ A/cm}^2$ for the requisite energy loading (at 2 Amagat). This consideration leads to the choice of $J_{EB} = 0.6 \text{ A/cm}^2$ within the discharge. In order to deliver 100 J in 250 ns into the chosen discharge geometry, the impedance must be tuned by varying the concentration of HgBr_2 down to 0.32%.

The laser electrical efficiency for these conditions is plotted in Figure 48 as a function of output mirror reflectivity (for a plane-plane cavity). Also shown is the laser energy, numerically equal to the efficiency for the 100 J discharge input. In this calculation a factor of 0.95 has already been inserted, as an estimate of the coupling efficiency from PFN energy to discharge energy. This factor is justified by the experiments we have performed, and has indeed been included in the efficiency modeling of Section II-A-3-k.

The computed electrical efficiency of Figure 48 includes an injected power level of 10 kW/cm^2 at the beginning of the pulse, which raises the electrical efficiency by 13%, as discussed in Section III-F. This accounts for the increase over the 2.0% observed electrical efficiencies (Section II-A-3-d). The computed impedance variation is shown in Figure 49.

It is to be noted that 1 m device experimental data exists for the conditions: $J_{EB} = 0.9 \text{ A/cm}^2$; $[\text{HgBr}_2] = 0.4\%$; $E/N = 0.9 \times 10^{-16} \text{ Vcm}^2$ and deposition uniformity 0.8 (anode-cathode spacing 4.5 cm). In this experiment an electrical efficiency of 1.95% was recorded at a specific energy of 1.6 J/l without injection. This is close to the design point and verifies the efficiency predictions in that region.

The modeling described above assumes that the discharge profile is a perfect "top hat" in the direction perpendicular to the anode-cathode axis. In practice there is a narrow roll-off region

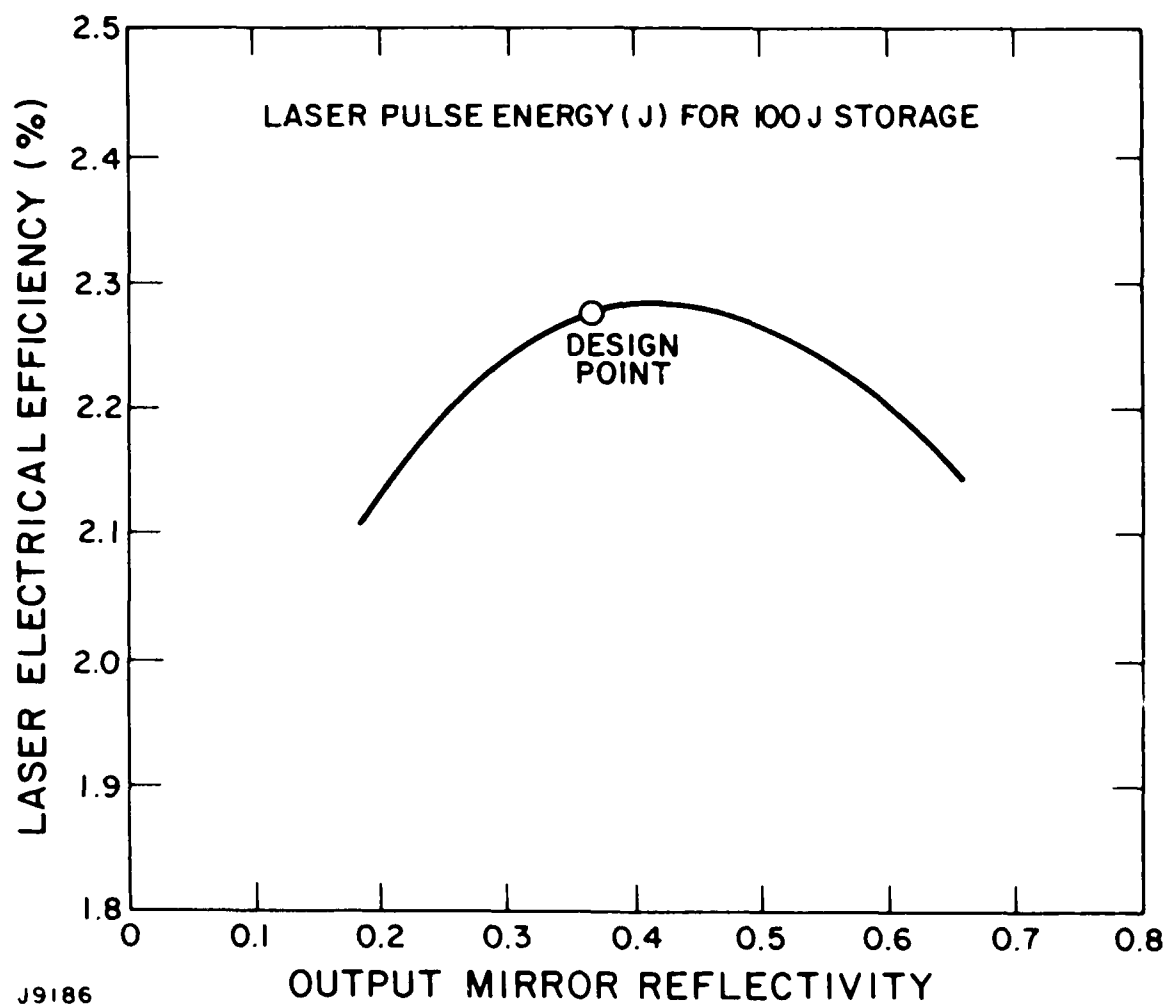
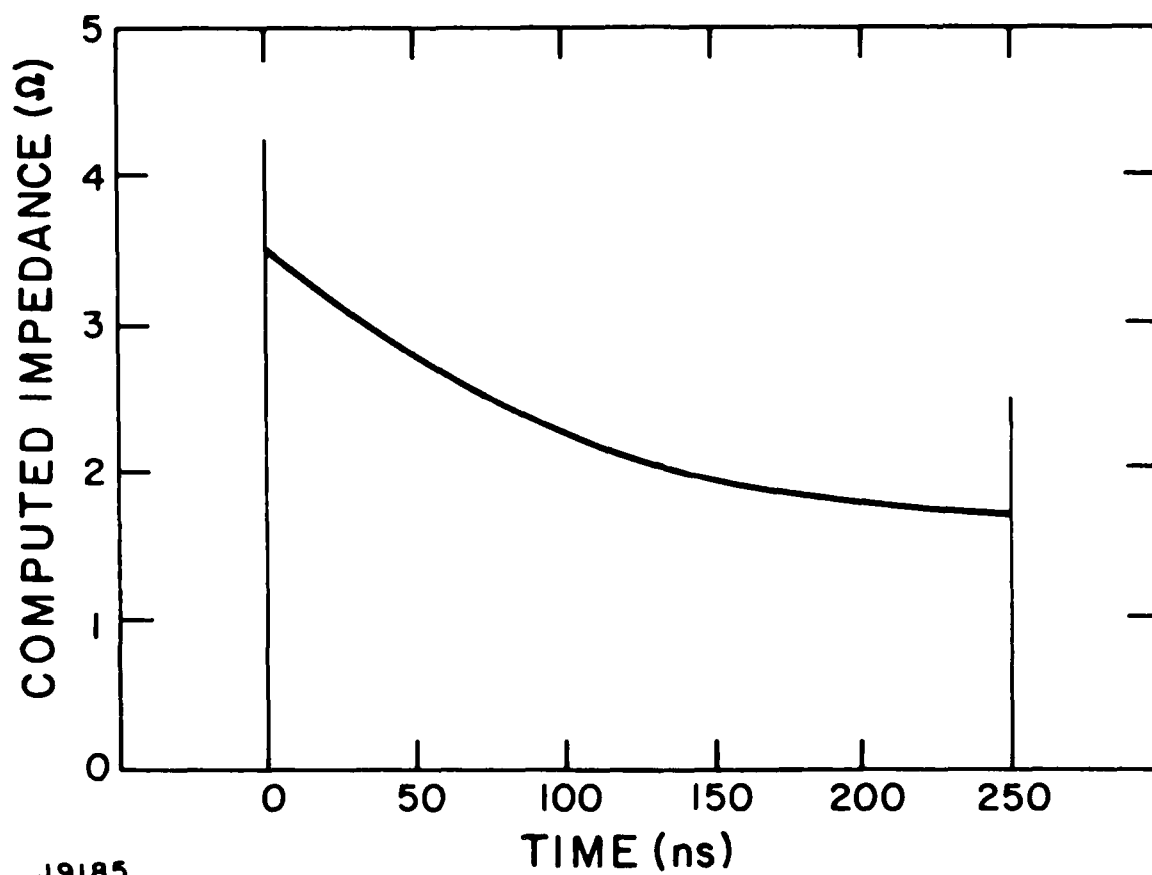


Figure 48. Design Point Energy and Electrical Efficiency vs Output Coupling



J9185

Figure 49. Computed Impedance Evolution for Design Point Discharge

which lies outside the optical resonator volume, leading to small losses. This loss factor is calculated accurately in the following section, in which the anode-cathode deposition uniformity is also derived.

3. E-Beam Deposition Profiles

Using the code which has been experimentally verified (Section II-A-3-i) deposition has been calculated for the 4 kG design point magnetic guide field. The transverse isodeposition contours are shown in Figure 50. The cathode plane lies at 1 cm and the anode lies at 7 cm. (The cathode screen transmission is unity in this simulation, but is accounted for correctly in the total e-beam energy budget). The anode is given an electron reflection coefficient of 0.3, corresponding to its high Z composition. The primary electron voltage is 300 kV and the simulation includes the scattering and energy losses due to a 1/2 mil Ti foil at 0 cm. The argon density is 2 Amag. Each contour represents 5% of the peak deposition.

Deposition profiles derived from Figure 50 but transverse to the anode-cathode axis are shown in Figure 51. These profiles determine the discharge power profile to a very large extent. Because of two-step discharge ionization, the central 4 cm of the discharge is enhanced by ~ 50% relative to the wings. With allowance for this we may use Figure 51 to show that the 4 x 6 cm optical aperture will intercept the discharge transverse power distribution with 92% efficiency.

4. Anode-to-Cathode Uniformity

Use of the segmented laser model (Section II-A-3-k) allows us to predict the anode-to-cathode variation of laser output power, again assuming plane-plane optics for the purpose of discussion. With an injected laser power of 10 kW/cm^2 (the result is very insensitive to the precise level of injection) we compute that lasing near the cathode will be at 0.96 of the intensity near the anode, for a deposition uniformity of 0.8.

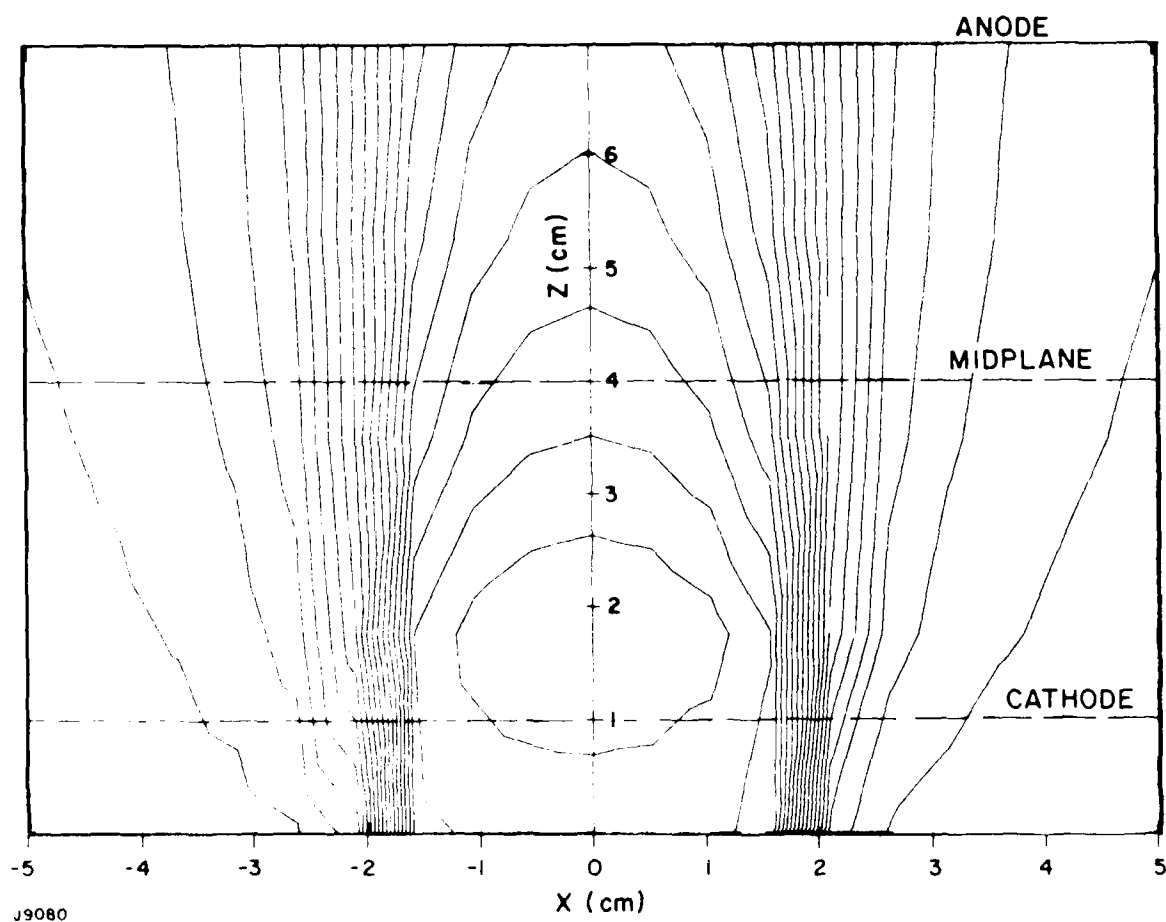


Figure 50. Isodeposition Contours for Design Point

Q. 2

DEPOSITION PROFILES TRANSVERSE TO THE ANODE-CATHODE
AXIS, AT VARIOUS DEPTHS, $B = 4 \text{ kG}$

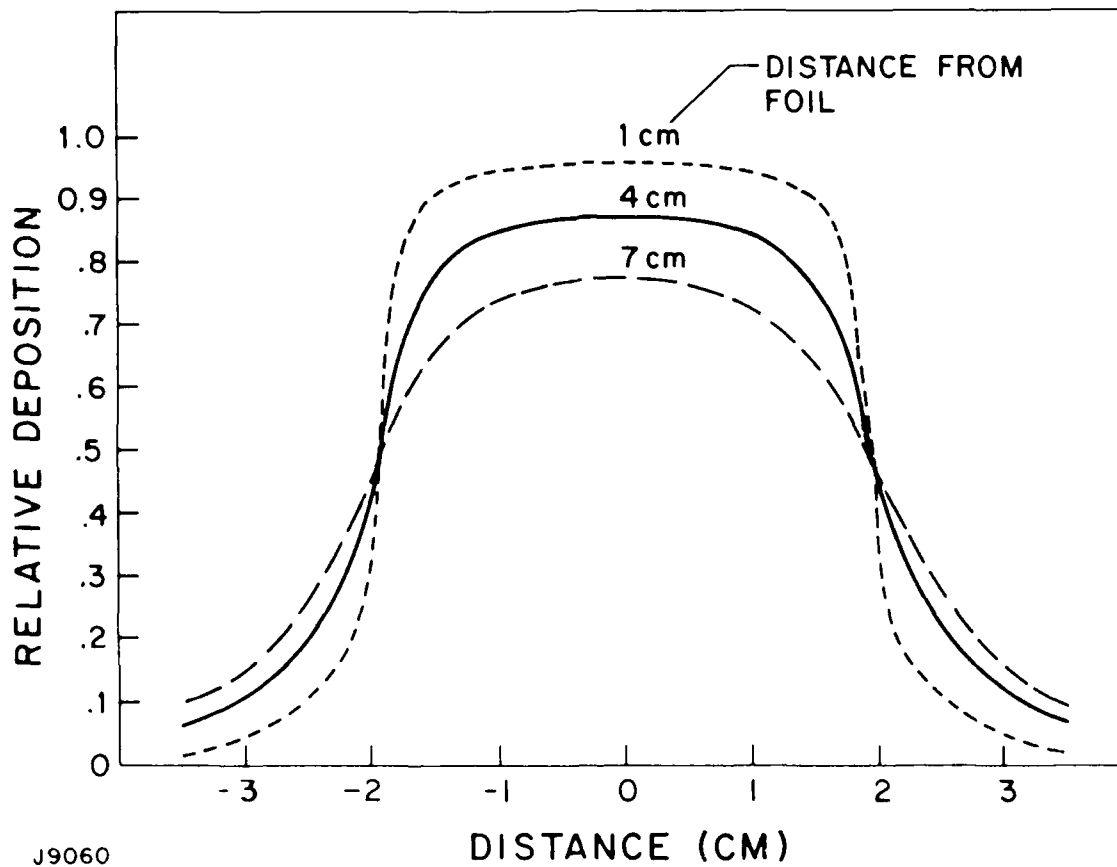


Figure 51. Deposition Profiles Transverse to the Anode-Cathode Axis, at Various Depths

The overall spatial uniformity of the laser output will be discussed in Section III-K. At present we note that from consideration of the discharge power distribution alone, the intensity is very nearly uniform from anode to cathode, but has a profile in the transverse direction given on average by the "4 cm" curve of Figure 51. Apart from a slight "roll-off" in the edge 0.1 cm, the intensity uniformity meets the $\pm 20\%$ V specification, insofar as it is controlled by the discharge power distribution. It is mentioned above that only 8% of the discharge power is not accessed by the 4 x 6 cm optical aperture. This factor reduces the electrical efficiency to 2.08%, giving an actual design output of 2.08 J.

D. LASER CAVITY DESIGN

In this section we describe the details of the laser cavity design together with the various requirements that led to this design. The major components of the cavity include (1) the discharge electrodes, (2) current, and (3) high-voltage feedthroughs.

1. Discharge Electrodes

It has been shown in experiments performed on the 1 m device (see Section II-A-3-j) that if the electric field produced by the discharge electrodes is kept uniform ($\pm 5\%$) in the region of the e-beam, then the discharge energy deposition is determined solely by the e-beam. In the present electrode configuration the electrodes are designed to provide uniform electric fields in the central 4 cm e-beam region. The edges of the electrodes where field enhancement (30% higher than the field at the center) occurs, are brought out to regions where the computed e-beam deposition is $< 5\%$ of that on the e-beam midplane. A half-cross-section view, in the plane perpendicular to the optical axis, of the electrodes is shown in Figure 52. Also shown are computed vacuum electric field values on the electrode surfaces.

It has also been shown in the 1 m device experiments (see Section II-A-3-i) that the preferred discharge polarity is to have discharge current flow co-linear with the e-beam, that is, to have the cathode closest to the e-gun. In this configuration the discharge electric field is in the direction to accelerate the e-beam electrons. This partially counteracts e-beam stopping by the gas and improves e-beam deposition uniformity.

The cathode must be partially transmitting to the e-beam. It must also be partially transparent to the flow in order that the gas in the region between the foil and cathode is flushed to remove the e-beam heated gas. To prevent the discharge from reaching the foil and to avoid damage from localized pressure waves generated in the event of a constricted discharge arc, the foil must be separated from the cathode by a gap. On the 1 m device a spacing of 1 cm was found to be sufficient for this. There

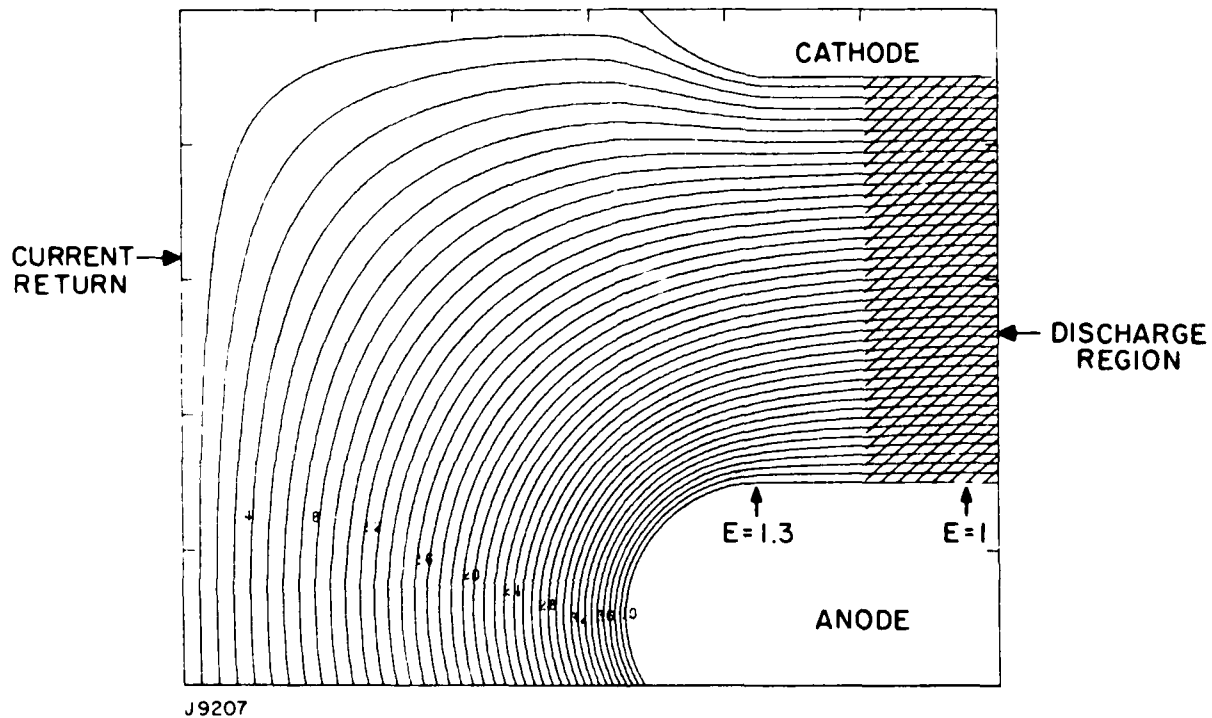


Figure 52. Equipotential Plot of Discharge Region

the foil routinely survived arcs (generated with the capacitor discharge circuit) with greater than 10 kJ stored energy dissipated in the arc. In the present design the discharge energy is limited by the PFN to 100 J, so the conditions are much less severe. In addition, arcing is only expected to occur if there is a fault in the e-beam. In our discharge circuit design we will incorporate a discharge inhibit circuit which will prevent discharge voltage from being applied when an e-gun fault is detected. However, a spacing of 1 cm is chosen here for safety.

The cathode is heated by the e-beam and by the discharge. Active cooling is required to cool the cathode to keep its average temperature to within 0.5°C of the core flow so that the temperature disturbance in the active medium is minimized (see Section III-E).

The cathode design chosen consists of parallel 1 mm outside diameter tubes oriented in the flow direction, spaced $1/3$ cm apart in the optical axis direction. The geometrical transmission of the e-beam through this structure is therefore 67%.

Since the cathode is made up of parallel tubes rather than a smooth surface, the field produced will be nonuniform close to the cathode surface. The field produced by such an arrangement can be calculated.⁽²¹⁾ In Figure 53 we show an equipotential plot in the vicinity of the cathode. For the present design the electric field nonuniformity is calculated to be $\leq 2\%$, 2 mm away from the cathode surface. Similar nonuniformities existed in the 1 m experiments (see Section II-A-3-1) and were found not to affect discharge stability.

The side of the cathode facing the e-gun will be heated by the e-beam. Assuming all of the intercepted e-beam power is deposited in the surface of the tubes, the heating power per cm^2 is $J_{eb}V_{eb}$, where J_{eb} is the beam current density through the

21. "Vacuum Tubes," Karl R. Sprangenberg, McGraw-Hill, 1948.

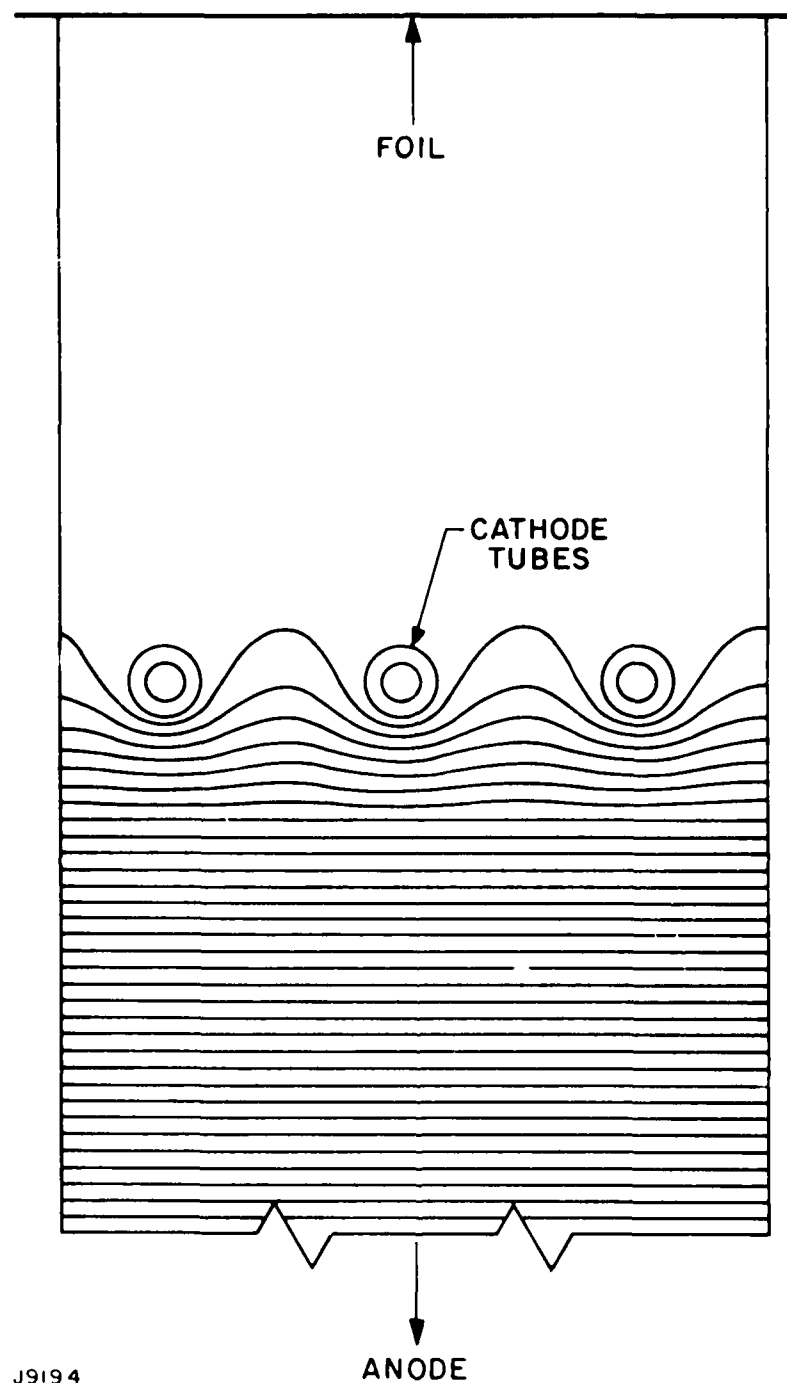


Figure 53. Equipotential Plot in the Region Near the Cathode

foil and V_{eb} is the beam voltage. For the present design the average power loading on the cathode by the e-beam is $\approx 6 \text{ W/cm}^2$ on the surface of the cathode tubes. On the side facing the anode, the cathode will be heated by the discharge. The power deposited by the discharge is a small fraction of $J_d V_{sh}$, where J_d is the discharge current density on the cathode tube surface and V_{sh} is the cathode sheath voltage drop. In the present design $J_d \approx 120 \text{ A/cm}^2$ and V_{sh} is estimated to be $\approx 300 \text{ V}$.⁽²²⁾ The average power deposited on the cathode tubes by the cathode fall is then a fraction of 1 W/cm^2 . Active cooling is provided by coolant flow in the cathode tubes to maintain their temperature to within 0.5°C . The instantaneous surface temperature rise immediately after the e-beam pulse can be calculated using the time-dependent heat diffusion equation. For platinum this temperature rise is estimated to be $\approx 70^\circ\text{C}$. The corresponding temperature rise on the discharge side is negligible. The instantaneous surface temperature rise will decay by conduction into the tubes in μs time scale and will not present a problem.

The cathode surface will be bombarded by energetic ions during the discharge and some sputtering will occur. For refractory metals the sputtering rate is typically $10 \mu\text{g/coulomb}$.⁽²³⁾ For this application in 10^8 pulses at 120 A/cm^2 and 250 ns pulses, the erosion is estimated to be $3.0 \times 10^{-2} \text{ g/cm}^2$ of cathode surface or about 0.6 mil loss. The tube used will have a wall thickness of at least 6 mils so sputtering will not be a problem for cathode integrity. Clearly, for 10^{10} pulse lifetime the problem is more severe. The solution will be to make the solid electrode the cathode. In this case the e-beam voltage will have to be raised about 60 kV to achieve the same e-beam deposition uniformity.

22. "Basic Data of Plasma Physics," Sanborn C. Brown, the M.I.T. Press, 1959.

23. "Gaseous Conductors," James D. Cobine, Dover Pub. Inc. 1958.

Any sputtered metal will be carried by the flow and be deposited on the heat exchanger surfaces. On the average the gas flow will hit about ≈ 10 such surfaces on each trip around the loop. The amount of sputtered metal that may be coated out on the optical windows can be estimated as follows. The total amount of metal sputtered in 10^8 pulses is given by

$$M = I \tau_p 10^8 \times 10^{-5} \text{ g/coulomb} \quad (2)$$

where I is the discharge current and τ_p is the discharge pulse length. In this case $I = 10^4$, and $\tau_p = 250 \text{ ns}$, therefore $M = 2.5 \text{ g}$. The total surface area of the flow loop is $A \approx 2.7 \times 10^5 \text{ cm}^2$. Since the gas sees ≈ 10 surfaces each time around the flow loop, the coating thickness T on the windows is then given by

$$T = \frac{M}{A} \frac{1}{\rho} e^{-10 P} \quad (3)$$

where $\rho = 21 \text{ g/cm}^3$ is the density of platinum, and P is the surface sticking probability. Taking a sticking probability of 0.3 (a conservative estimate) we get a coating thickness of 2.2 \AA . The effect of such a thin coating on window transmission is negligible. For 10^{10} shot lifetime, a well-filtered boundary layer shield flow at the windows may be necessary.

2. Current Returns

In order to maximize the laser electrical efficiency, the risetime of the discharge circuit must be kept small, compared to the pulsewidth. As we indicate elsewhere, we can allocate 30 nH to the cavity and its connectors. This puts a constraint on the allowable inductance in the laser cavity. To minimize inductance the current returns for the discharge must be placed close to the discharge channel. This necessitates bringing the current return through the flow via a set of bars. As in the 1 m experiments, in

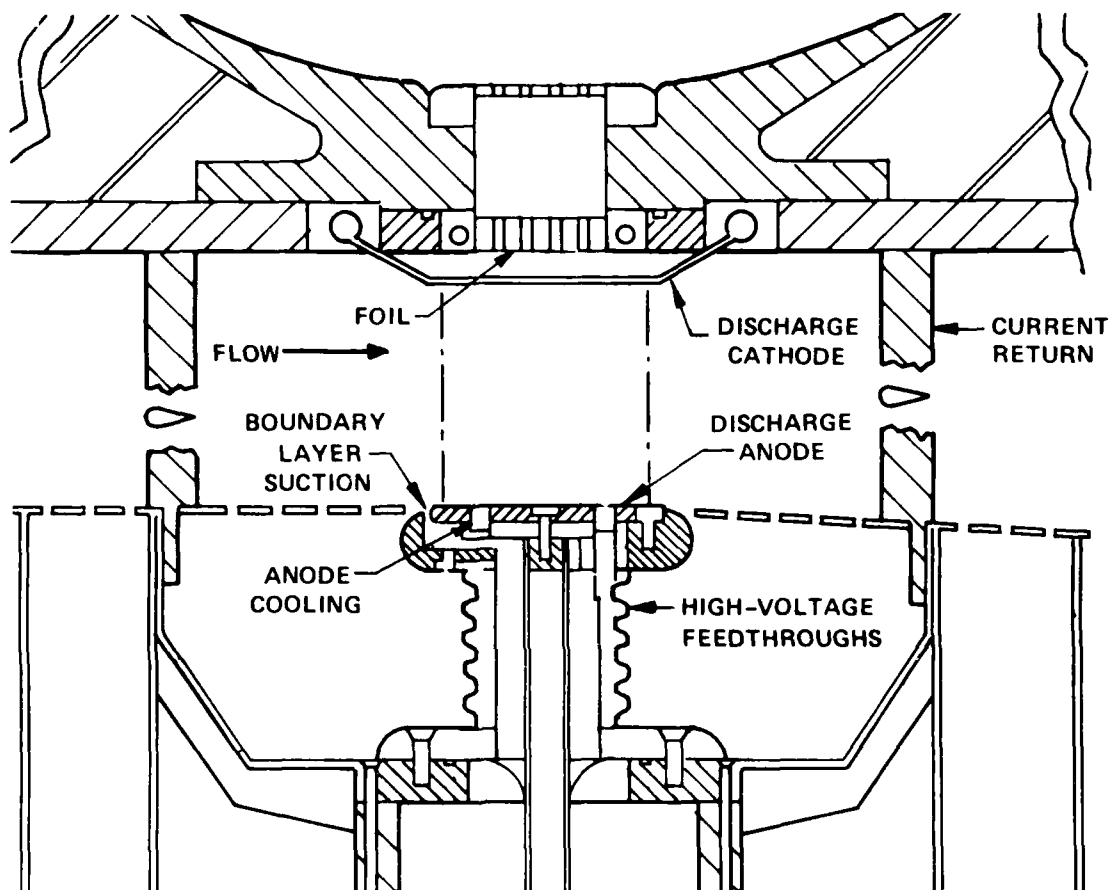
this design the anode is pulsed to high voltage while the cathode is held at ground potential. The current returns are then also at ground potential. In order to prevent arcing between the anode and the current returns a minimum spacing is required. For the mixtures used in this laser the maximum holdoff field has been measured in both the cable gun and meter device experiments and was found to be > 12 kV/cm. The maximum designed discharge voltage on the anode is 32 kV. To allow for local field enhancement around the current return bars and to allow a safety margin, the minimum spacing between the current returns and anode is chosen to be 5 cm.

Symmetric current returns are placed up and down stream from the discharge channel (see Figure 54). If the spacing of the current return bars is kept small compared with their distance to the discharge channel, then the return current can be approximated by a continuous current sheet for inductance calculations. In this case, with symmetric current returns, the circuit inductance is given by

$$L \leq \frac{\mu_0}{4} \frac{A}{\ell} \quad (4)$$

where A is the area enclosed by the current returns and ℓ is the length of the discharge region in the optical direction. For the present design $A = 300 \text{ cm}^2$ and $\ell = 62.5 \text{ cm}$. The inductance is calculated to be $\approx 15 \text{ nH}$. To keep the current return bar spacing small compared with their distance to the discharge channel, 15 3/16 in diameter current return bars spaced 4 cm apart are used per side in this design.

In order to minimize disturbance to the flow the current return bars are placed inside alumina tubes with the outside shaped like airfoils. The pressure drop then is negligible.



J9208-A

Figure 54. Discharge Electrode Geometry

3. High Voltage Feedthroughs

The high-voltage feedthroughs support and provide connections from the discharge modulator to the anode. Five parallel feedthroughs are used along the anode to minimize inductance. These are similar in design to those used in the 1 m device. Five centimeter long alumina sections are used for voltage standoff. In the laser mixture surface breakdown in ceramic was found not to be a problem, so the 5 cm insulator length allowed should standoff >60 kV, which is a factor of two greater than the maximum discharge voltage used. Therefore, breakdowns in the region at the back of the anode should not be a problem.

The feedthroughs will be operating at cavity temperature. The output cables from the discharge modulator will not be capable of withstanding this temperature so that connectors will be required to take up the temperature drop. To avoid inductance problems the connectors can be made to be like coaxial transmission lines, all the way up to the feedthroughs (see Figure 54). The impedance of the connectors can be matched to that of the modulator output cables. The connectors then add negligible inductance to the circuit. Since the discharge impedance is $\approx 3 \Omega$, with 5 feedthroughs, the connectors should be made like 15Ω coaxial lines. This can easily be accomplished with metalized alumina tubes.

The total inductance of the discharge cavity including all the connectors will therefore be ≤ 30 nH. This value is used in our discharge modulator design (see Section III-I).

E. FLOW-LOOP DESIGN

The laser device is specified such that 80% of the energy at the output aperture is confined in a beam of total angle which is ten times that of the first Airy disc. The associated constraints on phase front errors at the output aperture are assessed here. This allowed phase front error is related to laser medium homogeneity requirements, and this in turn is used to determine acoustic wave suppression and thermal homogeneity requirements in the gas. Acoustic attenuator design features are also developed. Thermal homogeneity requirements are coupled to flow-loop design in the following section.

1. Phase Distortion

To estimate the allowable phase errors for a system far from the diffraction limit a sinusoidal phase error was assumed, for which the equations for maximum spot size are easily developed.

Phase variation across a circular aperture is considered in the form,

$$\psi = A [1 - \cos (2\pi Nr/D)] \quad (5)$$

where r is radial position across the aperture.

D is the aperture diameter

N is the number of periods across a diameter

$2A$ is the peak-to-peak phase variation.

If this is used to simulate separate eddies with a normalized scale length

$$L = 1/2 N \quad (6)$$

then

$$\psi = A \left[1 - \cos \left(\frac{\pi r}{LD} \right) \right] \quad (7)$$

For large wavefront errors diffraction is ignored and only the maximum wavefront slope is considered

$$\psi' = \frac{\pi A}{LD} \quad (8)$$

The condition that this be equal to 10 times the diffraction half-angle for a perfect lens, yields

$$\frac{\pi A}{LD} = \frac{(10) 1.22 \lambda}{D}$$

$$A = \frac{12.2 \lambda L}{\pi} \quad \frac{2A}{\lambda} = (0.78) (XDL) L \quad (9)$$

where (XDL) is the ratio of far field spot diameter to Airy disc diameter. Thus the allowable peak-to-peak error (2A) depends linearly on L and for example if L = 0.1 and XDL = 1 times diffraction limit,

$$2A/\lambda = 0.78 \text{ waves} \quad (10)$$

2. Flow System Design Criteria

The laser gas, which is initially at temperature 490°K and a density of two amagats, undergoes an electrical energy deposition of 61.5 J/cc for a period of 250 ns to produce a laser energy density of 1.5 J/cc. The gas is predominantly argon, hence the temperature rise during this event at a constant volume is $T_2 - T_c = 62.4^\circ\text{C}$. Subsequent expansion of heated cavity gas is accurately represented as isentropic, thus final pressure relaxation to ambient reduces temperature in the ratio $T_f/T_2 = 0.953$ (temperatures in °K). The final excess gas temperatures is then $(T_f - T_c) = 36.4^\circ\text{C}$ after relaxation of a pressure pulse of strength $(p_f - p_c)/p_c = 0.128$. The internal energy decrease

during relaxation appears as compressive work done on the remainder of the gas in the flow-loop. This compression work, which is the difference between net deposited energy and remaining internal energy after relaxation, $\Delta W = 29.4 \text{ J/l}$, is distributed partly as energy dissipation in acoustic wave attenuators and partly as recompression work on a hot gas slug as it cools in passage through a heat exchanger. The above energy considerations combine with cavity dimensions and pulse rate for the basis of loop thermal conditioning described below. The pulse overpressure combines with cavity dimensions and medium homogeneity requirements for the basis of acoustic attenuator design described below.

Beam quality is sufficient to meet targeting requirements if the PTP phase front variation is 0.78 waves for ordered disturbances on a periodic scale of 1.6 cm according to Eq. (10). If this distortion combines equal contributions from optics and from cavity gas, this relates to cavity homogeneity through

$$\frac{\phi}{2\pi} = \frac{2l_0}{\lambda} \beta \left(\frac{\rho}{\rho_r} \right) \left(\frac{\Delta\rho}{\rho} \right) = 0.55 \text{ waves} \quad (11)$$

where l_0 is distance between cavity windows = 70 cm; $\lambda = 0.5 \text{ } \mu\text{m}$; $\rho/\rho_r = 2$ amagats; $\beta = 2.8 \times 10^{-4}$. Thus,

$$(\Delta\rho/\rho)_{\text{PTP}} = 3.4 \times 10^{-4} \quad (12)$$

If this ordered gas distortion is budgeted equally between uncorrelated thermal and pressure wave distortions, the medium homogeneity requirement for each is

$$\left(\frac{\Delta\rho}{\rho} \right)_{\text{PTP}} = 2.43 \times 10^{-4} \quad (13)$$

Since the ordered distortion used in deriving Eq. (13) has an associated scale of 1.6 cm, the maximum gradient in density is limited to

$$\frac{\nabla \rho}{\rho} \leq 5 \times 10^{-4} \text{ cm}^{-1} \quad (14)$$

This form is most useful in assessing allowed boundary layer, ordered, thermal distortions. In ordered periodic distortions of arbitrary period Λ , beam quality constraints limit the product of the LHS of Eq. (13) and Λ^{-1} to a constant value

$$\left(\frac{\Delta \rho}{\rho} \right)_{\text{PTP}} \Lambda^{-1} \leq 1.61 \times 10^{-4} \text{ cm}^{-1} \quad (15)$$

This form is useful in assessing allowed, ordered, thermal and pressure disturbances in the bulk flow. If thermal disturbances of scale Λ are randomly distributed in space, beam quality constraints confine the product of the LHS Eq. (15) and $(\Lambda/2)^{-1/2}$ to a constant value; thus

$$\frac{\Delta \rho}{\rho} \Lambda^{-1/2} \leq 1.91 \times 10^{-3} \text{ cm}^{-1/2} \quad (16)$$

This form is useful in assessing allowed thermal disturbances carried by disordered turbulent flow.

The active cavity length in the flow direction is $L_f = 4.0$ cm. Development of design is based on a minimum interpulse interval of 5.0 ms and an associated flush factor of 1.75 to yield a flow velocity of 14 m/sec. The active cavity length in the pump direction is 6.6 cm; however, the full flow dimension is $L_p = 7.35$ cm for reasons discussed below. The active cavity length along the optical axis is 62.5 cm, however, electrode termination and protection of windows from e-beam dictate a flow dimension $L_o = 70$ cm. The choice of a design flush factor, $FF = 1.75$

should be conservative. Voltage standoff measurements in the presence of previously discharge heated gas suggest lower flush factors are permissible (see Section II-A-2-p).

For reference, the performance parameters and cavity geometry described above are repeated in Table 4.

a. Muffler Performance Predictions

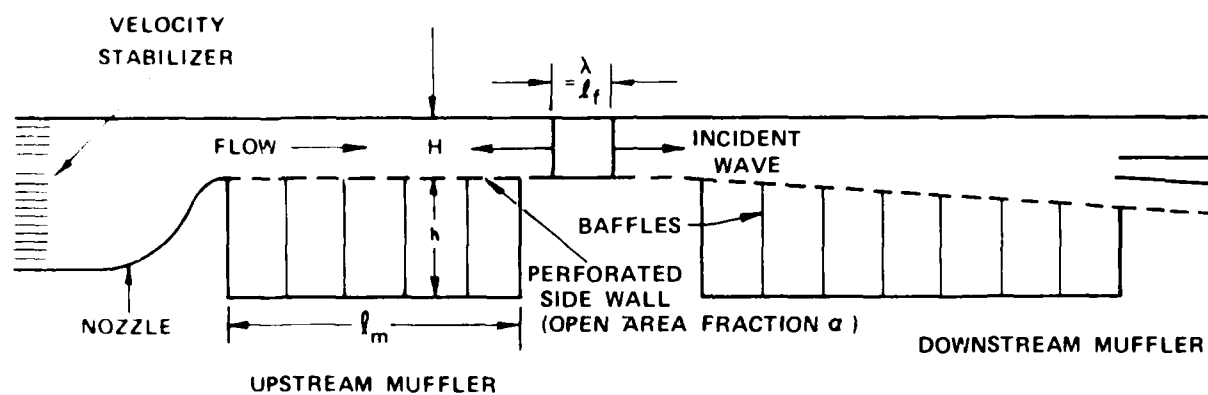
Pressure wave attenuation will be achieved by perforated wall segments in the flow channel both upstream and downstream from the laser cavity. This muffler configuration, when backed with closed cells containing a dissipative material, has been studied theoretically at AERL under IRAD support. Experimental studies have also been conducted under DARPA support as part of the XeF laser program. This modeling, which is the basis of the present system design, is validated by these measurements. In the case of small pulse overpressures appropriate to the present application, a geometrical similarity parameter, L' , allows a correlation of results for use as a design tool.

$$L' = \frac{H}{2 \alpha C_D} \sqrt{\frac{\Delta P_i}{2 \gamma p_c}} \quad (17)$$

where geometrical parameters are defined in Figure 55; C_D is the discharge coefficient through orifices in the perforated plate; $\Delta P_i/p_c$ is the incident pressure wave strength and γ is the ratio of gas specific heats = 1.67. At the present system cavity Mach number of 0.034 the zero Mach number solutions are appropriate and results are presented in Figure 56. The ratio of exit to inlet wave strength is shown for the design value of the ratio of incident wave to upstream muffler length, $\lambda/\ell_m = 1/5$, and for several values of the ratio of backing depth to flow channel height, h/H , as a function of normalized muffler length. For the

TABLE 4. LASER CAVITY OPERATING CONDITIONS

Cavity Temperature, T_c	490°K
Molecular Weight, m	40 g/mole
Ratio of Specific Heats, γ	5/3
Sound Speed, a_c	412 m/sec
Gas Density (2 Amagats), ρ_c	3.57 kg/m ³
Viscosity, μ_c	3.4 x 10 ⁻⁵ kg/ms
Minimum Interpulse Spacing	5.0 ms
Cavity Flow Length, l_f	4.0 cm
Minimum Flush Factor, FF_{min}	1.75
Average Pulse Rate, PRF	100 pps
Average Flush Factor, FF	3.5
Cavity Flow Velocity, u_c	14 m/sec
Reynolds Number (per meter), Re	1.47 x 10 ⁶ m ⁻¹
Laser Energy Density, e_l	1.5 J/
Electrical Energy Deposited in the gas, e_e	71.5 J/
Pulse Overpressure, $\Delta p/p$	0.128
Gas Temperature Rise After Pressre Relaxation	36.4°C
Laser Cavity Dimensions l_f', l_p', l_o'	4 x 6 x 62.5 cm
Flow Length Along Pump Direction, l_p	7.35 cm
Flow Length Along Optical Axis, l_o	70 cm
Average Gas Temperature Rise	7.6°C
Acoustical Power Deposited in the Upstream Muffler	1.1 kW



J9078

Figure 55. Flow Channel Mufflers with Finite Backing Volume

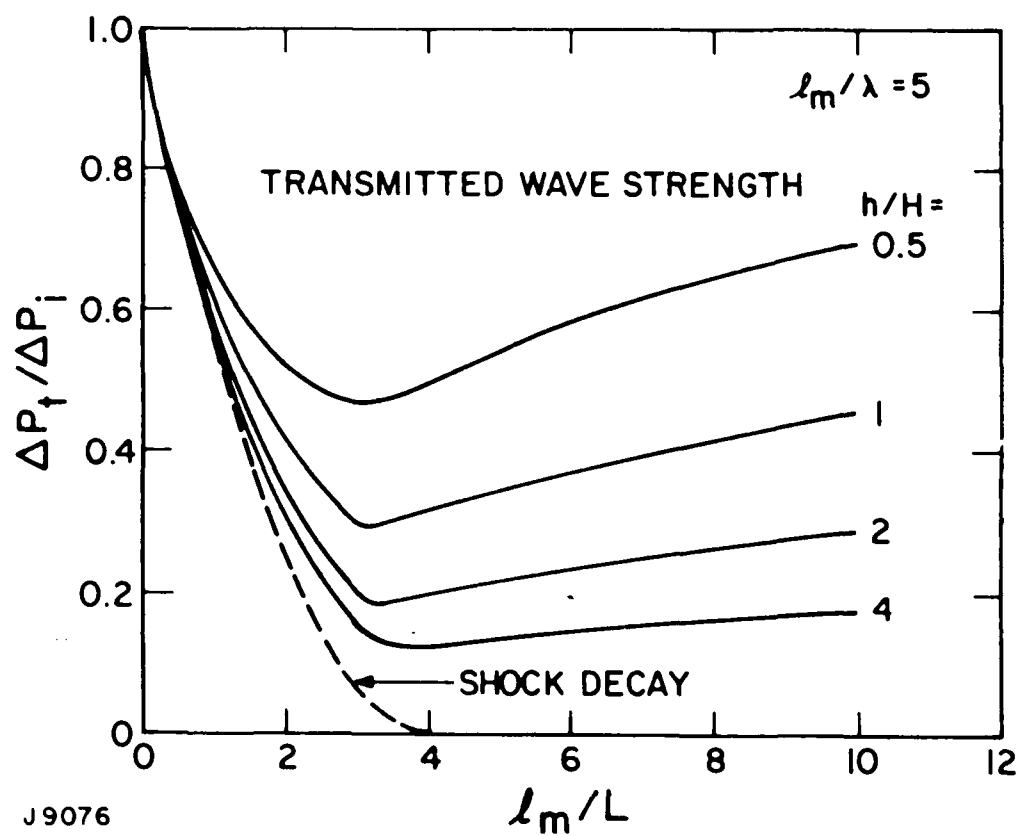


Figure 56. Transmitted Peak Wave Strength Through Perforated Side Wall Muffler

selected $h/H = 2.0$ a minimum in the ratio of transmitted to incident wave strength of 0.18 is observed for $\ell_m/L = 3.4$. Since the upstream muffler length is $\ell_m = 20$ cm and incident wave strength is approximately half the cavity pulse overpressure, $\Delta p_i/p_c = 0.064$, Eq. (17) provides the specification of effective upstream muffler transparency $\alpha C_D = 0.086$. The upstream transmitted wave passes through a converging nozzle and is reflected from a plate/film velocity stabilizer of 40% geometrical blockage. This reflected wave, which is of strength ~ 0.20 that of the incident wave, returns through the muffler and is attenuated by another factor of 0.50 according to the modeling basis for Figure 56. Thus, the upstream pressure wave would show a peak overpressure of 1.15×10^{-4} upon reentry to the cavity. This return pressure pulse is distributed over a length of order $\ell_m/2 = 10$ cm, consequently, the product

$$\frac{\Delta p}{p_c} \Lambda^{-1} = \frac{1}{\gamma} \frac{\Delta p}{p_c} \Lambda^{-1} = 6.9 \times 10^{-5} \text{ cm}^{-1} \quad (18)$$

is well within the medium homogeneity requirements of Eq. (15). A similar analysis of the downstream muffler shows that single-pulse pressure disturbances are suitably attenuated for purposes of medium homogeneity for this compact muffler geometry. Other considerations in selection of muffler geometrical features include growth of upstream boundary layers and incorporation of a diffuser in the downstream muffler as well as overall system component arrangements. These considerations are discussed below.

3. Flow-Loop Design Approach, Arrangements and Sizing

Laser cavity operating conditions have been discussed above and are summarized in Table 4. Medium homogeneity requirements have also been discussed. Flow-loop design is based on these requirements and the requirements of (1) efficient operation for low flow power demand, (2) compactness for ultimate space board application, (3) compatibility with the hot reactive laser gas environment, and (4) reliability of loop components and peripheral equipment for long lived, maintenance-free operation. This section addresses the areas of thermal conditioning of the gas loop, flow-loop pressure drop, flow power requirements, and liquid coolant loop requirements.

For reference, two section views of the laser flow-loop are shown in Figures 57 and 58. Major flow elements are (1) muffler and diffuser downstream from the cavity for purposes of pressure wave attenuation and flow pressure recovery, (2) heat exchanger for removal of deposited electrical energy and dissipated flow power, (3) converging transition to circular flow cross section, (4) vaned turn, (5) fan and drive, (6) fan diffuser, (7) vaned turn, (8) diverging transition from circular to rectangular cross section, (9) velocity stabilizer to provide uniform velocity in the cavity, (10) converging nozzle, and (11) upstream muffler. Arrangements, performance requirements and component sizing are discussed in the following sections.

4. Cavity Thermal Conditioning Requirements

Gradients in cavity temperature for ordered disturbances at uniform pressure are limited by Eq. (14) as,

$$\begin{aligned}\nabla T/T &\leq 5 \times 10^{-4} \text{ cm}^{-1} \\ \nabla T &\leq 0.259^\circ \text{ cm}^{-1}\end{aligned}\tag{19}$$

Cavity temperature nonuniformity at uniform pressure, for an ordered disturbance of scale Λ , is limited by Eq. (15) as,

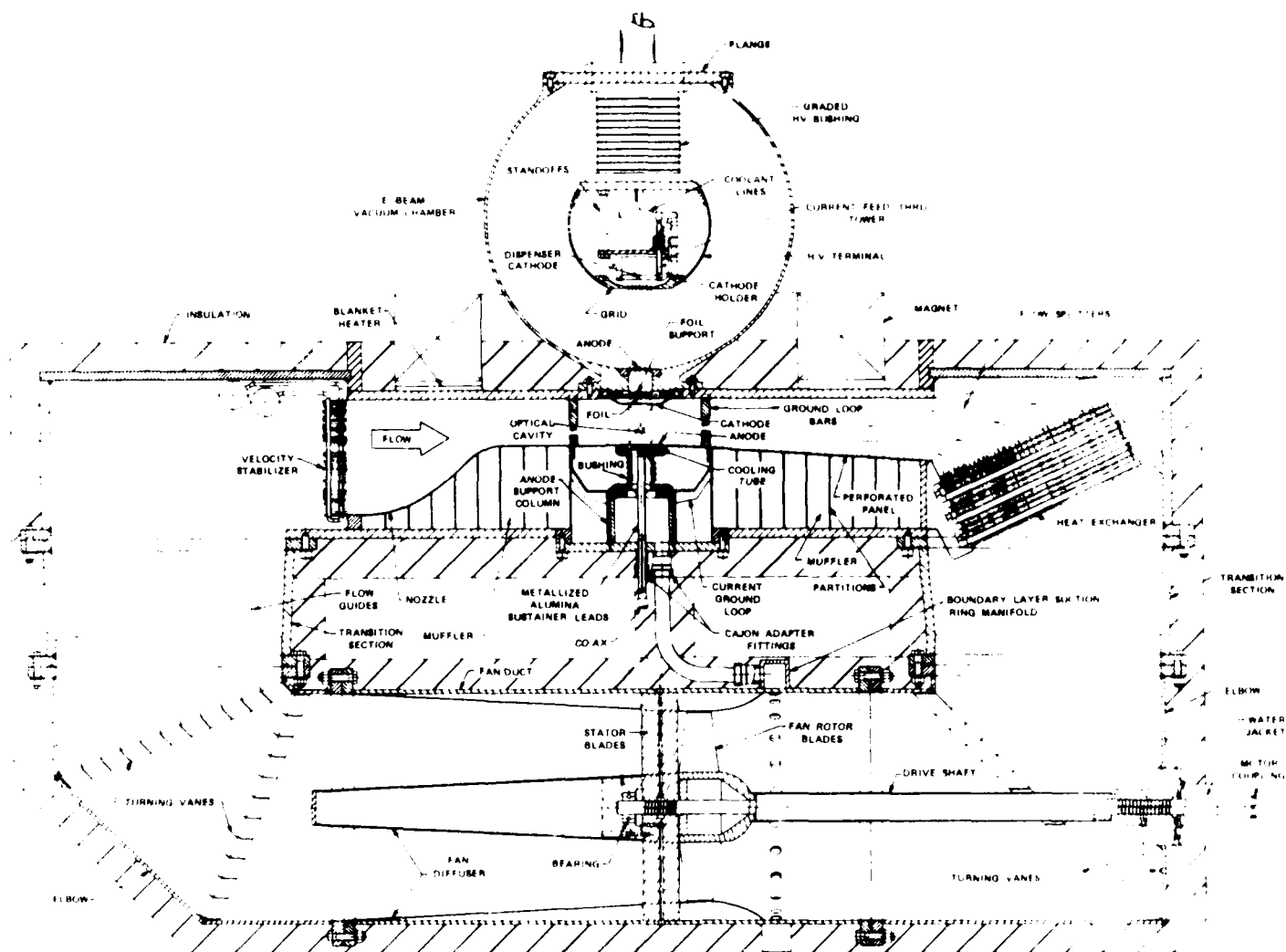


Figure 57. Sectional View of the Laser Flow Loop, Side View

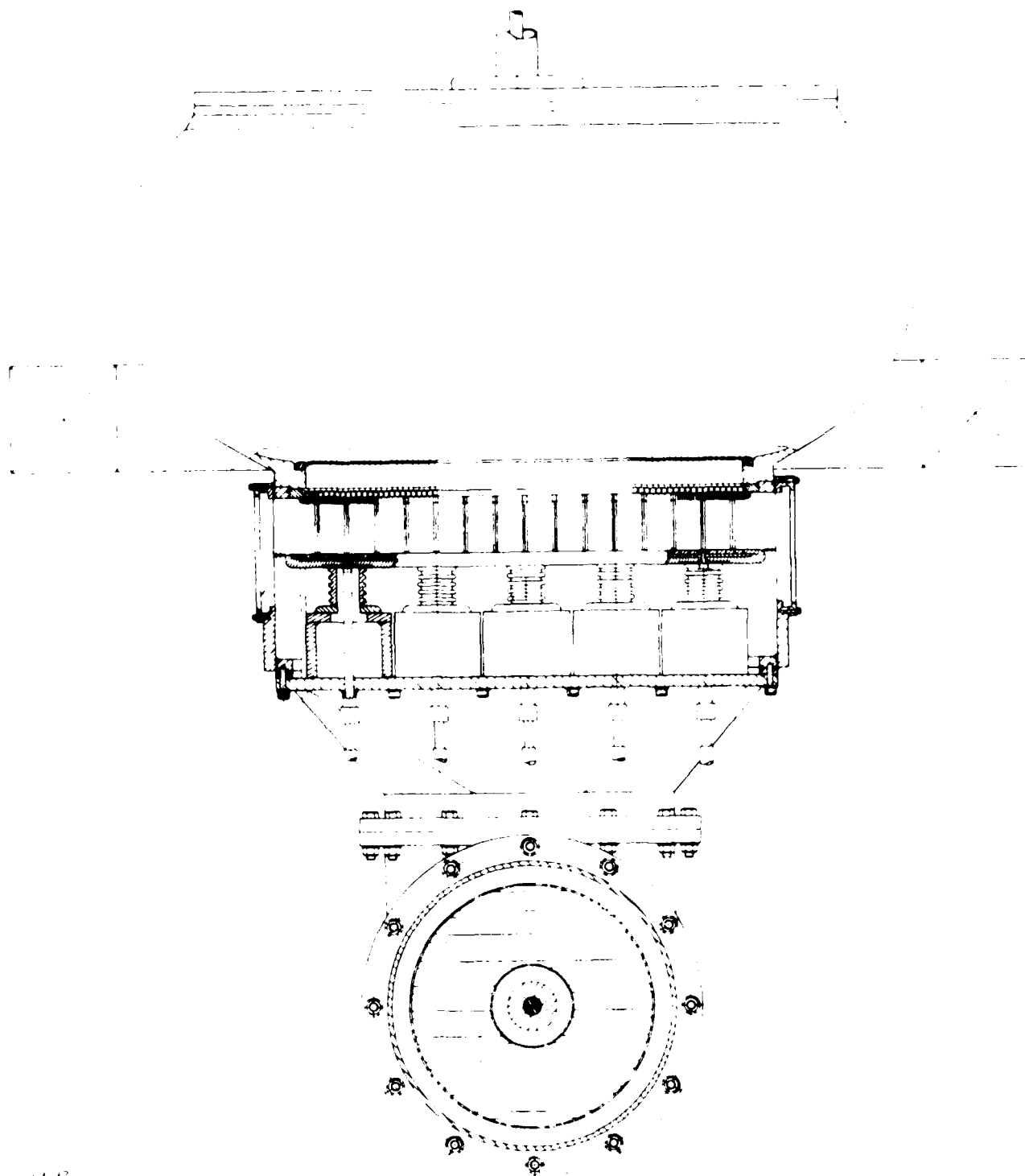


Figure 58. Sectional View of the Laser Flow Loop,
Upstream View

$$(\Delta T/T)_{PTP} \leq 1.61 \times 10^{-4} \Lambda \text{ (cm)} \quad (20)$$

$$(\Delta T)_{PTP} \leq 0.079^\circ\text{C} \Lambda \text{ (cm)}$$

Disordered thermal disturbances of scale Λ are limited by Eq. (16) as,

$$\Delta T \leq 0.94^\circ\text{C} \Lambda^{1/2} \text{ (cm)} \quad (21)$$

5. Boundary Layer Thermal Control Requirements

Between the velocity stabilizer and the cavity, differences between gas and wall temperatures will produce ordered average temperature variations in wall boundary layers superimposed on a disordered turbulent temperature field. Here, ordered and disordered boundary layer temperature variations are examined independently with constraints imposed by Eqs. (19) and (21), respectively. After flow contraction through a nozzle or area ratio 2.5 the flow channel boundary layers may be assumed to originate at the entry to the upstream muffler (See Figure 57). Turbulent boundary layer growth along a smooth wall is given by Schlichting⁽²⁴⁾ as

$$\delta(x) = 0.37 \times R_{e_x}^{-1/5} \quad (22)$$

where δ is boundary displacement thickness, x is distance from the origin and R_{e_x} is Reynolds number based on x . At the upstream edge of the cavity^x electrode, $x = 22 \text{ cm}$, thus $\delta = 0.64 \text{ cm}$. This value is appropriate for the solid wall, however, for the perforated wall a thickness of twice this value is assumed, $\delta_p = 1.29 \text{ cm}$.

24. Schlichting, H., Boundary Layer Theory, Pergamon Press, London, 1955.

The velocity variation through the boundary layer is given by Schlichting as,

$$u/u_c = (y/\delta)^{1/7} \quad (23)$$

where y is distance normal to the wall. Reynold's analogy between velocity and temperature variations in the boundary layer provides the approximation

$$\frac{T(y) - T_c}{T_w - T_c} \approx \frac{u_c - u(y)}{u_c} \quad (24)$$

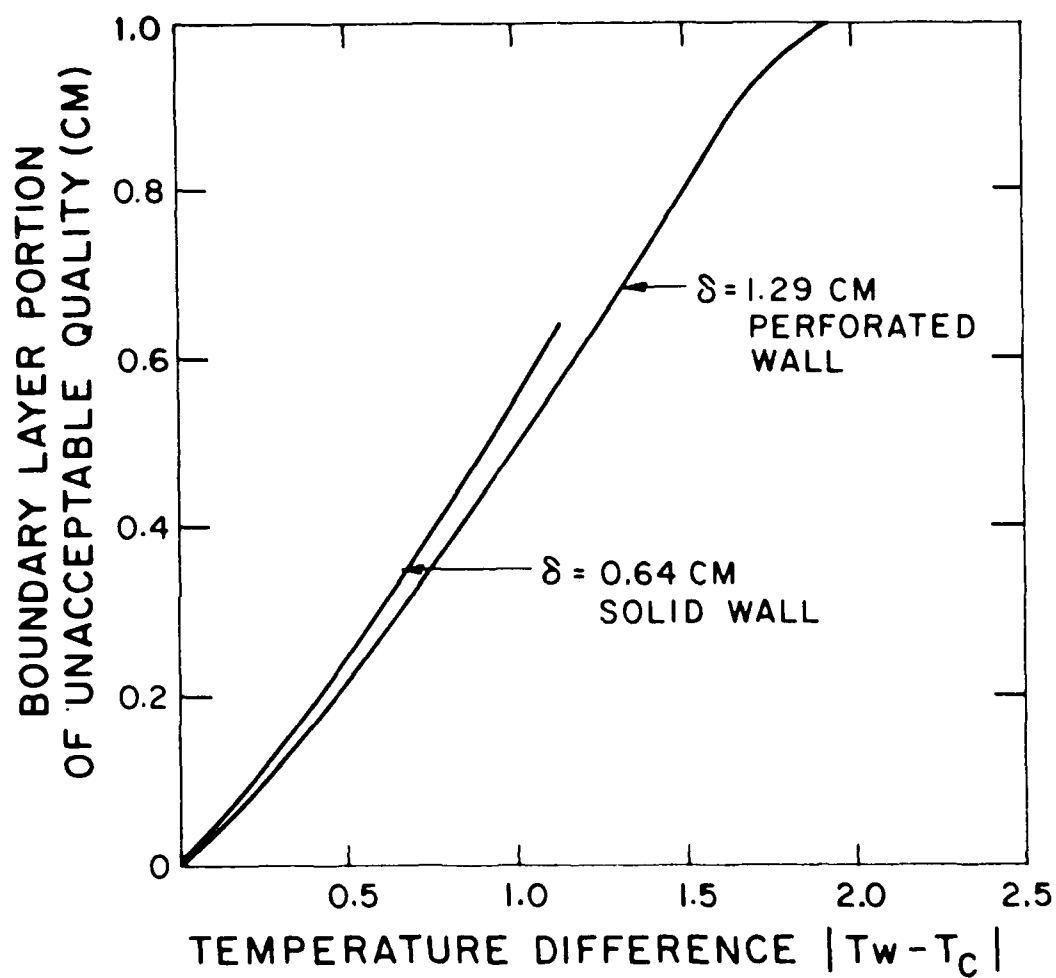
where T_w is the uniform wall temperature. Temperature gradient is related to (y/δ) through Eqs. (23) and (24) as

$$\frac{dT}{dy} = \frac{T_w - T_c}{u_c} \frac{du}{dy} = - \frac{T_w - T_c}{7\delta (y/\delta)^{6/7}} \quad (25)$$

Equation (25) when constrained by Eq. (19), indicates that a portion of the boundary layer near the wall will not contribute to useful laser energy extraction and this portion grows with increasing $(T_w - T_c)$. Equations (19) and (25) combine to give the extent of unuseable boundary layer flow as

$$\frac{y}{\delta} = \left(\frac{T_w - T_c}{1.75\delta} \right)^{7/6} \quad (26)$$

Equation (26) is plotted in Figure 59 for boundary layer thickness at laser cavity entry. The solid flow channel wall may be held to within 0.5°C of the cavity gas temperature without difficulty, thus indicating a lost portion in useable channel flow of 0.25 cm.



J9079

Figure 59. Boundary Layer Portion of Unacceptable Beam Quality vs Wall to Cavity Temperature Difference

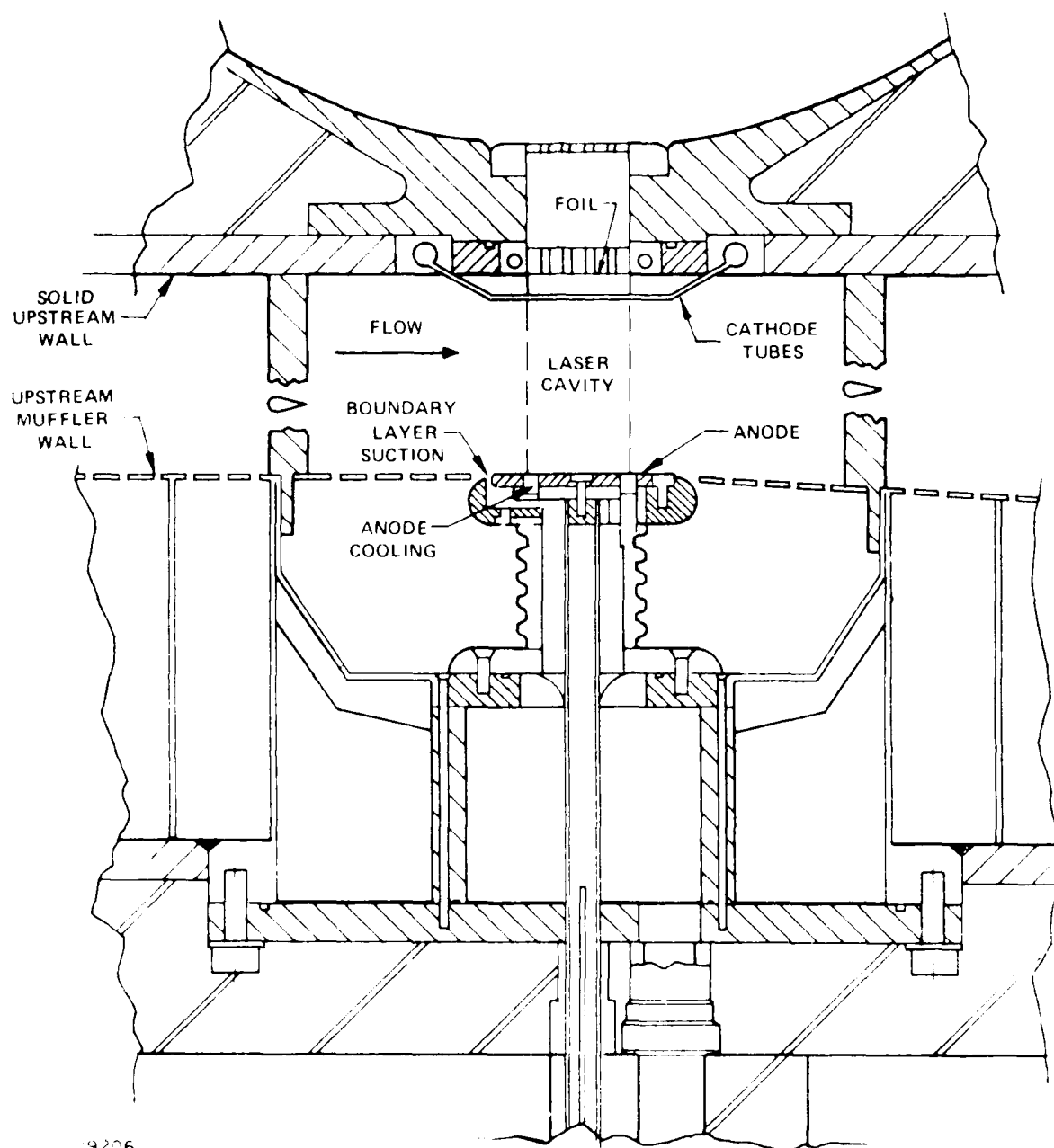
However, the discharge cathode will stand off by 1.0 cm from this wall for reasons discussed in the next section. Thus, even this exclusion is of no consequence. The perforated wall must be held to within 0.6°C of the cavity gas temperature if we wish to limit the rejected portion of the boundary layer to 0.25 cm. This may be achieved only if active cooling is provided in the backing volume of the upstream muffler, where as much as 1100 W of acoustical energy may be deposited.

Furthermore, boundary layer suction is proposed immediately upstream from the discharge anode to further reduce this ordered boundary layer temperature gradient. A portion 0.25 cm in height will be removed by the slit conduit shown in Figure 60. This removal of 20% of the boundary layer thickness will essentially restart the turbulent boundary layer, although disordered turbulence from the current boundary layer will survive. This disordered turbulence may carry temperature variation as large as $(T_w - T_c) = 0.6^{\circ}\text{C}$. On a scale order of the remaining boundary layer thickness = 1.0 cm. Equation (21) shows that this flow region satisfies cavity medium homogeneity requirements.

6. Treatment of Foil and Discharge Electrodes

Various heating contributors and loads to foil, discharge cathode and discharge anode are listed in Table 5. The foil will be recessed 1.0 cm behind the discharge cathode to prevent foil failure in the event of arcing. The cathode will be constructed as a row of cooling tubes so that main channel gas flow will carry away heated gas between foil and cathode. In this configuration foil heating of the gas is not an issue for cavity medium homogeneity, so attention is here focused on the cathode.

Cathode tubes of 1.0 mm outside diameter are spaced at 3.3 mm on centers. Tube ends are curved into coolant flow headers as shown in Figure 60. Straight tube segments parallel to the flow direction are 7 cm long and boundary layers grow along outsides of these tubes to a thickness of ~ 1.3 mm at mid-span, i.e., at the center of the laser cavity. Tube heating occurs mainly over the



9206

Figure 60. Section to Show Details in the Region of the Laser Cavity

TABLE 5. HEATING LOADS ON FOIL AND DISCHARGE ELECTRODES

<u>Element</u>	<u>Source</u>	<u>Heating Load</u>
Foil:	E-Beam	$0.72 \text{ W/cm}^2 = 180 \text{ W}$
Discharge Cathode:	E-Beam	$2.73 \text{ W/cm}^2 = 683 \text{ W}$
	Discharge	$0.5 \text{ W/cm}^2 = 125 \text{ W}$
	Gas Convective Cooling	47 W
	Total	855 W
Discharge Anode:	E-Beam	$1.10 \text{ W/cm}^2 = 276 \text{ W}$
	Discharge	$0.5 \text{ W/cm}^2 = 125 \text{ W}$
	Gas Convective Cooling	47 W
	Total	448 W

central 4.0 cm of span where e-beam and discharge are active. For flat wall boundary layers Eq. (26) defines the unuseable portion due to unacceptable medium homogeneity. For the present boundary layer growth along a tube row, temperature varies periodically along lines parallel to the optical axis, and the path averaged difference between local and cavity temperature is approximately half the maximum difference at each tube station. Therefore for local allowed temperature gradients at tube stations the RHS of Eq. (19) is replaced by $0.50^{\circ}\text{C cm}^{-1}$ and Eq. (26) is replaced by

$$\frac{Y}{\delta} = \left(\frac{T_w - T_c}{3.5 \delta} \right)^{7/6} \quad (27)$$

If the entire 1.3 mm of boundary layer flow is excluded from the laser cavity the allowed average tube wall temperature excess is obtained from Eq. (27) as,

$$T_w - T_c = 0.46^{\circ}\text{C} \quad (28)$$

This requirement has influence on design of the liquid side of the cathode tubes.

The discharge anode with upstream boundary layer suction is shown in Figure 60. If a turbulent boundary layer is started at the suction slit, its thickness at electrode center is, $\delta = 0.15$ cm. If the entire renewed boundary layer is excluded from the laser cavity the allowed anode wall temperature excess is given by Eq. (26),

$$T_w - T_c = 0.26^{\circ}\text{C} \quad (29)$$

Temperature uniformity in the anode will be maintained by liquid coolant channels spaced at intervals of 1.0 cm and arranged parallel to the flow direction. Coolant will be conveyed by spreaders at upstream and downstream ends of these channels, as shown in Figure 60. If coolant channels are spaced at intervals, w , and are of diameter, d , the wall temperature variation is quadratic between channels with the form

$$T(x) - T_c = \frac{q}{2kt} (hx - x^2) \quad (30)$$

where q is anode heat flux = 1.79 W/cm^2 ; k is anode thermal conductivity which for copper is $3.77 \text{ W/cm}^\circ\text{C}$; and x is distance from a coolant tube. The maximum temperature difference is at mid-span, $x = h/2$,

$$T_m - T_c = \frac{q}{8k} \frac{h^2}{t} \quad (31)$$

If channel spacing is 1.0 cm the temperature uniformity requirement Eq. (29) is satisfied by Eq. (31) for a coolant passage diameter of 0.23 cm.

7. Heat Exchanger Performance Requirements

The heat exchanger shown in Figure 57 at the downstream end of the flow channel serves the purpose of removal of deposited electrical energy and flow dissipation energy from the gas stream.

The heat exchanger is potentially a major contributor to flow-loop power requirements but this is somewhat alleviated by increasing the flow entry area as for example in Figure 57. Heat exchanger effectiveness is controlled primarily by the ratio of flow length to a transverse characteristic dimension, hydraulic diameter. Pressure drop, $(p_i - p_e)$, hence flow power is controlled primarily by this ratio times the flow speed to the third power. Heat exchanger performance is correlated with the following expression,

$$\frac{p_i - p_e}{\frac{1}{2} \rho u_m^2} = 4f \frac{\ell}{d_h} = N P_r^{2/3} \ln \frac{T_i - T_w}{T_e - T_w} \quad (32)$$

where ρ is gas density; u_m is average gas speed at the minimum heat exchanger flow cross section; ℓ is heat exchanger length in the flow direction

$$d_h = \frac{4A_f}{A_w} \quad (33)$$

is the hydraulic diameter; A_f is the minimum flow cross section; A_w is heat exchanger surface area; P_r is Prandtl number = $c_p \mu / k$. Heat exchanger effectiveness, S , is a measure of the degree of equilibration of the gas to wall temperature, T_w , in transit through the heat exchanger,

$$S = \frac{T_i - T_w}{T_e - T_w} \quad (34)$$

The friction factor f is weakly dependent on Reynolds number in turbulent flow. The heat exchanger efficiency, in terms of effectiveness per unit power expenditure at fixed flow conditions, is proportional to N^{-1} , which is also weakly dependent on Reynolds number. This parameter N has a value of 2.0 in Reynolds analogy between heat transfer and pressure drop for unseparated flow, therefore this value is viewed here as ideal lower limit.

Flow power is given as

$$P = \dot{V}(p_i - p_e) \quad (35)$$

where \dot{V} is the volumetric flow rate $= u_i A_i$; u_i is HX entry flow speed and A_i is the entry flow cross section. It is convenient to combine Eqs. (32) and (35) in the following arrangement,

$$P = \dot{V}^3 A_c^{-2} \left(\frac{A_c}{A_i} \frac{N}{\sigma} \right)^2 \left(\frac{\rho}{2} P_r^{2/3} \right) \ln S \quad (36)$$

where σ is the ratio A_f/A_i and A_c is flow cross section in the laser cavity. The term $(N/\sigma)^2$ is primarily controlled by heat exchanger geometry and to a weaker extent by Reynolds number, and the term $(\frac{\rho}{2} P_r^{2/3})$ is a property of the gas. In this form one sees that a fixed flow rate, \dot{V} , cavity area A_c and fixed HX effectiveness, S , the flow power is proportional to the product of geometrical features $\left(\frac{A_c}{A_i} \frac{N}{\sigma} \right)^2$.

A comparison of three types of heat exchangers was made on the basis of this product: (1) fin/tube, (2) staggered, bare, round tubes, and (3) aligned, flattened tubes.⁽²⁵⁾ In the hot chemical reactive environment of the $HgBr_2$ laser, special attention must be given to soldering, brazing and degree of complexity of geometrical forms. Since these three types of heat exchangers are fabricated with a minimum amount of soldering or brazing, and since they are assembled from preformed flat and cylindrical stock, they appear well suited to the present application. On the basis of effectiveness, S , the fin tube heat exchangers are preferred, provided their fabrication features are compatible with the laser environment. If the fin tube class were not compatible with the laser environment, flattened tubes, which are of much simpler construction, may be a reasonable alternative if accompanied by increased inlet area. For present design consideration

25. Kays and London, Compact Heat Exchangers, McGraw Hill, New York, 1955.

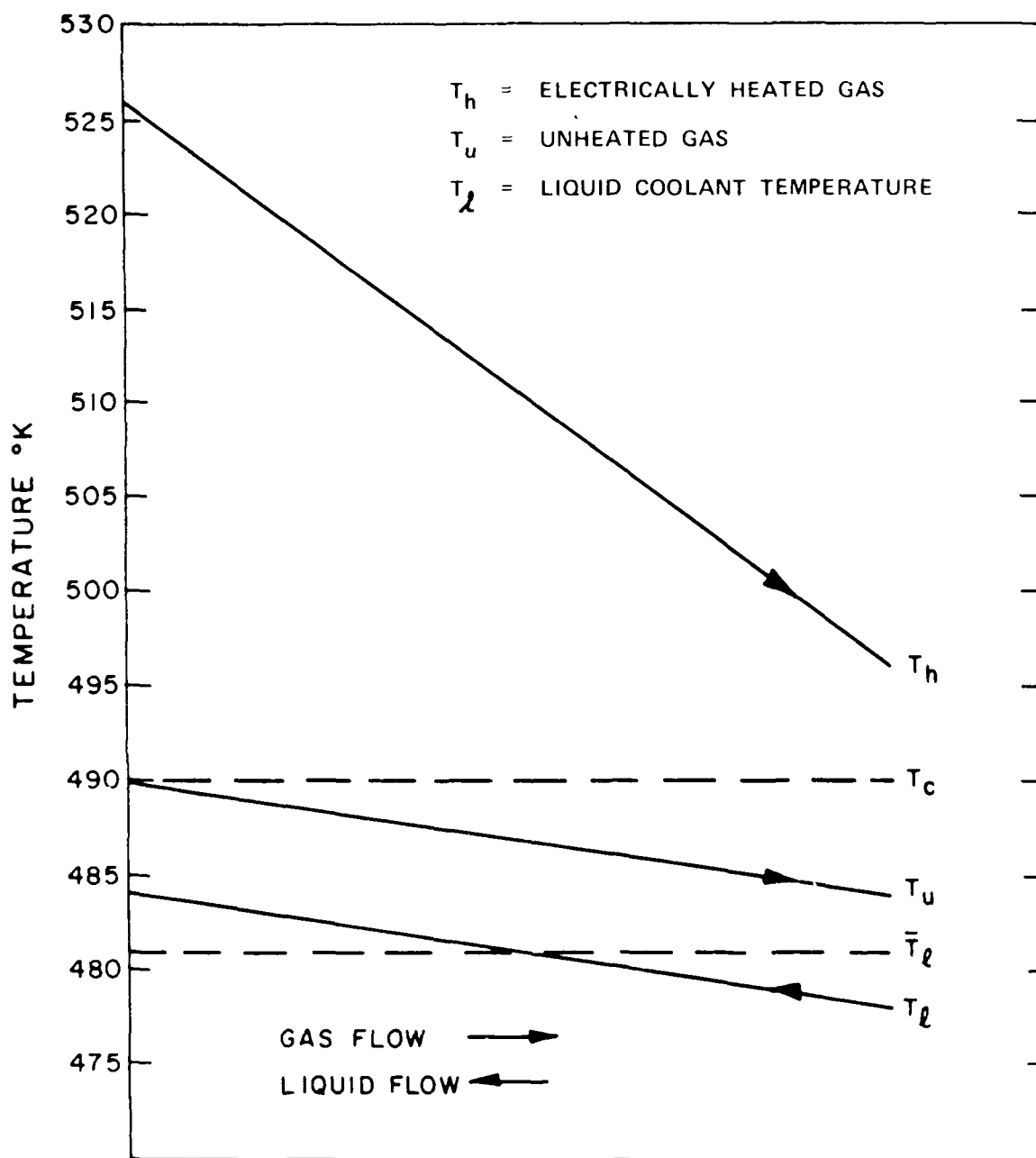
the fin tube unit 8.0-3/8 T^[25] was selected with an inlet area to cavity flow area ratio of 4.0. This area ratio was selected after design by iteration of the entire flow loop, with consideration given to the trade-off between large inlet area and achievable uniformity of flow over this inlet. Consideration was also given to device compactness and to the fraction of flow-loop pressure drop attributed to diffuser and heat exchanger.

The electrically heated gas temperature, after pressure relaxation, exceeds initial cavity temperature by 36.4°C (Table 4). If electrically heated and unheated gas slugs are specified to exit the heat exchanger at $T_c + 6^\circ\text{C}$ and $T_c - 6^\circ\text{C}$, respectively, the the average wall temperature and HX effectiveness can be simply calculated as, $T_w = T_c - 9^\circ\text{C}$ and $S = 3.0$. The coolant liquid temperature rise in a counter flow heat exchanger is independently selected as 6°C to provide the HX temperature maps of figure 61.

8. Flow Conditioning

Flow-loop design is based on (1) efficient operation for low power demand, (2) compactness for ultimate space based application, (3) compatibility with the hot reactive laser gas environment, and (4) reliability of loop components and peripheral equipment for long lived, maintenance free operation. The loop design must, of course, satisfy the cavity medium homogeneity requirements discussed previously. Design was carried out in an iterative fashion to arrive at a balance between compactness and flow efficiency. Potential sources of large head losses, such as the diverging flow section downstream from the cavity and heat exchanger, received special consideration to design detail to bring these losses into balance. This section discusses the basis for design features which are shown in Figure 57.

Cavity geometry and flow conditions of Table 4 provide a flow rate and cavity dynamic head of



J9211

Figure 61. Gas and Liquid Average Temperature vs Distance Through the Heat Exchanger

$$\dot{V} = 0.720 \text{ m}^3/\text{sec} \quad (37)$$

$$q_c = \frac{1}{2} \rho u_c^2 = 350 \text{ n/m}^2$$

it is useful at the outset to estimate the magnitude of flow-loop power in relation to overall device power requirements. For this purpose consider a fan efficiency of $\eta_f = 70\%$, an electric motor efficiency of $\eta_m = 85\%$ and a mechanical transmission (i.e., bearing and seal efficiency) $\eta_b = 90\%$. Then, for each flow-loop pressure drop of one cavity dynamic head, the fan electrical power required is

$$P = \eta_f^{-1} \eta_b^{-1} \eta_m^{-1} \dot{V} q_c = 470 \text{ W} \quad (38)$$

Of the total available power of 20 kW, one-half is given to the discharge. If 20% of the remaining 10 kW is given to all aspects of the flow-loop, the total loop pressure drop should be safely designed to less than three cavity dynamic heads. With care in design of critical components the compact flow-loop of Figure 17 is compatible with this goal, and hence it provides a fair balance between flow efficiency and system compactness.

a. Cavity Diffuser Design Criteria

The cavity diffuser is incorporated in the downstream diffuser as shown in Figure 17. It serves the purpose of partial recovery of cavity dynamic pressure and of providing improved uniformity in flow distribution to the entry of a heat exchanger of large area ratio, $D_{HX} = A_1/A_c = 4.6$. The perforated diffuser wall diverges from the downstream edge of the discharge anode. Space limitations allow an entrance of the solid wall to begin where shown in Figure 17.

The perforated wall divergence angle is 3.5° , which is an established value for maintenance of attached flow in conventional diffusers. The region of performance of this diffuser is shown in the performance map of Reneau, et al.,⁽²⁶⁾ which is presented here as Figure 62. The ratio of downstream muffler length l_M to cavity length in the pump direction l_p is 6.0. Boundary layer suction at the upstream edge of the anode was discussed above as a means of maximizing the utilization of the discharge region for laser energy extraction. The renewed boundary layer growth reaches a displacement thickness of 0.3 cm at the diffuser inlet, to provide the ratio $\delta/l_p = 0.04$. The two lines a-a in Figure 62 show that the boundary of the zone for flow attachment depends on this ratio and the design point is well within this zone. Tests which formed the basis of Figure 62 showed little sensitivity to Reynolds number over a range of from 1.5×10^3 to 5×10^4 based on the length l_p . These results, therefore, appear valid for the present case where $Re = 10^5$.

The area ratio of flow exit to inlet, for the perforated wall segment is 1.37. Pressure recovery through this diffuser is obtained by interpolation of measurements by Reneau, et al.,⁽²⁶⁾ as

$$C_p = \frac{p_2 - p_c}{q_c} = 0.4 \quad (39)$$

where p_2 is diffuser exit static pressure, and p_c and q_c are cavity static and dynamic pressures. If one assumes the total loss of surviving dynamic pressure at the diffuser exit, one obtains a stagnation pressure loss

26. Reneau, L.R., Johnston, J.P., Kline, S.J., "Performance and Design of Straight, Two-Dimensional Diffusers," Journ. of Basic Eng., March, 1967.

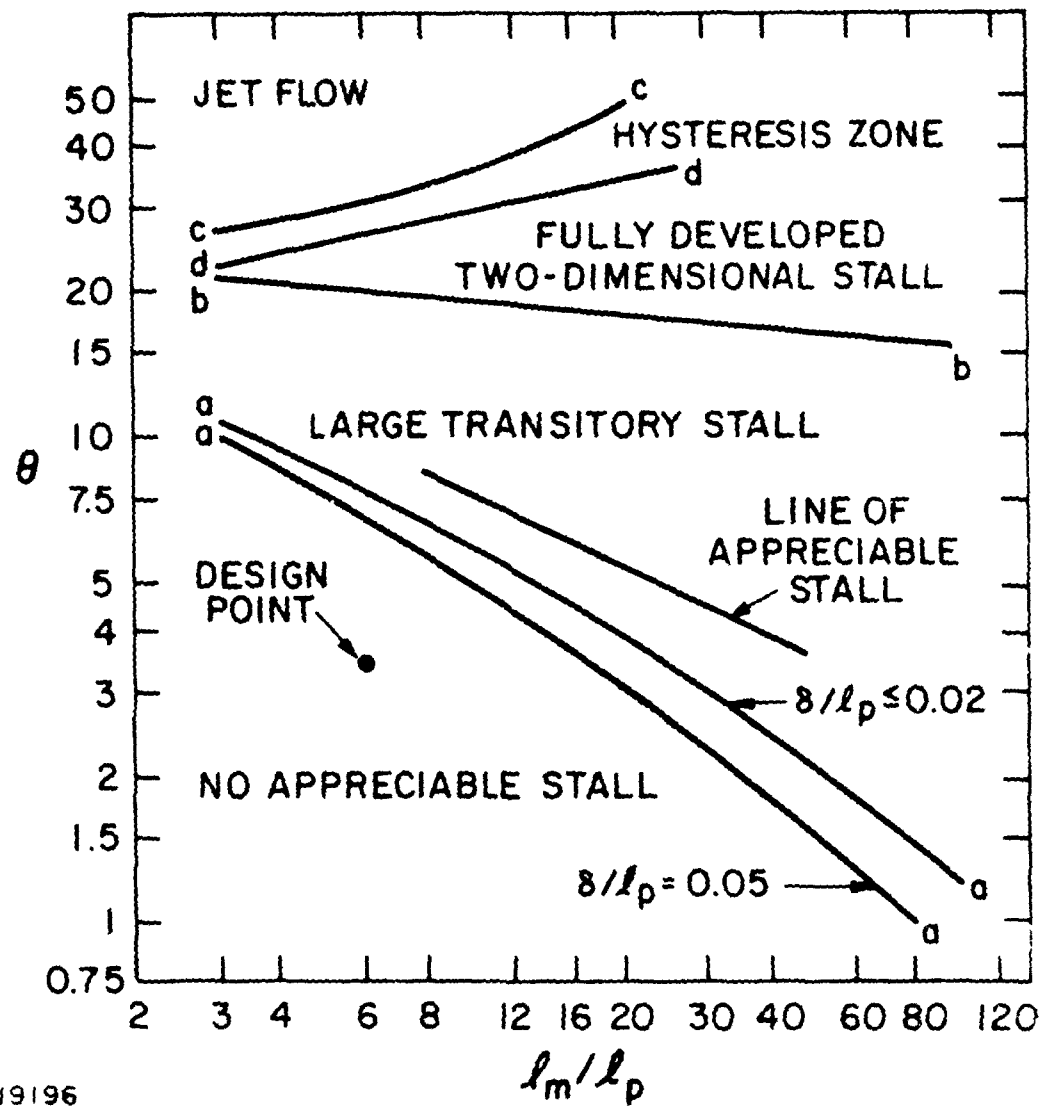


Figure 62. Flow Regimes in Straight-Wall, Two-Dimensional Diffusers

The design entry area is four times the cavity flow cross section, $D_{HX} = 4.0$. The pressure drop through the heat exchanger is obtained from Eq. (32) using the characteristics of HX type 8.0 - 3/8 T^[25] and the selected effectiveness $S = 3$ in Eq. (34).

$$\frac{\Delta p}{q_c} = \frac{\Delta p}{q_m} \frac{q_m}{q_i} \frac{q_i}{q_c} = \frac{\Delta p}{\frac{1}{2} \rho u_m^2} \left(\frac{u_m}{u_i} \frac{u_i}{u_c} \right)^2 \quad (41)$$

$$\frac{\Delta p}{q_c} = \frac{\Delta p}{\frac{1}{2} \rho u_m^2} (\sigma D_{HX})^{-2} = \frac{8.8}{D_{HX}^2} = 0.55$$

The length of the heat exchanger in the flow direction is obtained from Eq. (32) as

$$L = 24.6 d_h = 8.9 \text{ cm} \quad (42)$$

c. Transition Sections, Turns and Return Leg

Downstream from the heat exchanger the flow passes through a transition section from rectangular to circular flow cross section. The circular cross-sectional area is selected to be twice the cavity flow cross section, $D = 2$. This choice is based again on iterative design with selection based on a balance between loop compactness and flow power. This transition is followed by a vaned turn as shown in Figure 57. Vanes are inserted to control fine scale mixing as discussed in Section III-E-8-b and also to provide uniform flow to the driving fan. At the low operating Reynolds number of 4.4×10^4 based on vane chord, flow separation is anticipated, hence vanes will contribute little to gain in pressure recovery through the turn. Consequently, the pressure loss through the subsequent vaned turn, i.e., each predicted to equal one local dynamic head,

$$\frac{\Delta p}{q_c} = \frac{\Delta p}{q} \frac{q}{q_c} = \frac{\Delta p}{q_c} \cdot \frac{1}{D^2} = 0.25 \quad (43)$$

The contracting transition suffers little head loss so it is simply included with return leg wall losses. Wall losses are estimated on the basis of fully developed pipe flow with a diameter of 36 cm, a Reynolds number of 2.6×10^5 and a length of 2.0 m

$$\frac{\Delta p_o}{q_c} = 4f \frac{L}{d} \frac{1}{D^2} = \frac{0.11}{D^2} = 0.03 \quad (44)$$

The diverging transition contains splitter plates to provide a uniform distribution of flow to the plenum located upstream from the velocity stabilizer. These splitter plates serve to provide uniform entry conditions to the velocity stabilizer but do not aid in pressure recovery through the transition. Consequently, one entry dynamic head is assumed to be lost in this transition

$$\frac{\Delta p_o}{q_c} = \frac{1}{D^2} = 0.25 \quad (45)$$

d. Fan and Fan Diffuser

A specific fan selection cannot be made until a detailed system design is completed. For present flow power considerations a vane-axial fan of ~ 30 cm (12 in.) diameter may be fabricated to meet present flow rate and pressure head requirements with an associated fan efficiency of $\eta_f = 70\%$. Uniform flow entry is provided by vanes in the upstream turn followed by a straight flow length of one blade diameter and a slight flare at the fan entry. Efficient fan operation requires that it be followed by a fan diffuser. If the fan inlet area is 63% of the approach area in the

circular duct as in Figure 57, the entry dynamic pressure is 2.5 times that of the approach flow

$$q_i = 2.5q = 2.5q_c \frac{1}{D^2} = 0.63q_c \quad (46)$$

For reference it is noted that with no fan diffuser one may suffer stagnation pressure loss of 0.63 cavity dynamic heads. A diffuser divergence total angle of 5.5° was chosen for the outer diffuser wall, and a nacelle taper of 4.9° was chosen with an abrupt truncation at the entry to the downstream turn (see Figure 57). This configuration is appropriate to maintenance of attached flow and one may conservatively estimate the diffuser head loss at 40% of the fan inlet dynamic pressure, i.e.,

$$\frac{\Delta p_o}{q_i} = 0.4$$

or

$$\frac{\Delta p_o}{q_c} = \frac{\Delta p_o}{q_i} \frac{q_i}{q} \frac{q}{q_c} = \frac{1.0}{D^2} = 0.25 \quad (47)$$

e. Velocity Stabilizer

A flow impedance is inserted at the upstream end of the converging nozzle for purposes of suppressing large-scale turbulence and providing flow to the cavity with uniform velocity. This is indicated at a heat exchanger in Figure 57 so that it may provide fine scale control, if necessary, to cavity temperature level and uniformity. For present purposes it may be viewed simply as an impedance which introduces a pressure loss of three entry dynamic heads,

$$\frac{\Delta P}{q_c} = \frac{P}{q_1} \frac{q_1}{q_c} = \frac{3}{D_{VS}^2} \quad (48)$$

where D_{VS} is the flow area ratio between stabilizer inlet and cavity. This is also the nozzle area ratio, which is chosen as 2.5, again on the basis of balance between system compactness and flow-loop power.

f. Nozzle, Upstream Muffler and Boundary Layer Suction

The nozzle is formed by the arcs of two circles of radius ratio equal to the area ratio of 2.5. The ratio of inlet height to length is 3/4. Parallel entry and exit flow and arc tangency at the junction complete the design specification. Head losses in the nozzle are insignificant.

This nozzle geometry provides sufficiently rapid expansion to restart the boundary layer at its exit. Head loss in the upstream muffler is determined by assuming smooth wall boundary layer growth on the solid walls and rough wall boundary layer growth along the perforated wall, or approximately

$$\frac{\Delta P}{q_c} = 4 \bar{C}_f \frac{l_m}{d_h} = 4 \cdot \frac{3}{2} C_f \frac{l_m}{d_h}$$

where

$$d_h = 2 \frac{P_o}{\left(\frac{P}{P_o} + 1\right)} = 13.3 \text{ cm} \quad (49)$$

$$C_f = 0.2 \delta$$

where δ is the smooth wall displacement thickness at the cavity cathode, given in Section III-E-5 as 0.64 cm. Thus,

$$\frac{\Delta p}{q_c} = 0.06 \quad (50)$$

A portion of the boundary layer from the upstream muffler wall will be removed to maximize the utilization of electrically heated gas in contributing to laser energy. This removed gas, which is 3.5% of the total cavity flow, is drawn to the fan inlet by the existing static pressure drop. Power required to achieve this is thus a fixed portion, 3.5%, of the total fan power and appears as a multiplier $\sigma_{BL} = 1.035$ in the final determination of power requirements.

g. Summary

Loop stagnation pressure losses are summarized in Table 6 in forms with unspecified values of heat exchanger, return leg, and velocity stabilizer area ratios, and in forms with design values of 4.0, 2.0 and 2.5, respectively. Small losses to return leg walls and upstream muffler have been omitted. A scaling relation is seen to result

$$\frac{\Delta p_o}{q_c} = 0.6 + \frac{8.8}{D_{HX}^2} + \frac{4.0}{D^2} + \frac{3.0}{D_{VS}^2} \quad (51)$$

This relation was developed early in the design study and was used to provide the balanced design of component losses shown in the table.

The design total stagnation pressure loss

$$\Delta p_o / q_c = 2.63 \quad (53)$$

TABLE 6. ELEMENTS OF FLOW-LOOP STAGNATION PRESSURE LOSS

	$\Delta P_o/q_c$	$\Delta P_o/q_c$
Diffuser	0.6	0.60
Heat Exchanger	$8.8 D_{HX}^{-2}$	0.55
Vaned Turns (2)	$2.0 D^{-2}$	0.50
Expansion Transition	$1.0 D^{-2}$	0.25
Fan Diffuser	$1.0 D^{-2}$	0.25
Velocity Stabilizer	$3.0 D_{VS}^{-2}$	<u>0.48</u>
Total		2.63

combines with Eq. (38) for a determination of loop power

$$P = \eta_f^{-1} \eta_b^{-1} \eta_m^{-1} \dot{V} q_c \frac{\Delta p_o}{q_c} \sigma_{BL} \quad (53)$$

where $\sigma_{BL} = 1.035$ as discussed in Section III-E-8-f. Practical efficiencies for fan, drive train and motor are 70%, 90% and 85%, respectively. The design value for electric power demand to drive the flow-loop is then,

$$P = 1.29 \text{ kW} \quad (54)$$

Additional power requirements to drive the liquid coolant loop are discussed below.

9. Fan and Drive Train Requirements

The design loop pressure drop of Eq. (52) is referenced to cavity pressure by

$$\frac{\Delta p}{p} = \frac{\Delta p}{q_c} \frac{q_c}{p} = \frac{\Delta p}{q_c} \frac{\gamma}{2} M_c^2 = 2.63 \frac{\gamma}{2} M_c^2 \quad (55)$$

Operating conditions given in Table 4 provide a cavity Mach number $M_c = 0.034$ and volumetric flow rate $\dot{V} = 0.746 \text{ m}^3/\text{sec}$. Thus,

$$\frac{\Delta p}{p} = 2.5 \times 10^{-3} \quad (56)$$

These operating requirements are referenced to ambient condition and standard English operating units for fan design as

$$\dot{V} = 1580 \text{ cfm (cubic feet per minute)} \quad (57)$$

$$\Delta p = 1.0 \text{ in. w (inches of water)} \quad (58)$$

Operating speed regime may be obtained from the following performance correlation

$$\frac{\Delta p}{p} = K \gamma M_t^2 \quad (59)$$

where K is the fraction of peak head at which blade stall occurs and M_t is blade tip Mach number. A choice of $K = 0.05$ and Eq. (56) provide a tip Mach number from Eq. (59) and a tip speed from the laser gas sound speed of 412 m/sec.

$$M_t = 0.173 \quad u_t = 71.3 \text{ m/sec} \quad (60)$$

If the blade disc outside diameter is 30 cm the corresponding rotational speed is

$$f = 4540 \text{ rpm} \quad (60)$$

Specific fan selection cannot be made until flow-loop design is finalized. However, fabrication of vane-axial fans for military and space application predict a fan efficiency in excess of 70% for the above operating conditions.

10. Liquid Coolant Loop Design

Silicone heat transfer fluids meet present operating temperature requirements and easily meet current space application life-time requirements when operated in the absence of air. They are also very compatible with all conventional materials used in coolant loops. Candidate materials are Dow-Corning products SYLTHERM [®] -444 and DC550. Analysis here is based on the properties of type 444 fluid.

The coolant loop is designed to remove total electrical power deposited in the gas and in the structure as well as flow power dissipated in the flow loop. Total dissipated power from electron gun, discharge and flow dissipation are listed in Table 7.

TABLE 7. HEAT LOAD SOURCES AND DISTRIBUTION

SOURCES	
E-Beam	$P_e = 2.25 \text{ kW}$
Discharge	$P_d = 9.50 \text{ kW}$
Flow	$P_f = 1.00 \text{ kW}$
Total	$P_t = 12.75 \text{ kW}$

DISTRIBUTION (REMOVAL)	
Foil	180 W
Discharge Cathode	855 W
Discharge Anode	448 W
Upstream Muffler	1100 W
Exterior Walls	450 W
Heat Exchanger	9687 W
Total	12.75 kW
External Heat Exchanger	12.30 kW

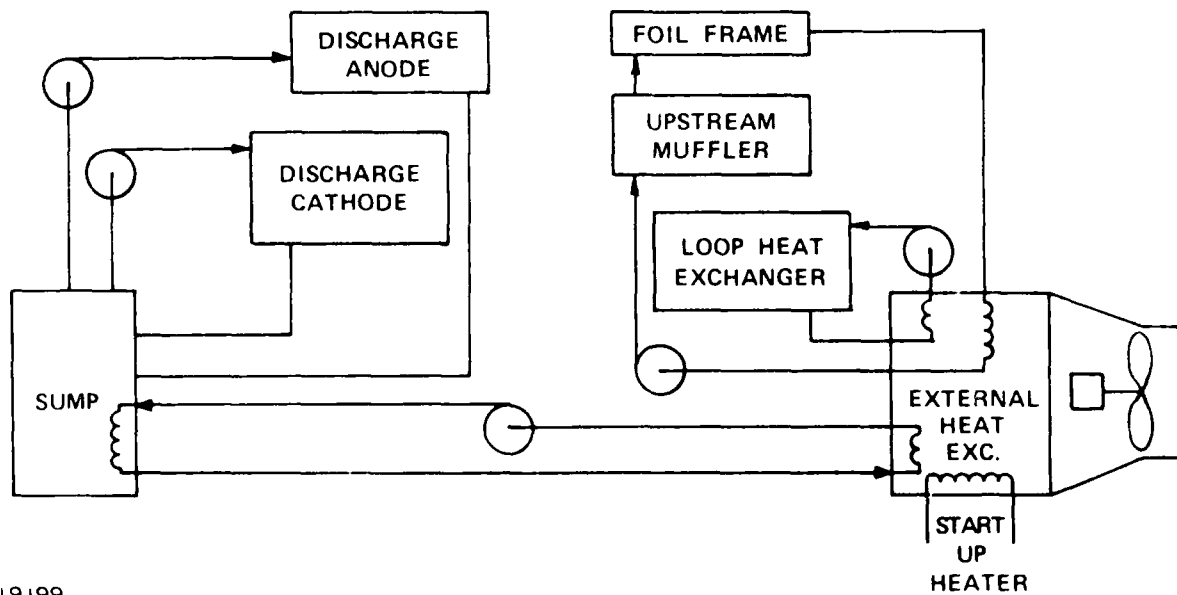
This deposited power will be removed by cooling at various locations in amounts listed in Table 7. Component locations are shown in Figure 57 with exception of the upstream muffler HX and external HX. Wall temperature requirements for various elements, discussed in Section III-E-4, have varying tolerances which are best met by independent element flow and temperature control as shown schematically in Figure 63.

Cathode and anode wall temperature constraints demand accurate liquid temperature control. This will be accomplished with a reservoir (sump) whose temperature will be controlled by wall cooling and regulated heat exchange with the external HX. Additional control will be provided by separate regulation of liquid flow rates to cathode and anode. The higher liquid inlet temperature to the anode as compared to the cathode will be accomplished by anode supply line cooling.

The upstream muffler wall must be held to within 0.6°C of cavity temperature. The muffler heat exchanger will be located in the muffler backing volume, hence liquid temperature control is more relaxed. Wall temperature control will be achieved by regulated liquid flow rate based on wall temperature monitoring.

The loop heat exchanger will have regulated liquid flow and cavity gas temperature will be the control monitor. The external heat exchanger will be air cooled in the breadboard design. The small fan required is not considered in the power budget since it will be replaced by radiation cooling the space application.

Pump power requirements for the liquid demand of each element have been computed on the basis of flow demands and specific element geometries. Geometric details of elements have been discussed in Section III-E-4. The major power demand is the cooling of the discharge cathode tubes. This is a result of the load requirements, the ΔT constraint and the small tube inside diameter of 0.071 cm over the 4.0 cm long region of e-beam operation. A low value of pump efficiency of 33% is anticipated since flow throttling is the basis of temperature control. Drive motors of



J9199

Figure 63. Liquid Coolant Loop Operation Schematic

such small power demand are realistically expected to have efficiencies of $\sim 75\%$. The design liquid loop electrical power requirements are

$$P = \eta_p^{-1} \eta_m^{-1} \times 68.5 \text{ W} = 274 \text{ W} \quad (1)$$

11. Flow-Loop Design Summary

Allowed phase errors at the output aperture have been assessed for specified laser targeting requirements. These allowed errors have been budgeted equally between optics distortions and cavity medium inhomogeneities. Cavity medium inhomogeneities were budgeted equally between thermal distortions and pressure wave distortions. Flow-loop thermal conditions and pressure wave suppression designs were carried out on this basis. Predicted overall cavity inhomogeneities are 64% of that budgeted to meet performance requirements. This implies that the optical axis may be scaled up by a factor of 2.5 while still remaining within the allowed budget.

In addition to cavity medium homogeneity requirements and device performance requirements, the flow-loop design approach addresses (1) efficient operation for low power demand, (2) compactness for ultimate space based application, (3) compatibility with the hot reactive laser gas environment, and (4) reliability of loop components and peripheral equipment for long lived, maintenance free operation.

Flow-loop electrical power demand for the considered compact loop design is predicted to be

$$P_f = 1.29 \text{ kW} \quad (62)$$

Liquid coolant flow power is conservatively predicted to be

$$P_{\ell} = 0.27 \text{ kW}$$

(63)

Total flow-loop electrical power demand of 1.56 kW is 15.6% of the electrical power demanded by the discharge. An increase in the cavity scale in the flow direction from 4.0 to 6.0 cm is predicted to require a total flow power which is ~ 20% of that for the discharge.

F. OPTICS AND INJECTION LASER

1. Approach

The system must have a spectral width of $< 1 \text{ \AA}$, average power of 200 W, beam quality better than 10 times the diffraction limit, and efficiency $> 1\%$. A free running HgBr laser has a spectral width of about 6 \AA , hence spectral control is necessary. The beam quality requirement dictates the use of an unstable resonator.

An unstable resonator generally has energy moving outwards from its axis in such a way that the light cannot be collimated in both directions. The angular diversity that occurs in such devices makes the normal frequency selective devices impractical. The problem might be solved by using a ring resonator with unidirectional flow of energy; but that approach is rejected because of the extra complication and loss of efficiency.

A practical system can be configured either as a Master Oscillator followed by a Power Amplifier (MOPA), or as a master oscillator followed by an Injection Locked Oscillator (ILO). The ILO approach has two major advantages. Firstly, the injected pulse may be much shorter than the final output pulse, and secondly much higher amplification is available by this route. The success of the injection approach does rely on the medium having sufficient homogeneous broadening. Results of the injection experiments during Phase I of this program (see Section II-A-2-o) confirm the homogeneous broadening. The approach has been proven to give high amplification without sacrifice of beam quality, using a wide variety of active media. (27-29) It has been

27. Gibson, A.J. and Thomas, L., "Injection-Locking of a Flashlamp-Pumped Dye Laser Without Longitudinal Mode Matching," J. Phys. D: Appl. Phys. (Great Britain, Vol. 11, p. 159, 1978.
28. Pacala, T.J. and Christensen, C.P., "Control of XeF Laser Output by Pulse Injection" Appl. Phys. Lett. 36 (8), p. 620, April 1980.
29. Buczek, V.J., Freiberg, Robert J. and Skolnick, M.L., "Laser Injection Locking: Proc. IEEE Vol. 61 No. 10 p. 1411, October 1973.

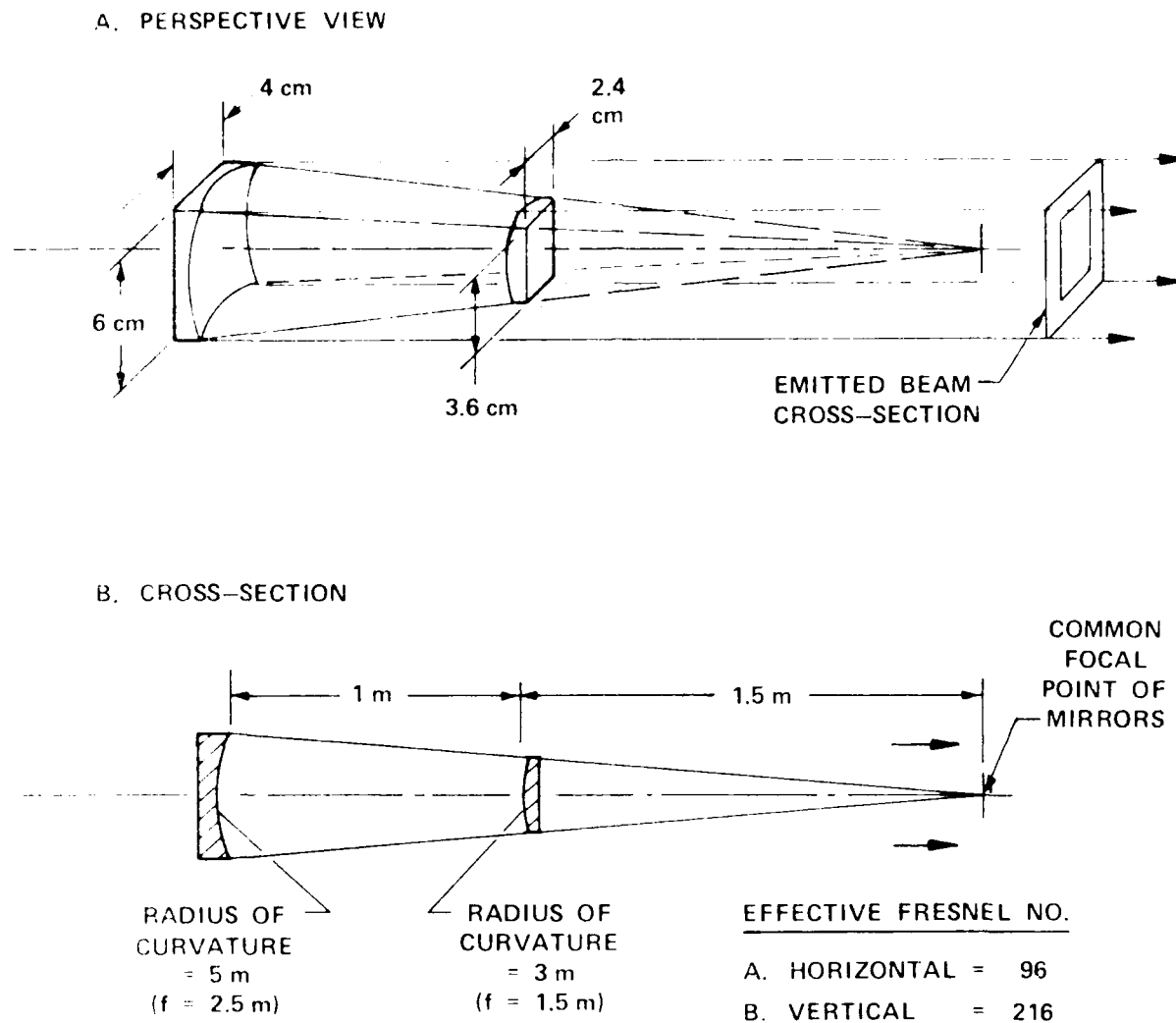
demonstrated to work well when injecting unstable resonators. (30-31) The injection reduces the buildup time of the injected oscillator with a resulting increase in output energy.⁽³²⁾ A few watts of injected power are ample to give good spectral locking of the type of laser proposed, but the discussion of the next section will demonstrate the desirability of injecting considerably more power from this master oscillator, to reduce buildup time in the ILO.

2. Resonator for the Injection Locked Oscillator (ILO)

Analysis of the laser cavity trade-offs leads to choice of an unstable resonator of length 1 m, and transverse dimensions of 6 by 4 cm. The active medium will be 62.5 cm long by 6 by 4 cm. The requirements are met by the confocal unstable resonator shown schematically in Figure 64. It has a magnification ratio of 1.67 and a corresponding feedback of 36%. It uses mirrors with radii of curvature of 5 and 3 m. Since it has confocal geometry it will have a collimated output, and thus utilize the medium efficiently.

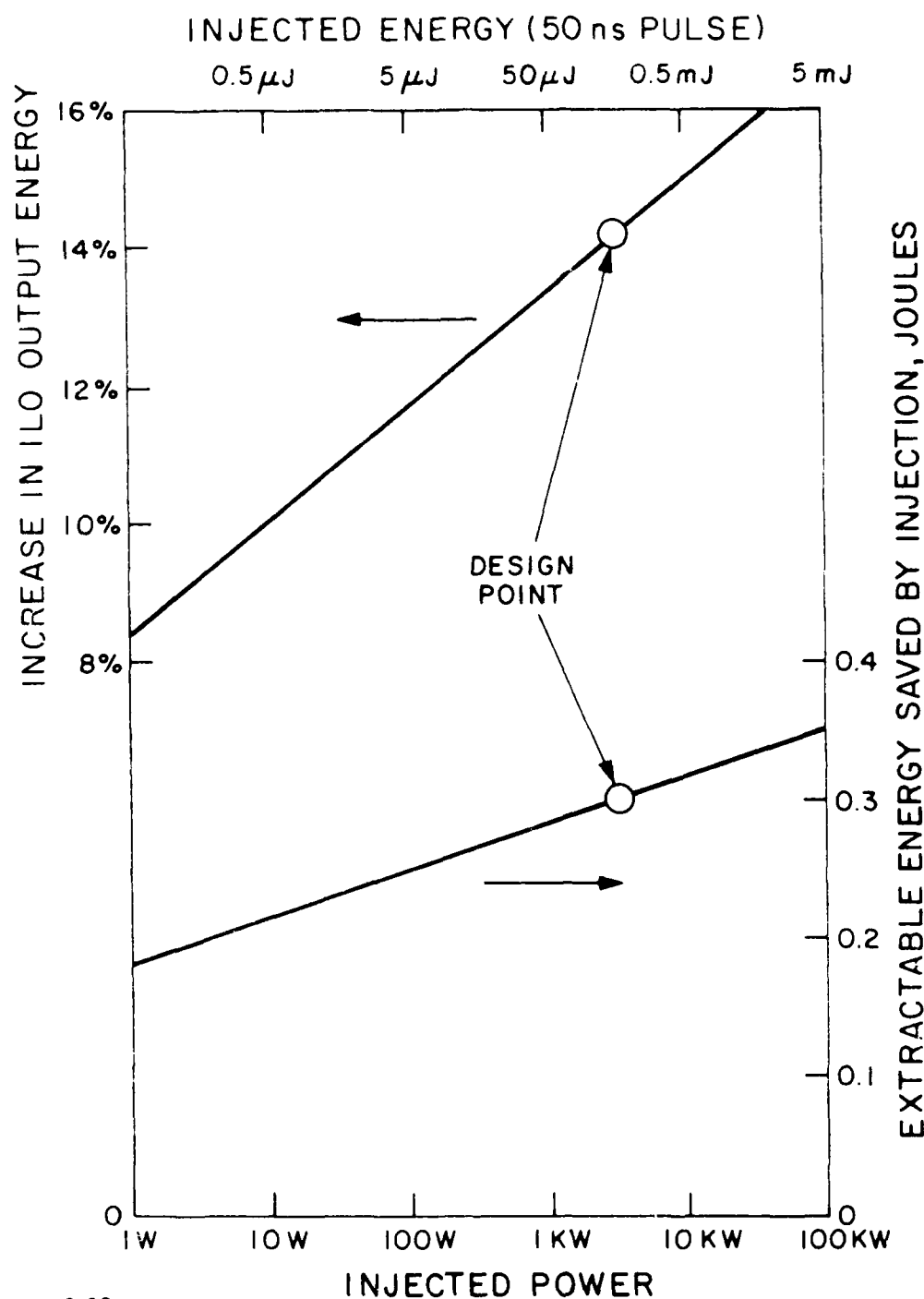
The transient buildup of the lasing is discussed in Appendix A. The buildup time of this ILO without injection, if restricted to 1 Å spectral width, would exceed 50 ns. It is shown that injection of 3 kW will save 35 ns of this buildup time. Based upon the nominal 250 ns pulse, this reduction in the delay time will add 13% to the energy of the output, as well as giving spectral control without adding any lossy elements in the resonator. The savings in buildup time and consequential increase in output of the laser, for various values of injected power, are listed in Table A-1 and plotted in Figure 65.

30. Park, Y.K., Guiliani, G., and Byer, R.L., "Stable Single-Axial-Mode Operation of an Unstable-Resonator Nd:YAG Oscillator by Injection Locking," Optics Letters, Vol. 5, No. 3, p. 96, March 1980.
31. Goldhar, J. and Murray, J.R., "Injection-Locked, Narrow-Band KrF Discharge Laser Using an Unstable Resonator Cavity," Optics Letters, Vol. 1, No. 6, p. 199, December 1977.
32. J. Goldhar, J., Rapoport, W.R. and Murray, J., "An Injection Locked Unstable Resonator Rare-Gas Halide Discharge Laser of Narrow Linewidth and High Spatial Quality," IEEE Journal of Quantum Electronics Vol. QE-16, No. 2, February 1980.



J9148

Figure 64. Proposed Resonator for Unstable ILO (Schematic)



J9162

Figure 65. Increased Output of ILO vs. Injected Power

The injection must span the critical time during the pumping cycle when the gain first appears and the transient buildup commences. Light injected before this time, or after, will be ineffective. The system can be regarded as behaving like a multipass power amplifier immediately after the injection. The beam quality of the initial output is dominated by the beam quality of any portion of the injected light that sufficiently matches the mode-structure of the unstable resonator to survive in the resonator long enough to be amplified to high level before exiting. Thereafter the feedback will take over as the source of the lasing, and the mode characteristics of the unstable resonator will impress themselves more and more strongly. At this point any further injection will be insignificant compared with the energy already circulating in the resonator.

One might question whether the optical lengths of the master-oscillator and the ILO should be precisely matched, so that the longitudinal modes are correspondingly matched in frequency. The longitudinal intermode frequency interval for these resonators will be about 150 MHz, hence there will be about 500 such modes overlapping. If the resonators are not closely matched, there will be overlap between a sufficient number of these modes for successful injection. However there is a more important consideration helping us, in that the round trip gain of the ILO is sufficiently high during the transient buildup time that the resonant properties of the ILO will not have a significant filtering action on the injected longitudinal modes during that portion of the cycle. The resonant properties of the ILO will become important later in the cycle when the active medium goes into saturation and the net round trip gain becomes unity, because only at that time will the fluxes in the successive passes have nearly equal intensities so that the interference effects become significant. In other words, the longitudinal matching is not a problem.

Clearly however the injected light must have the required spatial characteristics for surviving many passes of the ILO and

then emerging with the required beam quality. This problem will be addressed in the next section.

3. Injection Interface

The ILO will be injected through a coupling mirror that is shared between the master oscillator and the ILO, for maximum efficiency. Otherwise a large portion of the injecting laser's output would be lost by reflection on entering the ILO.

An inherent property of unstable resonators is that the light traveling in opposite directions does not repeat itself, whereas in a stable resonator the light does repeat itself. This presents a dilemma when trying to match the transverse modes from a stable resonator into those of an unstable one.

This problem has been addressed by Goldhar et al.⁽³²⁾ They have developed a recipe for ensuring satisfactory spatial mode matching when injecting an unstable resonator from a stable resonator using a shared mirror. Given that the mode of the stable resonator has to have its wavefront match the surface of the shared mirror, the recipe requires choosing the size of the injected spot such that when it reaches the opposite mirror its radius of curvature R closely matches the geometric wavefront of the expanding mode of the unstable resonator. They verified experimentally that this does work, achieving good injection locking and near diffraction limited output from the injected laser.

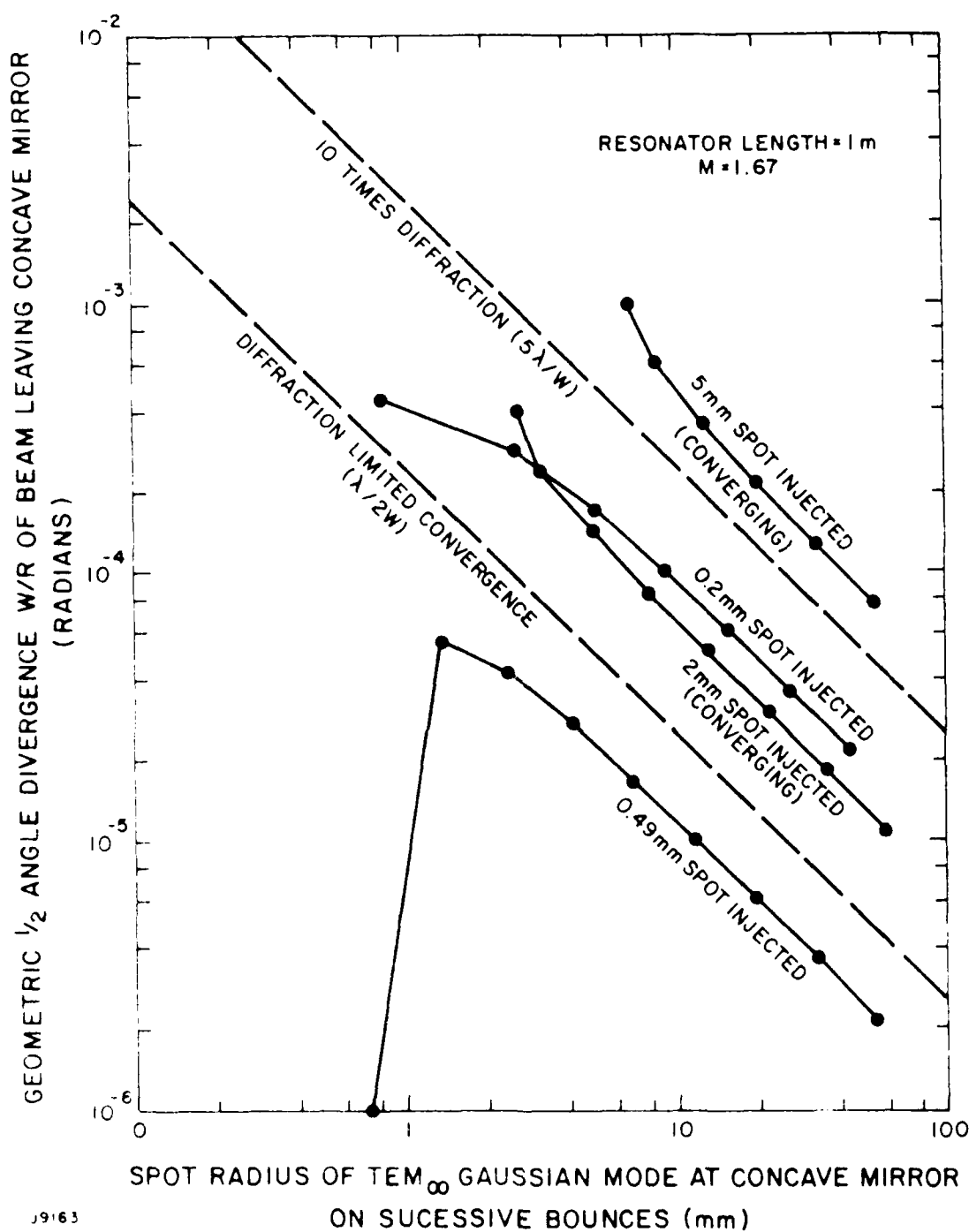
When this recipe is applied to the proposed resonator of Figure 64, it yields an optimum spot radius w , for the lowest order Gaussian mode of the stable resonator at the shared mirror, to be 0.49 mm. We have analyzed the subsequent evolution of such a fundamental mode, after injection, using the Kogelnik and Li formulation for the propagation of such a mode.⁽³³⁾ The beam was

33. Kogelnik, H. and Li, T., "Laser Beams and Resonators," Applied Optics. Vol. 5, No. 10, p. 1550, October 1966.

tracked after repeated bounces from the opposing mirrors until it reached a radius where it would exit from the unstable resonator. The result is plotted as the lowest curve in Figure 66. The ratio w/R is plotted against the spot radius w for the propagating beam at the successive interactions with the mirror that is in the exit plane. This ratio w/R is the semi-angle of the geometric divergence of the beam. For comparison, the semi-angle of the diffraction limit, $\lambda/2w$, is plotted as a dashed line that appears immediately above the first plot. It is clear that a Gaussian beam injected through the shared mirror with a fundamental spot radius of 0.49 mm will indeed successfully inject the laser and result in an output beam that is very nearly diffraction limited.

Also plotted in Figure 66 are the results of a similar analysis of beams that are injected through the shared mirror with fundamental Gaussian spot radii of 2 and 0.2 mm. It can be seen that, although these have greater divergence than in the optimum situation, they will still emerge with less than 5 times diffraction limited divergence. The additional plot for a 5 mm Gaussian radius injected spot shows that it will have divergence approaching 20 times the diffractive limit. It is clear that, while a radius of about 0.5 mm is ideal, a factor of two either way is not too critical in this application, but a greater mismatch should be avoided.

The above analysis shows that if a fundamental Gaussian mode of about 0.5 mm spot radius is injected as described during the critical time when the gain is first appearing, then it will make multiple passes in the resonator, growing on each pass by the magnification ratio, until it emerges with much the same beam quality as that with which it entered (assuming no medium distortions). A higher order mode entering at the same place and with its wavefront matched to the same shared mirror, must likewise match the same wavefront curvature on the opposing mirror, and hence can be expected to expand in the same manner. It however will start with a larger diameter and hence will make a lesser number of passes



J9163

Figure 56. Divergence of Injected Gaussian TEM_{00} Mode as it Propagates in IL0

before it exits. Hence it will see less gain and be discriminated against. It follows that the light that first emerges from the injected oscillator will have a higher proportion of the energy in the lower order mode than that which was injected. Subsequently the spatial filtering action of the feedback mechanism will come into play, and the output will become more and more dominated by the characteristics of the unstable resonator (see Section III-k).

4. Master Oscillator for Injection

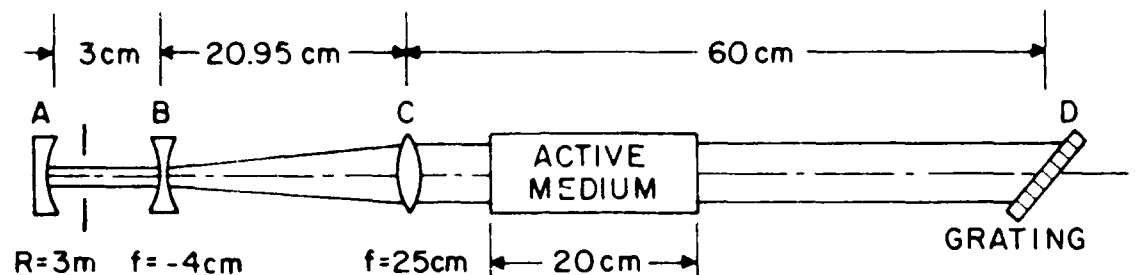
It now remains to design a suitable oscillator for providing the injection signal, having as its output mirror the shared one of 3 m radius of curvature. It should have a Gaussian fundamental mode of ~ 0.5 mm spot radius at this mirror.

A stable resonator which meets these objectives is shown schematically in Figure 67. The Kogelnik and Li type analysis⁽³³⁾ gives the parameters that are tabulated in Figure 67. The 0.52 mm spot radius at the shared mirror is a sufficiently good match to ensure successful injection, as shown in the preceding section. Further details of the design are discussed in Appendix B.

It is anticipated that an aperture of ~ 1.4 mm diameter, placed as indicated in the resonator, will allow sufficient modes to oscillate so that the laser is not too critical in its alignment, and yet will give a beam quality from this oscillator that is within two times the diffraction limit. Such details will finally be optimized experimentally.

5. Spectral Control

A diffraction grating will have adequate spectral selectivity to ensure a width of $< 1 \text{ \AA}$. It will use a substrate of Corning 13B or Schott Zerodur, which both have temperature expansion coefficient of $\sim 3 \times 10^{-8}/^\circ\text{C}$. This will ensure spectral stability over a temperature range $> \pm 100^\circ\text{C}$. It will need adjustment capability with a precision and stability of 2 arc sec to tune to the center of the HgBr line, and then maintain the tuning stable within 0.1 \AA . The development to spectral widths of 0.2 \AA



POSITION	A	B	C	D
TEM ₀₀ SPOT RADIUS	0.52 mm	0.52 mm	3.19 mm	3.19 mm
" " DIAM.	1.04 mm	1.04 mm	6.38 mm	6.38 mm

J9164

Figure 67. Proposed Master Oscillator for Injection ILO (Schematic)

or less (Appendix C) can be done either with a diffraction grating at a higher angle of incidence or with an intracavity etalon. A suitable etalon would have a spacing of about 1 mm. Trade-offs in the selection will involve efficiency, stability and ease of control. The technology for the spectral control is well developed within AERL as a result of the extensive experience over a period of 10 years with the JNAI program for isotope separation, where spectral widths and absolute wavelength accuracy of $< 0.02 \text{ \AA}$ have been routinely achieved, with corresponding stability.

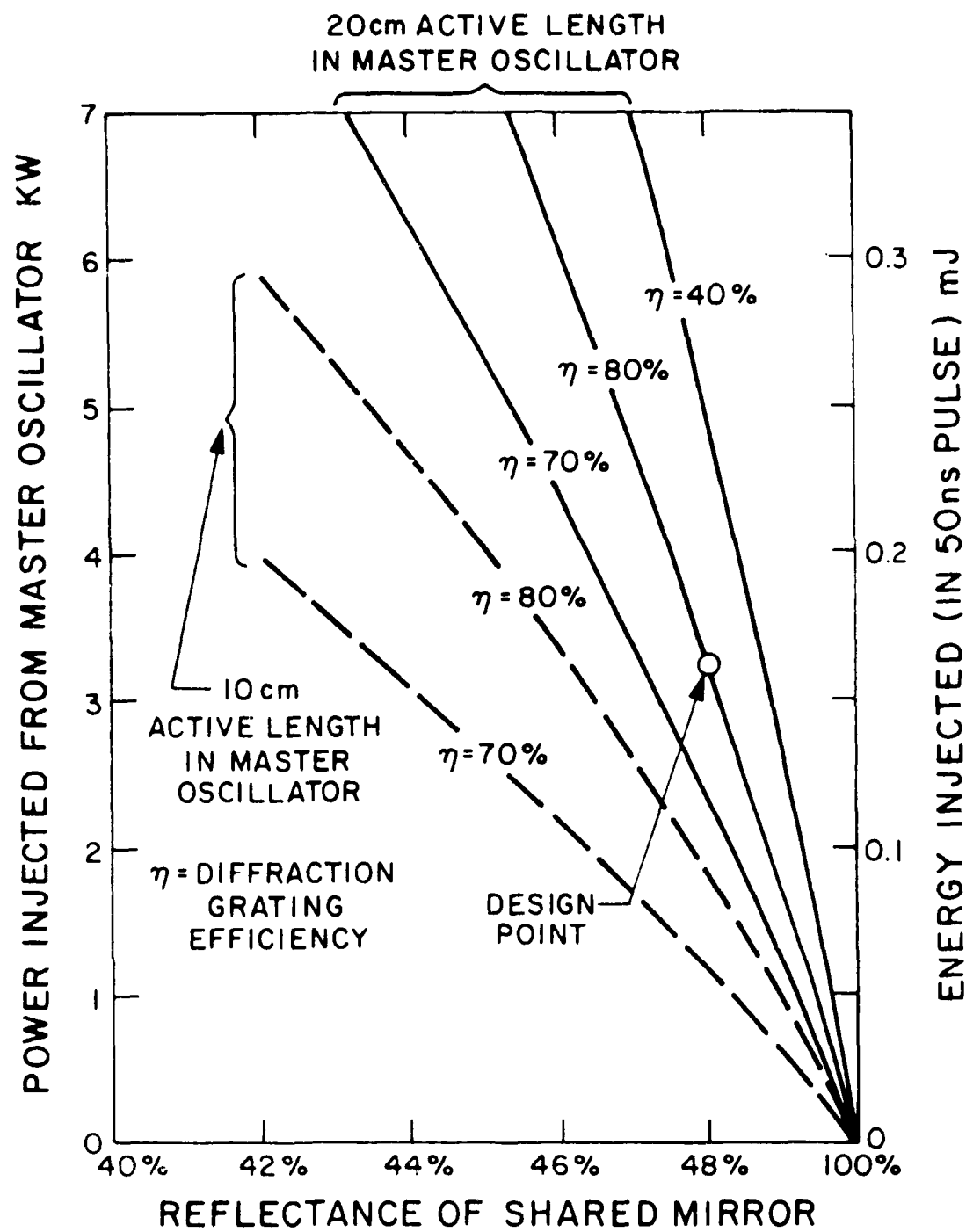
6. Choice of Shared Mirror between Resonators

There is a conflict between desiring a high reflectance for this mirror to reduce leakage of lasing light from the unstable resonator, and desiring a lower reflectance to increase the efficiency of the injecting laser.

Commercially available diffraction gratings have only 80% guaranteed absolute diffraction efficiency at the wavelength of 5000 \AA . When higher efficiencies are cited they invariably turn out to be "relative" values, or for the infrared. This drives the optimum reflectance for the output mirror (which is this shared mirror) to $< 90\%$, as illustrated by the curve of Figure 68, which plots the anticipated output power of the oscillator versus the reflectance. Diffraction gratings with higher efficiency are within the state of the art. However it is questionable whether the small increase in overall efficiency of the system would warrant much effort in this direction.

It is technically feasible to design the mirror with low reflectance locally in the region of the injection, and higher reflectance elsewhere. However analysis shows that the gain to be achieved in the overall output, compared with best optimization with a uniform mirror, would be only 2%. Hence the additional risk to the beam quality, and the complication, is not justified.

The trade-off in selection of the mirror reflectance is heavily influenced by the relationship between injected power and resultant increase in efficiency of the unstable resonator, which



J9160

Figure 68. Power for Master Oscillator vs Reflectance

is shown in Figure 65. The data from Table 8 and Figure 65 are combined in a plot 'A' of Figure 69, to show the increase of ILO efficiency as a function of the shared mirror reflectance, excluding the effect of leakage of ILO light through the shared mirror. This additional loss is plotted as curve 'B' of the same figure. Curve 'C' is obtained from the difference, and shows the net efficiency increase of the ILO, from the injection, as a function of the shared mirror reflectance. A choice of 98% is sufficiently close to optimum, and will increase the output of the system by 13%, as a result of the injection.

Higher reflectance than 98%, while giving a little more efficiency, would be unwise because scatter and absorption losses and problems would then start becoming significant.

The combination of spectral control and added efficiency that come from the ILO approach makes it very attractive for this application.

7. Injection Laser

For system simplicity we choose an avalanche discharge laser similar to that built at NOSC.⁽³⁴⁾ However in the place of UV preionization we would use corona discharge preionization using a "corona bar" behind one of the discharge electrodes. This technique has worked well with small discharge pumped rare gas-halide lasers.⁽³⁵⁾ It has the advantage of not requiring spark sources which may be difficult to make for long life operation.

The laser small-signal gain and pulselength is expected to be similar to those of the NOSC device. In this case to achieve 10 cm gain for 75 ns pulselength, a mixture of Ne/N₂ HgBr₂ will be used with a discharge energy input of 100 J/l. For the required 20 x 1 x 1 cm gain volume the input power will be 200 W

34. Shay, T., private communication.

35. Pike, C. private communication.

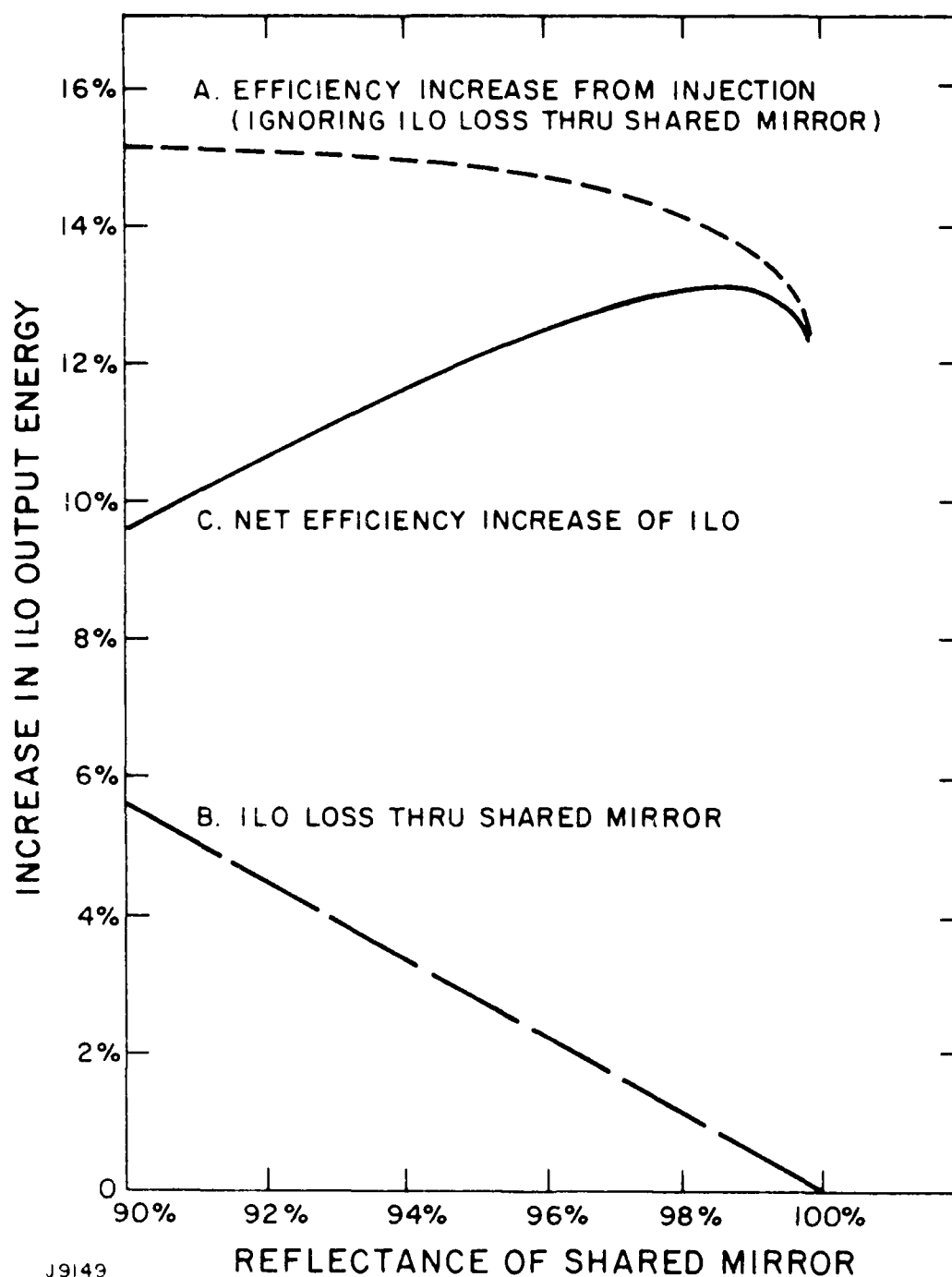


Figure 69. Increased Output of ILO vs. Reflectance of Shared Mirror

at 100 pps. Allowing for an electrical circuit efficiency of 0.8 the power consumed by the injection laser will be 240 W.

The flow required for the injection laser can be taken from the main flow loop. The flow required will be of order of 1% of the main flow and will be neglected here.

G. E-BEAM

1. Design Approach and Rationale

The operating parameters of the e-beam are listed in Table 8. In this section, we will first discuss the general approach of the e-beam design, in view of the overall device requirements. This will be followed by a more detailed description of our preliminary design of the e-beam system, including two main options for electrical pulsing.

The important elements of the design are:

- Thermionic Dispenser Cathode
- Bakeable Vacuum System
- Conduction Cooled Titanium Foil Window
- Grid Switched dc or Externally Pulsed High Voltage Options.

The rationale for these choices are as follows:

Thermionic Dispenser Cathode was chosen as the most viable candidate for achieving a broad area uniform emission of 2 A/cm^2 for the required 10^8 pulses, being scalable to 10^{10} pulses and lifetimes of several times 10^4 hrs. Near term requirements can be met and exceeded based on already demonstrated cathode performance, including verified heater power consumption of $\leq 6 \text{ W/cm}^2$.

Bakeable Vacuum System has been incorporated into the design of the e-gun to ensure reliable activation and efficient cathode performance. A base vacuum of $\leq 10^{-9}$ torr, and $\leq 10^{-7}$ steady-state vacuum under e-beam operation is considered as a realistic design goal. This can be achieved using standard high-vacuum technology with oil-free pumps, all metal seals and ceramic bushings with a bakeout capability of 350°C . Further reduction of outgassing can be achieved by electron bombardment cleanup, if necessary.

Conduction Cooled Titanium Window is selected to provide long life under cyclic stresses as required for the present application. The relatively modest foil loading of $\sim 2 \text{ W/cm}^2$ can be handled by a pure titanium foil, but increased heat conductivity is achieved by coating the foil with a thin layer of copper.

TABLE 8. E-BEAM DESIGN PARAMETERS

Voltage	300 kV
Emission Density (Cathode)	2 A/cm ²
Current Density (Gas)	1 A/cm ²
Pulse Duration	0.25 μ s
Rise, Fall, Droop	max 10%
Area	250 cm ²
Total Current (Gas)	250 A
Impedance	1200 Ω
Pulse Energy	20 J
Rep. Rate	100 Hz
Average Power	2000 W
Life	10 ⁸ pulses

Grid Switched dc and Externally Pulsed High-Voltage Options
are considered as two possible alternatives for powering the e-gun. Key components to be considered are the step-up transformer required for the external pulsing, and the graded bushing for the grid switched approach. The preliminary design of the e-gun structure can be adapted for either method, being conservatively sized for dc voltage standoff. Selection of externally pulsed high voltage would, however, allow a more compact design of the gun.

2. E-gun Design Description

a. Vacuum Chamber

The vacuum chamber for the e-gun is a cylindrical vessel with hemispherical ends, as shown in Figure 70. It has two large openings for the foil system and the negative high-voltage terminal ports for attaching pumps and gauges. The chamber is a vessel under external pressure, and therefore, is liable to failure due to elastic instability. In view of the discontinuous structure created by the large cutouts the shell is designed with a big safety factor on buckling. The chamber is constructed of stainless steel and uses metal seals in accordance with standard high-vacuum technology practice.

The inside of the chamber will be ground and polished to a smooth surface in order to minimize both electrical stress and outgassing. Final finishing is by a Diversey dip process which removes all contaminants of the surface and produces a finish similar to electropolishing. The average electric field at 300 kV is 20 kV/cm with a maximum value at the negative terminal of 33 kV/cm.

b. High Voltage Terminal

The high-voltage terminal also shown in Figure 70 has the large central port to the chamber and is also constructed of stainless steel. It has a conical shaped section in the center of the back for attachment of the high-voltage bushing. On the front face there is a large flange which can also be termed as the grid of the gun. The terminal is split with the front 2/3 separable from the rear 1/3 which contains the internal parts.

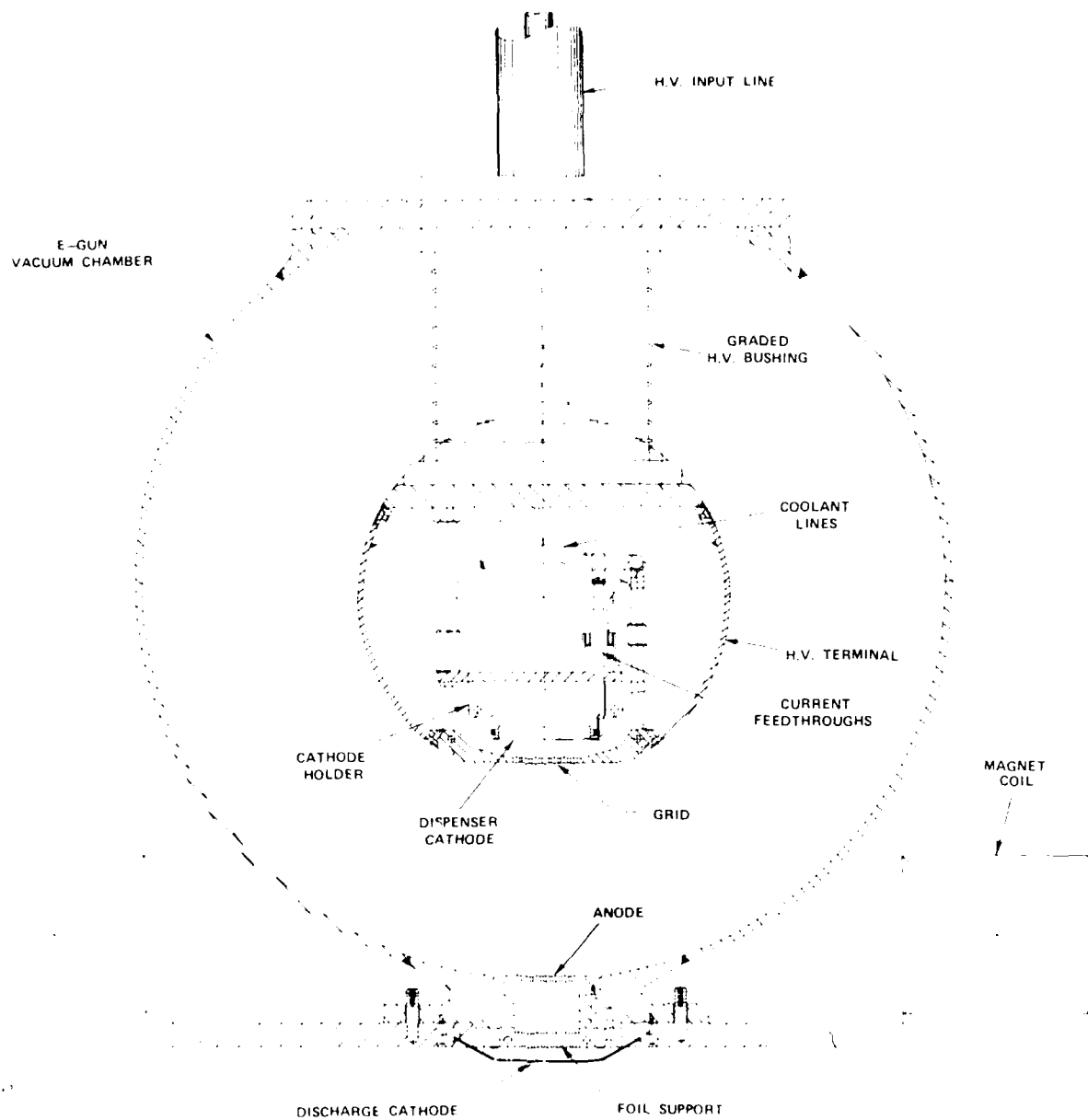


Figure 70. E-Gun Schematic Drawing

The cathode forms one wall of a copper liquid cooled box, and is indirectly heated by tungsten filaments. The 4 cm x 62.5 cm dispenser cathode assembly consists of modular blocks as shown in Figure 71. The heaters are operated at 1400°C or less to ensure long life. A stack of heat shields behind the cathode provides thermal insulation in order to conserve heater power. Space behind the cathode box is utilized for electrical connections and cooling pipes.

c. High-Voltage Bushing

The high-voltage bushing will be a brazed ceramic and metal ring structure which must stand off 300 kVdc voltage, provide mechanical support for the e-beam terminal, and which must also have sufficient temperature capability to permit bakeout. There are accelerating tube sections commercially available which have suitable characteristics. The bushing shown in Figure 70 would operate at an average electric field of 15 kV/cm. A coaxial line (solid or cable) from the high-voltage power supply terminates inside the bushing. This coaxial line will be made to carry heater power, control power and coolant connections inside the inner conductor as required. Also, inside the bushing a high impedance grading resistor chain must be provided for dc operation. If pulsed operation is adopted, the bushing will be capacitively self-grading and no resistor chain will be necessary. The interior of the bushing will be filled with SF_6 at a few atmospheres pressure to make its voltage capability at least as good as the vacuum side. It is assumed that the coaxial line and grading resistors will be removed during bakeout.

d. Pumping Bakeout and System

The required base vacuum of $\leq 10^{-9}$ torr will be achieved by an oil-free pumping system, metallic seals throughout, and bakeout at 350°C . The roughing system will consist of a rotary pump and cryogenic absorption pumps. Valves and gauges are provided to control and monitor the system. The estimated outgassing rate based on $\sim 10^{-11}$ torr l/sec/cm^2 outgassing rate and ~ 200 l/sec , which can be provided by an

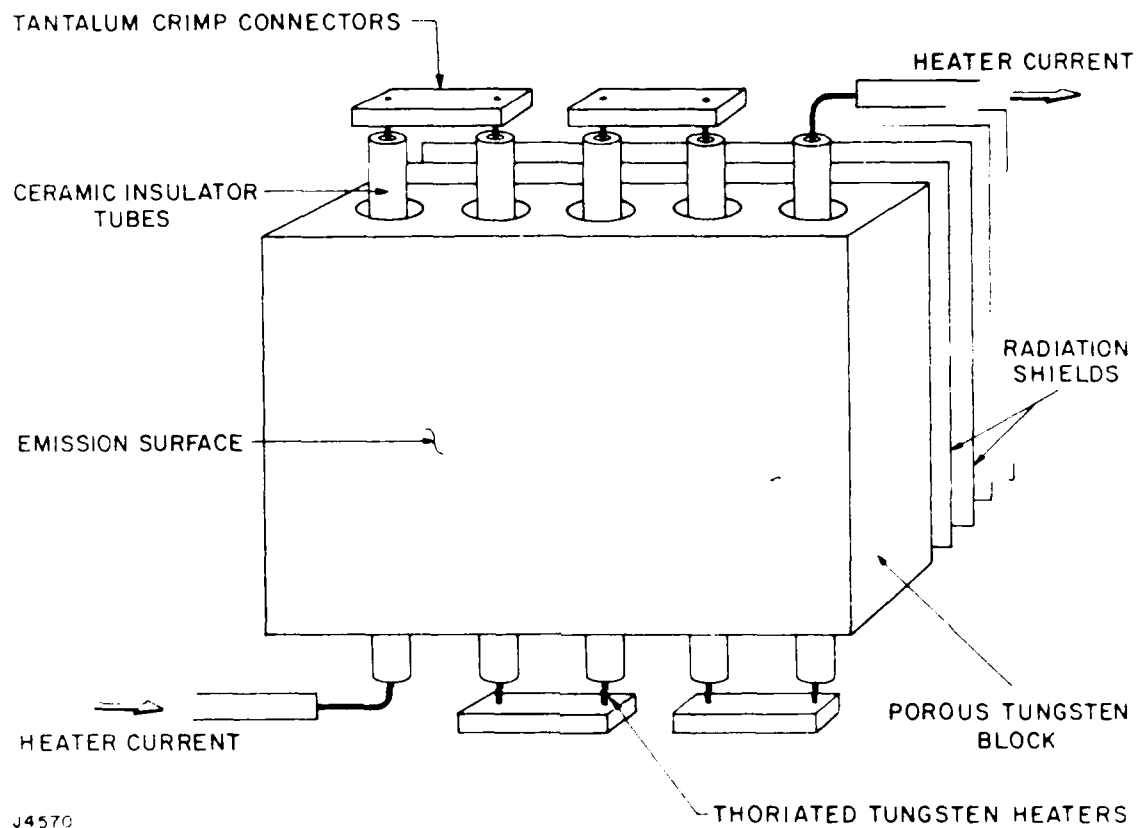


Figure 71. Dispenser Cathode Assembly Schematic

ion pump of standard type. This pumping capacity should also be sufficient to handle the anticipated gas load due to surface desorption by electron bombardment and be able to maintain a steady-state background level of $< 10^{-7}$ torr during e-beam operation, assuming a desorption coefficient of about 10^{-2} molecules/electron.

The e-gun chamber has been designed so that it may be separated from the laser cavity and enclosed in an oven for bakeout. The baking temperature of 350°C is consistent with the temperature capabilities of all components including the foil support structure.

e. Foil and Foil Support

The foil system consists of a titanium alloy foil of 0.5 mil thickness supported by a perforated plate having $\sim 3/16$ -in. diameter circular holes and a geometrical transmission factor of $\sim 50\%$. Considering the size and operating conditions of this device the proposed foil system is designed to provide simple and effective cooling and adequate fatigue life.

The foil material, Ti-6Al-4V, has excellent strength in the temperature range the foil will experience. Its fatigue strength and notch sensitivity are well known at this time and the use of annealed material provides a significant degree of ductility which will allow the foil of yield to accommodate possible imperfections in the machining of the support plate.

The support plate will be made of beryllium-copper 10 alloy to secure a combination of good structural strength at operating temperature and high thermal conductivity to permit a simple cooling system. An equilateral triangular hole layout will be used to maximize the open area of the foil structure.

3. E-Beam Pulsed Power

The pulsed power needed for e-beam operation, see Table 8, is modest in terms of energy per pulse and average power, however, the 200 J/pulse must be delivered in an approximately square pulse of $0.25 \mu\text{s}$ duration at 300 kV with high efficiency. It is also

required that the power supply and its components has long life expectancy, at least 10^8 pulses, and a degree of reliability consistent with other subsystems in order to meet the overall systems reliability specification. It is logical to examine the total reliability of the power supply and e-gun in view of the possible design trade-offs. The most evident trade-off is between internal grid-switching of the gun and external high-voltage pulsing.

a. Internal Grid Switching Option

This option puts the main burden on the gun design in terms of its dc voltage holdoff capability, failure modes and possible damage, and ability to recover from arcing. The critical components in terms of survivability is the high-voltage bushing and the foil. The bushing must have dc grading and should not be designed for higher electric fields than ~ 25 kV/cm. The foil should be designed with sufficient protection against arcing such as provided by the drift space between anode and foil shown in Figure 70. Also, provisions must be made to interrupt the prime power source within one interpulse time, or < 5 ms. This can be done with an SCR controller in the prime XF-rectifier circuit.

The high-voltage power supply itself in this case is simply an RC or LC charged capacitor that has to store ~ 5 times the pulse energy or ~ 100 J at 300 kV to limit the droop to $\sim 10\%$. Pulse rise and fall times can be made short and are principally limited by the inductance and capacitance of the gun structure and the grid pulser circuit, which operates at low (10-15 kV) voltage and typically uses a thyatron switched PFN to produce the desired pulse duration.

b. External High-Voltage Pulsing

Compared to the grid switched dc e-gun, the short pulse length will allow much high stress levels to be used in the design of an externally pulsed e-beam. Vacuum stress levels of ≥ 60 kV/cm are used in this case for commercial vacuum tubes operating at the 300 kV level, such as klystrons. The impedance level of $\sim 1000 \Omega$

is also typical of high power klystrons and commercial pulse modulators exist that are designed for $\geq 10^9$ pulses. The main difference between this application and typical klystron tubes is approximately 10 times shorter pulselength. The critical component for our system would be the step-up transformer required to get from ~ 40 to 300 kV with < 25 ns rise and fall time. Although we see no fundamental reason why this transformer could not be built, it is not a shelf item and would require development and testing. It should be designed with a bifilar secondary winding for providing filament power; this would eliminate the separate isolation transformer needed for the dc scheme. A possible hybrid approach would also be worth considering, i.e., using a combination of external pulsing and grid switching. The relative timing of the two switches can be used as a means to optimize the pulse shape and energy transfer efficiency of the e-beam system.

c. E-Beam Power Requirement

The overall power requirement of the e-beam system is dominated by the high-voltage power supply and the heaters for the thermionic dispenser cathode. The average e-beam power is 2 kW. A conservative estimate of the transfer efficiency of prime power into the e-beam is 80%. The power requirement on the high-voltage power supply is therefore 2.5 kW. The total area of the dispenser cathode is 250 cm^2 . The projected power consumption of the cathode for the design vacuum conditions, is 2.7 W/cm^2 in radiation from the emitting area, or 675 W. Radiation losses from other areas of the cathode structure are estimated to be 200 W and conduction will contribute another ~ 400 W. The overall power consumption of the 250 cm^2 cathode would therefore be 1.3 kW. This makes the overall power requirement for the e-beam system 3.8 kW.

H. MAGNETIC FIELD DESIGN

1. Field Requirement

In the present design a magnetic field is used to guide and confine the e-beam from the e-gun cathode through the e-gun grid, e-gun anode, foil support structures and active laser volume. The guide field serves the following functions:

Firstly, the magnetic field prevents beam spreading in the active volume due to scattering from the foil and laser medium. This improves the e-beam energy deposition uniformity both along the e-beam and transverse to the e-beam. It also allows for sharper edge definition of the discharge so that less discharge energy is wasted in the weakly pumped fringe regions where no useful laser energy is extracted. These issues have been addressed in Section III-C. For this the field strength should be maximized.

Secondly, it prevents pinching of the e-beam due to a transverse self-magnetic field produced by the discharge which would otherwise constrict the discharge, and lead to a highly nonuniform discharge energy disposition. For this the applied field needs to be much greater than the discharge self-field.

In the present design we have chosen a field intensity of 4 kG. This is a compromise between keeping the magnetic stresses on the field coil from being excessive and the desire to have sharper edge definition on the discharge volume. With this field intensity beam steering by self-magnetic field of the e-beam is negligible in the e-gun and beam pinching in the discharge is negligible.

The size of the field coil was chosen to be 120 x 70 cm measured on the center of the winding. This allows the magnet to be conveniently fitted around the e-gun and also produces a field with acceptable divergence in the discharge region.

A computer simulation of a single current loop was used to obtain the amount of current required and the uniformity of the field generated in the discharge region. The loop center was 15 cm above the center of the discharge region, (Z direction)

± 60 cm long (X direction) and ± 35 cm wide (Y or flow direction), see Figure 72. It was found that 3.62×10^5 A-turns are required to produce a field of 4,000 G at the center of the discharge region. The strength of the coil needed for other field values can be obtained by direct proportion.

2. Field Uniformity

Table 9 gives data for the field uniformity in the discharge region. The origin of the X, Y, Z coordinates is the center of the discharge region, (Figure 72) 15 cm below the plane of the current loop. B_z is the field in the Z or principal direction. B_r/B_z is the ratio of the field at right angles to B_z , to its principal value. We are particularly interested in the magnetic field in the gas flow or X-direction because this determines the divergence of the beam in the Y-direction. The ratio of B_x to B_z is shown in the last column. This table shows that the greatest spreading of the B-field is in the Y-direction, amounting to about 7.5% of the principal field. However, in the important X-direction, the spreading is only of the order of one-half percent or less.

3. Coil Design

The overriding consideration in designing a magnet coil is the conservation of electric power. For this reason, the only coil that could be seriously considered is a superconducting coil in which the principal use of electric power is for refrigeration. A permanent magnet could not be chosen for this application because of the large magnetizing force required. Also, coil configurations which include windings on both sides of the discharge region are considered to be quite impractical in view of (a) the increased refrigeration which is roughly proportional to the number of coil units and (b) the large intercoil compressive forces that would have to be taken through the dewar insulation and across the gas duct. This would further increase the required refrigeration because of heat leaks in the structures supporting the coils, and would greatly complicate the construction of the gas

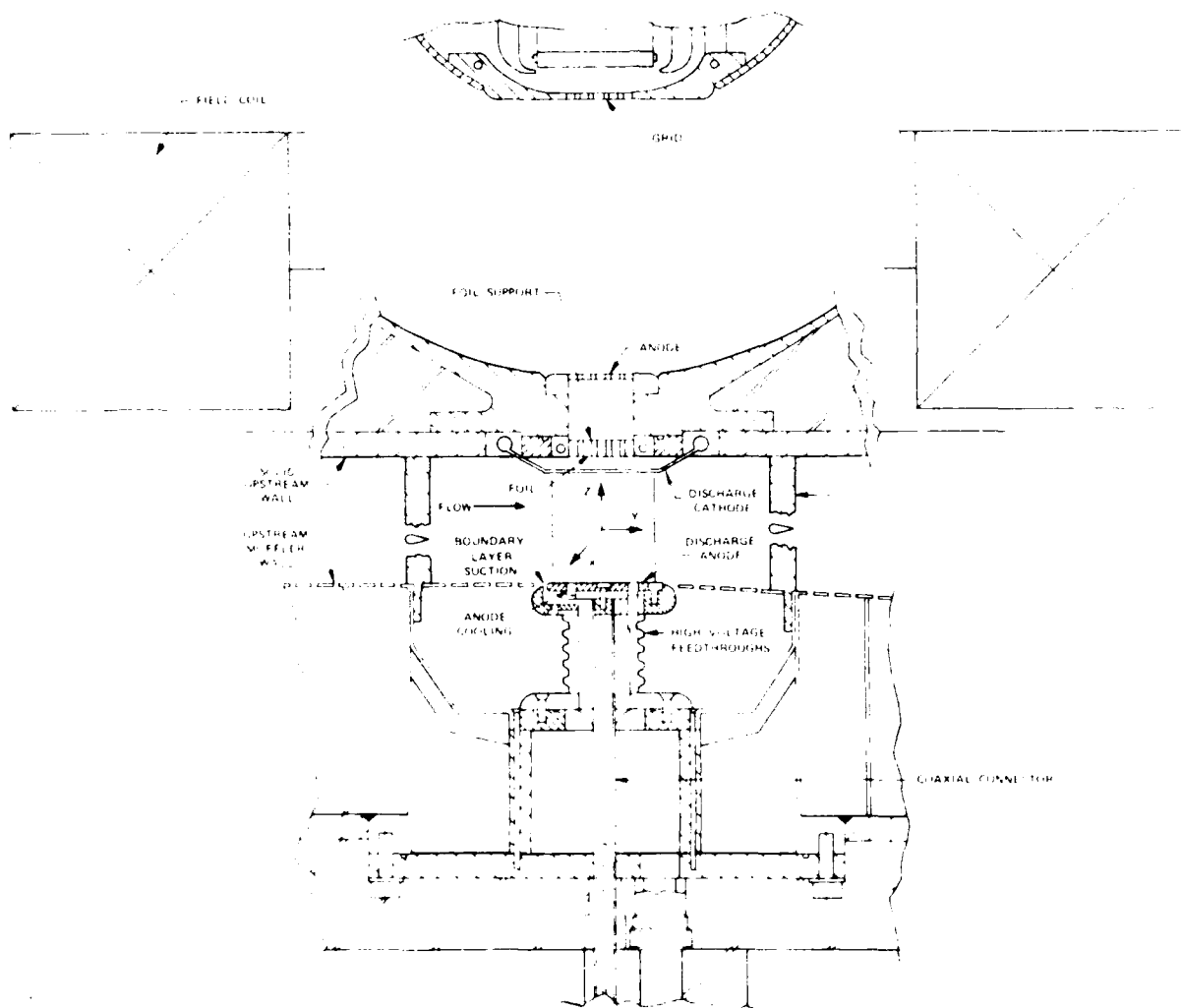


Figure 72. Magnetic Field Coordinates

TABLE 9. CALCULATED FIELD INTENSITIES

$\frac{x}{\text{cm}}$	$\frac{y}{\text{cm}}$	$\frac{z}{\text{cm}}$	$\frac{B_z}{(10^3 \text{ G})}$	$\frac{B_{\perp}}{B_z}$	$\frac{B_x}{B_z}$
0	0	0	4.00	0	0
		-4	3.65	0	0
		4	4.32	0	0
0	2.5	0	4.00	-0.045	0
		-4	3.65	-0.051	0
		4	4.33	-0.037	0
20	0	0	4.12	-0.079	0
		-4	3.64	-0.098	0
		4	4.47	-0.060	0
20	2.5	0	4.12	-0.084	0.006
		-4	3.73	-0.102	0.006
		4	4.48	-0.064	0.006
30	0	0	4.27	-0.157	0
		-4	3.80	-0.189	0
		4	4.71	-0.122	0
30	2.5	0	4.27	-0.160	0.005
		-4	3.80	-0.192	0.005
		4	4.72	-0.124	0.005

flow duct. On the other hand, a simple superconducting loop can provide the required magnetic field with only a small amount of refrigeration, and no reaction forces on external objects provided that they are nonmagnetic.

A typical superconducting coil assembly is shown in Figure 73. Details of the design could, of course, be left to the coil manufacturer. However, this figure illustrates some of the considerations that determine the coil size and the required refrigeration. The superconductor, may be either niobium-titanium, or niobium-tin, both commercially available materials. Niobium tin has the advantage that it can operate at a higher temperature and therefore uses less refrigeration power. However, both types of superconductor can be accommodated without straining the state of the art and without exceeding 1 kW of power.

A niobium-titanium coil operating between 4.2° and 4.5° in a bath of liquid helium is chosen for illustration. Consider that the solid has a cross section of 6.5×6.5 cm and an ampere turn value of 3.6×10^5 so that a 4,000 G field would be obtained in the laser discharge region. The peak magnetic field at the surface of the conductor bundle is given by

$$B_{\max} = \frac{nI \mu_0}{4D}$$

where D is the height of a square winding. With $nI = 3.6 \times 10^5$, B_{\max} is 1.75×10^4 G. This is a reasonable and conservative peak field for a superconductor. The windings are subjected to an internal compression of 2.0 atm, well within the capability of common insulating materials and common superconducting wires. Therefore, the winding can be layer built with porous glass cloth used as interlayer insulation and for the distribution of liquid helium in the windings. The conductor itself can be insulated with formvar or similar material.

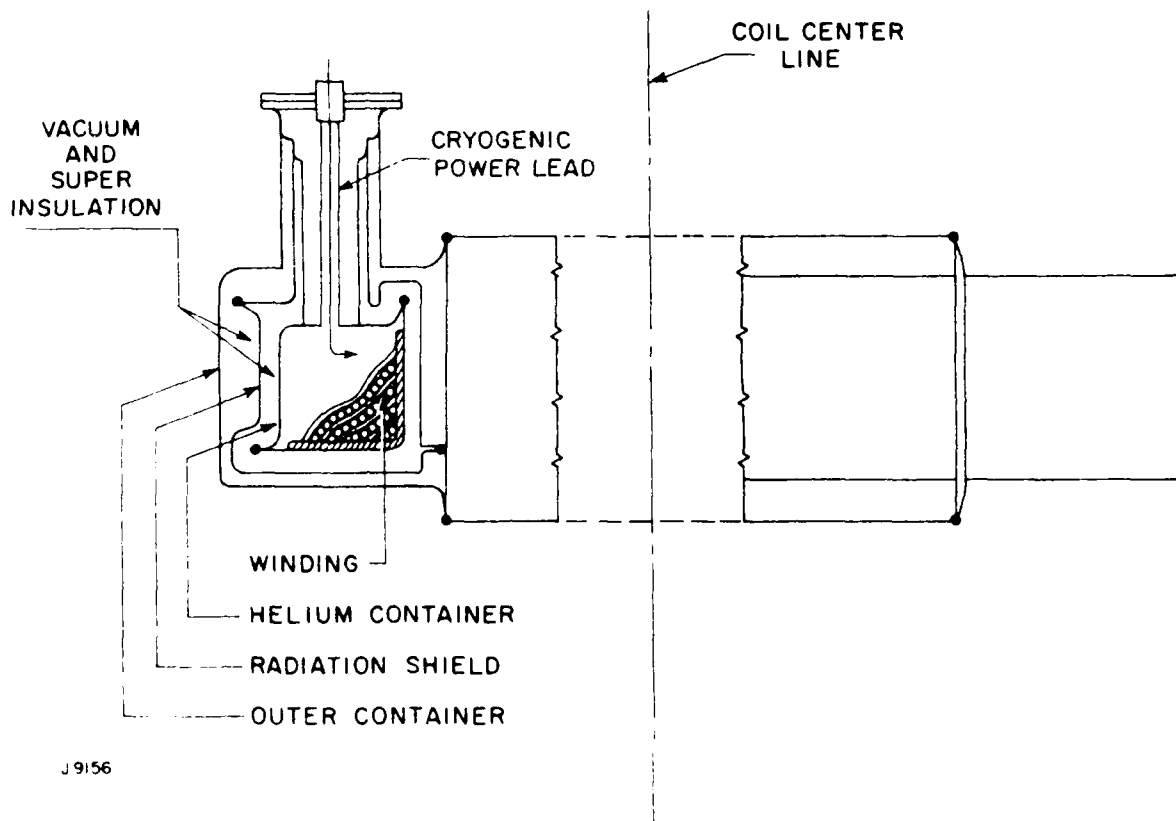


Figure 73. Typical Superconducting Coil Assembly

It is important to choose a fine wire so that the current per turn is small. In this illustrative design, the wire chosen is niobium 46% titanium and a copper to superconductor ratio of 1:1. The wire diameter is 0.020 in. and the current supplied is 200 A. At a peak field of 20,000 G, this conductor can carry 266 A and therefore it is conservatively loaded. The overall packing factor in the coil is 0.065 which is extremely low and therefore there is ample room for interlayer insulation. The reason that so low a current is chosen is because the principle source of heat to the superconducting coil is the power generated in the leads that conduct current to the coil. In a space environment, the upper terminal of the leads could be fixed at the temperature of the dewar radiation shield, $\sim 80^{\circ}\text{K}$ and the lower terminal at 4.2°K . Under these conditions, the heat generated in a pair of suitably designed leads is 0.0015 W/A (this is half the power generated for leads operating from 4° to 300°). Thus, with 200 A, 0.3 W is generated merely in the power leads.

4. Dewar Construction

The dewar can consist of three concentric containers made of polished stainless steel. Each container is fabricated in two parts joined by seam welding. The inner container holds the coil and liquid helium. The intermediate container is a radiation shield at about 80°K . Cooling for this temperature is automatically available from the refrigeration cycle. The outer container is at whatever environmental temperature is encountered in the satellite. The assumption here is that it will be $\sim 300^{\circ}\text{K}$. The spaces between the three containers are evacuated and several layers of lightly flocked superinsulation are used in these spaces to limit radiation heat transfer even more than would be obtained with simple polished surfaces. This type of construction is quite standard. The radiation heat transfer from the liquid helium container with this type of insulation is estimated at 0.018 W. A larger source of heat leak is by conduction in the tubing of the

turrets used for introducing the current leads and the liquid helium transfer tube. For example, if the helium container turret consists of two tubes 1.5 in. diameter, by 0.010 in. thick, by 8 in. long, the estimate is that these will consume 0.089 W of refrigeration. Thus the total refrigeration requirement for this coil is calculated to be 0.41 W. A 1/2 W refrigerator will provide an adequate margin of safety.

During high G-loading, the mechanical forces of the three container can be supported by snubbers in the vacuum space, designed to limit motion, but making no direct contact under normal circumstances.

For a space environment, the helium container should be kept full and all boil off taken through the current leads and returned to the refrigeration system. The weight of the coil, liquid helium, dewar, but excluding the refrigerator is estimated at 32.5 kg.

5. Refrigerator Power

A ground based commercial refrigerator supply 1 W of refrigeration at 4°K would consume ~ 3 kW. However, for space applications, the efficiency has been very greatly improved. R.W. Breckenridge, Jr. (36) has constructed the critical part of a refrigerator for space applications and has tested it. It produces 1 W of refrigeration at 3.6° and consumes 1300 W. The efficiency at 4.5° would be slightly higher and Dr. Breckenridge has estimated that 650 W would be the input power requirement for 1/2 W of refrigeration. This refrigerator weighs 100 lbs and occupies a space of 10 in. x 24 in. x 26 in. The refrigeration cycle is a reverse Claude cycle with double ended, reciprocating engines.

The coil charging supply will provide 200 A at ~ 1.2 V.

36. Breckenridge, R.W., Jr., AFDDL-TR-68-59, Oct. 1968, "Exploratory Development of a 1 W, 3.6°, Reciprocating Refrigerator for Space Applications." (A.D. Little, Cambridge, MA.)

4. Use of Niobium Tin

The design just presented uses niobium-titanium superconductors and, except for the refrigerator, every item is commercially available and conservatively sized. Therefore, there is no need to consider other superconductors such as niobium tin, which, at the present writing, would be considered totally experimental. Nevertheless, a niobium tin coil could be constructed with the same size conductor as the superconducting wire, but operation at 4.2°K requires a liquid helium, not liquid nitrogen, refrigerator. The principal reason for this is the wall loss of the liquid helium. The temperature of the refrigerator is about 4.2°K, and the heat loss from the liquid helium is about 100 W/m². The heat loss from the liquid nitrogen is about 10 W/m².

NO-A185 884

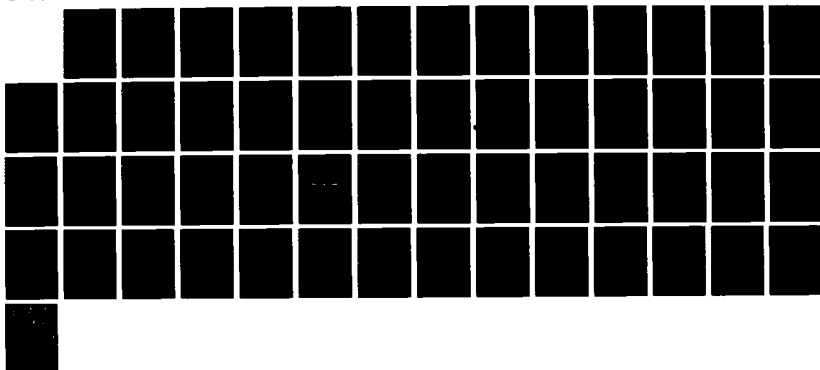
SPACE-BASED BLUE-GREEN LASER(U) AVCO EVERETT RESEARCH
LAB INC EVERETT WA J C HSIA ET AL. OCT 81
N00123-80-C-1135

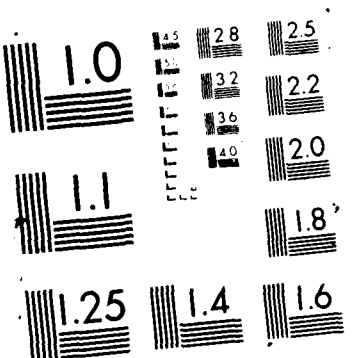
3/3

UNCLASSIFIED

F/G 9/3

ML





I. PULSE DISCHARGE MODULATOR DESIGN

1. Circuit Topology

In designing the discharge modulator for the HgBr Phase II laser, two types of discharge circuit were considered: Blumlein and line pulser.

a. Blumlein Circuit

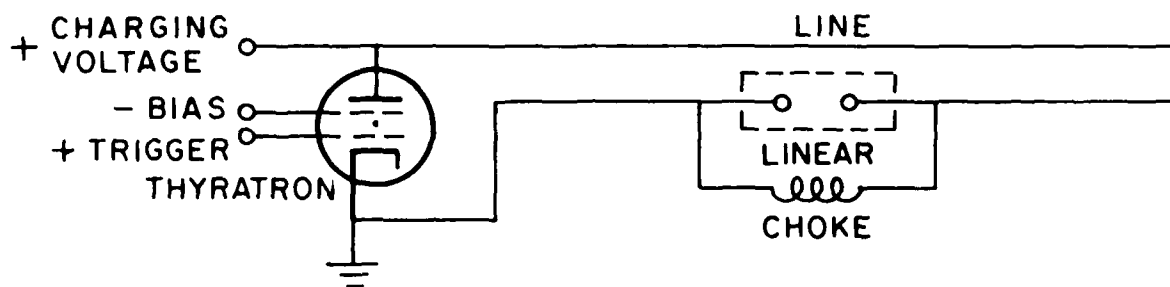
Figure 74 is a schematic diagram of the laser using a Blumlein circuit to pulse the discharge. The Blumlein circuit has the advantage that the output voltage into a matched load is equal to the charging voltage, V_0 . Into an open circuit the Blumlein gives twice the charging voltage. This occurs when the wave initiated by the thyatron is reflected at the open circuit and the voltage between the grounded side of the load and the common side of the energy storage line then goes from $+V_0$ to $-V_0$. Since the ungrounded side of the load is at $-V_0$ with respect to the common side of the energy storage line, the voltage across the load (open circuit) will be $2V_0$.

A disadvantage of the Blumlein circuit is that the switch current is twice the current into a matched load. This occurs because the voltage across the load and the charging voltage are equal but the thyatron sees Z_B , the stripline impedance, whereas the load impedance is $2Z_B$. This places more stringent requirements on thyatron d_i/d_t and inductance. The voltage produced during the rising part of the pulse by a Blumlein circuit across a matched load can be shown to be

$$V = V_0 \left(1 - e^{-\frac{4Z_B}{L_L} t} - \frac{e^{-\frac{Z_B}{L_S} t} - e^{-\frac{4Z_B}{L_L} t}}{1 - \frac{L_L}{4L_S}} \right) \quad (65)$$

where L_L = load inductance

L_S = switch inductance



J9147

Figure 74. Blumlein Circuit

Therefore, the time constant associated with the switch is $T = L_s/Z_B$.

b. Line Pulser Circuit

Figure 75 is a schematic diagram of the line pulser circuit, an alternative to the Blumlein for exciting the laser discharge. In this circuit a section of line is charged to twice the desired load voltage. When the switch is closed the charged line section is connected to the load. The resulting voltage into a matched load is half the charging voltage. However, a compensating advantage of this circuit is that the switch current is equal to the current in the load. In this circuit the voltage produced during the rising portion of the pulse across a matched load can be shown to be:

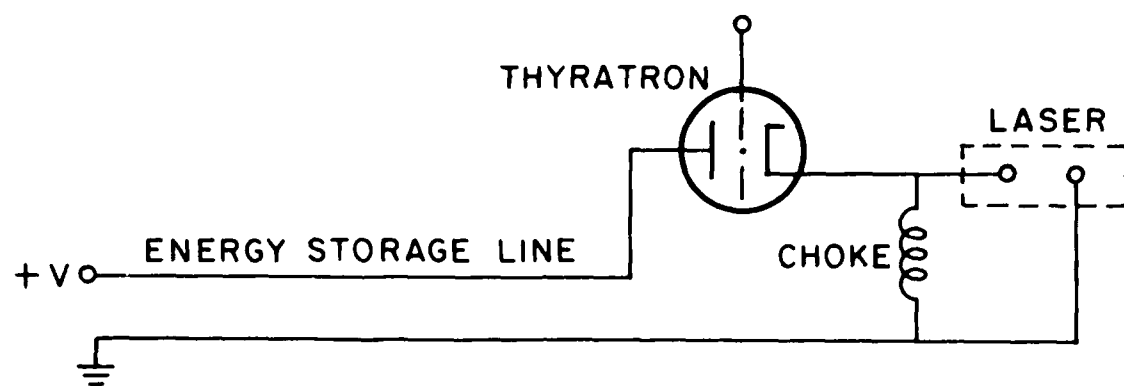
$$V = \frac{V_0}{2} \left(1 - e^{-\frac{2Z_0}{L_L + L_s}} \right) \quad (66)$$

The time constant associated with the switch inductance is then $T = L_s/2Z_0$. However, since Z_0 (line pulser) = $2Z_B$ (Blumlein) the inductance which can be accepted in the line pulser circuit is 4 times that in the Blumlein. An examination of the circuit verifies that the thyatron sees an impedance of $2Z_0$ in the line pulser circuit.

The thyatron operating conditions for both the Blumlein and line pulser circuits were discussed with the three major thyatron manufacturers in the western world, EG&G, English Electric Valve and ITT. They all preferred the higher voltage, lower current conditions in the line pulser circuit.

2. Networks

We shall discuss the design criteria for lumped element networks for the line pulser circuit.



J9146

Figure 75. Line Pulser

Figure 76 shows the classical Guillemin five section networks. Since in our modulator design the inductance of the capacitors is small but the thyatron does have significant inductance, a design in which the thyatron inductance can be included as part of the network would be preferred. This eliminates the type C and F networks from consideration. The type D requires coupling between the inductors to give the required mutual inductances. This will be difficult to achieve at the low inductance values required. The type A network would meet our requirements but the series configuration will tend to give excessive stray inductance and the uncharged capacitors add weight without storing energy. This leaves the type B network which meets all our requirements with no significant disadvantages.

In order to simplify the design a number of test cases were analyzed using the Control Data Syscap network analysis program. The energy storage subsystem will consist of eight identical pulse forming networks with one terminal of each network connected to the common thyatron and the other terminal connected to one of eight output cables. The analysis was performed on one of the eight parallel networks. For comparison purposes a simple five section "transmission line" network was analyzed as shown in Figure 77. The overshoot and slow fall time are characteristic of this network. Figure 78 shows the performance of the unmodified B network. Figure 79 shows a variation of the B network with the first four capacitors and inductors equal, the last capacitor twice the others and last inductor a variable.

The version shown in Figure 79(c) was chosen for further analysis. In Figure 80 the first inductor is varied while the other components are kept constant. This shows that increasing the output inductor improves performance by reducing overshoot. A conceptual drawing of a stripline connected pulse forming network is shown in Figure 81.

3. Thyatrons

The factors which influence thyatron operation at high di/dt levels have only been recently understood. The major factors that determine the rate of current rise are 1) the trigger

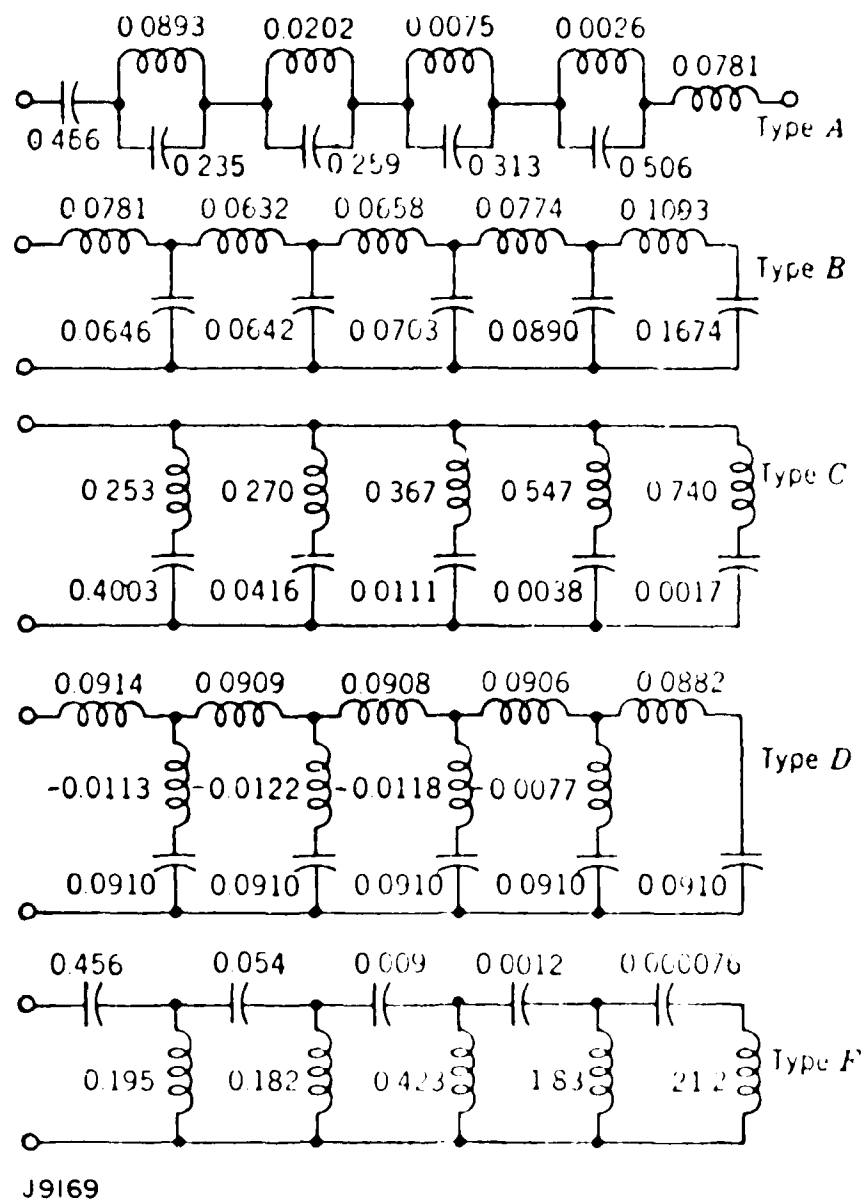


Figure 76. Equivalent Forms for Five-Section Guillemin Voltage-Fed Network. Multiply the values of the inductances by $Z_N \tau$ and the values of the capacitances by τ/Z_N . The inductances are in henrys and the capacitances in farads if pulse duration τ is expressed in seconds and network impedance Z_N in ohms. (Adapted from "Pulse Generators," G.N. Glasoe and J.V. Lebacqz, Boston Technical Publishers, Lexington, MA 1964.)

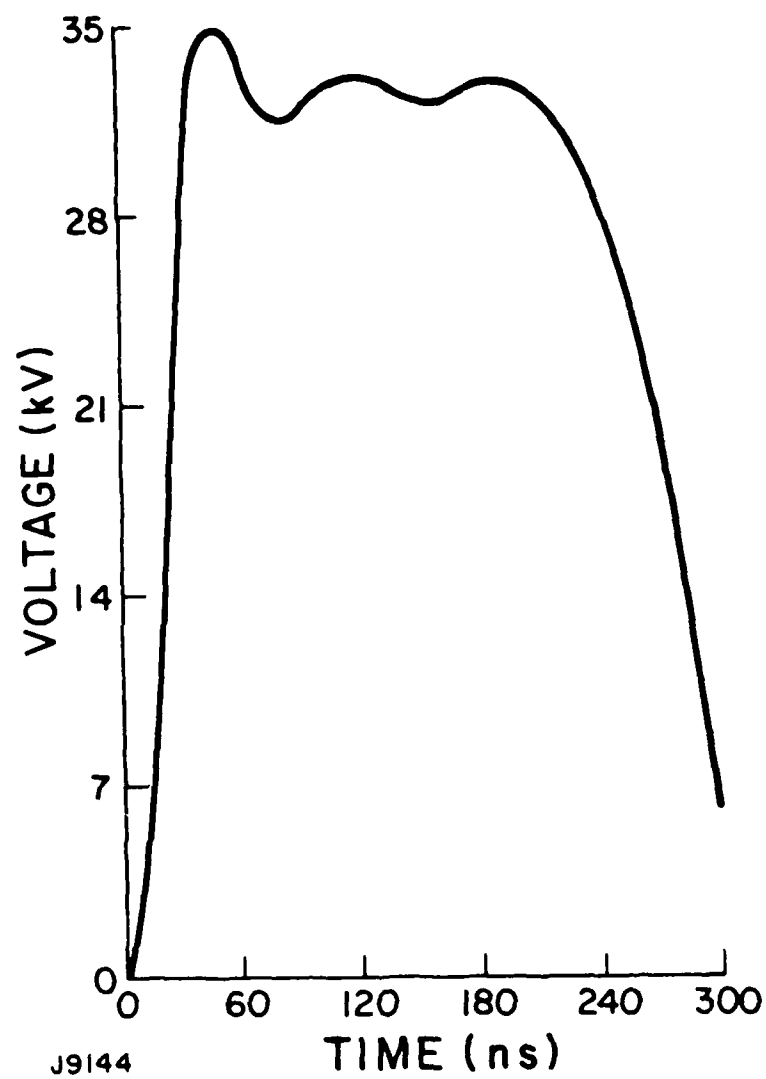


Figure 77. Transmission Line Pulse Forming Network

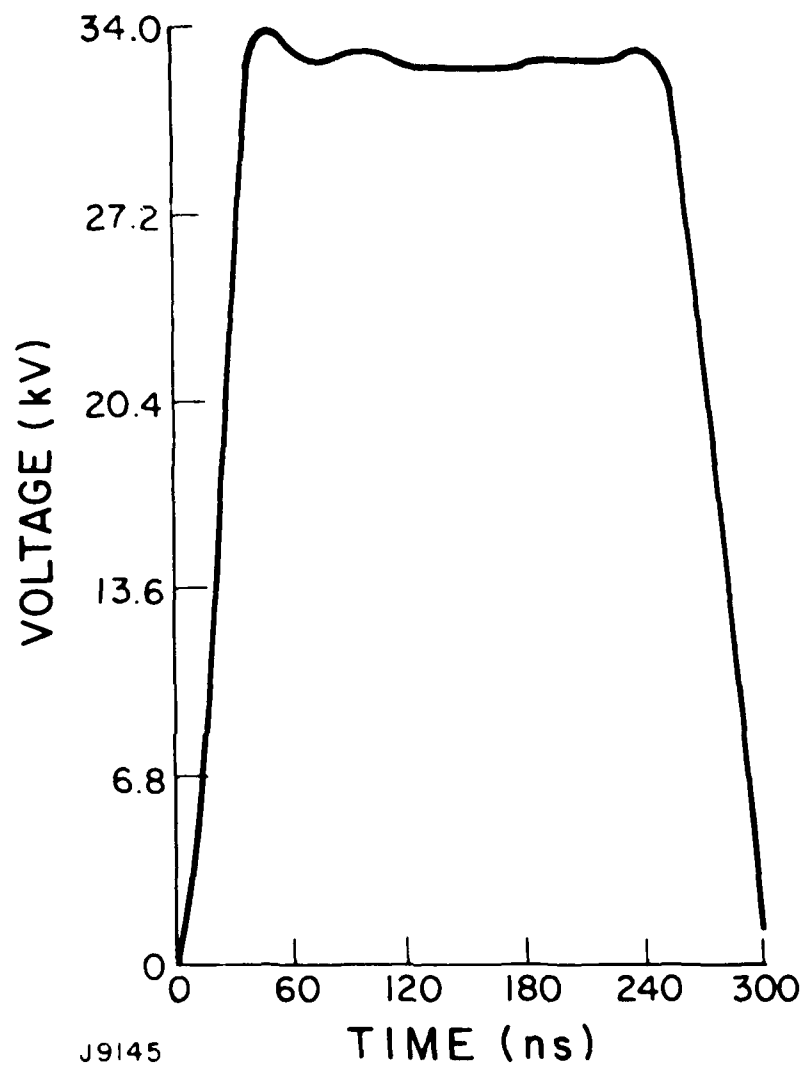


Figure 78. Performance of Unmodified Type B Network

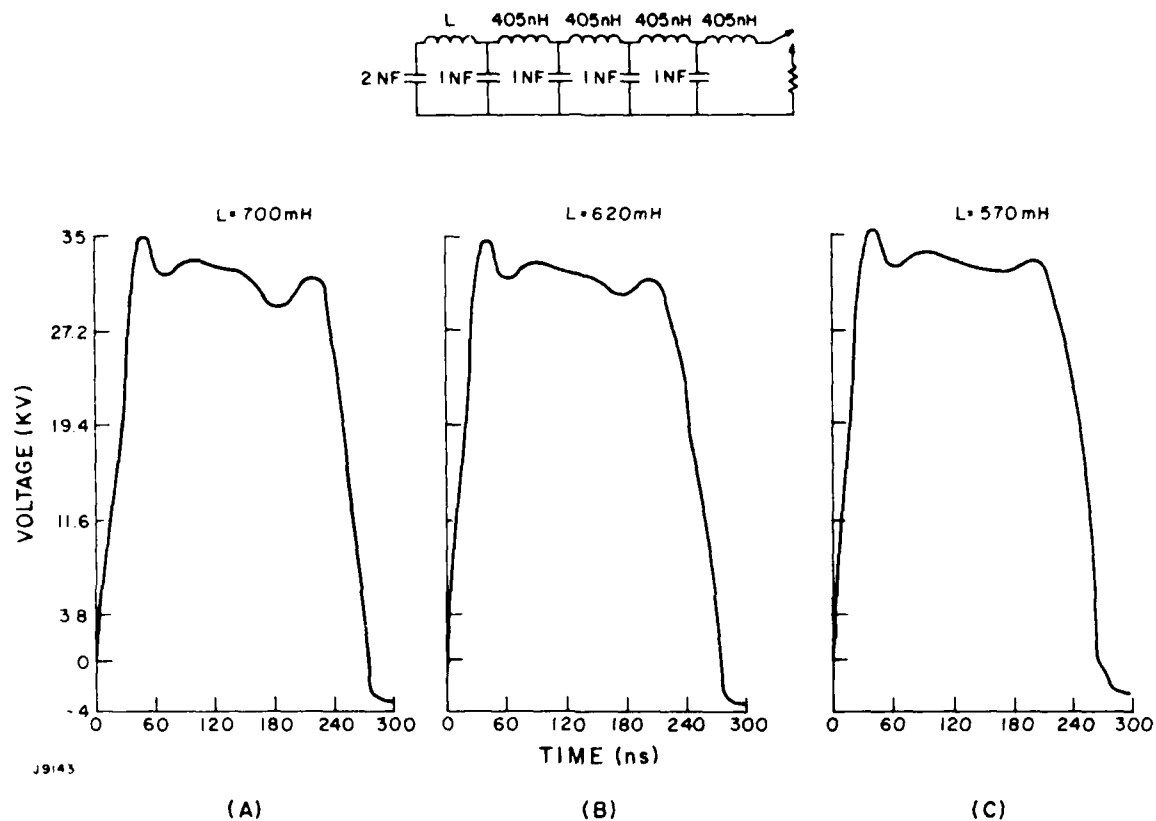


Figure 79. Performance of Modified Type B Network

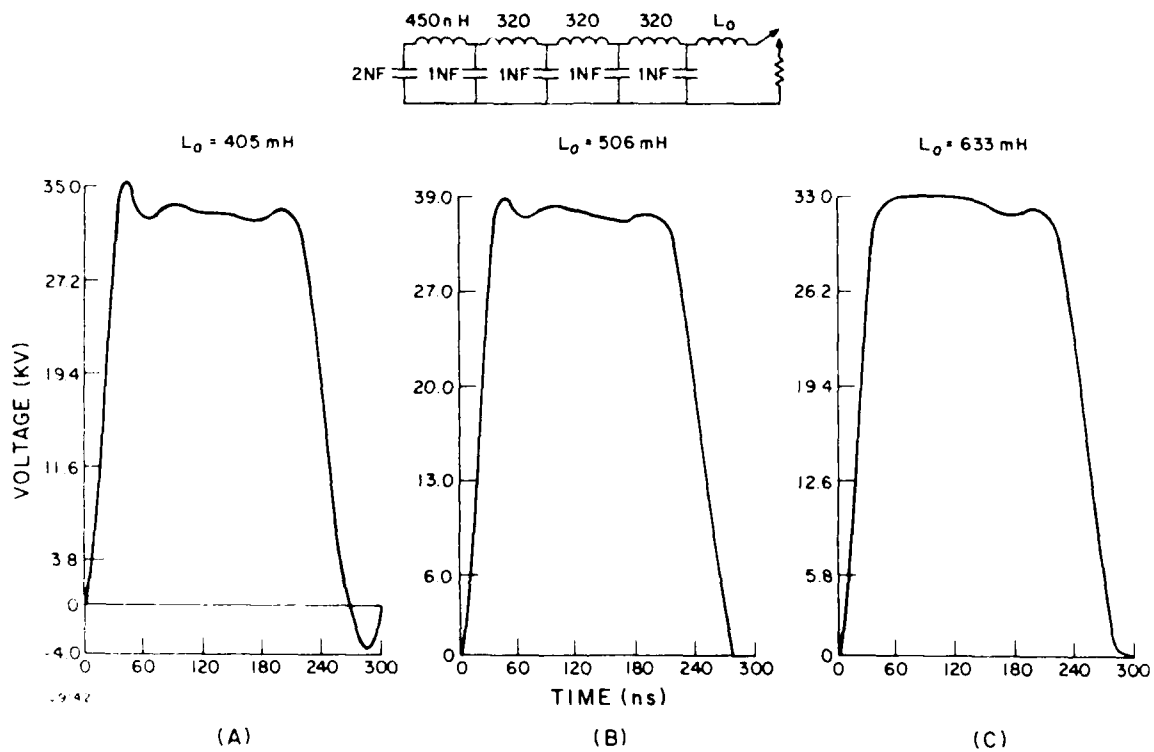


Figure 80. Performance of Modified Type B Network with Change in Output Inductor



203

plasma density and distribution at the onset of commutation (determined by the grid configuration and the method of triggering), 2) the plasma growth rate (determined by the fill gas pressure), and 3) the effective inductance (determined by the distribution of the internal discharge as well as by the geometry of the tube and its external current return).⁽³⁷⁾

To achieve minimum switching delay and maximum circuit di/dt , the tube must be designed for such operation and the correct method of triggering must be used.

To obtain the best initial conditions for commutation, the trigger discharge must establish a relatively high plasma density near the cathode surface. To obtain low inductance, the discharge must be spread over the cathode surface to the maximum extent. To aid this process, an auxiliary (or priming) grid is used. The auxiliary grid is located between the cathode and the control grid, and its geometry is designed to confine the trigger plasma near the cathode.

To fully form the discharge before commutation, the auxiliary discharge is prepulsed at a high current level. A high current auxiliary grid prepulse is necessary but not sufficient to achieve high di/dt . When the ion density near the grid baffle apertures reaches a value of $\sim 10^{11}$ ions/cm³, the tube will commutate, regardless of the state of the discharge near the cathode. If a weak auxiliary current is used (e.g., 20 to 100 mA), triggering density will not be reached, and a separate control grid pulse must then be used to trigger the tube. It has been reported that di/dt is lower when the trigger pulse is applied to the control grid as opposed to the auxiliary grid.⁽³⁸⁾

37. Turnquist, D., Caristi, R., Friedman, S., Merz, S., Plante, E. and Reinhardt, N., IEEE Trans. on Plasma Science, Vol. PS-8, No. 3, Sept. 1980.

38. Friedman, S., Goldberg, S., Hamilton, J., Merz, S., Plante, E. and Turnquist, D., Proc. IEEE Thirteenth Pulse power Modulator Symp. Buffalo, N.Y. pp. 129-134, 1978.

To prevent premature commutation, negative control grid bias is used. The effect of the bias is to lengthen the time available for the auxiliary current to grow and to spread ion the cathode. A small bias (~20 V) produces a small 4% increase in commutation delay, but a large 25% increase in di/dt .⁽³⁷⁾

A new model has been developed for the hydrogen thyatron that can predict the behavior of thyatron-switched pulse circuits. It is assumed that the thyatron can be modeled by two series elements 1) a constant inductance, dependent only on geometry, and 2) an exponentially falling resistance or voltage, with a time constant τ_i dependent only on gas pressure.⁽³⁷⁾

Thyatron specifications contain a "Plate Breakdown Factor," P_b , intended to limit anode dissipation to tolerable levels. Although it has long been recognized that this factor is inadequate to describe the problem, it has only recently been possible to quantify anode dissipation in high di/dt circuits. The results of this analysis is to replace the old P_b factor with a new factor, defined as

$$\pi_b = \text{voltage} \times \text{repetition rate} \times di/dt \text{ (epy prr } di/dt)$$

The model described in Ref. 37 has been used to calculate anode heating when switching a transmission line charged to a voltage, V . Defining a circuit time constant, L/Z (with L the total switch and connecting inductance, and Z the total impedance of the line plus the load directly across the switch), it can be shown that the anode dissipation energy per pulse, W , is a function of τ_i/τ_L as shown in Figure 82, and the power dissipation is directly proportional to π_b .⁽³⁷⁾ Anode dissipations consistent with the above calculation have been observed in practice for tubes operated at high di/dt . At a few tens of kilovolts with a fast circuit, the anode dissipation can become substantial, i.e., several hundred watts per kilohertz of repetition rate. The magnitude depends critically on τ_i , normally for thyatrons about 30 ns (corresponding to a 20 ns fall time). This can be reduced to at least 20 ns at higher pressures (> 0.6 torr). On the other

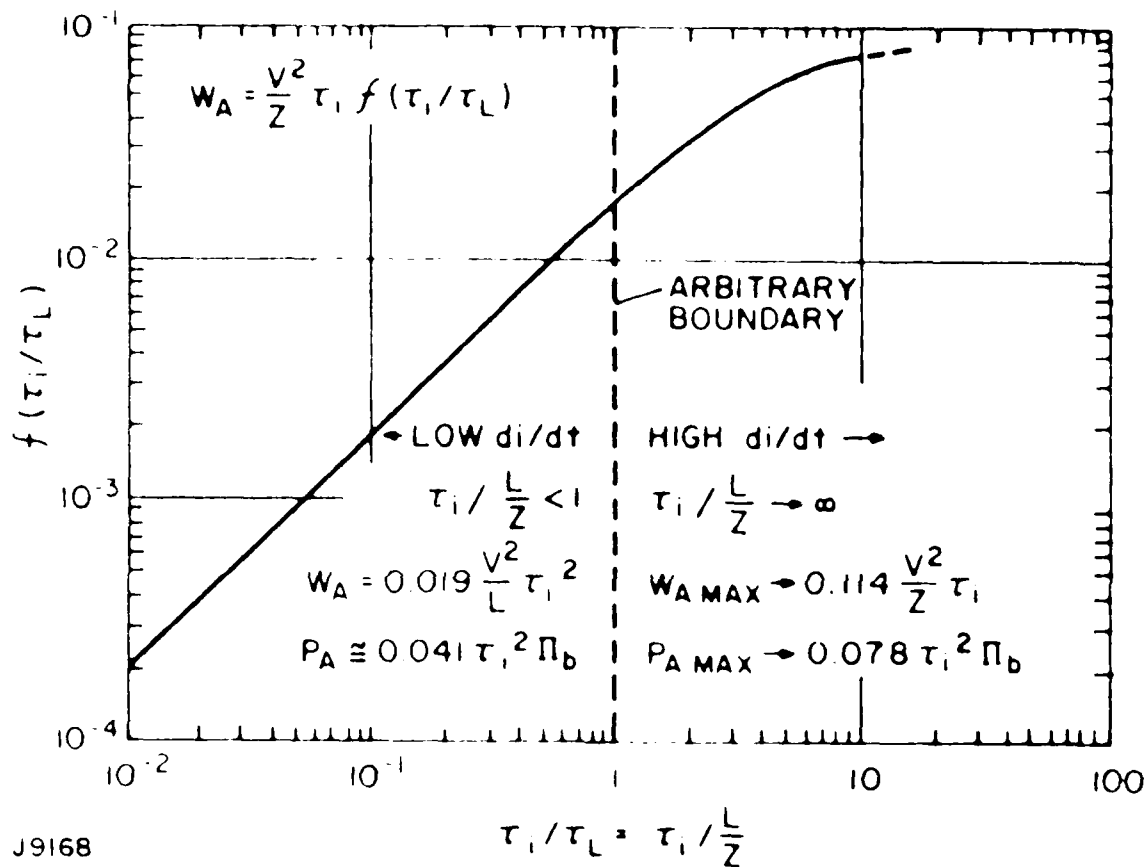


Figure 82. Anode Heating in a Transmission Line Circuit
(Adapted from Ref. 37)

hand, reduction of pressure can cause much higher r_i , with the resultant high dissipation causing excessive anode heating. Thyratrons for fast switching applications must therefore operate at relatively high fill pressures to minimize anode dissipation as well as to promote high di/dt .

If the initial plasma conditions are properly established during triggering, and the resistive fall limit is not reached, then the self-inductance of the tube and its current return will dominate the switching operation. The inductance can be calculated from the physical dimensions of the discharge and the current return, making the assumption that the discharge fills the tube to the diameter of the grid apertures.

Some recent results at Los Alamos⁽³⁹⁾ have shown that the number of pulses that a thyatron can switch before ceasing operation under high di/dt operation is a function of repetition rate in some thyratrons. Examination of the thyatron components after testing at high di/dt and high-repetition rates shows erosion of the tips of the cathode structure. The tubes used (EG&G) have a complex interleaved cathode structure designed to give the maximum cathode area in the minimum space. This suggests that the current under high di/dt operating conditions is supplied primarily by the tips of the cathode structure. At high-repetition rates heated generated at the tips of the cathode structure would not have time to thermalize and spread uniformly throughout the cathode structure, thus resulting in excessive temperatures at these points and therefore erosion. This further suggests that thyratrons with a less complex and more rugged cathode structure may have longer lifetimes under high di/dt and high repetition rate conditions.

The thyatron manufacturer ITT can supply a thyatron which meets our design point requirements in the line pulser configuration. The ITT data is derived from thyratrons on the Stanford

39. Private Communication, McDuff, G., 1981.

linear accelerator where $\sim 10^7$ hr of life data has been obtained. For the design point conditions the thyatron lifetime extrapolates to 2×10^4 hr at 100 Hz, which is 7×10^9 pulses.

4. Modulator Efficiency

The loss power of individual modulator components has been calculated in detail and is summarized in Table 10. The modulator delivers a power of 10 kW to the laser discharge, and hence its overall efficiency is 89%.

TABLE 10. ENERGY BUDGET FOR MODULATOR

<u>Item</u>	<u>Loss (W)</u>
Power Transformer	200
High-Voltage Rectifier Diodes	30
Charging Choke	28
Charging Thyatron - Filaments	136
Reservoir	35
Conduction	~ 1
Damping Networks and Stray Capacitance	100
Energy Storage Capacitor Losses	5
Output Thyatron - Filaments	441
Reservoir	68
Commutation	100
Conduction	45
Control Circuitry	<u>100</u>
TOTAL	1289

J. GAS CLEANUP/MAKEUP

1. Chemical Processes

In order to efficiently use the HgBr laser for space applications it will be necessary to reuse the laser mixture many times. The most extended efforts to address the issue of the gas mixture recyclability involve experiments currently underway at NOSC.⁽⁴⁰⁾ The drop-off in output power as a function of time is analyzed for a UV preionized discharge pumped laser⁽⁴⁰⁾ which is repetitively-pulsed at ~ 40 pps. The laser mixture, $\text{HgBr}_2/\text{N}_2/\text{Ne}$, is circulated around a flow-loop to remove the excess heat produced in the discharge. When the laser is turned on the output energy is ~ 35 mJ/pulse. This corresponds to an intrinsic efficiency of 0.7%. This is near optimal for this type a system operated in a single pulse mode.⁽⁴¹⁾ The laser power drops to the half power point in about 45 min, or 110,000 shots. The ratio of the discharge volume to the flow volume is about 1 to 300, so that each discharge volume ($\sim 45 \text{ cm}^3$) can be used ~ 350 times before the power drops to 50%. This suggests that in order to maintain the output to at least 90% of its initial value, 1.5% of the mix must be continually replaced or purified.

The laser system proposed here has an average discharge volume flush factor of 3.5 (flush factor of 1.75 at 200 Hz) so that, after accounting for the higher J/l, $\sim 0.7\%$ of the flow must be processed. Figure 83 shows the correlation between the fraction of the flow removed and the mass of HgBr_2 which must be handled for 10^8 shots. From this graph it can be seen that if 0.7% of the flow is processed, 800 kg of HgBr_2 must be either replaced or purified and returned to the system.

40. Celto, J.E., private communications.

41. Schimitschek, E.J. and Celto, J.E., Appl. Phys. Lett. 36, 176 (1980).

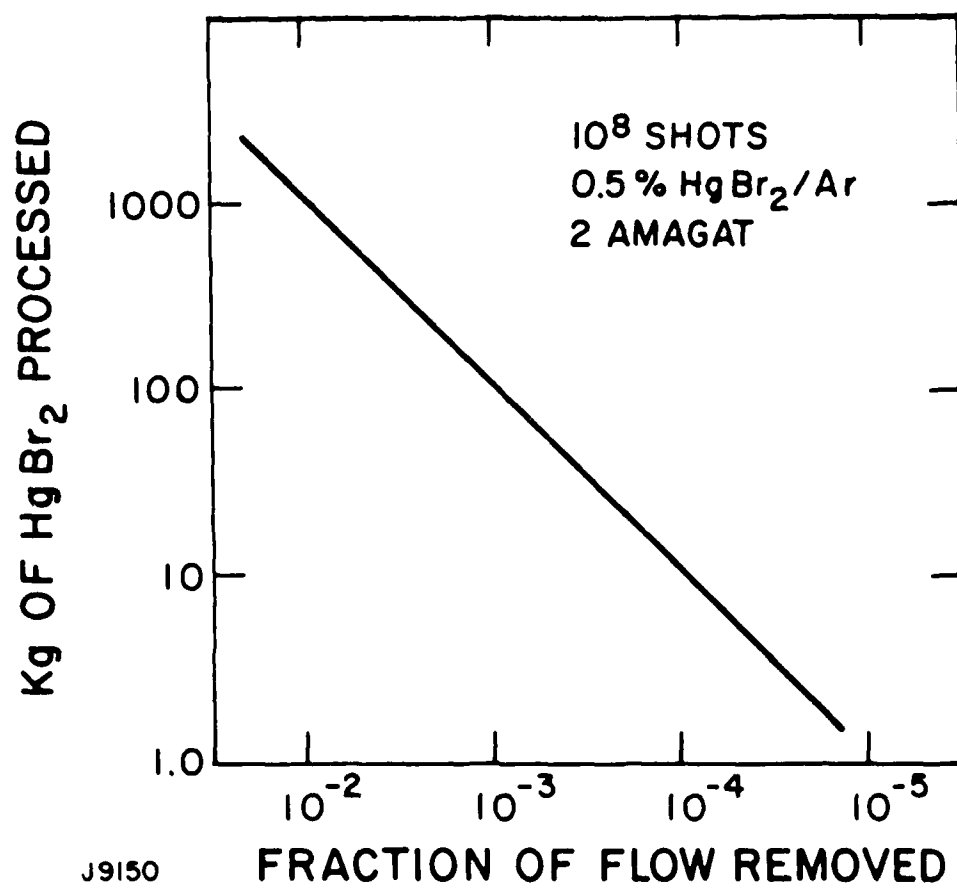
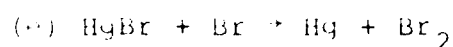
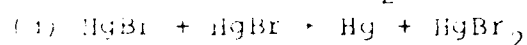
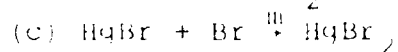
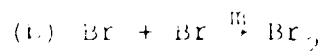
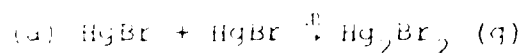


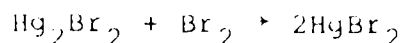
Figure 83. Amount of HgBr₂ Processed vs. Fraction of the Flow Removed

In order to evaluate what possible purification or replenishing procedures are necessary and to see how to make improvements on the recyclability, it is necessary to look at the chemical reactions involved in the regeneration of HgBr_2 from the excitation products. Model calculations indicate that $\sim 20\%$ of HgBr_2 molecules in the discharge region will end up as $\text{HgBr}(x)$ and Br . The following reactions are then possible from the interaction of HgBr and Br .



The rate constants for reactions (a) and (b) have been measured and found to be $1.5 \times 10^{-30} \text{ cm}^6 \text{ sec}^{-1}$ (42) and $1 \times 10^{-32} \text{ cm}^6 \text{ sec}^{-1}$ (43) respectively. The rate constants for the other reactions are not known so that it is difficult to estimate the relative importance of these processes. However, reasonable estimates of the rate constants would indicate that these processes would go to completion in a few tenths of a millisecond. This would then leave a mixture of HgBr_2 , Hg , Br_2 and Hg_2Br_2 in the argon buffer gas.

There is the possibility that Hg_2Br_2 could react ion the discharge with Br_2



or with Br



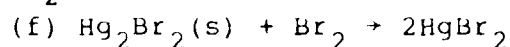
However a large portion will most likely condense on the walls of the flow-loop. Then, depending on the local Hg density, the Hg_2Br_2 will remain on the walls as a solid or decompose into

42. Greig, G., Gunning, H.E., and Strausz, O.P., J. Chem. Phys. 52, 3684 (1970).

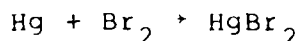
43. Clyne, M.A.A., and Woon-Fat, A.R., Trans. of Faraday Soc.

Hg and HgBr_2 . The deposition of Hg_2Br_2 in the flow-loop was observed in the NOSC⁽⁴⁰⁾ apparatus as soon as the laser was turned on. Data for the vapor composition⁽⁴⁴⁾ over Hg_2Br_2 also indicates that, under the temperature and HgBr_2 pressure conditions of the proposed system, if the local Hg pressure rises to 0.4 torr, Hg will react with HgBr_2 to condense out as Hg_2Br_2 .

Br_2 will react with the solid Hg_2Br_2 at the walls.



This process was observed in supplementary experiments at NOSC.⁽⁴⁰⁾ Also possible is the direct reaction



However, it is expected that, as was the case for $\text{Hg} + \text{Cl}_2$,⁽⁴⁵⁾ this reaction will occur only at the walls and thus the rate is limited by the collision frequency with the walls.

The processes outlined thus far show how the system can return completely to the thermodynamically favored state of pure HgBr_2 in argon. However, there is not sufficient data to determine the rate of the final recombination process and thus it is not known what the quasi-equilibrium concentrations of Hg and Br_2 will be in the following system. Since Hg could interfere with the $\text{HgBr}^*(B)$ production and Br_2 could be a significant absorber, it is important to determine the rates of the wall reactions under the proposed conditions.

What is clear from this analysis is that if either Br_2 or Hg is removed from the cycle, then a decrease in laser output will result. Therefore, the materials used in the laser system must not only be unreactive with HgBr_2 , but also with Hg and Br_2 . Reactivity could result in a loss of HgBr_2 or the production of absorbers such as Br_2 or a volatile metal halide. The NOSC laser apparatus had tungsten and stainless steel in contact with the flowing gas.

44. Lewis, J.S., *Icarus*, 11, 367 (1969).

45. Medhekar, A.K., Rokni, M., Trainor, D.W., and Jacob, J.R., *Chem Phys. Lett.* 65, 600.

Since tungsten reacts with Br_2 at their temperature⁽⁴⁰⁾ and stainless steel will react with both Br_2 and HgBr_2 , reactions with these metals is a likely cause for the decrease in laser output they observed.

Experiments designed to test various metals for use as electrode material were conducted at Westinghouse Laboratories.⁽⁴⁶⁾ Electrodes made from the material to be tested were vacuum sealed inside a quartz cell with enough HgBr_2 to fully vaporize and provide a pressure of 1-2 torr at the 175°C operating temperature. Discharge voltage was capacitively coupled to the electrode from a 100 kHz high-voltage supply. The electrode materials tested were stainless steel (304, 316), molybdenum, platinum, and nickel. Of these, only platinum allowed extended running of the discharge without loss of $\text{HgBr}^*(\text{B})$ fluorescence. With the other materials the HgBr^* fluorescence severely decayed in a few hours with an accompanying appearance of several mercury emission lines.

The results of these experiments indicate that platinum will be a good material to coat the metal surfaces in the laser cavity and flow-loop. Additional evidence in support of this comes from data on the surface chemistry of platinum. Measurements of the mercury vapor decomposition pressure for various platinum mercury amalgams⁽⁴⁷⁾ indicated that at the maximum mercury pressure allowed by the Hg_2Br_2 condensation (0.4 torr), no amalgams will form.

Possible reactivity of platinum with bromine is not clear. Br_2 is known to react with Pt⁽⁴⁸⁾ at $\sim 150^\circ\text{C}$ to form PtBr_4 . However, this compound is unstable above 180°C and PtBr_2 is formed. This compound is likewise unstable above 250°C . Unfortunately, both gold and platinum show a maximum in

46. --- LBN, C.S., private communications.

47. Jangq, V.G. and Dortbudak, T., *Metallkd*, 2, 64, 715 (1973).

48. Canterford, J.H. and Colton, P., *Halides of the Second and Third Row Transition Metals*, (John Wiley and Son Ltd., London (1968)).

the rate of corrosion in Cl_2 at the temperature at which the corresponding chloride decomposes.⁽⁴⁹⁾ The success of the Westinghouse experiments with platinum electrodes is most likely due to the reaction of the PtBr_2 formed with Hg to form the more stable HgBr_2 . In this way, platinum may play an important role as a catalyst to enhance the otherwise slow recombination $\text{Hg} + \text{Br}_2$.

With the return of platinum metal to the surface by the reaction of PtBr_2 with Hg there will be no net loss of platinum. However it is not clear what affect this process may have on the protective function of a platinum coating. In the flow-loop, the coating can be made thick enough so that the integrity of the coating can be maintained.

It is clear from this discussion that all the metal surface should be coated with platinum. The electrical insulators for the electrode support can be made out of alumina. Because of the porous nature of the surface of this material, it may be necessary to allow for a certain amount of seasoning during the laser setup phase, but there is no evidence to suggest any reactivity between alumina and the other species present. The MgF_2 overcoating on the cavity windows is expected to be likewise inert.

By constructing the cavity and flow-loop out of materials which do not chemically interfere with the reaction mix it should be possible to greatly improve on the recyclability over that observed in the NOSC experiments.

However, additional problems could arise from outgassing of H_2 from the metal surface. The H_2 will react with Br_2 to form HBr . There are two possible sources of the H_2 . One is the hydrogen dissolved in the stainless steel during the fabrication process and the second is hydrogen infused into metal during electroplating.

49. ASTM, H.B., Corrosion Handbook, (John Wiley and Sons, New York, 1946).

The first source can be taken care of by baking all the metal parts prior to electroplating. The outgassing rate has been measured for stainless steel baked under varying conditions.⁽⁵⁰⁾ In order to keep the pressure of HBr to $< 10\%$ of the HgBr_2 density in 10^8 shots, it will be necessary to limit the outgassing rate to $< 1 \times 10^{-9}$ torr liter $\text{cm}^2 \text{ sec}^{-1}$. The data in Ref. (50) indicates that this outgassing rate at 490°K can be obtained by baking the stainless steel for 16 hr at 400°C .

The amount of the H_2 infused into the stainless steel during electroplating can not be handled in the same manner because the integrity of the coating may not withstand the high temperatures necessary for the outgassing process. However, since the electroplating is done for only a few hours at near room temperature, the amount of time to release this gas will be correspondingly short, especially after bringing the laser system up to the operating temperature.

The difficulties of outgassing H_2 can be taken care of by baking all metal parts before plating and by allowing the final system to be pumped on at operating temperature for a few days before running the laser.

2. Gas Cleanup System

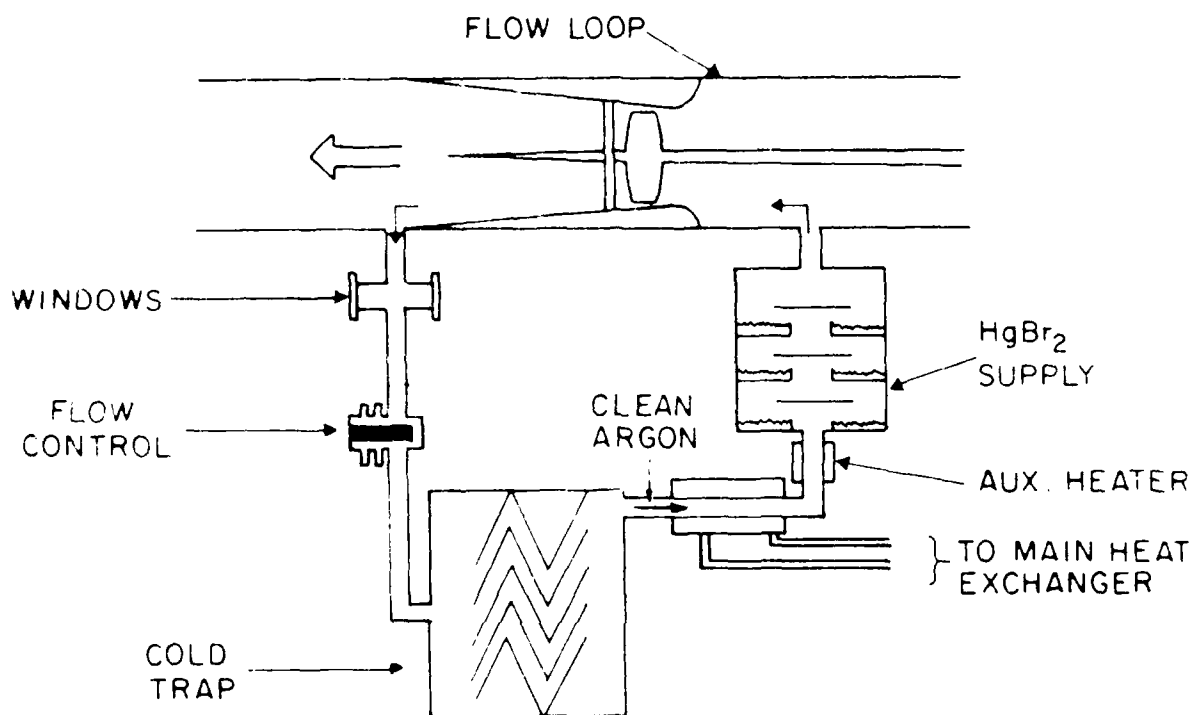
The discussion above has indicated that the use of nonreactive materials such as platinum, alumina, and glass in the laser system should allow the laser mix to be recycled indefinitely. Some difficulties however could arise such as porosity or cracking in the metal protective coating, unexpected secondary reactions, or slow outgassing of some components. These processes could introduce impurities into the flow stream and thus reduce the laser output during the course of the long life test.

50. Power, Bd., and Robson, F.C., 1961 Vacuum Symp. Trans., p. 1175, 1962.

For this reason, the flow-loop will be equipped with a system for trapping out all the material from a certain fraction of the flow and replenishing it with pure HgBr_2 . By analyzing the material trapped, it will be possible to determine the source of any such impurity so that modification can be implemented accordingly. It should then be possible to reduce the fraction of processed flow to the point where the trapped material can be thrown away. If this is not possible then the analysis can be used to design an HgBr_2 purification scheme.

A schematic of the trapping/replenishing system is shown in Figure 84. A fraction of the flow enters the system from the high pressure portion of the flow-loop. In this first segment of the purification line there will be a set of sapphire windows which will allow transmission spectra to be taken of the gas flow. This information will be used to monitor the HgBr_2 density as well as detect and identify impurities. A throttle valve in the line will be used to control the fraction removed. The gas then enters the trap. Most of the possible contaminant will have low enough vapor pressures to be effectively trapped at room temperature. This includes, in addition to the HgBr_2 , materials like metal halides and organic oils and greases. If analysis of the gas flow indicates lower temperatures are necessary, a second trap will be added in series. At this point the gas is reheated by using a portion of the laser waste heat removed by the main heat exchanger in the flow loop. Pure HgBr_2 supply canister is adjusted to provide the correct HgBr_2 density in the laser system. The fresh HgBr_2/Ar mix is then returned to the system on the low pressure side of the flow-loop.

The system will be designed to handle 5 kg of HgBr_2 . This is the amount of HgBr_2 which would have to be added to the system if 5×10^{-5} of the flow was processed for 10^6 sec of operation. However, because the trapping system will be used as a diagnostic tool in the early phases of testing, it will be designed to effectively trap out 10^{-3} of the flow (for a correspondingly shorter period of time).



J9160X

Figure 84. Schematic of Flow Purification Cycle

The amount of power which must be extracted from the gas mix in the trap is approximated by the following expression

$$Q = \dot{n}_{\text{Ar}} C_p \Delta T + \dot{n}_{\text{HgBr}_2} \Delta H_{\text{subl}}$$

where \dot{n}_{Ar} and \dot{n}_{HgBr_2} are the molecular flow of argon and HgBr_2 , respectively, C_p is the heat capacity of argon, ΔH_{subl} is the heat of sublimation of HgBr_2 and ΔT is the temperature. If the fraction of the flow processed is 5×10^{-5} , and the trap is kept at 300°K then the power removed from the flowing gas is 14 W. This power can be dissipated by a 150 cm^2 radiator at room temperature.

K. OVERALL SYSTEM DESCRIPTION AND PERFORMANCE

In this section we want to (a) summarize the overall operating characteristics of the laser system, (b) summarize the design issues associated with long lifetime reliability, and (c) relate the features of our design to an actual space based SLC application.

1. Efficiency

In Table 11, we have listed the power consumption of each subsystem for the design operating conditions.

First, the discharge power listed represents the average power consumed by the entire pulsed power system in transferring a net 10 kw from wall plug to the laser device terminals. At these terminals, the laser device is projected at 2.08% efficiency so we calculate 208 W output. The power consumption figures consider power supply transformer and diode losses, charging inductor and storage capacitor losses, switching losses and the filament heater requirements for the thyatron switches. Also, trigger generator losses are included in the power consumption figure for the pulsed power, thus it is a true wall plug calculation considering all inputs to this system.

The second power in the table is the wall plug power consumed by the pumping systems as required to provide cooling flows for the heat exchanger and the main flow. These systems are sized for an average 100 Hz but the main loop flow is sized for a minimum interpulse time (i.e., 200 Hz flow capacity). The pump motors and fan efficiencies are rated at conservative values. The main loop fan has been designed to provide flow for a conservative flush factor of 1.75 and also provides the excess flow required for the cathodes, gas cleanup, etc.

The heat exchanger pressure drops and corner turning pressure losses in the flow-loop are based upon accepted design calculation approaches. Thus, we believe the calculated loop pump power losses represent an accurate design estimate. The heat exchanger cooling flow power calculation is based upon accepted design methods and similarly should be an accurate estimate.

TABLE 11. TOTAL POWER CONSUMPTION 2 J/PULSE

	(kW)
Discharge Pulse Power	11.29
Flow-Loop	1.56
E-Gun	3.59
Magnet	0.65
Injection Laser	.24
Controls	<u>.2</u>
TOTAL	17.53 kW
Laser Output Power	208 W
Overall Efficiency	1.19%

Cooling fluid pump power can be significantly reduced by special pump development not proposed here. However, additional losses may be required to circulate the coolant to radiators on the spacecraft. As these powers are liable to be small, we consider these two issues to be a wash.

The third power listed in Table 11 is the power consumed by the e-beam. This power includes the actual e-beam current, the heater losses, all foil transmission losses and the losses associated with the e-beam power supply and modulator. We do not include the power associated with the vacuum pumps, even though it is relatively negligible, since we feel this would not be an issue for the space based SLC laser.

The fourth power consumption listed is associated with the superconducting (SC) magnet. In this case we refer to a NASA design report for the projected cooling requirements for a space based 4°K refrigeration system. This reference provides a design value for the spacecraft bus power necessary to provide our projected requirement of SC cooling at 4°K .

The fifth power listed in Table 11 is the power required for the narrowband oscillator. This is an overall figure based upon reasonable design estimates for this system.

We have also included an arbitrary 200 W allowance for controls, alignment systems, etc. As these systems would be solid state and inherently low loss, this seems generous.

The total power consumed by all components necessary to make the laser work in the space based environment is 17.5 kW. The projected power out is 208 W. The projected overall efficiency is 1.2%.

2. Beam Quality

In the proposed design narrowband single transverse mode light is injected into the unstable HgBr oscillator for the first 50 ns of the 250 ns pulse. Provided that the injected frequency is at the gain maximum of the 502 nm band feature the transverse round trip gain at this maximum will be unity, and the injected frequencies will not increase further in amplitude, and the oscillation

loss. The frequency stability is thus assured throughout the pulse. Further discussion of this is given in Appendix C.

It is possible to estimate the phase and amplitude uniformity of the unstable oscillator output during the latter 200 ns of the pulse. This is controlled by imperfection in the optics and phase distortion in the gaseous medium. Medium distortion is discussed in Section III-E-1. As a starting point the modes of the design point resonator have been computed using the standard integral methods. Figure 85 shows the computed⁽⁵¹⁾ lowest order mode intensity profile in the smaller transverse dimension (4 cm). The 6 cm dimension shows smaller peak-to-peak intensity fluctuations. Phase excursions across the mode are $< \pm 10^\circ$.

When a random phase perturbation is introduced to the resonator there is a degree of multiplication of the error during the several transits made before exit. Because the light passes through different transverse positions the errors are not always cumulative, but add in an appropriate rms fashion. A treatment has been given⁽⁵²⁾ for aberrations which are uniform along the optical axis and which are separable in the x and y coordinates. The aberration $F(x,y)$ in the plane just before the convex feedback mirror and in the limit of a geometric mode, is given by

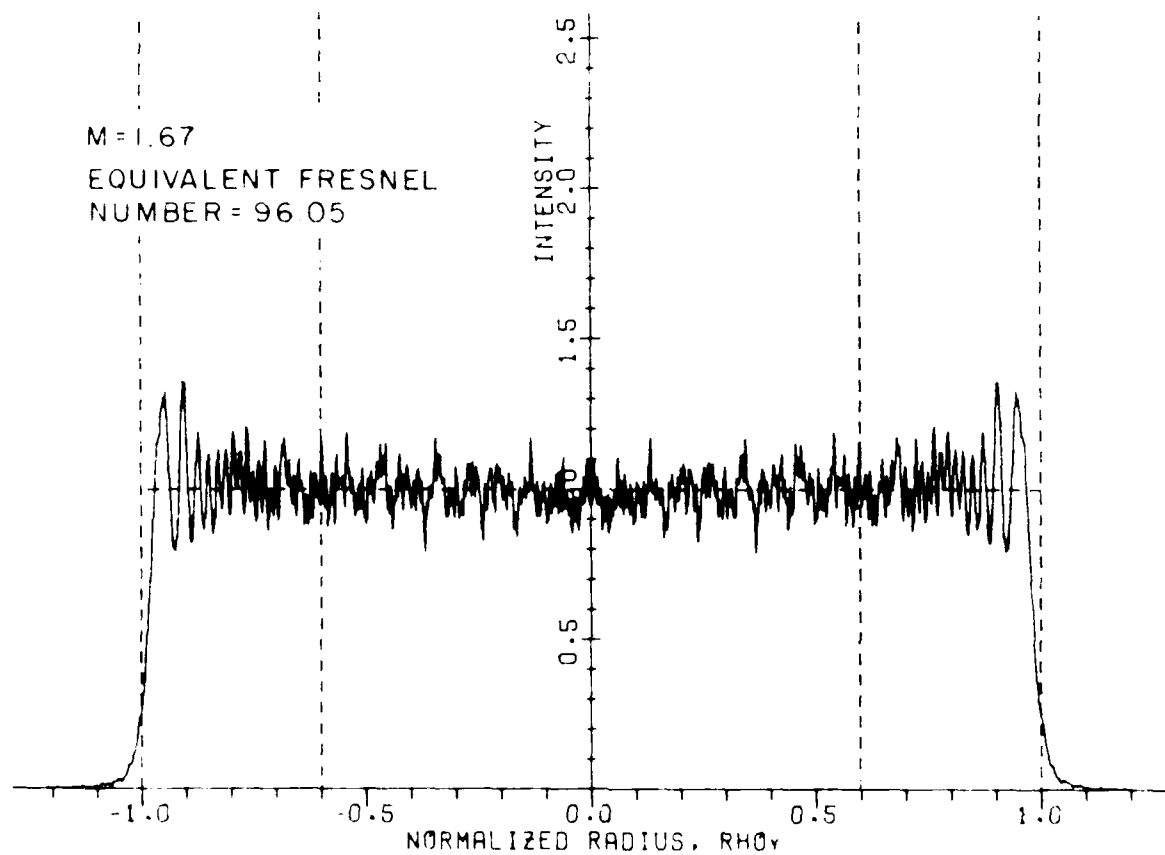
$$F(x,y) = \sum_{k=1}^{\infty} \alpha_k (F'_{xk} x^k + F'_{yk} y^k) \quad (67)$$

where

α_k = effective number of optical passes of k^{th} order aberration

51. AERL Resonator Code

52. Anan'ev, Yu.A., Sov. T. Quant. Elect. 1, No. 7, p. 565 (1972).



J9184

Figure 85. Computed Intensity Profile for 4 cm Dimension of Design Point Unstable Resonator

$$= \frac{1}{(M^k - 1)} M^k + \frac{M^{k+1} - 1}{(k+1)(M-1)}, \quad \begin{array}{l} \text{confocal positive branch} \\ \text{unstable resonator} \end{array}$$

$M =$ mode magnification $= 1/\sqrt{1-L_c}$ and L_c is the geometric output coupling

$F'_{xk}, F'_{yk} =$ one pass k^{th} order aberration coefficients of power series expansion of aberration. The coefficients α_k are plotted in Figure 86 as a function of M and k . For our design point $M = 1.67$ and the scale length for phase perturbations is such that $2 \lesssim k \lesssim 4$ applies, so we derive an aberration multiplier of 2 from Figure 86.

At this point it is appropriate to specify the phase uniformity requirement to give a 10 (XDL) far field divergence. In the first instance we consider the effect of the output mirror obscuration on the far field pattern.

The relationship between the normalized phase error correlation length (L) and the allowable peak-to-peak variation in waves ($2A/\lambda$) is given fairly well by the geometric sinusoidal approximation (derived in Section II-E-1):

$$\frac{2A}{\lambda} = (0.78) (\text{XDL}) L$$

where (XDL) is 10 and A is the amplitude of the optical perturbation (80% of energy within (XDL)). This result follows from three separate treatments which give consistent results:

1. Assumption of sinusoidal phase error
2. Use of a random phase error with a Gaussian distribution over the aperture
3. Computer simulation with specific bumpy wavefronts

By this criterion using the anticipated perturbation normalized scale length $L = 0.2$ we find the maximum allowable peak-to-peak variation = 1.56 waves. When we fold in the aberration multiplier of 2, we require a single pass homogeneity of 0.78 waves.

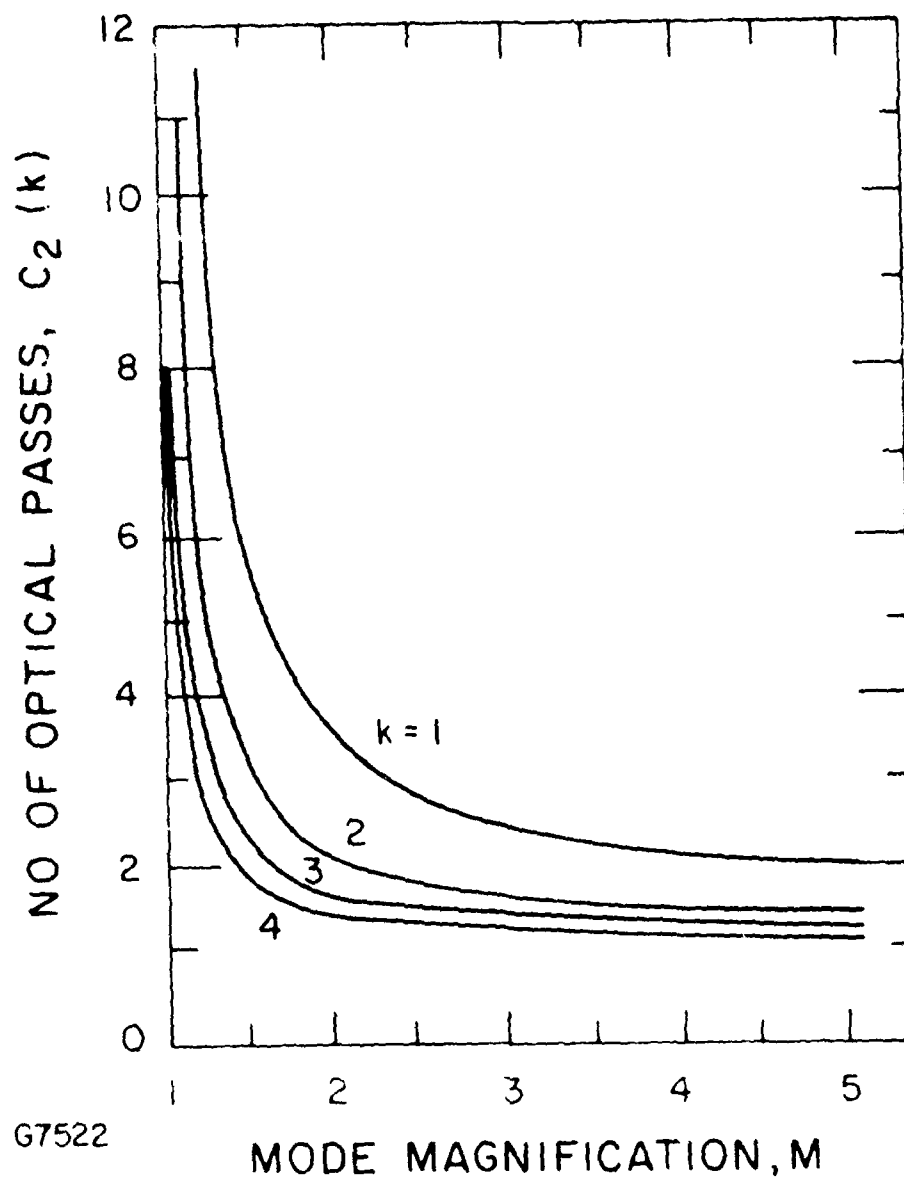


Figure 86. Aberration Multiplier for Unstable Resonators. These represent the effective number of passes seen by a particular order aberration.

The present design for 10 (XDL) allows the use of a centered output coupling mirror. The effect of a centered obscuration on the far field energy distribution⁽⁵³⁾ is shown in Figure 87. The resonator design point has $L_c = 1-M^{-2} = 0.67$. From Figure 87 we note that 95% of the far field energy lies within 10 (XDL) and 90% lies within 5 (XDL).

When we fold together the effects of center obscuration and random phase-front error at the exit plane, the rms addition modifies the optics plus medium homogeneity requirement downward to ~ 0.70 waves in a single pass. It is to be noted that the use of a corner obscuration is substantially better than a center obscuration and that it should be considered for the production of higher quality beams, when they are required.

From above, both the mode phase front and the centered obscuration contribute appreciably < 10 (XDL) to the far field divergence. The principle contributors to far field divergence are medium homogeneity and optical imperfection, which between them must contribute < 0.70 waves, peak-to-peak across the resonator aperture. In Section III-E, 0.55 waves have been allowed for medium inhomogeneity due to the gas flow, and the predicted phase-front distortion is rather less than this. The surface flatness of the intracavity windows and the laser mirrors can be as good as $\lambda/20$ within current polishing technology. There are two windows within the cavity (4 surfaces) and two mirrors (equivalent to 4 surfaces). The window material, sapphire, can have good bulk optical homogeneity ($\pm \lambda/10$ in selected pieces). An rms addition leads to the optics phasefront error = 0.22 waves. This is less than the optics budget of 0.43 waves which is allowed after the 0.55 waves flow budget is removed from the total 0.70 waves (rms addition).

5. AERL Computation

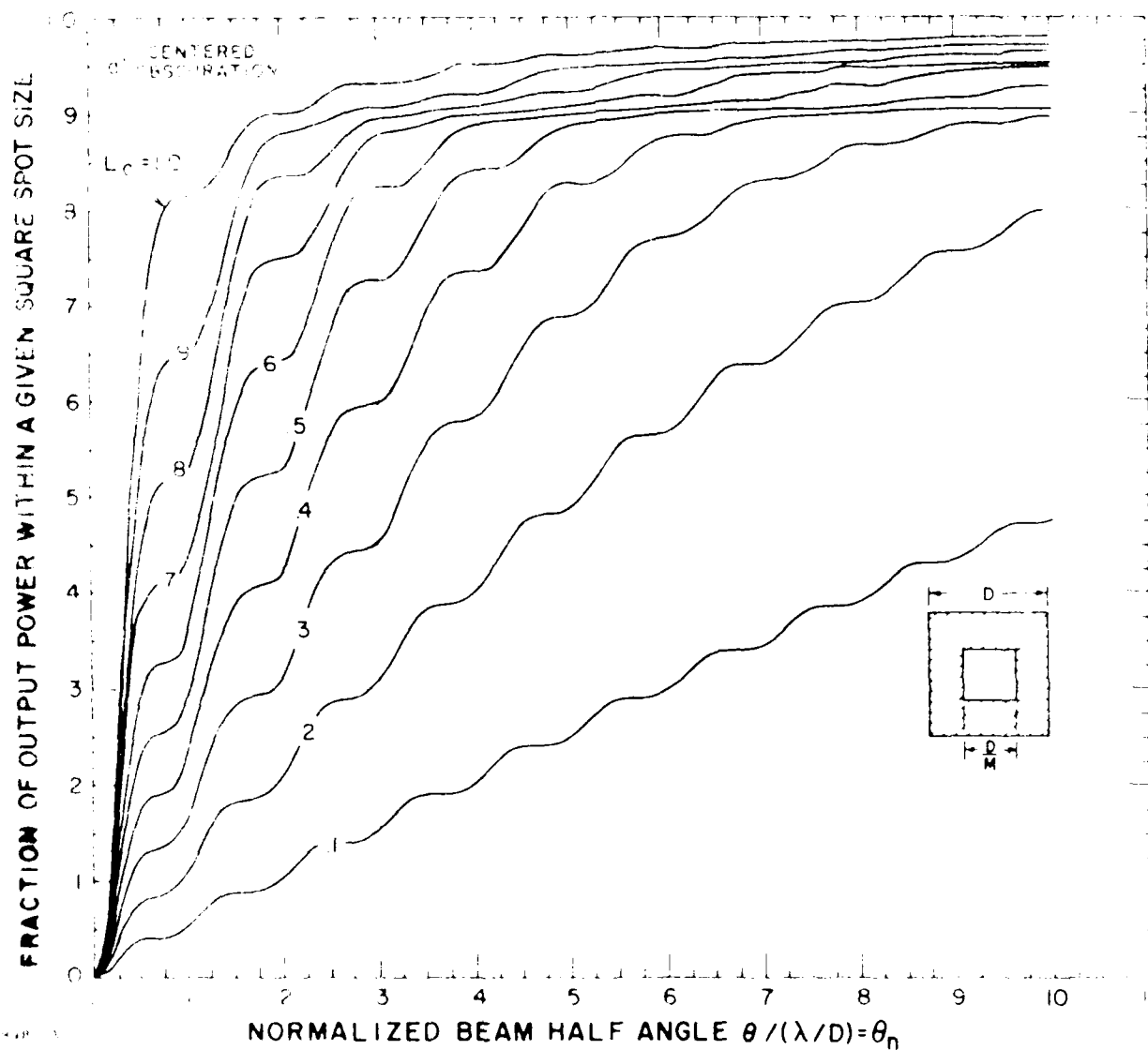


Figure 87. Far Field Encircled Energy as a Function of Spot Size, for Centered Feedback Mirror Resonator

The near-field intensity profile has diffraction fluctuations near the edges (Figure 85), which will wash out in the far field and in any case can be greatly reduced by "softening" the mirror edge. From Section III-C-1 the discharge uniformity is good to $\pm 20\%$ over the whole aperture, and this will apply to the near-field laser output, given the small allowed phase perturbations and the correspondingly small angle perturbations on geometric rays.

Thus, we project that the beam quality requirement of 80% of the beam energy within $10\times$ diffraction limit far-field divergence can be met comfortably by the present design.

3. Lifetime

For this design we have addressed several key issues in order to project the 10^8 lifetime required of this laser.

First, we have addressed the issue of pulsed power component selection required to achieve 10^8 shots, with ultimate capability of 10^{10} shots.

We have elected thyratrons to drive our system as these devices are known to provide reliable, predictable operation for times exceeding 10^9 pulses in radar and other applications. Under the conditions of our proposed design we project, based upon manufacturer's data, $\sim 8 \times 10^9$ shot lifetime. Longer life, if necessary, can be achieved via redundancy and this is implicit in our approach.

The other components of the modulator circuit are inductors, diodes, etc. operating under no particular stress. Thus, as is usual in power supplies, if their environment is properly controlled, these components should provide many years of service reliably.

The modulator for the e-beam involves ~ 20 J/pulse if the e-beam is pulsed. Thus the modulator can be one-fifth of the discharge modulator by coupling it to the e-beam via a pulse transformer. While the pulse e-beam voltage is large, 300 kV, it is not excessive and should not represent a lifetime issue for this transformer after reasonable development.

The e-beam itself has unknown questions concerning vacuum breakdown. As the energy available on a vacuum arc-over is small (~ 20 J) negligible damage to the electrodes is expected from a vacuum arc. Data exists for ion accelerators used in neutral beam injectors (for magnetic fusion) which indicates rapid voltage standoff recovery to the original operating conditions when little energy is involved in an arc. Thus, while occasional "tics" may occur, the system should recover and they should be very infrequent; much less than 1% of the pulses.

The most often mentioned concern with e-beam sustained discharges is survivability of "that thin foil." This concern is addressed in our design in two ways. First, we indicate that experience with the Phase I cavity shows that arcs of very large energy do not damage the foil. This observation is consistent with many other devices at AERL where 10's of kilojoules are required in an arc to the electrodes to cause collateral foil damage. As we will have only 100 J available/pulse we anticipate no foil problems from arcs.

The other potential source of problems for a "thin foil" is the pressure induced stress. The static stresses and the temperatures involved in this laser design lead to negligible creep for the foil material chosen. Thus, creep is not a lifetime issue. Dynamic stresses have been calculated and shown to be within safe limits even when extrapolated to 10^{10} shots.

The final key issue in long duration running/reliability is the impact of $HgBr_2$ and its fragments on the loop components and the impact of any resulting corrosion products on laser performance.

Data is limited concerning this corrosion. However, we have designed for the best known materials and anticipate that the resultant corrosion will be very low. To meet the present program objective, we need to reduce the buildup of poisons in the laser and by only a factor of about 100 over NOSC data. The experiment on which the NOSC data was taken was made of such materials as stainless steel.

Westinghouse data shows stainless is a very bad actor in HgBr_2 discharges, while platinum, quartz, glass, etc., are not. Thus, since we are designing with these latter materials, we believe our design approach will achieve the desired results.

APPENDIX A

BUILDUP OF LASING AND SAVINGS FROM INJECTION

1. SUPER RADIANCE

Whenever optical gain is achieved in a medium as a result of stimulated emission, there is always an accompanying super-radiance consisting of amplified spontaneous emission.

It can be shown that the spectral radiance from such a super-radiating medium (in the case of high gain G and of large ratio between population of upper and lower states of the transition) can be expressed, (1)

$$B = \frac{2h\nu^3}{c^2} \cdot G(\nu), \quad (A-1)$$

where c is the velocity of light in the medium in which the measurement of brightness is being made. Now suppose we collect all the power emitted through an aperture of area A , and within the diffraction-limited solid angle $\Omega = \pi^2/\lambda^2$. Then the spectral power P collected is

$$P = A B \Omega = \pi^2 \cdot \frac{2h\nu^3}{c^2} G(\nu) \quad (A-2)$$

$$P = 2h\nu^3 \cdot G(\nu) \quad (A-3)$$

1. Yariv, A., "Quantum Electronics," 2nd edition, p. 297, Published, John Wiley & Sons, Inc., New York, 1975.

Hence, in frequency interval $\Delta\nu$, the power P emitted into the diffraction angle (into both polarizations) is

$$P = 2h\nu \cdot G \cdot \Delta\nu. \quad (A-4)$$

Around 5,000 \AA , $h\nu \cdot \Delta\nu = 47 \text{ nW/\AA}$.

Hence, for the HgBr system under discussion, the equivalent input power resulting from the spontaneous emission is 47 nW/ \AA per polarization per spatial mode.

2. THE HgBr ILO

This device will be restricted to 1 \AA spectral width and will be better than ten times diffraction limited (i.e., < 100 spatial modes). Both polarizations will be allowed. Hence, the equivalent input power from the spontaneous emission has an upper bound P_{sp} given by

$$P_{sp} = 9.4 \text{ }\mu\text{W} \quad (A-5)$$

3. BUILDUP TIME

The buildup time can be estimated by calculating the number of round-trips of the ILO needed to build from P_{sp} to P_{sat} (saturation power). A lower bound can be obtained by assuming the small-signal gain of 3.8%/cm turns on instantaneously. In the early part of the pulse cycle, the loss $\alpha \approx 0.5\%/cm$. The feedback is 36%, and the length of the active medium is 6.25 cm. Hence, the net round-trip gain G_1 will be

$$G_1 = 0.36 \exp (2 \times 0.0375 \times 62.5) = 39 \quad (A-6)$$

The number of round trips to build to the saturation power of 4.6 MW will then be

$$N = \ln \left(\frac{4.6 \times 10^6}{9.4 \times 10^{-6}} \right) / \ln G_1 = 7.3 \quad (\text{A-7})$$

Since the resonator is 1 m long, this gives a buildup time

$$\tau = 49 \text{ ns} \quad (\text{A-8})$$

The actual buildup time will be longer because we have ignored turn-on time on the pumping as well as saturation effects.

This buildup time can be markedly reduced by injecting power many orders in magnitude higher than the spontaneous equivalent input. To estimate the reduced value of the buildup time, the value of the injected power is substituted for the 9.4 μ W in relation (A-7). The resultant buildup times are indicated in Table A-1.

4. ENERGY LOSS DURING BUILDUP

Suppose the total power in the active transverse modes is initially P_0 , either from spontaneous emission or from injection, and a time varying excess gain $g(t)$ is applied. Then if there were not output coupling, the power would rise according to

$$P = P_0 \exp \left(\frac{L_d}{L_r} C \cdot \int g(t) dt \right) \quad (\text{A-9})$$

$$= P_0 \exp \left(\frac{L_d}{L_r} C \bar{g} t \right),$$

TABLE A-1. BUILDUP TIME WITH INJECTION

	1 W	10 W	100 W	1 kW	10 kW	100 kW	No Injection
Power Injected							
No. of Round Trips Needed	4.2	3.6	2.9	2.3	1.7	1	7.3
Buildup Time Saved	28 ns	24 ns	19.5 ns	15 ns	11 ns	7 ns	49 ns

where \bar{g} is the time averaged excess gain. When the output coupling is taken into account, this becomes

$$P = P_o \exp \left\{ \left(L_a \bar{g} - \ln M \right) \frac{ct}{L_r} \right\}. \quad (A-10)$$

Hence, the time taken to reach the saturation power P_s

$$\tau = \frac{L_r}{c (L_a \bar{g} - \ln M)} \cdot \ln \left(\frac{P}{P_o} \right). \quad (A-11)$$

The maximum power that could possibly be extracted from the medium is

$$P_m = AL_a g(t) \phi_s = L_a g(t) P_{sat} \quad (A-12)$$

where A is the cross-sectional area of the active medium and ϕ_s is the saturation flux density. Hence, the maximum energy lost during the buildup time τ is

$$E_{lost} = \tau \bar{g} L_a P_{sat}.$$

Hence, from relation (A-11), we have

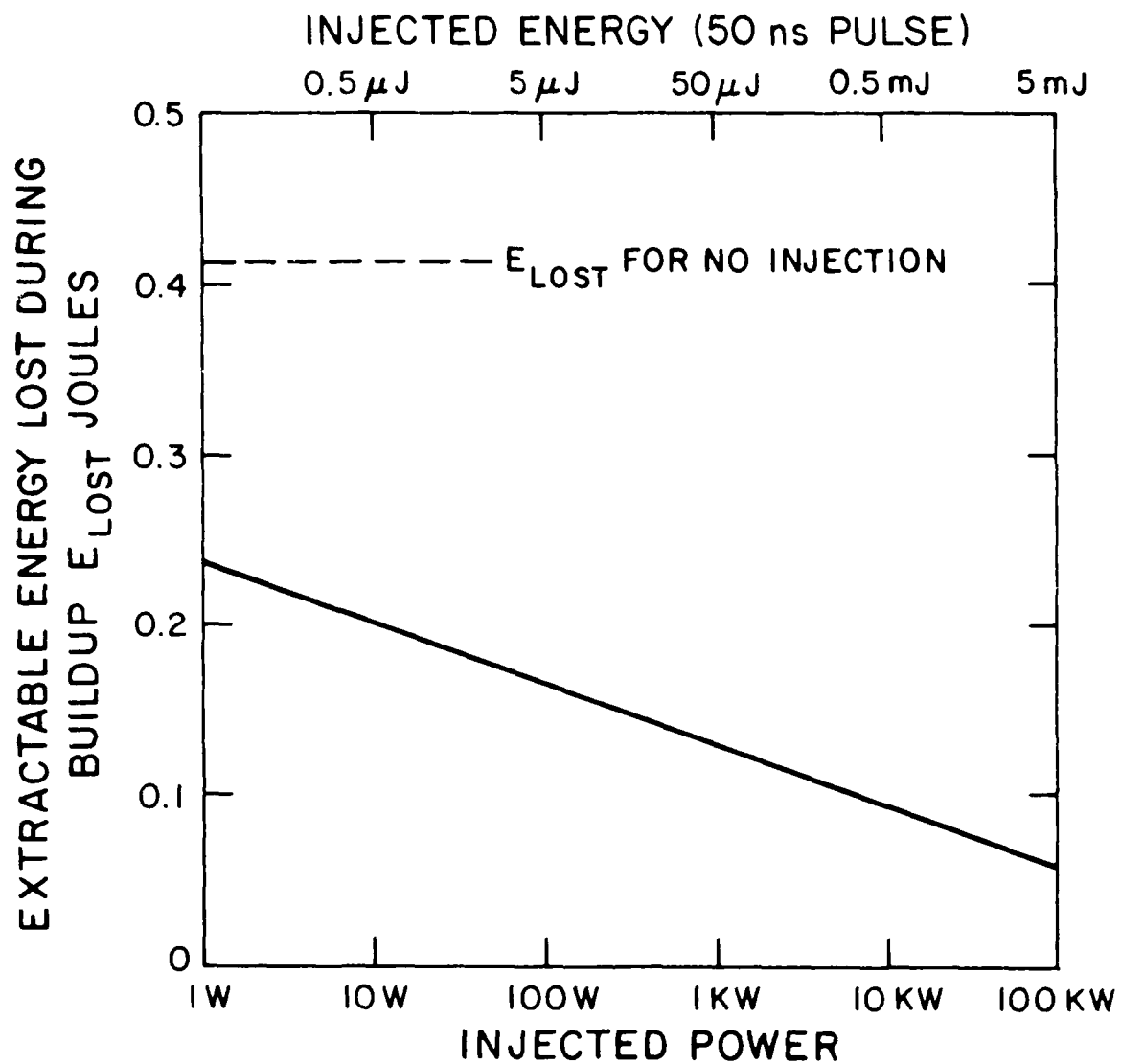
$$E_{lost} = \left(1 - \frac{\ln M}{L_a \bar{g}} \right)^{-1} \cdot \frac{L_r}{c} \cdot P_s \ln \left(\frac{P_{sat}}{P_o} \right). \quad (A-13)$$

In general $L_a \bar{g} \gg \ln M$ during buildup (or else it won't buildup), hence we have

$$E_{lost} \approx \frac{L_r}{c} \cdot P_s \ln \left(\frac{P_{sat}}{P_o} \right) \quad (A-14)$$

The saturating flux density will be $\approx 1.9 \times 10^5 \text{ W/cm}^2$, so $P_s \approx 4.6 \text{ MW}$. From relation (A-5) the equivalent input from spontaneous emission is $9.4 \text{ } \mu\text{W}$. Hence, if the ILO is not injected, then the value of E_{lost} is $\sim 0.41 \text{ J}$.

The value of E_{lost} can be reduced substantially by injection, as illustrated in Figure A-1 which shows a plot of E_{lost} vs injection. It can be seen that injection of as little as 1 mJ in a 100 ns pulse will save more than 0.3 J of E_{lost} .



J9161

Figure A-1. Saving of Lost Energy by Injection

APPENDIX B

DESIGN OF MASTER OSCILLATOR FOR INJECTION

The master oscillator must inject the ILO through a shared mirror of high reflectance. It must inject a beam which is predominantly in the TEM_{00} mode with Gaussian spot radius of ~ 0.5 mm. A stable resonator which meets these objectives is shown schematically in Figure 66. The Kogelnik and Li type analysis⁽¹⁾ gives the parameters that are tabulated in Figure 66. The 0.52 mm spot radius at the shared mirror is a sufficiently good match to ensure successful injection of the ILO.

It is anticipated that an aperture of ~ 1.4 mm diameter, placed as indicated in the resonator, will allow sufficient modes to oscillate so that the laser is not too critical in its alignment, and yet will give a beam quality from this oscillator that is within two times the diffraction limit. Such details will finally be optimized experimentally.

The expected power from this oscillator as a function of the reflectance of the shared mirror, is plotted in Figure 67. Curves are included for different values of the diffraction grating efficiency, and for an alternative design using only 10 cm length of active medium.

The curves of Figure 67 are obtained using the relation

$$\frac{\phi_{out}}{\phi_{sat}} = \frac{(1 - R_1)}{(1 + R_1)} \left(\frac{g_o}{\frac{1}{2L_a} \ln \left(\frac{1}{R_1 R_2} \right) + \alpha} - 1 \right). \quad (B-1)$$

1. Kogelnik, H. and Li, T., "Laser Beams and Resonators," Applied Optics, Vol. 5, No. 10, p. 1550, October 1966.

The appropriate values of the parameters are listed in Table B-1. The useful area of the active medium is taken as the area of the gaussian spot (6.4 mm diameter) in the medium.

TABLE B-1. PARAMETERS FOR OSCILLATOR

SYMBOL	PARAMETER	VALUE
P_{sat}	Saturation flux density	$1 \times 10^5 \text{ W/cm}^2$
r_1	Reflectance of shared mirror	92% \rightarrow 99%
r_2	Effective reflectance of grating	70% \rightarrow 90%
g_0	Small-signal gain	10%/cm
α	Loss	0.3%/cm
L_A	Length of active medium	10 cm, 20 cm
P_{out}	Output flux density	----

The need for a high reflectance for the output mirror, which is also the injection mirror for the ILO, drives the choice of reflectance to 98%. A diffraction efficiency of 80% is the appropriate value for a good commercially obtained grating at this wavelength. Hence, from Figure 67, the expected output of this oscillator will be about 3 kW, i.e., 0.15 mJ in a 50 ns pulse.

APPENDIX C

NARROW BAND HgBr LASER OPERATION

The laser bandwidth required for the Phase II program is 1 Å. As a part of our Phase I work we have demonstrated efficient energy extraction in < 1 Å by using injection locking (see Section II-A-2-o). Therefore, we do not anticipate any problems in meeting the present bandwidth requirements. However, for the planned Phase III laser, a bandwidth of < 0.2 Å is required. This has thus far not been demonstrated. In this section we discuss the physics of narrow band energy extraction relevant to HgBr lasers and suggest techniques by which the required Phase III bandwidth may be attained.

The $B(^2\Sigma^+) \times (^2\Sigma^+)$ lasing transition of HgBr has been identified as predominantly a $v' = 0 \rightarrow v'' = 22$ transition, but no work has been done to clarify the effect of rotational fine structure or isotope shift. Both are examples of inhomogeneous phenomena which in principle could lead to detrimental effects in the operation of a laser amplifier designed to amplify a narrow-spectrum injected signal: If the injected signal interacts strongly with only a fraction of the molecular inversion then amplification of spontaneous emission may eventually lead to a loss of frequency locking. In this section we take a first look at the important inhomogeneities and estimate their effect on injection locking.

The B-X is a $^2\Sigma^+$ transition, a type whose rotational fine structure is well documented.⁽¹⁾ The significant rotational quantum number is K, the total angular momentum neglecting spin. Because the spin is 1/2, each K level (except K = 0) is actually split into 2 J levels ($J = K \pm 1/2$). The selection rule $\Delta K = \pm 1$ leads to two branches a P and R branch. To our knowledge no spectroscopy of HgBr (or any similar diatomic)

has ever been done with sufficient resolution to detect the rotational fine structure, but we can still estimate its magnitude. The position (in. cm^{-1}) of the fine structure lines may be described by ⁽¹⁾

$$\nu = \nu_e + 2 \bar{B}m - (\Delta B) m^2 \quad (\text{C-1})$$

where ν_e is the electronic frequency; \bar{B} the average of the rotational constant $(B_u + B_l)/2$ of the upper (B) and lower (X) level; $\Delta B = B_l - B_u$; and

$$m = K_l \text{ for the P branch}$$

$$= K_u + 1 \text{ for the R branch}$$

$$K_l = 0, 1, 2, \dots$$

The rotational constant of either electronic level may be estimated from

$$B \cong \frac{h}{8\pi^2 c \mu r_e^2} \quad (\text{C-2})$$

where μ is the reduced mass (57 amu) of HgBr and r_e the internuclear separation of HgBr. To our knowledge r_e has never been measured, but that of a similar diatomic, HgCl, has been measured to be $2.2 \times 10^{-8} \text{ cm}^1$. We expect r_e to be very nearly the same for HgBr. Thus we obtain from Eq. (C-2)

1. Herzberg, G., Diatomic Molecules (Van Nostrand, New York, 1963).

$$B = 0.07 \text{ cm}^{-1} \quad (\text{C-3})$$

From the empirical relationship⁽¹⁾ between r_e and the vibrational constant ω_e

$$r_e^2 \omega_e = \text{constant} \quad (\text{C-4})$$

and Eq. (C-2) we may now estimate the difference ΔB between rotational constants to be

$$\Delta B \cong 0.02 \text{ cm}^{-1}$$

where we have used the values⁽²⁾ $\omega_e(X) = 187$, $\omega_e(B) = 135 \text{ cm}^{-1}$. Thus we estimate that $\bar{B} = 0.06 \text{ cm}^{-1}$.

The laser operates at a temperature of $\sim 500^\circ\text{K}$. In thermal equilibrium the rotational-level population distribution of the B-level is given by

$$N(K_u) = (2K_u + 1) e^{-B_u K_u (K_u + 1) hc/kT} \quad (\text{C-5})$$

which for $B_u = 0.05 \text{ cm}^{-1}$ and $T = 500^\circ\text{K}$ peaks at $K_u \cong 60$. This implies that about 100 upper rotational levels are significantly populated. Since the line strengths of the fine-structure transitions are proportional to K for $K \gg 1$,⁽¹⁾ we expect the intensities of the transitions to be proportional to $K_u N(K_u)$. From Eq. (C-1) we estimate that the P and R branches are about 50 cm^{-1} wide and that they are separated by much less than their widths (about 10 cm^{-1}).

2. Wieland, K., Z. Electroch. 64, 761 (1960).

with sufficient resolving power the fine structure of the $\delta\lambda$ transition could be resolved, since the separation between adjacent rotational lines is greater than the Doppler width ($\approx 0.02 \text{ cm}^{-1}$). In the absence of collisions, extraction of laser power from a small number of rotational lines could be difficult. Under HgBr lasing conditions (2 Amagats Ar gas, $\sim 3 \times 10^{14}$ electrons/cm³, 300-ns laser pulse) however, we estimate that collisions will continuously equilibrate the populations of the rotational levels, even if all the laser energy is being extracted on a small number of fine-structure transitions. Our estimate is based on a comparison with CO₂, for which it is known^(3,4) that at a background density of ~ 1 Amagat the rotational-level equilibration time is $\tau_R \approx 0.15 \text{ ns}$; extraction on a single line depletes one rotational level, which is continuously repopulated at a rate $R = f/\tau_R$, where f is the fractional thermal population in that level. Extrapolating to HgBr we expect an even shorter τ_R (since the rotational levels are more closely spaced than those of CO₂) and an f of 0.02, hence we expect $R \approx 10^6 \text{ sec}^{-1}$. This rate alone should suffice to continuously repopulate a single rotational level from which laser power is being extracted. The presence of electrons will increase R still further and make this aspect of efficient single-line extraction even more promising. In addition, for simultaneous extraction from several levels R is multiplied by the number of levels; if we wish to extract with a 1 cm^{-1} (0.2 \AA) spectral-width laser the number of levels involved is on the order of 10.

We turn our attention to the other major source of inhomogeneity: the isotope shift. The two isotopes of Br, Br⁷⁹, Br⁸¹, of nearly equal abundance, are responsible for the largest shift (37 cm^{-1}) which was resolved in the spectroscopic work

3. Schappert, G., *appl. Phys. Lett.* 23, 319 (1973).

4. Feldman, B., *IEEE J. Quant. Electr.* QE-9, 1070 (1973).

of Ref. 2. The shifts due to the 5 isotopes of Hg are about a factor of 5 smaller and have not been resolved. Because of the large widths of the P and R branches (as discussed above) we expect that 1 cm^{-1} bandwidth extraction from the various molecules containing different Hg isotopes to be possible. From the presently available information it is difficult to say whether 1 cm^{-1} extraction from a medium containing both isotopes of Br will be as efficient as broadband extraction. Therefore, it may be necessary to use gas containing only one isotope of Br in a device designed to amplify as a 1 cm^{-1} spectral width signal.

Finally, we remark on an aspect which in our opinion is the most likely to produce line broadening in an amplifier: The central frequency portion of the injected signal may strongly saturate the available gain, while the spectral wings of the injected signal may see a larger (less saturated) gain. This effect could conceivably introduce an increase by a factor of the order of 2 in the spectral of the amplified signal over that of the injected light. Fortunately, this effect is easily overcome by injecting a signal with a spectral width narrower than that desired in the amplified signal and/or by carefully suppressing the spectral wings of the injected signal.

DISTRIBUTION LIST

Department of the Navy
Naval Ocean Systems Center
271 Catalina Boulevard
San Diego, CA 92152
Attn: Code 4232 (photoreproducible & 9 copies)

Defense Advanced Research Projects Agency
1400 Wilson Boulevard
Arlington, VA 22209
Attn: LTC R.P. Benedict/DEO (1 copy)

END

12-87

DTIC